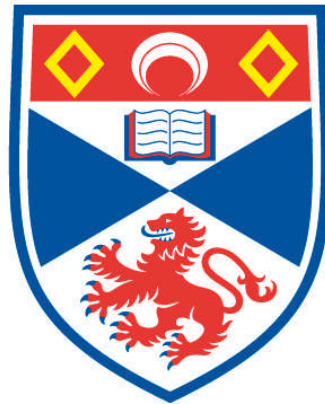


**AN ANALYTICAL, PHENOMENOLOGICAL AND
NUMERICAL STUDY OF GEOPHYSICAL AND
MAGNETOHYDRODYNAMIC TURBULENCE IN TWO
DIMENSIONS**

Luke A. K. Blackbourn

**A Thesis Submitted for the Degree of PhD
at the
University of St Andrews**



2013

**Full metadata for this item is available in
Research@StAndrews:FullText
at:**

<http://research-repository.st-andrews.ac.uk/>

Please use this identifier to cite or link to this item:

<http://hdl.handle.net/10023/4291>

This item is protected by original copyright

**This item is licensed under a
Creative Commons License**

An analytical, phenomenological and numerical study of geophysical and magnetohydrodynamic turbulence in two dimensions

by

Luke A. K. Blackbourn



University of
St Andrews

Submitted in conformity with the requirements
for the degree of Doctor of Philosophy
School of Mathematics and Statistics
University of St Andrews

November 18, 2013

Abstract

In this thesis I study a variety of two-dimensional turbulent systems using a mixed analytical, phenomenological and numerical approach. The systems under consideration are governed by the two-dimensional Navier–Stokes (2DNS), surface quasigeostrophic (SQG), alpha-turbulence and magnetohydrodynamic (MHD) equations. The main analytical focus is on the number of degrees of freedom of a given system, defined as the least value N such that all n -dimensional ($n \geq N$) volume elements along a given trajectory contract during the course of evolution. By equating N with the number of active Fourier-space modes, that is the number of modes in the inertial range, and assuming power-law spectra in the inertial range, the scaling of N with the Reynolds number Re allows bounds to be put on the exponent of the spectrum. This allows the recovery of analytic results that have until now only been derived phenomenologically, such as the $k^{-5/3}$ energy spectrum in the energy inertial range in SQG turbulence. Phenomenologically I study the modal interactions that control the transfer of various conserved quantities. Among other results I show that in MHD dynamo triads (those converting kinetic into magnetic energy) are associated with a direct magnetic energy flux while anti-dynamo triads (those converting magnetic into kinetic energy) are associated with an inverse magnetic energy flux. As both dynamo and anti-dynamo interacting triads are integral parts of the direct energy transfer, the anti-dynamo inverse flux partially neutralises the dynamo direct flux, arguably resulting in relatively weak direct energy transfer and giving rise to dynamo saturation. These theoretical results are backed up by high resolution numerical simulations, out of which have emerged some new results such as the suggestion that for alpha turbulence the generalised enstrophy spectra are not closely approximated by those that have been derived phenomenologically, and new theories may be needed in order to explain them.

Acknowledgements

I would first like to thank Dr Chuong Tran, without whom this work would not have been possible, and whose patience and insight have been an inspiration during the write-up of this thesis, and Prof. David Dritschel, who introduced me to scientific computing, and has provided much support and helpful advice over the past four years. I am indebted to Dr Richard Scott for providing the code that got the whole project started, and the open source community, as well as the Max Planck Institute for Solar System Research, for providing the tools, free of charge, that I have used in every aspect of the numerical simulations.

I would also like to thank the current and past members of the Vortex Dynamics group, who have assisted me along the long road to submission, both professionally and personally, as well as the members of ‘geek soc’, who have helped me to broaden my mathematical horizons significantly.

Finally, but certainly not least, I would like to thank all of my family and friends who have supported me and without whom I would have probably not stepped outside the office for the past month, in particular my parents whose love and guidance have brought me to where I am today.

I am grateful to the Engineering and Physical Sciences Research Council (EPSRC) for their financial support.

Declaration

I, Luke Blackburn, hereby certify that this thesis, which is approximately 41,300 words in length, has been written by me, that it is the record of work carried out by me and that it has not been submitted in any previous application for a higher degree.

I was admitted as a research student in September 2009 and as a candidate for the degree of Doctor of Philosophy in September 2009; the higher study for which this is a record was carried out in the University of St Andrews between 2009 and 2013.

Date: **Signature of Candidate:**

I hereby certify that the candidate has fulfilled the conditions of the Resolution and Regulations appropriate for the degree of Doctor of Philosophy in the University of St Andrews and that the candidate is qualified to submit this thesis in application for that degree.

Date: **Signature of Supervisor:**

In submitting this thesis to the University of St Andrews I understand that I am giving permission for it to be made available for use in accordance with the regulations of the University Library for the time being in force, subject to any copyright vested in the work not being affected thereby. I also understand that the title and the abstract will be published, and that a copy of the work may be made and supplied to any bona fide library or research worker, that my thesis will be electronically accessible for personal or research use unless exempt by award of an embargo as requested below, and that the library has the right to migrate my thesis into new electronic forms as required to ensure continued access to the thesis. I have obtained any third-party copyright permissions that may be required in order to allow such access and migration, or have requested the appropriate embargo below.

The following is an agreed request by candidate and supervisor regarding the electronic publication of this thesis: access to printed copy and electronic publication of thesis through University of St Andrews.

Date:

Signature of Candidate:

Signature of Supervisor:

Contents

Abstract	ii
Acknowledgements	iii
Declaration	iv
Contents	v
List of Notations	ix
1 Introduction	1
1.0 Published papers	1
1.1 The classical theory of turbulence	1
1.1.1 The two-dimensional case	7
1.1.2 Other two-dimensional turbulent systems	10
1.2 Dissipation rates and spectra in turbulence	11
1.3 A dynamical systems approach to turbulence	16
1.3.1 Lyapunov exponents and the number of degrees of freedom	17
1.3.2 Commonly used results	22

CONTENTS	vii
1.4 Numerical Methods.	25
1.4.1 The pseudospectral method and fast fourier transform	28
1.4.2 Fourth-order Runge–Kutta and integrating factor	30
2 The Navier-Stokes Equations	35
2.1 Introduction	35
2.2 Number of degrees of freedom	40
2.2.1 Degrees of freedom using the energy norm	42
2.2.2 Degrees of freedom using the enstrophy norm	43
2.3 Forced-dissipative Navier–Stokes	46
2.3.1 A theoretical understanding of the effects of Ekman drag	50
2.3.2 Simulation results	55
2.4 Concluding remarks	60
3 The Surface Quasigeostrophic Equation	64
3.1 Introduction	64
3.2 Analysis	68
3.2.1 Lyapunov stability analysis and degrees of freedom	69
3.2.2 Inertial-range scaling	71
3.3 Simulations	75
3.3.1 Simulations with bimodal initial conditions	76
3.3.2 Simulations with trimodal initial conditions	80
3.4 Conclusion	85
4 A Family of Generalised Models of 2D Turbulence	87

4.1	Introduction	87
4.2	Smoothness and locality of transfer in physical and Fourier space	91
4.3	Numerical results	95
4.4	Conclusion	111
5	Magnetohydrodynamics	116
5.1	Introduction	116
5.2	Triad analysis	121
5.3	Degrees of freedom	125
5.4	Limit of zero and infinite Prandtl Number	129
5.4.1	Theoretical understanding	129
5.4.2	Numerical results	133
5.5	Dynamical behaviour in the moderate and strong advection regimes	143
5.5.1	Moderate advection regime	144
5.5.2	Strong advection Regime	151
5.6	Conclusion	164
6	Summary and outlook	171
	Bibliography	177

\mathbf{u}	velocity
\mathbf{b}	magnetic field
ω	vorticity
θ	generalised vorticity / potential temperature
ψ	streamfunction
a	magnetic potential
p	pressure
j	current
U	characteristic velocity scale
L	characteristic length scale
E	energy (when unambiguous)
$E_{\mathbf{u}}$	kinetic energy
$E_{\mathbf{b}}$	magnetic energy
$E_{tot} = E_{\mathbf{u}} + E_{\mathbf{b}}$	total energy
$r = E_{\mathbf{b}}/E_{\mathbf{u}}$	magnetic-to-kinetic energy ratio
$r_0 = r(t = 0)$	initial magnetic-to-kinetic energy ratio
Z	enstrophy
E_g	generalised energy
Z_g	generalised enstrophy
ϵ	energy dissipation rate
χ	enstrophy dissipation rate
T	Time of maximum dissipation
$\epsilon_T = \epsilon(t = T)$	maximum energy dissipation rate
\mathcal{E}	energy spectrum
\mathcal{Z}	enstrophy spectrum
k_ν	classical (Kolmogorov) dissipation wavenumber
k_T	Taylor microscale wavenumber
k_d	dissipation wavenumber based on number of active modes

$\langle \cdot \rangle$	domain average
$[\cdot]$	dimension of
$\nabla^\perp = (\partial_y, -\partial_x)$	perpendicular gradient
$\mathbf{k}^\perp = (k_y, -k_x)$	perpendicular wavenumber
R	linear numerical resolution
2D	two-dimensional
3D	three-dimensional
NS	Navier–Stokes
SQG	surface quasigeostrophic
MHD	magnetohydrodynamic
CFL	Courant–Friedrichs–Lewy condition
BKM	Beale–Kato–Majda criterion
CKS	Caffisch–Klapper–Steel criterion
C_c	Courant number

Chapter 1

Introduction

1.0 Published papers

Much of this thesis is based on a number of papers published during the course of my PhD. Chapter 2 is based on Tran *et al.* (2009) and Blackburn & Tran (2011), published in Physical Review E. Chapter 3 is partially based on Tran *et al.* (2011), which is published in the Journal of Fluid Mechanics. Chapter 5 is based on Blackburn & Tran (2012), published in the Journal of Fluid Mechanics, Tran & Blackburn (2012) which is published in the journal Fluid Dynamics Research, Tran *et al.* (2013*a*) which is published in the Journal of Fluid Dynamics, and Blackburn & Tran (2013) which has been submitted to the journal Physics of Fluids.

1.1 The classical theory of turbulence

Turbulence is a ubiquitous property of our world, with examples such as tobacco smoke curling in air, milk mixing into tea, and air turbulence causing rough aeroplane flights universally recognised. The fascination with the beauty and mystery of turbulence has a long and illustrious history, from the writings of the Roman poet Lucretius,

through the drawings of Leonardo da Vinci, and it has captured the imagination of some of the world’s most famous scientists. The field embraces large swathes of mathematics and physics, from fractals to quantum field theory, from functional analysis to engineering. Yet many basic properties of turbulence are still not understood, indeed there is no rigorous mathematical definition of turbulence, just a list of ‘typical’ properties of turbulent systems, such as high irregularity, chaotic and rotational motion, and many fundamental questions remain unanswered. This disparity between the almost universality of, and lack of understanding about, turbulent systems makes this research area both important and fascinating.

While turbulent theory has been a topic of interest for millennia, it is only within the last two centuries that progress has been made on understanding this complex subject. Early work by Bernoulli (1738) and Euler (1757) paved the way for the mathematical foundation, which was solidified in the 19th century by the work of Navier, Stokes, Cauchy, Poisson and Saint-Venant (see *e.g.* (Navier, 1822; Stokes, 1845)), to produce the famous Navier–Stokes (NS) equations, which govern the evolution of the velocity field in an incompressible Newtonian fluid,

$$\frac{\partial \mathbf{u}}{\partial t} + \mathbf{u} \cdot \nabla \mathbf{u} = -\nabla p + \nu \Delta \mathbf{u}, \quad (1.1)$$

$$\nabla \cdot \mathbf{u} = 0, \quad (1.2)$$

where \mathbf{u} is the velocity field, p is the pressure and ν is the kinematic viscosity. However it was another century before much progress was made on these equations. Many of the earlier results were phenomenological in nature, and derived from experiments. Reynolds (1883) pioneered many experimental techniques, and popularised the idea of what is now known as the Reynolds number, the ratio of the strength of the inertial forces to viscous forces, in categorising flows. There are a number of different definitions of the Reynolds number, with the most well-known begin

$$Re = \frac{UL}{\nu} \quad (1.3)$$

where U is some ‘typical’ large-scale velocity and L is a ‘typical’ length scale of the system. This definition comes about through nondimensionalising the NS equation by redefining the velocity and length scales

$$\mathbf{x} = L\tilde{\mathbf{x}}, \quad (1.4)$$

$$\mathbf{u} = U\tilde{\mathbf{u}}, \quad (1.5)$$

$$t = \frac{L}{U}\tilde{t}, \quad (1.6)$$

to give

$$\frac{\partial \tilde{\mathbf{u}}}{\partial \tilde{t}} + \tilde{\mathbf{u}} \cdot \tilde{\nabla} \tilde{\mathbf{u}} = -\tilde{\nabla} \tilde{p} + \frac{1}{Re} \tilde{\Delta} \tilde{\mathbf{u}} \quad (1.7)$$

where $\tilde{\nabla} = \partial_{\tilde{\mathbf{x}}}$. As a general rule high Reynolds number flow is turbulent and thus chaotic, while at low Reynolds number it is laminar and behaves essentially linearly. The motion in a fluid is often understood as consisting of large numbers of eddies of different sizes, with the dynamics of the system largely controlled by their breakup, which leads to the following thought experiment. For a set small value of ν consider a large-scale eddy, with velocity and length scales U and L of order unity, which corresponds to a large Reynolds number. This eddy is then virtually inviscid, with the nonlinear inertial forces acting on it far more strongly than the viscous stresses. Under the action of the nonlinear terms these large-scale eddies are observed to break up into smaller eddies, passing their energy downscale. With this breakup the eddy size L decreases, meaning that smaller eddies effectively have larger Reynolds numbers, until the eddy breakup reached such small scales that viscosity becomes important and the energy is lost to mechanical friction. This is the basis of the ‘Richardson cascade’ (Richardson, 1922) which suggested that, in a turbulent flow, energy is continually passed down from the large-scale structures to the small scales, where it is destroyed by viscous stresses. Richardson’s ideas were expanded through the groundbreaking work of Kolmogorov in his set of papers that effectively founded the field of mathematical

analysis of turbulence (Kolmogorov, 1941*a,b,c*). By treating the velocity components as statistically homogeneous isotropic random variables, an assumption which could be expected to hold over a range of length scales for flows with large Reynolds numbers, Kolmogorov derived the ‘local scale of turbulence’

$$\lambda = (\nu^3/\bar{\epsilon})^{1/4}, \quad (1.8)$$

the turbulent time-scale

$$\sigma = \sqrt{\nu/\bar{\epsilon}} \quad (1.9)$$

and the equation describing the variance of the velocity increment

$$\overline{|u_i(\mathbf{x} + \mathbf{r}) - u_i(\mathbf{x})|^2} = C\bar{\epsilon}^{2/3}r^{2/3}, \quad (1.10)$$

where u_i is the i th component of the velocity field, the overbar denotes the time average, $\bar{\epsilon}$ is the mean energy dissipation rate per unit mass and $r = |\mathbf{r}|$. These results rely on the assumption that as $\nu \rightarrow 0$ the energy dissipation rate approaches a finite non-zero value. In three dimensions this assumption is generally accepted, while Taylor (Taylor, 1917) pre-empted this when he noted that ‘eddy motion must tend to produce . . . very large vorticity . . . in a very small volume. It is only in this way that the effect of viscosity can make itself felt in a fluid of very small viscosity.’ While Kolmogorov’s derivation of these laws is rather in-depth, they can be derived using the following argument, taken from Davidson (2004). Let u and v be typical velocities associated with the largest and smallest eddies, with l and η the length scales of the largest and smallest structures. It is observed that eddies tend to break up on the timescale of their turnover time, so large-scale eddies with energy u^2 break up on a timescale of l/u , giving an energy transfer rate of around $\Pi = u^3/l$. For steady-state turbulence this must match the small-scale energy dissipation rate, which is given by $\epsilon \sim \nu S_{ij}S_{ij}$ where S_{ij} is the rate of strain associated with the smallest eddies, $S_{ij} \sim v/\eta$. Equating Π and ϵ and noting that at the smallest scales the Reynolds number $Re = v\eta/\nu$ should be of order unity,

we obtain the Kolmogorov results.

The energy transfer comes about through the straining action of larger-scale vortices on smaller-scale vortices, which was expected to be a local interaction since the action of the very large scales produces what is effectively a constant background flow, while the very small-scale vortices act as random variables, meaning they effectively cancel each other out. It is this idea of scale-local transfer which means that the Fourier-space representation, which automatically amplifies the importance of scale, is such a useful tool (see *e.g.* Batchelor & Townsend, 1949, p239). The Fourier-space equivalent of the Kolmogorov scaling above says that there is a self-similar energy spectrum

$$\mathcal{E}(k) = C\bar{\epsilon}^{2/3}k^{-5/3} \quad (1.11)$$

where $\mathcal{E}(k)$ gives the energy present at scales $1/k$ (Obukhov, 1941*a,b*). This spectrum extends down to the dissipation wavenumber $k_\nu \sim 1/\lambda = (\bar{\epsilon}/\nu^3)^{1/3}$, around which most dissipation occurs, and after which dissipative effects are expected to cause it to exponentially decay. The total energy E is then given by

$$E(t) = \int_0^{k_\nu} \mathcal{E}(k) dk. \quad (1.12)$$

There are as yet no analytical results that will, given a turbulent system, yield the form of the energy spectrum. While it can be obtained from (1.10) using the fact that if the second order structure function has the power law $\overline{|u_i(\mathbf{x} + \mathbf{r}) - u_i(\mathbf{x})|^2} \propto r^n$ then for $0 < n < 2$ the energy spectrum has the form $\mathcal{E}(k) \propto k^{-(n+1)}$ (Frisch, 1995), the most usual method nowadays is based on the following dimensional analysis arguments. We assume that in the inertial energy-cascading range the energy spectrum depends only on the mean energy dissipation rate $\bar{\epsilon}$ and the wavenumber k , which have dimensions $[\bar{\epsilon}] = L^2T^{-3}$ and $[k] = L^{-1}$ respectively, where L is the unit of length and T is the unit of time. Finally the energy spectrum should have units $[\mathcal{E}(k)] = L^3T^{-2}$. Assuming that $\mathcal{E}(k) = C\bar{\epsilon}^\alpha k^\beta$, where C is a dimensionless constant, and solving the resulting two

linear equations in α and β gives the Kolmogorov form of the energy spectrum $\mathcal{E}(k) = C\bar{\epsilon}^{2/3}k^{-5/3}$. As it turns out, in three dimensions this seems to be the correct form, with much experimental and numerical evidence backing it up, and it is remarkable that such a simple argument can give such precise results. The production and maintenance of such an energy spectrum in the presence of a large-scale forcing relies on a steady and viscosity-independent energy flux, which makes it possible to rid the virtually inviscid energy inertial range of the injected energy, allowing for a statistical steady state to be established. This necessarily entails the production of small scales, and plays a key role in the possible development of singularities. The mechanism for the growth of the smallest scales in the system is found by taking the curl of equation (1.1) to give the evolution of the vorticity

$$\frac{\partial \boldsymbol{\omega}}{\partial t} + (\mathbf{u} \cdot \nabla) \boldsymbol{\omega} = (\boldsymbol{\omega} \cdot \nabla) \mathbf{u} + \nu \Delta \boldsymbol{\omega} \quad (1.13)$$

where $\boldsymbol{\omega} = \nabla \times \mathbf{u}$. The first term on the right hand side, which is known as the vortex stretching term, controls the growth of the vorticity, which is a manifestation of the transfer of energy downscale. The relationship between the growth of the vorticity and possibly singularity development is embodied in the famous Beale–Kato–Majda (BKM) criterion (Beale *et al.*, 1984) which states that smoothness of solutions is controlled by the time integral of the maximum vorticity. A ‘strong’ flux may be expected to be able to transfer significant amounts of energy downscale to wavenumber k_ν even in the limit of large k_ν (*i.e.* small ν). In this case the inviscid system could possibly produce finite-time singularities. If, however, the flux is ‘weak’, energy may not be transferred downscale fast enough in the inviscid limit, so dissipation rates may decay pointwise in time as $\nu \rightarrow 0$. There is as yet no analytical method for showing the strength of the downscale flux, which is produced by the extremely complex interactions between all of the Fourier modes of the system. However, phenomenological arguments can give some insights. Looking at the individual triad interactions that make up the nonlinear terms of the equation, and which drive the flux, can give information about the flux strength,

which in turn can help one to understand the dynamics of the system.

In the years since Kolmogorov's 1941 papers much time and effort has been spent trying to get a deeper understanding of turbulence, especially the places where Kolmogorov's theories partially break down, for example the problem of intermittency, which itself has led to many interesting new areas of mathematics including the study of multifractals. Yet in spite of all the work that has been expended there are still many outstanding issues regarding three-dimensional (3D) NS turbulence, most famously the question of the existence and smoothness of solutions. This question has been named by the Clay Institute as one of the Millennium problems (Fefferman, 2000). Given the challenging nature of 3DNS turbulence, researchers started looking into two-dimensional (2D) models that could give all of the dynamics of 3D turbulence, without the same level of mathematical difficulty. It is these 2D systems that we shall examine in this thesis.

1.1.1 The two-dimensional case

The 2DNS equation is at first sight similar to its 3D counterpart, in particular it obeys the same advection-diffusion equation (1.1). The differences become apparent when one studies the equation for the evolution of the vorticity $\omega = (\nabla \times \mathbf{u}) \cdot \mathbf{k}$,

$$\frac{\partial \omega}{\partial t} + \mathbf{u} \cdot \nabla \omega = \nu \Delta \omega. \quad (1.14)$$

The major obvious difference to 3D turbulence is that equation (1.14) is missing the vortex-stretching term on the right-hand side which has the effect that in two dimensions there are two inviscidly conserved positive-definite quantities, rather than the one in 3D turbulence, namely the energy $E = \frac{1}{2} \|\mathbf{u}\|^2$ and the enstrophy $Z = \frac{1}{2} \|\omega\|^2$. These extra conservation laws may be expected to change the dynamics of the system, and this is indeed the case, a fact that was noticed early on in the development of turbulent theory. In Taylor (1917) it was argued from experimental data that, because mean eddy

velocity in wind with a large mean flow is independent of direction, that is $\bar{v}^2 = \bar{u}^2 = \bar{w}^2$, eddies that form from the friction between the air and the ground are intrinsically 3D, with ‘some relationship between u , the component of eddy velocity in the direction of the wind, and the other two components’ (Taylor, 1917, p72). It was also noted that an appreciable fraction of the wind energy could only be dissipated if there were very large magnitudes of vorticity concentrated into very small sets with Taylor once again showing amazing foresight by noting in the same paper that ‘[i]n order that regions of large vorticity may occur it is necessary that the motion be three-dimensional, for the vorticity of any portion of a fluid remains constant during two-dimensional motion’. (a very astute observation that is later born out through ideas concerning multifractal sets). Since in two dimensions vortex stretching is absent and the maximum vorticity decays, this scenario cannot come about.

Around three decades later Lee (1951) showed that two-dimensional turbulence cannot satisfy Kolmogorov’s turbulence hypothesis, and attempting to impose the classical $k^{-5/3}$ energy spectrum and forward energy cascade results in a mathematical contradiction, once again due to the conservation of vorticity and lack of vortex stretching. Just two years later, Fjørtoft (1953) showed that in two dimensions the nonlinear term can be described in terms of triad interactions that preserve both the energy and enstrophy, and because of this interactions tend to transfer energy to smaller wavenumber (the inverse cascade) and transfer enstrophy to higher wavenumber (the direct cascade). This is in stark contrast to the behaviour in three dimensions where energy is transferred downscale. However Fjørtoft did not make any predictions about the form of the ranges through which the energy and enstrophy would be transferred.

A decade later, a series of papers by Kraichnan, Leith and Batchelor (KLB) really set the stage for the study of 2D turbulence by studying it as a system in its own right and applying Kolmogorov’s theories in the light of the previous results by Lee, and Fjørtoft. Kraichnan (1967) started by studying the interactions that drove the transfer of energy and enstrophy in 2D turbulence. By using similarity arguments and noting

that a persistent flux through an inertial range should be wavenumber independent, Kraichnan envisaged the existence of two inertial ranges. One of these supported an inverse energy flux, giving an energy spectrum of the form

$$\mathcal{E}(k) = C\epsilon^{2/3}k^{-5/3} \quad (1.15)$$

where ϵ is the energy dissipation rate, in which the enstrophy transfer is identically zero, which transports energy from intermediate to low wavenumbers. Simultaneously there is the forward-transferring enstrophy inertial range, having an energy spectrum

$$\mathcal{E}(k) = C'\chi^{2/3}k^{-3}, \quad (1.16)$$

although physical arguments on the locality of the enstrophy transfer led Kraichnan to believe that this should be modified by a logarithmic term (see Kraichnan, 1971).

Two years later, Batchelor (1969) directly applied Kolmogorov's theory of 3D turbulence to the 2D decaying case, making the assumption that the forward-cascading enstrophy was equivalent to the 3D energy, including the assumption that the extension of isovorticity lines would amplify the vorticity gradients enough that the enstrophy dissipation rate χ_ν would tend towards a non-zero constant χ in the inviscid limit. On this basis Batchelor derived the same enstrophy inertial range as Kraichnan, although making the claim that the constant C' in (1.16) should be universal. Using similar arguments, the enstrophy dissipation wavenumber, where the inertial and viscous forces have comparable effects and essentially marks the end of the inertial range, was expected to be given by

$$k_\nu = \frac{\chi^{1/6}}{\nu^{1/2}}. \quad (1.17)$$

Batchelor also noted that this scaling for the enstrophy inertial range gave a logarithmic divergence of the total enstrophy in the inviscid limit, arguing that for large ν the depletion of the original enstrophy reservoir caused by its downscale transfer would eventually lead to a diminishing of the transferring flux, leading to a lower value of χ

for the statistically steady state.

1.1.2 Other two-dimensional turbulent systems

Finding a 2D system that more accurately mimics the dynamics of the 3D turbulence equations has been a motivating force in some of the study of other lower-dimensional systems, including the 1D Burgers equation (Burgers, 1940) and Constantin–Lax–Majda (CLM) model (Constantin *et al.*, 1985*c*; Ohkitani, 2011). In two dimensions one method of generating generalised models of turbulence is to alter the relationship between the advecting velocity field \mathbf{u} and the advected scalar quantity, known as the generalised vorticity and here called θ . An example of this is the SQG equation in which the generalised vorticity, which represents the potential temperature in a geophysical context, is given by $\theta = \Lambda\psi$ where Λ is the Zygmund operator, which we discuss in chapter 3. Initially introduced in meteorology as a simplification of the quasigeostrophic equations it was first studied as a possible model for the 3DNS equation because it does not suffer the same problem of nonlocality of transfer that Kraichnan noticed affect the 2DNS equation (Kraichnan, 1967), and displays a number of properties that are similar to the 3DNS system. The SQG equations, along with the 2DNS equations, are then both members of an extended family of turbulent systems, known as alpha turbulence, in which the relationship between the streamfunction and generalised vorticity is given by $\theta = \Lambda^\alpha\psi$ for some number α . In chapter 4 we study this system for a range of α between 0.5 and 4, seeing how the value of α controls the degree of nonlinearity of the system, although the connection is not as simple as it may at first seem.

The NS equations can also be altered by changing the system that they are supposed to be describing, for example changing the fluid from a viscous Newtonian fluid to one which is electrically conducting, in which case the moving charges in the fluid will create a magnetic field, in line with Maxwell’s equations, that will then feed back on the flow via the Lorentz force. This is the basis of the MHD equations, discussed in chapter 5, which we study in two dimensions. These equations have often been

dismissed as uninteresting due to Cowley's anti-dynamo hypothesis, which states that no axisymmetric magnetic field can be maintained through a self-sustaining dynamo action by an axially symmetric current (Cowling, 1934). (Note that in this thesis we use the term anti-dynamo in a slightly different context to the use here). However in chapter 5 we show that the 2D MHD equations still display very rich behaviour, with the conversion of kinetic into magnetic energy, called dynamo action in this thesis, as well as the conversion from magnetic into kinetic, known as anti-dynamo, playing vital roles in the mechanics of the system.

The first line of attack when faced with systems such as those described above is often to use phenomenological arguments to gain a deeper level of understanding. This is often done through dimensional analysis and is the basis of Kolmogorov theory. All of the systems described above have already been subject to such methods, however there are still useful avenues of inquiry, such as triad analysis which, despite having been utilised for decades, can still reveal new useful results. Phenomenology can only get you so far, however, so to provide verification we discuss a new technique, using local Lyapunov exponents, which can often analytically recover the phenomenological results. Finally, we present the results of high-resolution numerical simulations, implemented as described in subsection 1.4, with which we can test the veracity of the mathematics. These three methods, phenomenology, analysis and numerics, can be seen to greatly complement one another.

1.2 Conservation laws, dissipation rates, dissipation wavenumbers and spectra in turbulence

In this section we shall consider the basic 2D advection-diffusion equation, however much of the analysis done here can be easily transferred to other systems. The equation for the advection and diffusion of a (possibly active) scalar θ by a divergence-free 2D

velocity field $\mathbf{u} = (\partial_y \psi, -\partial_x \psi)$, where ψ is the usual streamfunction, is given by

$$\frac{\partial \theta}{\partial t} + J(\psi, \theta) = \nu \Delta \theta, \quad (1.18)$$

where ν is the diffusivity. Multiplying equation (1.18) by θ , averaging over space, and using (1.50), gives the equation for the time evolution of the variance of θ ,

$$\frac{1}{2} \frac{d}{dt} \|\theta\|^2 = -\nu \|\nabla \theta\|^2 = -\chi_g(t) \quad (1.19)$$

where we have used the fact that θ has periodic boundary conditions in the x - and y -directions. The quantities $Z_g = \frac{1}{2} \|\theta\|^2$ and $\nu \|\nabla \theta\|^2 = \chi_g$ are known as the generalised enstrophy and generalised enstrophy dissipation rate because of the 2D turbulence case when $\theta = \omega$. Similarly, multiplying by ψ and integrating gives

$$\left\langle \psi \frac{\partial \theta}{\partial t} \right\rangle = \nu \langle \psi \Delta \theta \rangle. \quad (1.20)$$

Depending on the functional relationship between θ and ψ , it may then, using integration by parts or similar, be possible to write this equation in the form

$$\frac{1}{2} \frac{d}{dt} E_g = -\epsilon_g, \quad (1.21)$$

where E_g is known as the generalised energy and ϵ_g is the generalised energy dissipation. The form of these conserved quantities can have major effects on the dynamics of the system. For example the dual conservation of energy and enstrophy in the 2DNS system puts very strong constraints on the ability of an initial energy spectrum to spread out in wavenumber space, meaning that for small viscosities enstrophy cannot spread downscale enough to get dissipated.

Given a smooth initial temperature field, say $\theta_0(x, y) = \theta(x, y, 0)$, and fixed $\nu > 0$, the dissipation rate $\chi_g(t)$ is bounded if solutions are globally regular. For ‘small enough’ values of ν , the relevant dynamical behaviour is that $\|\nabla \theta\|$ grows initially, with the

dissipation rate then achieving a global maximum, say $\chi_{g,T} = \chi_g(T)$, at some time $t = T$, before decaying to zero. In general, $\chi_{g,T}$ and T may depend on ν – a possibility intimately related to the question of finite-time blowup of inviscid solutions, or they may become independent of ν in the inviscid limit. The go-to example of this is the Burgers equation (Burgers, 1940)

$$\frac{\partial u}{\partial t} + u \frac{\partial u}{\partial x} = \nu \frac{\partial^2 u}{\partial x^2}, \quad (1.22)$$

which was originally derived as a one-dimensional model for the 3DNS equations. For positive ν a smooth initial condition $u_0(x)$ remains smooth for all time, while the energy dissipation rate $\epsilon(t) = \nu \langle |\partial_x u|^2 \rangle$ behaves as suggested above, reaching a maximum at some time $t = T$ before decaying to zero. When $\nu = 0$ equation (1.22) has the implicit travelling wave solution $u(x, t) = u_0(x - ut)$ while the derivative $\partial_x u$ satisfies

$$\partial_x u = \frac{u'_0}{1 + tu'_0} \quad (1.23)$$

which diverges as $t \rightarrow -1/u'_0(x_0)$ provided $u'_0(x_0) < 0$ for some x_0 where $u'_0(x_0)$ is the steepest slope of $u_0(x)$ occurring at $x = x_0$. These two regimes ($\nu > 0$ and $\nu = 0$) smoothly blend into each other as $\nu \rightarrow 0$ when $\epsilon_T \rightarrow -1/u'_0(x_0)$ (see Tran & Dritschel, 2010). This system nicely demonstrates the connection between singularities, the time of maximum dissipation T and the maximum dissipation rate $\chi_{g,T}$ for some turbulent system, in that if $\chi_{g,T} \rightarrow \chi_0 \neq 0$ as $\nu \rightarrow 0$, with $T \rightarrow T_0$, the inviscid solution may be expected to become unbounded at $t = T_0$. Note that, in general, T is not related to the inviscid singular time, which would correspond to the onset of sharp increase in $\epsilon(t)$ as in the case of Burgers flow (Tran & Dritschel, 2010). In the event that T grows without bound as ν is decreased (irrespective of the behaviour of $\chi_{g,T}$), then finite-time singularities are highly unlikely. Since viscous dynamics are much easier to simulate than their inviscid counterparts, the above approach can be particularly useful in addressing the issue of inviscid singularities.

The behaviour of the dissipation rate depends on the power spectrum of the scalar $\frac{1}{2}\|\theta\|^2$, which for a periodic domain is defined as

$$\mathcal{Z}(k) = \sum_{k-1/2 \leq |\mathbf{k}| < k+1/2} |\hat{\theta}_{\mathbf{k}}|^2, \quad (1.24)$$

where $\hat{\cdot}$ denotes the Fourier transform, which gives the ‘theta-density’ in scales around $1/k$. This is generally assumed to take a self-similar form $\mathcal{Z}(k) = Ck^{-\alpha}$ in the range between the large energy-containing scales and the dissipation wavenumber k_ν , after which it decays exponentially. This means that the total generalised enstrophy Z_g is equal to

$$\begin{aligned} Z_g &= \int_{k_0}^{k_\nu} \mathcal{Z}_g(k) dk, \\ &= C \int_{k_0}^{k_\nu} k^{-\alpha} dk, \end{aligned} \quad (1.25)$$

while the dissipation rate χ_g is given by

$$\begin{aligned} \chi_g &= \nu \|\nabla\theta\|^2, \\ &= \nu \int_{k_0}^{k_\nu} k^2 \mathcal{Z}(k) dk, \\ &= C\nu \int_{k_0}^{k_\nu} k^{2-\alpha} dk. \end{aligned} \quad (1.26)$$

The behaviour of the dissipation rate now depends on the value of α . In particular we can discern three cases, when $\alpha > 3$, $\alpha = 3$ and $\alpha < 3$. In the first case, when $\alpha > 3$, we then have

$$\chi_g = \frac{C\nu}{\alpha - 3} \left[k_\nu^{-(\alpha-3)} - k_0^{-(\alpha-3)} \right], \quad (1.27)$$

which will converge to zero as $\nu \rightarrow 0$ regardless of the relationship between k_ν and ν ,

as long as $k_\nu \rightarrow \infty$ as $\nu \rightarrow 0$. In the second case, if $\alpha = 3$, we have the result that

$$\begin{aligned}\chi_g &= C\nu \log k|_{k_0}^{k_\nu}, \\ &= C\nu [\log k_\nu - \log k_0],\end{aligned}\tag{1.28}$$

where now the behaviour as $\nu \rightarrow 0$ depends on the behaviour of the dissipation wavenumber k_ν , in particular if $k_\nu \sim \nu^{-\beta}$ for any $\beta > 0$, then

$$\chi_g = -C\beta\nu \log \nu - C\nu \log k_0\tag{1.29}$$

which will then still decay as $\nu \rightarrow 0$, for any β , although at a much slower rate than that when $\alpha > 3$. Finally, if $\alpha < 3$, then we have

$$\begin{aligned}\chi_g &= \frac{C\nu}{3-\alpha} k^{3-\alpha}|_{k_0}^{k_\nu}, \\ &= \frac{C}{3-\alpha} [\nu k_\nu^{3-\alpha} - \nu k_0^{3-\alpha}],\end{aligned}\tag{1.30}$$

Once again the behaviour in the inviscid limit depends on the form of k_ν . If it behaves like $\nu^{-\beta}$ as $\nu \rightarrow 0$ then we have

$$\chi_g \sim \frac{C}{3-\alpha} [\nu^{1-(3-\alpha)\beta} - \nu k_0^{3-\alpha}],\tag{1.31}$$

which will decay to zero if $\beta < 1/(3-\alpha)$, converge to some finite χ_0 if $\beta = 1/(3-\alpha)$ and diverge if $\beta > 1/(3-\alpha)$. This first case presumably represents the scenario where the flux of generalised enstrophy is not strong enough to maintain the smallest scales, while in the second case the cascade is vigorous enough to excite the dissipation wavenumber even for diminishing ν . This is expected to be what happens for 3DNS turbulence. The final case, when the exponent of χ is negative, would correspond to diverging χ_g as $\nu \rightarrow 0$, which is unphysical for the reasons described in the previous chapter.

1.3 A dynamical systems approach to turbulence

The first analytical result to be derived directly from the 3DNS equations was Kolmogorov's 4/5-th law, which states that in homogeneous isotropic turbulence the third-order structure function has the scaling

$$S_3 = \overline{|(\mathbf{u}(\mathbf{x} + \mathbf{r}) - \mathbf{u}(\mathbf{x})) \cdot \hat{\mathbf{r}}|^3} = -\frac{4}{5}\bar{\epsilon}r \quad (1.32)$$

where $r = |\mathbf{r}|$ and $\hat{\mathbf{r}} = \mathbf{r}/|\mathbf{r}|$ is the unit vector in the direction of \mathbf{r} . Since this result there has been relatively little analytical progress in answering some of the deeper questions in turbulence, indeed the very existence of solutions is only known locally in time. One of the most famous results that has come about is the Beale-Kato-Majda (BKM) Criterion (Beale *et al.*, 1984), which we mentioned above, which states that if at some time $T_* > t_0$ a solution becomes singular, we necessarily have the result that

$$\int_{t_0}^{T_*} \|\omega\|_\infty dt = \infty, \quad (1.33)$$

while the opposite also holds, in that if the integral of the maximum vorticity is bounded on some interval $[t_0, T_*)$ then the solution is regular in $[t_0, T_*]$. More recently bounds for the dimensions of the attractors of the forced 2D (Babin & Vishik, 1983; Constantin *et al.*, 1985*b*, 1988) and 3D (Constantin *et al.*, 1985*a*; Foias *et al.*, 2001; Constantin *et al.*, 1988; Gibbon & Titi, 1997) NS equations have been derived, largely based on the work of Ruelle (1982). These results have relied on the existence of a global attractor to derive global Lyapunov exponents, while in the present case of a purely dissipative system the attractor is trivial. In the next section we introduce an analytical method, introduced in Tran *et al.* (2009), that extends these methods, allowing us to compute local Lyapunov exponents that capture the local-in-time dynamics of the system, and thus doing away with the need for a global attractor.

1.3.1 Lyapunov exponents and the number of degrees of freedom

Chaotic dynamics are characterised by the stretching and folding of volume elements in phase space (solution space). In the presence of dissipation, these can be accompanied by volume contraction. For a finite-dimensional system, volume elements can eventually collapse onto complex sets of zero volume having fractal structures, whose generalised dimensions, such as the box-counting and Hausdorff dimensions, are significantly lower than the phase-space dimension. For infinite-dimensional systems, volume contraction can occur for finite-dimensional volume elements. Furthermore, given a sufficiently large positive integer N (depending on physical parameters and initial conditions), this contraction can occur for arbitrarily oriented n -dimensional volume elements following a trajectory—solution ‘curve’ in function phase space—provided that $n \geq N$. This is the case if the sum of the largest N Lyapunov exponents at each point of the trajectory $\lambda_1 \geq \lambda_2 \geq \dots \geq \lambda_N$, which can possibly be different for different trajectories, is negative. The smallest N (which will be denoted by N still) satisfying this condition thus defines the minimum dimension in phase space for which all n -dimensional ($n \geq N$) volume elements along a given trajectory contract during the course of evolution. This volume contraction means that the chaotic nature of the local dynamics can be ‘captured’ and ‘contained’ within a linear subspace having dimension not higher than N . (This subspace may continuously change along the trajectory, though its dimension does not exceed N .) For this reason, N can be thought of as an effective dimension of the dynamical system in question, in the sense that its local dynamics can be adequately described by an N -dimensional model. When an attractor (or a global attractor) exists and N is common to every trajectory having initial data containing the attractor, its box-counting and Hausdorff dimensions are both bounded from above by N (Hunt, 1996), which is conveniently defined as the number of degrees of freedom. More precisely, these are bounded from above by the Lyapunov dimension D_L , which

satisfies $N - 1 \leq D_L \leq N$ and is defined by (Kaplan & Yorke, 1979; Farmer, 1981)

$$D_L = N - 1 + \frac{1}{\lambda_N} \sum_{i=1}^{N-1} \lambda_i. \quad (1.34)$$

In this study we determine the upper bounds for a number of systems freely decaying from a smooth initial field in a doubly periodic domain of length scale L (taken to be 2π in all simulations). Note that the global attractor for this case is trivial and has zero dimension. However, the present problem can be nontrivial because it is concerned with transient dynamics, most importantly during the stage of fully developed turbulence. The bounds obtained are expressible in terms of physical parameters, generally found to scale in some way (depending on the chosen norm for the phase space) with the Reynolds number Re , which will have some suitable definition. These scaling behaviours can then be compared with heuristic arguments based on physical and mathematical estimates of the viscous dissipation wavenumber.

Consider the solution $\theta(\mathbf{x}, t)$ to some advection-diffusion equation, which for the sake of this analysis is assumed to exist for all time, starting from a smooth initial condition, which defines a trajectory through phase space. We shall consider some arbitrary point on this trajectory at a time $t = T$. Take an arbitrary orthonormal set of n phase space vectors $\{\vartheta_1, \vartheta_2, \dots, \vartheta_n\}$ which are orthonormal with respect to some inner product $\langle \cdot \rangle_*$, with the associated norm $\| \cdot \|_*$. In the linear subspace spanned by $\{\vartheta_1, \vartheta_2, \dots, \vartheta_n\}$, consider an n -dimensional ball $B(\cdot, r)$ of radius r centred at the point in the trajectory discussed above. The n -dimensional volume V of $B(\cdot, r)$ is given by

$$\begin{aligned} V &= \|\vartheta_1 \wedge \vartheta_2 \wedge \dots \wedge \vartheta_n\|_* \\ &= \|\vartheta_1\|_* \|\vartheta_2\|_* \dots \|\vartheta_n\|_* \\ &= Cr^n \end{aligned}$$

where C is a constant that depends only on the dimension and \wedge is the wedge product

(see Temam (1997) for a formal definition of the wedge product) which generalised the cross product to higher dimensions in order to study areas and volumes. The rate of change of this volume is then given by

$$\begin{aligned}
\frac{dV}{dt} &= \sum_{i=1}^n \|\vartheta_1\|_* \cdots \|\vartheta_{i-1}\|_* \frac{d\|\vartheta_i\|_*}{dt} \|\vartheta_{i+1}\|_* \cdots \|\vartheta_n\|_*, \\
&= \|\vartheta_1\|_* \cdots \|\vartheta_n\|_* \sum_{i=1}^n \frac{1}{\|\vartheta_i\|_*} \frac{d\|\vartheta_i\|_*}{dt}, \\
&= V \sum_{i=1}^n \frac{d}{dt} \ln \|\vartheta_i\|_*, \\
&\equiv V \sum_{i=1}^n \lambda_i,
\end{aligned} \tag{1.35}$$

where λ_i , which gives the exponential rate of change of the i -th phase space vector in our set, is known as the Lyapunov exponent. When this sum is negative, the volume of the n -dimensional ball $B(\cdot, r)$ contracts exponentially. If the system is dissipative, the sum of all of the Lyapunov exponents will be negative. This means that there exists an N such that

$$\sum_{i=1}^N \lambda_i < 0 \leq \sum_{i=1}^{N-1} \lambda_i. \tag{1.36}$$

However this value of N only holds for the specific subspace on which it is defined. In order to get an N that holds for all subspaces, we use the following process. At an arbitrary point on the trajectory (*i.e.* at an arbitrary instance in time $t > 0$), we calculate the greatest growth rate λ and identify the corresponding most unstable ‘direction’ by considering the problem of maximising λ with respect to all admissible ϑ . We denote by (λ_1, ϑ_1) the solution of this problem, where for convenience ϑ_1 has been normalised, *i.e.* $\|\vartheta\| = 1$. The second greatest rate λ_2 and the corresponding second most unstable direction ϑ_2 orthogonal to ϑ_1 is obtained by the same maximisation problem subject to the orthogonality constraint, *i.e.* $\langle \vartheta_1 \vartheta_2 \rangle = 0$. By repeating this procedure n times, we obtain the set $\{\vartheta_1, \vartheta_2, \dots, \vartheta_n\}$ of mutually orthonormal functions and the corresponding set of ordered rates $\lambda_1 \geq \lambda_2 \geq \dots \geq \lambda_n$. These may be defined as the first n local

Lyapunov exponents, and their existence is guaranteed since the maximisation problems are expected to return unique solutions. Note that for the conventional Lyapunov exponents, existence can be a major issue, even for low-dimensional systems of a few degrees of freedom. Note that by construction $B(\cdot, r)$ is now optimally ‘oriented’ to be least contracting. This means that if $\sum_{i=1}^n \lambda_i$ is negative, then volume contraction becomes universal for all n - or higher-dimensional balls locally centred at the point in question. Furthermore, if this point is taken arbitrarily on the trajectory, which is the case in this study, then volume contraction becomes universal along the trajectory.

We now consider the process of actually determining N . Let θ be a solution to the advection-diffusion equation (1.18) with ϑ a disturbance to this solution at some arbitrary time. Suppose that the linearised equation for some disturbance ϑ is given by

$$\vartheta_t = \mathcal{L}(\theta, \vartheta) - \nu \Delta \vartheta \quad (1.37)$$

where \mathcal{L} is linear in ϑ . By taking the scalar product ($\langle \cdot \rangle$) of (1.37) with ϑ we obtain the evolution equation for the L^2 -norm $\|\vartheta\|$,

$$\|\vartheta\| \frac{d}{dt} \|\vartheta\| = \langle \vartheta \mathcal{L}(\theta, \vartheta) \rangle - \nu \|\nabla \vartheta\|^2. \quad (1.38)$$

Evolution equations for other norms can be worked out similarly, for example the evolution of the H^1 -norm is found by multiplying (1.37) by $(-\Delta)\vartheta$ and taking the scalar product. For the rest of the section we shall assume that we are using the L^2 norm. The exponential growth (or decay) rate λ for $\|\vartheta\|$ can be readily deduced and is given by

$$\lambda = \frac{d}{dt} \ln \|\vartheta\| = \frac{1}{\|\vartheta\|^2} [\mathcal{L}(\theta, \vartheta) - \nu \|\nabla \vartheta\|^2]. \quad (1.39)$$

These rates provide a comprehensive picture of solution stability, quantitatively describing how solutions with nearby initial data disperse from one another.

The exponential rate of volume contraction or expansion is then given by

$$\frac{d}{dt} \ln V = \sum_{i=1}^n \frac{1}{\|\vartheta_i\|^2} [\mathcal{L}(\theta, \vartheta_i) - \nu \|\nabla \vartheta_i\|^2]. \quad (1.40)$$

The determination of N then reduces to minimising n such that the sum of the right-hand side of equation (1.40) is negative. We use the mathematical techniques developed in the 1980s by Babin & Vishik (1983) and Constantin *et al.* (1985*b*, 1988); Constantin (1987) for estimating the attractor dimension of forced 2DNS turbulence. See also the paper Doering & Gibbon (1991) for the same treatment in the streamfunction and vorticity setting.

Upon calculation of the number of degrees of freedom, it is possible to estimate a number of quantities that are usually calculated purely heuristically, including the energy spectrum and the exponential dissipation rate at the dissipation wavenumber. For this we shall assume that we are working with one of the classical systems where the energy dissipation rate approaches a finite non-zero limit as $\nu \rightarrow 0$, which is expected to happen for the 3DNS system and possibly the SQG and MHD systems as well. We shall then make the following two approximations: first that the number of degrees of freedom N is equivalent to the number of active Fourier modes N_c , which seems reasonable from the definition of the number of degrees of freedom as the number of independent ‘directions’ needed to fully describe the flow, and second that the active Fourier modes are those with wavenumbers less than the dissipation wavenumber k_d . We then get the relationship

$$N \approx N_c \approx \left(\frac{k_d}{k_0}\right)^d \approx \frac{L^d k_d^d}{(2\pi)^d}, \quad (1.41)$$

where the domain is assumed to be a d -torus of side length L . An optimal estimate for N automatically gives rise to an optimal estimate for k_d . At this wavenumber, the

exponential dissipation rate $r_d = \nu k_d^2$ (due to viscosity) is given by

$$r_d \propto \frac{\nu N^{1/d}}{L^2}. \quad (1.42)$$

Around k_d nonlinear and viscous effects are expected to be in balance. Hence r_d provides a quantitative measure for the strength of the system's nonlinearity, in the sense that greater r corresponds to stronger nonlinear effects.

Consider power-law energy spectra of the form $\mathcal{E}(k) = Ck^{-\alpha}$, where C is a constant, whose dimension apparently depends on the exponent α . The spectrum of $\|\nabla \mathbf{u}\|^2$ is then $2Ck^{2-\alpha}$, so the energy dissipation rate ϵ is given by

$$\epsilon \approx \frac{2\nu C}{3-\alpha} k_d^{3-\alpha} \quad (1.43)$$

for $\alpha < 3$. It follows that

$$N^{1/d} \approx L \left(\frac{\epsilon}{\nu C} \right)^{1/(3-\alpha)}. \quad (1.44)$$

Given an estimate for N in terms of L , ν and ϵ and possibly other controlled dynamical quantities, (1.44) implicitly determines α in terms of these quantities. Furthermore, (1.44) has a built-in constraint on the behaviour of ϵ , particularly in the inviscid limit.

1.3.2 Commonly used results

In this section we list a couple of mathematical results that are used in this thesis. For most of the mathematical and all of the numerical results, unless explicitly stated, we shall be working on the 2-torus Ω of side length L (which is equal to 2π for all numerical simulations) and all functions are assumed to have zero average. The domain average,

$$\langle f \rangle = \frac{1}{L^2} \int_{\Omega} f \, d\mathbf{x} \quad (1.45)$$

which is used for the usual Hilbert-space inner product, defines the usual L^2 norm

$$\|f\|^2 = \langle |f|^2 \rangle, \quad (1.46)$$

as well as the L^p norms

$$\|f\|_p^p = \langle |f|^p \rangle, \quad (1.47)$$

with all other norms defined explicitly as needed. The Jacobian of two functions θ and ψ , which is defined as

$$J(\psi, \theta) = (\partial_x \psi)(\partial_y \theta) - (\partial_y \psi)(\partial_x \theta) \quad (1.48)$$

occurs naturally in many 2D fluid dynamical systems. For differentiable functions in a periodic domain, or functions that decay at infinity, integration by parts gives the equalities

$$\begin{aligned} \langle \phi J(\psi, \theta) \rangle &= - \langle \psi J(\phi, \theta) \rangle, \\ &= - \langle \phi J(\theta, \psi) \rangle, \end{aligned} \quad (1.49)$$

which means that

$$\langle \theta J(\psi, \theta) \rangle = \langle \psi J(\psi, \theta) \rangle = 0. \quad (1.50)$$

Simple application of the product rule also gives us the result

$$\Delta J(\psi, \theta) = J(\psi, \Delta \theta) + 2J(\psi_x, \theta_x) + 2J(\psi_y, \theta_y). \quad (1.51)$$

while a simpler manipulation gives

$$J(\theta, \psi)^2 = |\nabla \theta|^2 |\nabla \psi|^2 - |\nabla \theta \cdot \nabla \psi|^2, \quad (1.52)$$

from which it immediately follows that

$$|J(\theta, \psi)| \leq |\nabla\theta||\nabla\psi| \quad (1.53)$$

where we have equality when isolines of θ and ψ are perpendicular. The Jacobian is identically zero when the isolines are parallel, which occurs when $\theta = \theta(\psi)$.

The next sets of inequalities apply to an orthonormal set of functions $\{\vartheta_i\}_{i=1}^n$. The Rayleigh-Ritz inequalities derive from the fact that for $n \gg 1$ there are approximately n eigenfunctions of the operator $(-\Delta)$ within the wavenumber radius \sqrt{n}/L . Their (repeated) eigenvalues are $(\ell^2 + m^2)/L^2$, where $\ell^2 + m^2 \leq n$. These constitute the first n eigenvalues (in nondecreasing order) of $-\Delta$ and sum up to approximately n^2/L^2 . It then follows from the Rayleigh-Ritz principle that

$$\sum_{i=1}^n \|\nabla\vartheta_i\|^2 \geq c_1 \frac{n^2}{L^2}, \quad (1.54)$$

(see *e.g.* Weinberger, 1987). In the following sections we shall be working with the energy inner product $\langle\vartheta_1, \vartheta_2\rangle_E = \langle\nabla\vartheta_1 \cdot \nabla\vartheta_2\rangle$ and the enstrophy semi-inner product $\langle\vartheta_1, \vartheta_2\rangle_Z = \langle\Delta\vartheta_1\Delta\vartheta_2\rangle$, along with their respective norms and seminorms $\|\theta\|_E = \langle|\nabla\theta|^2\rangle^{1/2}$ and $\|\theta\|_Z = \langle|\Delta\theta|^2\rangle^{1/2}$ which we shall call the ‘energy norm’ and ‘enstrophy norm’ respectively. The energy norm is a norm rather than a seminorm since we shall assume that we are working on the set of functions with zero average. For a set of vectors ϑ_i that are orthonormal with respect to the energy seminorm, that is they satisfy $\langle\vartheta_i, \vartheta_j\rangle_E = \delta_{i,j}$, we have the slightly modified inequality

$$\sum_{i=1}^n \|\Delta\vartheta_i\|^2 \geq \frac{c_2^2}{L^2} n^2, \quad (1.55)$$

while a set that is orthonormal under the enstrophy semi-norm satisfies

$$\sum_{i=1}^n \|\nabla\Delta\vartheta_i\|^2 \geq \frac{c_2^2}{L^2} n^2, \quad (1.56)$$

where c_1 is a nondimensional constant independent of the set $\{\vartheta_i\}_{i=1}^n$. It is an interesting comparison that the 2D inequality that corresponds to (1.54) is

$$\sum_{i=1}^n \|\nabla \vartheta_i\|^2 \geq c_2 \frac{n^{5/3}}{L^2}. \quad (1.57)$$

Another analytical result based on the set $\{\vartheta_i\}_{i=1}^n$ which is orthonormal under the usual inner product is the Lieb–Thirring inequality (Constantin *et al.*, 1988; Temam, 1997; Tran *et al.*, 2009), which in two dimensions is given by

$$\left\| \sum_{i=1}^n \vartheta_i^2 \right\| \leq c_2 L \left(\sum_{i=1}^n \|\nabla \vartheta_i\|^2 \right)^{1/2}. \quad (1.58)$$

We then have the similar results for a set which is orthonormal under the energy norm, giving

$$\left\| \sum_{i=1}^n |\nabla \vartheta_i|^2 \right\| \leq c_2 L \left(\sum_{i=1}^n \|\Delta \vartheta_i\|^2 \right)^{1/2}, \quad (1.59)$$

and a set which is orthonormal under the enstrophy norm, which satisfies

$$\left\| \sum_{i=1}^n |\Delta \vartheta_i|^2 \right\| \leq c_1 \left(\sum_{i=1}^n \|\nabla \Delta \vartheta_i\|^2 \right)^{1/2}. \quad (1.60)$$

In three dimensions we have the inequality

$$\left\| \sum_{i=1}^n |\vartheta_i|^2 \right\| \leq c_4 L^{3/2} \left(\sum_{i=1}^n \|\nabla \vartheta_i\|^2 \right)^{3/4}. \quad (1.61)$$

1.4 Numerical Methods.

Due to the extreme complexity of turbulent systems, it is often not yet possible to analytically verify the claims made through phenomenological arguments, for example Kolmogorov’s 5/3 power law for the energy spectrum in the inertial range of

3D turbulence. It thus often falls to experiments and numerical simulations to verify or discredit such ideas. As far as experiments go, difficulties in accurately measuring small-scale quantities, and physical factors such as the fact that in reality fluids are not a continuous medium but are actually composed of discrete atoms, make useful experimental results hard to come by, especially at very high Reynolds numbers. This makes numerical simulation an indispensable tool.

The idea of numerically calculating the solutions to partial differential equations was championed by Richardson (Richardson, 1911), who proposed the method of finite differences. Back then, of course, all calculations were done by hand, and Richardson calculated that it would take 64,000 people doing the calculations constantly to be able to keep up with physical weather patterns (Richardson (1922) p219)¹. With the meteoric rise of electronic computers after the second world war, Richardson's dreams of numerically integrating partial differential equations in reasonable time started coming true, although sadly Richardson did not live to see his ideas fully realised, dying around the time that vacuum tubes were just starting to replace transistors. The realisation of using computer simulations to verify mathematical results happened around a decade and a half later, when Batchelor (1969) adapted Kolmogorov's phenomenological arguments to 2D turbulence, where it was just about possible to put them to the test using the computation power available at the time. Although the 10×10 resolution used is small by today's standards, it was the starting point for numerous studies that have massively increased our understanding of turbulence.

Since Batchelor's (or more accurately his PhD student Robert Bray's) early simulations, there have been massive leaps forward in all areas of numerical computation. On the hardware side, computers are now unimaginably faster, with standard desktops running at around 3GHz, compared to around 0.5MHz on the EDSAC 2 used in Batchelor's time (University of York, 2013). Along with the increase in CPU speed, the size of memory has vastly increased, along with a decrease in access time, leading to fewer

¹It is interesting that in his book Richardson calls the poor people doing the calculations "computers".

computational bottlenecks. The introduction of hyperthreading, multiple-core shared-memory CPUs and high-speed networks, along with the steadily decreasing cost, has meant that high-performance hardware is nowadays readily available. To go with the hardware, there has been a massive improvement in the software used to write the simulations in. Fortran is still the language of choice for high-performance computing, and while it has been shunned by many outside the scientific computing community, it has vastly improved from the old FORTRAN, in ease of writing and number of features. Along with improvements in the language itself, much work has gone into compiler optimisation, and there are a wide range of external libraries that can be used to do common tasks such as discrete Fourier transforms.

Using the same basic methodology that Batchelor did in his 1969 paper, while using the far superior tools that are currently available, we have been able to run large numbers of high-resolution simulations of various turbulence systems, which we can then compare with the analytical and phenomenological results. While computationally derived results will never equal mathematical proof² they can give some useful insights into the systems in question.

For all of the simulations in this thesis the physical time and length scales involved are determined (although they are not explicitly given) by the initial conditions and intrinsic properties of the flow. For example by using the initial kinetic energy as well as the energy centroid wavenumber (which is equivalent to the wavenumber of a unimodal initial reservoir) it is straightforward to calculate the eddy turnover time, which defines the large-scale temporal scaling of the flow. The largest possible length scale of the flow is given by the size of the domain, which is 2π , while small length scales such as the Taylor microscale in 2DNS turbulence are given by $k_T^{-1} = \|\omega\|/\|\nabla\omega\|$.

The codebase used in this project was originally kindly provided by Richard Scott³ and used essentially unaltered to run the first set of SQG simulations as described in

²apart from some proof-by-exhaustion methods such as that of the map colouring theorem by Appel & Haken (1976).

³Department of Mathematics and Statistics, University of St Andrews

§3.3.1. This code was then re-written and modularised, using the same algorithms and data structures, into Fortran 95 to simulate the forced 2DNS equations analysed in §2.3. After this, the entire code-base was re-written in Fortran 95/03, making a number of major alterations in the data structures and subroutines used, although retaining the algorithms basic underlying algorithms. At this time the Fourier Transform used was upgraded from FFTW2 to FFTW3, and support for parallel processing using OpenMP was added. This code, with regular updates as seen fit, was used for all of the alpha turbulence and MHD simulations in chapter 4 and chapter 5, as well as the later 16384 SQG simulations described in §3.3.2. As well as extensive bug-checking, whenever the codebase was re-written a set of standard simulations were run in order to check consistency between the old and new code. All graphics produced used either the Dislin⁴ scientific data plotting libraries for the field contour plots, or using the open source gnuplot⁵ graphing utility.

1.4.1 The pseudospectral method and fast fourier transform

Many theories of turbulence emphasise the fact that transfer of energy between different scales is a vital part of the dynamics of the system. This automatically makes Fourier analysis a very useful tool, and makes the pseudospectral method, which carries out much of the work in Fourier space, an obvious choice for numerical simulations of turbulent systems. There is the added bonus that differentials in physical space correspond to multiplication by the wavenumber in Fourier space, a process which is well-suited to parallelisation. One disadvantage is that nonlinear terms are not so simple, with for example the product of two physical-space fields equivalent to a convolution in Fourier space, which necessitates R^{2d} multiplication operations, plus summations, for a linear resolution of R in d dimensions. The development of the Fast Fourier Transform, which can calculate the discrete Fourier transform of R^d points in $R^d \log R$ time, means

⁴<http://www.mps.mpg.de/dislin/>

⁵<http://www.gnuplot.info/>

that it is in fact faster to transform into physical space before carrying out nonlinear operations, do the operations in physical space, then transfer back into Fourier space. This is the basis of the pseudospectral method.

All of the simulations in this thesis make use of the FFTW (fastest Fourier transform in the west) library (Frigo & Johnson, 2005)⁶, using version 2 for the original SQG and 2DNS simulations, then moving on to version 3. FFTW is a free-software implementation of the discrete Fourier transform, available for both C and Fortran, which can work with a variety of input data, including a 2D real-to-complex Fourier and complex-to-real inverse Fourier transform which are utilised here. For a linear resolution R in two dimensions, the real physical space domain consists of $R \times R$ gridpoints, corresponding to a square periodic domain of side length 2π , while the spectral space is a grid of $R \times (R/2 + 1)$ lattice points corresponding to wavenumbers $(k_x, k_y) \in [-k_{\max} + 1, k_{\max}] \times [0, k_{\max}] \subset \mathbb{Z}^2$. The domain only needs to be half-complex (y -values from 0 to $R/2$) because the reality of the physical-space field $\theta(\mathbf{x})$ means that its Fourier transform $\hat{\theta}_{\mathbf{k}}$ satisfies the relation $\hat{\theta}_{-\mathbf{k}} = \hat{\theta}_{\mathbf{k}}^*$, where the star denotes the complex conjugate. The shape of this domain admittedly produces an anisotropy, with wavenumbers of the form $(k_x, 0)$ and $(0, k_y)$ only present up to $|\mathbf{k}| = R/2$ while wavenumbers having the form (k, k) have magnitudes up to $R/\sqrt{2}$. This does not, however, pose too many problems as long as there is sufficient dissipation to ensure that all wavenumber modes higher in magnitude than $R/2$ are negligibly excited.

One problem that arises from using the Fourier transform is that of aliasing which can cause energy that physically should be transferred to scales smaller than the grid-scale to be ‘reflected’ off the high-wavenumber spectral boundary, thus erroneously dumping energy at the intermediate scales. This problem is often negated by using Orszag’s 2/3 rule (Orszag, 1971), where the highest 1/3 wavenumbers are forced to zero at every timestep. While this method generally works well it has the effect that a relatively large portion of wavenumber space, and thus a large amount of computer

⁶fftw.org

memory, is wasted. Instead the simulations in this thesis make use of a spectral filter, used in (Hou & Li, 2007), of the form

$$\exp(-36(k/k_{\max})^{36}), \quad (1.62)$$

where $k_{\max} = R/2$ is the maximum wavenumber, which is applied every time a derivative is taken. As long as there is sufficient dissipation to dampen down the highest-wavenumber components, this spectral filter is reliable in preventing aliasing artefacts. While the use of the fast Fourier transform has given us a fast and efficient method of calculating the physical-space parts of the PDE, we still need a time-stepping algorithm for the physical evolution of the system. The algorithm used in this thesis is the fourth-order Runge–Kutta algorithm, which is described, along with some modifications brought about due to the dissipation term in the equations, in the next subsection.

1.4.2 Fourth-order Runge–Kutta and integrating factor

For a typical advection-diffusion equation

$$\frac{\partial \theta}{\partial t} = \mathcal{N}(\theta, t) + \nu \Delta \theta, \quad (1.63)$$

where \mathcal{N} is some nonlinear term, the time evolution of the Fourier mode $\hat{\theta}_{\mathbf{k}}$ is governed by

$$\frac{\partial}{\partial t} \hat{\theta}_{\mathbf{k}}(t) = \hat{\mathcal{N}}(\hat{\theta}_{\mathbf{k}}, t) - \nu |\mathbf{k}|^2 \hat{\theta}_{\mathbf{k}}, \quad (1.64)$$

where $\hat{\mathcal{N}}(\hat{\theta}_{\mathbf{k}}, t)$ is the result of transforming $\hat{\theta}_{\mathbf{k}}$ into physical space, applying the nonlinear term \mathcal{N} , then transforming back into Fourier space. For now we are going to ignore the dissipation term and concentrate on the nonlinear term. There are many time-stepping algorithms that are commonly used in the numerical integration of PDEs, with one of the most popular, which we shall be using, being the fourth-order Runge–Kutta algorithm, which fuses high accuracy (global errors in the order of $(\Delta t)^3$ for a

timestep Δt) with relative simplicity. We discretise the timestep so that $t_n = t_0 + n\Delta t$, and defining $\hat{\theta}_{\mathbf{k}}^n = \hat{\theta}_{\mathbf{k}}(t_n)$ we approximate $\hat{\theta}_{\mathbf{k}}^{n+1}$ by

$$\hat{\theta}_{\mathbf{k}}^{n+1} = \hat{\theta}_{\mathbf{k}}^n + \frac{1}{6}(K_1 + 2K_2 + 2K_3 + K_4)\Delta t \quad (1.65)$$

where

$$\begin{aligned} K_1 &= \widehat{\mathcal{N}}(\hat{\theta}_{\mathbf{k}}^n, t_n), \\ K_2 &= \widehat{\mathcal{N}}(\hat{\theta}_{\mathbf{k}}^n + K_1 \frac{\Delta t}{2}, t_n + \frac{1}{2}\Delta t), \\ K_3 &= \widehat{\mathcal{N}}(\hat{\theta}_{\mathbf{k}}^n + K_2 \frac{\Delta t}{2}, t_n + \frac{1}{2}\Delta t), \\ K_4 &= \widehat{\mathcal{N}}(\hat{\theta}_{\mathbf{k}}^n + K_3 \Delta t, t_n + \Delta t). \end{aligned} \quad (1.66)$$

The addition of the Laplacian term for the dissipation should now be a simple procedure, however we encounter a problem known as *stiffness*⁷ which can occur when the time step is constrained by the size of the eigenvalues of the dissipation term, which can vary over a couple of orders of magnitude for high resolution simulations. This new problem can be taken care of by using an integrating factor (Kassam & Trefethen, 2005), using the following method. First we define a new variable

$$\hat{\Theta}_{\mathbf{k}}(t) = \hat{\theta}_{\mathbf{k}}(t)e^{\nu|\mathbf{k}|^2 t}, \quad (1.67)$$

which, if $\hat{\theta}_{\mathbf{k}}(t)$ obeys (1.64) then evolves according to

$$\begin{aligned} \frac{\partial}{\partial t} \hat{\Theta}_{\mathbf{k}}(t) &= \left(\frac{\partial}{\partial t} \hat{\theta}_{\mathbf{k}}\right)e^{\nu|\mathbf{k}|^2 t} + \nu|\mathbf{k}|^2 \hat{\theta}_{\mathbf{k}}e^{\nu|\mathbf{k}|^2 t}, \\ &= (\widehat{\mathcal{N}}(\hat{\theta}_{\mathbf{k}}) - \nu|\mathbf{k}|^2 \hat{\theta}_{\mathbf{k}})e^{\nu|\mathbf{k}|^2 t} + \nu|\mathbf{k}|^2 \hat{\theta}_{\mathbf{k}}e^{\nu|\mathbf{k}|^2 t}, \\ &= \widehat{\mathcal{N}}(\hat{\theta}_{\mathbf{k}})e^{\nu|\mathbf{k}|^2 t}, \\ &= \widehat{\mathcal{N}}(\hat{\Theta}_{\mathbf{k}}e^{-\nu|\mathbf{k}|^2 t})e^{\nu|\mathbf{k}|^2 t}. \end{aligned}$$

⁷While there is no universally accepted definition of stiffness, see (e.g. Ascher & Petzold, 1998, p. 47) for a more thorough description.

This new variable is then numerically integrated with the Runge-Kutta scheme

$$\hat{\Theta}_{\mathbf{k}}^{n+1} = \hat{\Theta}_{\mathbf{k}}^n + \frac{1}{6}(K'_1 + 2K'_2 + 2K'_3 + K'_4)\Delta t \quad (1.68)$$

where

$$\begin{aligned} K'_1 &= \widehat{\mathcal{N}}(\hat{\Theta}_{\mathbf{k}}(t_n)e^{-\nu|\mathbf{k}|^2t_n})e^{\nu|\mathbf{k}|^2t_n}\Delta t \\ K'_2 &= \widehat{\mathcal{N}}([\hat{\Theta}_{\mathbf{k}}(t_n) + K'_1/2]e^{-\nu|\mathbf{k}|^2(t_n+\Delta t/2)})e^{\nu|\mathbf{k}|^2(t_n+\Delta t/2)}\Delta t \\ K'_3 &= \widehat{\mathcal{N}}([\hat{\Theta}_{\mathbf{k}}(t_n) + K'_2/2]e^{-\nu|\mathbf{k}|^2(t_n+\Delta t/2)})e^{\nu|\mathbf{k}|^2(t_n+\Delta t/2)}\Delta t \\ K'_4 &= \widehat{\mathcal{N}}([\hat{\Theta}_{\mathbf{k}}(t_n) + K'_3]e^{-\nu|\mathbf{k}|^2(t_n+\Delta t)})e^{\nu|\mathbf{k}|^2(t_n+\Delta t)}\Delta t \end{aligned} \quad (1.69)$$

This change of variables seems on the face of it to have turned the equations into a set that are explicitly time-dependent, with t_n as well as Δt explicit parts of the definitions of the K'_i , however it is simple to show that the t_n terms all cancel out. For the first coefficient K'_1 we have

$$\begin{aligned} K'_1 &= \widehat{\mathcal{N}}(\hat{\Theta}_{\mathbf{k}}(t_n)e^{-\nu|\mathbf{k}|^2t_n})e^{\nu|\mathbf{k}|^2t_n}\Delta t, \\ &= \widehat{\mathcal{N}}(\hat{\theta}_{\mathbf{k}}(t_n)e^{\nu|\mathbf{k}|^2t_n}e^{-\nu|\mathbf{k}|^2t_n})e^{\nu|\mathbf{k}|^2t_n}\Delta t, \\ &= \underbrace{\widehat{\mathcal{N}}(\hat{\theta}_{\mathbf{k}}(t_n))}_{\alpha}\Delta t e^{\nu|\mathbf{k}|^2t_n}. \end{aligned} \quad (1.70)$$

Similarly, we then get

$$\begin{aligned} K'_2 &= \widehat{\mathcal{N}}([\hat{\Theta}_{\mathbf{k}}(t_n) + K'_1/2]e^{-\nu|\mathbf{k}|^2(t_n+\Delta t/2)})e^{\nu|\mathbf{k}|^2(t_n+\Delta t/2)}\Delta t, \\ &= \widehat{\mathcal{N}}([\hat{\theta}_{\mathbf{k}}(t_n)e^{\nu|\mathbf{k}|^2t_n} + \frac{1}{2}\alpha e^{\nu|\mathbf{k}|^2t_n}]e^{-\nu|\mathbf{k}|^2(t_n+\Delta t/2)})e^{\nu|\mathbf{k}|^2(t_n+\Delta t/2)}\Delta t, \\ &= \underbrace{\widehat{\mathcal{N}}([\hat{\theta}_{\mathbf{k}}(t_n) + \alpha/2]e^{-\nu|\mathbf{k}|^2\Delta t/2})}_{\beta}\Delta t e^{\nu|\mathbf{k}|^2(t_n+\Delta t/2)}. \end{aligned} \quad (1.71)$$

$$\begin{aligned}
K'_3 &= \widehat{\mathcal{N}}([\widehat{\Theta}_{\mathbf{k}}(t_n) + K'_2/2]e^{-\nu|\mathbf{k}|^2(t_n+\Delta t/2)}e^{\nu|\mathbf{k}|^2(t_n+\Delta t/2)}\Delta t, \\
&= \widehat{\mathcal{N}}([\widehat{\theta}_{\mathbf{k}}(t_n)e^{\nu|\mathbf{k}|^2 t_n} + \frac{1}{2}\beta e^{\nu|\mathbf{k}|^2(t_n+\Delta t/2)}]e^{-\nu|\mathbf{k}|^2(t_n+\Delta t/2)}e^{\nu|\mathbf{k}|^2(t_n+\Delta t/2)}\Delta t, \\
&= \underbrace{\widehat{\mathcal{N}}([\widehat{\theta}_{\mathbf{k}}(t_n) + \beta/2]e^{-\nu|\mathbf{k}|^2\Delta t/2})\Delta t}_{\gamma} e^{\nu|\mathbf{k}|^2(t_n+\Delta t/2)}.
\end{aligned} \tag{1.72}$$

$$\begin{aligned}
K'_4 &= \widehat{\mathcal{N}}([\widehat{\Theta}_{\mathbf{k}}(qt_n) + K'_3]e^{-\nu|\mathbf{k}|^2(t_n+\Delta t)}e^{\nu|\mathbf{k}|^2(t_n+\Delta t)}\Delta t, \\
&= \widehat{\mathcal{N}}([\widehat{\theta}_{\mathbf{k}}(t_n)e^{\nu|\mathbf{k}|^2 t_n} + \gamma e^{\nu|\mathbf{k}|^2(t_n+\Delta t/2)}]e^{-\nu|\mathbf{k}|^2(t_n+\Delta t)}e^{\nu|\mathbf{k}|^2(t_n+\Delta t)}\Delta t, \\
&= \underbrace{\widehat{\mathcal{N}}([\widehat{\theta}_{\mathbf{k}}(t_n) + \gamma]e^{-\nu|\mathbf{k}|^2\Delta t})\Delta t}_{\delta} e^{\nu|\mathbf{k}|^2(t_n+\Delta t)}.
\end{aligned} \tag{1.73}$$

Combining the above gives

$$\begin{aligned}
\widehat{\theta}_{\mathbf{k}}(t_{n+1}) &= \widehat{\Theta}_{\mathbf{k}}(t_{n+1})e^{-\nu|\mathbf{k}|^2(t_n+\Delta t)}, \\
&= (\alpha e^{\nu|\mathbf{k}|^2 t_n}/2 + \beta e^{\nu|\mathbf{k}|^2(t_n+\Delta t/2)} + \\
&\quad + \gamma e^{\nu|\mathbf{k}|^2(t_n+\Delta t/2)} + \delta e^{\nu|\mathbf{k}|^2(t_n+\Delta t)})e^{-\nu|\mathbf{k}|^2(t_n+\Delta t)}, \\
&= \alpha/2 + \beta e^{\nu|\mathbf{k}|^2\Delta t/2} + \gamma e^{\nu|\mathbf{k}|^2\Delta t/2} + \delta e^{\nu|\mathbf{k}|^2\Delta t}.
\end{aligned} \tag{1.74}$$

One potential problem with using the integrating factor is for high-resolution simulations it is conceivable that $e^{\nu|\mathbf{k}|^2\Delta t}$ could potentially result in computational overflow if the exponent became too large, depending on the relationship between ν , k_{\max} and Δt . This has not been a problem for the current set of simulations, largely due to the fact that any increase in the resolution, and thus the maximum value of $|\mathbf{k}|$, was accompanied by a decrease in the timestep, for the reasons given below, as well as a decrease in the viscosity ν , however it is a factor that should be taken into consideration when modelling other fluid systems.

Assuming that we have taken care of the stability issue, the next important ques-

tion to consider when running simulations is how small must the timestep be to still produce an accurate approximation of the PDE. One well-known method for adjusting the timestep as necessary is given by the Courant–Friedrichs–Lewy (CFL) condition, described by Courant *et al.* (1928), based on the idea that if the maximum speed of wave propagation is given by $\|u\|_\infty$, the timestep must be chosen to be small enough that a wave peak does not ‘skip’ grid-points from one timestep to the next. Thus you want

$$\|u\|_\infty = C_c \frac{\Delta x}{\Delta t} \quad (1.75)$$

where Δx is the grid-point spacing, Δt is the timestep and the proportionality constant $C_c \leq 1$ is known as the Courant number. For simulations with a linear resolution R , Δx is equal to $2\pi/R$, while the Courant number, which depends on the details of the system being modelled, is in our case bounded by the conservative value of 0.8. This bound is ensured by monitoring the value

$$\frac{2\pi\|\mathbf{u}\|_\infty\Delta t}{R} \quad (1.76)$$

and each timestep, and as soon as it rises above 0.8 the timestep is decreased by multiplying by a factor of 0.8. Throughout all of the simulations performed for this thesis this is seen to be sufficient to ensure reasonable behaviour for the time evolutions of the PDEs.

Chapter 2

The Navier-Stokes Equations

2.1 Introduction

The 2DNS equations are simply the 3D equations (1.1) under the assumption that all fields are independent of the third coordinate, usually taken to be the z -coordinate. Under this assumption, the curl of the velocity field has only one component, which is usually just treated as a scalar vorticity $\omega = -\nabla^\perp \cdot \mathbf{u} = \partial_x u_y - \partial_y u_x$, and which satisfies the velocity-vorticity form of the equation

$$\frac{\partial \omega}{\partial t} + \mathbf{u} \cdot \nabla \omega = \nu \Delta \omega, \quad (2.1)$$

$$\nabla \cdot \mathbf{u} = 0. \quad (2.2)$$

For an infinite domain the velocity field can then be recovered from the vorticity ω , using the singular integral with the Biot–Savart kernel

$$\mathbf{u}(\mathbf{x}) = -\frac{1}{2\pi} \int_{\mathbb{R}^2} \frac{\mathbf{y}^\perp \omega(\mathbf{x} - \mathbf{y})}{|\mathbf{y}|^2} d\mathbf{y}. \quad (2.3)$$

The extra conserved quantities possessed by the 2D Euler equations are most clearly seen in the vorticity-streamfunction form of the equations, which comes about because

in two dimensions the divergence-free condition on the velocity field means that it can be written as $\mathbf{u} = \nabla^\perp \psi$, where $\nabla^\perp = (\partial_y, -\partial_x)$ is the perpendicular gradient and ψ is the streamfunction. The evolution of the vorticity $\omega = -\Delta\psi$ can then be written as

$$\frac{\partial\omega}{\partial t} + J(\psi, \omega) = \nu\Delta\omega \quad (2.4)$$

where $J(\psi, \omega) = (\partial_x\psi)(\partial_y\omega) - (\partial_y\psi)(\partial_x\omega)$. Multiplying (2.4) by ψ or ω and integrating over the domain, and using the properties of the Jacobian given in (1.50), gives the inviscid conservation of the energy $\frac{1}{2}\langle\psi\omega\rangle = \frac{1}{2}\|\mathbf{u}\|^2$ and the enstrophy $\frac{1}{2}\|\omega\|^2$. In fact equation (2.4) gives rise to an infinite number of inviscidly conserved quantities (Tran & Dritschel, 2006), namely for any function $f(\omega)$ the spatial average is inviscidly conserved, and if it is a convex function, *i.e.* $f''(\omega) > 0$, the spatial average decays under viscous dynamics, since we have

$$\begin{aligned} \frac{d}{dt}\langle f(\omega)\rangle &= \left\langle \frac{\partial}{\partial t}f(\omega)\right\rangle, \\ &= \left\langle f'(\omega)\frac{\partial\omega}{\partial t}\right\rangle, \\ &= -\langle f'(\omega)J(\psi, \omega)\rangle + \nu\langle f'(\omega)\Delta\omega\rangle, \\ &= \langle\psi J(f'(\omega), \omega)\rangle - \nu\langle\nabla f'(\omega)\cdot\nabla\omega\rangle, \\ &= \langle f''(\omega)J(\omega, \omega)\rangle - \nu\langle f''(\omega)|\nabla\omega|^2\rangle, \\ &= -\nu\langle f''(\omega)|\nabla\omega|^2\rangle, \end{aligned} \quad (2.5)$$

where we have used integration by parts a number of times. Since the L^p norms, including the L^∞ norm, are all convex functions, this means that they all decay under viscous evolution, which puts very strong constraints on the subsequent dynamics.

One of the assumptions in the KLB theory of turbulence is that the enstrophy dissipation rate $\chi = \nu\|\nabla\omega\|^2$ approaches a finite non-zero value in the inviscid limit. This is seen clearly in the use of χ in the values for the enstrophy inertial range and dissipation wavenumber. This may be justified in the forced case, where for $\nu > 0$ the

dissipation rate will always eventually statistically match the injection rate, however due to the smoothness of solutions for all finite time, the time taken to reach the maximum dissipation rate will happen at ever later times as the viscosity is decreased. In the unforced case a finite limiting dissipation rate is not at all obvious, however, and one of the consequences of a non-zero χ in the inviscid limit is that the palinstrophy must grow unbounded, presumably stemming from singular behaviour. This hypothesis however contradicts the mathematical studies that have shown that 2D Euler and 2DNS turbulence is regular for all finite time (Ladyzhenskaya, 1969; Beale *et al.*, 1984). In addition, numerical models have shown that the maximum dissipation rate converges to zero in the inviscid limit (Dmitruk & Montgomery, 2005). This has been proven by rigorous arguments that show that for the 2D Euler equations the palinstrophy $\|\nabla\omega\|^2$ grows no more rapidly than doubly exponential in time, a result which could be expected from the following heuristic argument. The equation for the evolution of the vorticity gradient in two dimensions is given by

$$\left(\frac{\partial}{\partial t} + \mathbf{u} \cdot \nabla\right) \nabla\omega = \omega \mathbf{n} \times \nabla\omega - (\nabla\omega \cdot \nabla)\mathbf{u} + \nu \Delta \nabla\omega, \quad (2.6)$$

which means that, following the flow, the evolution of the magnitude of the vorticity gradient is given by

$$\frac{D}{Dt} |\nabla\omega| = -\frac{\nabla\omega}{|\nabla\omega|} \cdot (\nabla\omega \cdot \nabla)\mathbf{u} \leq |\nabla\mathbf{u}| |\nabla\omega|. \quad (2.7)$$

By Grönwall's inequality, this gives the result that for a fluid particle, the magnitude of the vorticity gradient is bounded by

$$|\nabla\omega| \leq |\nabla\omega_0| \exp\left(\int_{t_0}^t |\nabla\mathbf{u}| dt\right). \quad (2.8)$$

This remains finite for finite time for all fluid particles as long as $\|\nabla\mathbf{u}\|_\infty$ is well behaved. This is heuristically expected to be the case as the transfer of energy upscale in two dimensions is not expected to explosively effect the growth of the velocity gradients,

and in fact the L^2 -norm of the velocity gradient is conserved. This means that the 2DNS equations behave in an essentially linear behaviour, displaying almost complete depletion of nonlinearity, which is in agreement with the argument for the effective linearity of 2DNS is based on the fact that ω is a smaller scale quantity than \mathbf{u} , so the transfer of ω downscale is expected to have a relatively weak feedback on \mathbf{u} . This is the idea behind the ‘degree of nonlinearity’ of a system, developed in Tran *et al.* (2010), and discussed more thoroughly in the next two chapters. As well as these purely heuristic arguments, Tran & Dritschel (2006) showed that using the assumption of a self-similar enstrophy spectrum no shallower than k^{-1} the enstrophy dissipation rate vanishes in the inviscid limit.

We can also see the essential linearity of the 2DNS equation based on an estimate that suggests a linear scaling of the number of active Fourier modes with the Reynolds number. We start by using the result from Tran (2005),

$$\nu \|\nabla \omega\|^2 \leq \|\omega\|_\infty \|\omega\|^2, \quad (2.9)$$

for the dissipation rate $\nu \|\nabla \omega\|^2$ at its peak. Since both vorticity norms on the right-hand side of equation (2.9) decay we have the bound

$$\|\nabla \omega\| \leq \frac{\|\omega_0\|_\infty^{1/2} \|\omega_0\|}{\nu^{1/2}}, \quad (2.10)$$

which is valid uniformly in time, and the bound

$$k_T = \frac{\|\nabla \omega\|}{\|\omega\|} \leq \frac{\|\omega_0\|_\infty^{1/2}}{\nu^{1/2}}, \quad (2.11)$$

which is valid at least up to (and probably beyond) the time of peak enstrophy dissipation. The bound for this enstrophy dissipation wavenumber k_T , which is similar to the Taylor microscale wavenumber in three-dimensional turbulence, compares favourably to k_ν as defined in the introduction as it could be significantly smaller than k_ν (Tran,

2005). By the very definition in equation (2.11), enstrophy dissipation is strongest in the vicinity of k_T , so the wavenumbers greater than k_T are effectively suppressed by viscous forces, and thus virtually inactive. The number of dynamically active modes N_c corresponding to $k \leq k_T$ is therefore given by

$$N_c \approx \frac{k_T^2}{k_0^2} \leq \frac{L^2 \|\omega_0\|_\infty}{\nu}, \quad (2.12)$$

where $k_0 = 1/L$ is the smallest wavenumber and the quantity $L\|\omega_0\|_\infty$ may be identified with the fluid velocity. With this identification, the term on the right-hand side of equation (2.12) may be defined as the Reynolds number Re . Hence, equation (2.12) can be rewritten in the more compact form

$$N_c \leq Re. \quad (2.13)$$

From our experience in numerical simulations of two-dimensional turbulence, the estimate (2.13) is sharp—in fact spot on. For example, for the standard numerical domain $2\pi \times 2\pi$ and an initial vorticity maximum $\|\omega_0\|_\infty \approx 4\pi$, the simulations of Dritschel *et al.* (2007) using $4\pi(8/3)^3/\nu$ grid points adequately resolved the dissipation scales. This resolution is obviously consistent with equation (2.13), within a single order of magnitude. As will be seen in the next section, the estimate (2.13) for N_c fully agrees with the number of degrees of freedom discussed above.

The rest of this chapter is based on the papers Tran *et al.* (2009), where we derive bounds for the number of degrees of freedom using two different norms and compare them to previous result for the dimension of the attractor for forced 2DNS turbulence, and Blackburn & Tran (2011), where we discuss the use of scale-neutral friction to remove large-scale energy in simulations of forced 2DNS turbulence

2.2 Number of degrees of freedom

Following the prescription laid down in §1.3.1 we consider a solution to equation (2.4) with a streamfunction $\psi(\mathbf{x}, t)$, corresponding to a vorticity $\omega(\mathbf{x}, t)$, and the linear evolution of a deviation ϕ of the stream function ψ (corresponding to a deviation $\Delta\phi$ of the vorticity ω) governed by the linearised equation

$$\frac{\partial}{\partial t}\Delta\phi + J(\phi, \omega) + J(\psi, \Delta\phi) = \nu\Delta^2\phi \quad (2.14)$$

with initial vorticity ω_0 (and initial stream function ψ_0). Two natural norms for the present problem are the energy and enstrophy norm, and we will refer to the phase space equipped with the energy (enstrophy) norm as the energy (enstrophy) space. In each space we carry out the orthonormalisation process as described in §1.3.1, where the energy-space inner product of two streamfunction deviations φ_1 and φ_2 is defined as $\langle\varphi_1, \varphi_2\rangle_E = \langle\nabla\varphi_1 \cdot \nabla\varphi_2\rangle$ and the inner product of ϑ_1 and ϑ_2 in enstrophy-space is $\langle\varphi_1, \varphi_2\rangle_Z = \langle(\Delta\vartheta_1)(\Delta\vartheta_2)\rangle$, with both of these inner products having the associated norms $\|\cdot\|_E$ and $\|\cdot\|_Z$. By taking the scalar product of equation (2.14) with ϕ and $(-\Delta)\phi$, we obtain the respective evolution equations for the energy norm $\|\phi\|_E$ and enstrophy norm $\|\phi\|_Z$,

$$\begin{aligned} \|\phi\|_E \frac{d\|\phi\|_E}{dt} &= \|\nabla\phi\| \frac{d\|\nabla\phi\|}{dt} \\ &= \langle\phi J(\psi, \Delta\phi)\rangle - \nu\|\Delta\phi\|^2 \end{aligned} \quad (2.15)$$

and

$$\begin{aligned} \|\phi\|_Z \frac{d\|\phi\|_Z}{dt} &= \|\Delta\phi\| \frac{d\|\Delta\phi\|}{dt} \\ &= -\langle\Delta\phi J(\phi, \omega)\rangle - \nu\|\nabla\Delta\phi\|^2. \end{aligned} \quad (2.16)$$

The respective exponential growth (or decay) rates λ and Λ for $\|\phi\|_E$ and $\|\phi\|_Z$ can readily be deduced and are given by

$$\lambda = \frac{d}{dt} \ln \|\phi\|_E = \frac{1}{\|\nabla\phi\|^2} [\langle\phi J(\psi, \Delta\phi)\rangle - \nu\|\Delta\phi\|^2] \quad (2.17)$$

and

$$\Lambda = \frac{d}{dt} \ln \|\phi\|_Z = \frac{-1}{\|\Delta\phi\|^2} [\langle\Delta\phi J(\phi, \omega)\rangle + \nu\|\nabla\Delta\phi\|^2]. \quad (2.18)$$

These rates provide a comprehensive picture of solution stability, quantitatively describing how solutions with nearby initial data disperse from one another. We now introduce the orthonormal sets $\{\varphi_i\}_{i=1}^n$ for the energy norm and $\{\vartheta_i\}_{i=1}^n$ for the enstrophy norm. These sets are assumed to have been created using the maximisation procedure described in 1.3.1, with the corresponding non-decreasing sets of eigenvalues $\{\lambda_i\}_{i=1}^n$ and $\{\Lambda_i\}_{i=1}^n$. We can now use standard inequalities to gain an upper bound for the value N such that the sum of the first N eigenvalues for each norm is non-positive.

2.2.1 Degrees of freedom using the energy norm

We begin by deriving an upper bound N in the energy space. From (2.17) we have

$$\begin{aligned}
\sum_{i=1}^n \lambda^i &= \sum_{i=1}^n (\langle \varphi_i J(\psi, \Delta \varphi_i) \rangle - \nu \|\Delta \varphi_i\|^2) \\
&= - \sum_{i=1}^n (\langle \Delta \varphi_i J(\psi, \varphi_i) \rangle + \nu \|\Delta \varphi_i\|^2) \\
&= - \sum_{i=1}^n (\langle \varphi_i J(\psi_x, \varphi_{i,x}) + \varphi_i J(\psi_y, \varphi_{i,y}) \rangle + \nu \|\Delta \varphi_i\|^2) \\
&= \sum_{i=1}^n (\langle \varphi_{i,x} J(\psi_x, \varphi_i) + \varphi_{i,y} J(\psi_y, \varphi_i) \rangle - \nu \|\Delta \varphi_i\|^2) \\
&\leq \sum_{i=1}^n (\langle |\varphi_{i,x}| |\nabla \psi_x| |\nabla \varphi_i| + |\nabla \varphi_i| |\varphi_{i,y}| |\nabla \psi_y| \rangle - \nu \|\Delta \varphi_i\|^2) \\
&= \sum_{i=1}^n (\langle |\nabla \varphi_i| \{ |\varphi_{i,x}| |\nabla \psi_x| + |\varphi_{i,y}| |\nabla \psi_y| \} \rangle - \nu \|\Delta \varphi_i\|^2) \\
&\leq \sum_{i=1}^n (\langle |\nabla \varphi_i|^2 \{ |\nabla \psi_x|^2 + |\nabla \psi_y|^2 \}^{1/2} \rangle - \nu \|\Delta \varphi_i\|^2) \\
&\leq \|\omega\| \left\| \sum_{i=1}^n |\nabla \varphi_i|^2 \right\| - \nu \sum_{i=1}^n \|\Delta \varphi_i\|^2
\end{aligned} \tag{2.19}$$

where integration by parts and the Cauchy–Schwarz inequality have been used. For further estimates of the terms on the right-hand side of equation (2.19) we employ the Lieb–Thirring inequality (1.59) and the Rayleigh–Ritz inequality (1.55). Substituting these into equation (2.19), we obtain

$$\sum_{i=1}^n \lambda_i \leq \left(\sum_{i=1}^n \|\Delta \varphi_i\|^2 \right)^{1/2} \left(c_1 \|\omega\| - \nu \frac{c_2}{L} n \right). \tag{2.20}$$

It follows that $\sum_{i=1}^n \lambda_i \leq 0$ when $n \geq c_1 L \|\omega\| / (c_2 \nu)$. Hence we deduce the bound

$$N \leq C_1 \frac{L \|\omega\|}{\nu} \leq C_1 \frac{L \|\omega_0\|}{\nu} = C_1 Re, \tag{2.21}$$

where Re has been redefined by replacing $L\|\omega_0\|_\infty$ with $\|\omega_0\|$. Note that the precise result should be that N is no greater than the least integral upper bound for $C_1 Re$; however, in writing equation (2.21), we have opted to ignore this exceedingly minor detail. Equation (2.21) gives a clear linear dependence of N on Re , which was obtained earlier by counting the active modes from the smallest wavenumber $k_0 = 1/L$ to the dissipation wavenumber $k_T = \|\nabla\omega\|/\|\omega\|$.

2.2.2 Degrees of freedom using the enstrophy norm

An upper bound for N in the enstrophy space is derived in a similar manner. From equation (2.18) we have

$$\begin{aligned}
\sum_{i=1}^n \Lambda_i &= - \sum_{i=1}^n (\langle \Delta\vartheta_i J(\vartheta_i, \omega) \rangle + \nu \|\nabla \Delta\vartheta_i\|^2) \\
&\leq \sum_{i=1}^n (\langle |\Delta\vartheta_i| |\nabla\vartheta_i| |\nabla\omega| \rangle - \nu \|\nabla \Delta\vartheta_i\|^2) \\
&\leq \left\langle \left(\sum_{i=1}^n |\Delta\vartheta_i|^2 \sum_{i=1}^n |\nabla\vartheta_i|^2 \right)^{1/2} |\nabla\omega| \right\rangle - \nu \sum_{i=1}^n \|\nabla \Delta\vartheta_i\|^2 \\
&\leq \left\langle \left(\sum_{i=1}^n |\Delta\vartheta_i|^2 \sum_{i=1}^n |\nabla\vartheta_i|^2 \right)^2 \right\rangle^{1/4} \langle |\nabla\omega|^{4/3} \rangle^{3/4} - \nu \sum_{i=1}^n \|\nabla \Delta\vartheta_i\|^2 \\
&\leq \left\| \sum_{i=1}^n |\nabla\vartheta_i|^2 \right\|_\infty^{1/2} \left\| \sum_{i=1}^n |\Delta\vartheta_i|^2 \right\|_\infty^{1/2} (2\pi L)^{1/2} \|\nabla\omega\| - \nu \sum_{i=1}^n \|\nabla \Delta\vartheta_i\|^2
\end{aligned} \tag{2.22}$$

where Hölder's inequalities with the pairs of conjugate exponents 4/3 and 4, and 3/2 and 3 have been used in the penultimate and final steps, respectively. For further estimates of the terms in this equation, we employ a few more analytic inequalities concerning the orthonormal set in the enstrophy space. First we have (Constantin, 1987; Constantin *et al.*, 1988)

$$\left\| \sum_{i=1}^n |\nabla\vartheta_i|^2 \right\|_\infty \leq c_3^2 \left(1 + \ln \sum_{i=1}^n L^2 \|\Delta\nabla\vartheta_i\|^2 \right) \tag{2.23}$$

where c_3 is a nondimensional constant independent of the set $\{\vartheta_i\}_{i=1}^n$. Second, equation (1.60) is used, along with the Rayleigh-Ritz inequality (1.56). By substituting these into equation (2.22) we obtain

$$\begin{aligned}
\sum_{i=1}^n \Lambda_i &\leq C' \left(1 + \ln \sum_{i=1}^n L^2 \|\nabla \Delta \vartheta_i\|^2 \right)^{1/2} \\
&\times \left(\sum_{i=1}^n L^2 \|\nabla \Delta \vartheta_i\|^2 \right)^{1/4} \frac{\|\omega_0\|_\infty^{1/2}}{\nu^{1/2}} - \nu \sum_{i=1}^n \|\nabla \Delta \vartheta_i\|^2 \\
&= \frac{\nu \xi^{1/4}}{L^2} \left[C' (1 + \ln \xi)^{1/2} \frac{L^2 \|\omega_0\|_\infty^{1/2} \|\omega_0\|}{\nu^{3/2}} - \xi^{3/4} \right] \\
&= \frac{\nu \xi^{1/4}}{L^2} [C' Re^{3/2} (1 + \ln \xi)^{1/2} - \xi^{3/4}]
\end{aligned} \tag{2.24}$$

where $C' = \sqrt{2\pi} c_1 c_3$, $\xi = \sum_{i=1}^n L^2 \|\nabla \Delta \vartheta_i\|^2$ and $Re = (L^4 \|\omega_0\|_\infty \|\omega_0\|^2)^{1/3} / \nu$. Note that from equation (1.56) we have $\xi \geq c_2^2 n^2$. Hence without the logarithmic term, it would be straightforward to substitute this into (2.24) and deduce an upper bound for N similar to equation (2.21) with the newly defined Re replacing its previously defined (and comparable) counterpart. Since we are interested in the case $\xi \gg 1$, the logarithmic term should introduce a small departure to the linear dependence of N on Re only. In order to account for the $\ln \xi$ term, we can ‘cover’ it by a fraction of ξ , say $\xi/2$. By elementary calculus we find that

$$C' Re^{3/2} (1 + \ln \xi)^{1/2} - \frac{\xi^{3/4}}{2} \leq \sqrt{2} C' Re^{3/2} (1 + \ln Re)^{1/2} \tag{2.25}$$

where a negative term has been dropped on the right. It follows that

$$\begin{aligned}
C' Re^{3/2} (1 + \ln \xi)^{1/2} - \xi^{3/4} &\leq \sqrt{2} C' Re^{3/2} (1 + \ln Re)^{1/2} - \frac{\xi^{3/4}}{2} \\
&\leq \sqrt{2} C' Re^{3/2} (1 + \ln Re)^{1/2} - \frac{(c_2 n)^{3/2}}{2}
\end{aligned} \tag{2.26}$$

The condition $\sum_{i=1}^n \Lambda_i \leq 0$ is satisfied when the right-hand side is nonpositive. This requires a straightforward condition for n which in turn yields the result

$$N \leq C_2 Re(1 + \ln Re)^{1/3}, \quad (2.27)$$

where $C_2 = (8C'^2)^{1/3}/c_2$.

As expected, equation (2.27) gives an essentially linear scaling of N with Re since the superlinear dependence on Re , due to the logarithmic term, is slight for large Re . Given that the same linear scaling was found earlier in the energy space, this is somewhat surprising. The reason is that the energy in two-dimensional turbulence is predominantly transferred to smaller wavenumbers while the enstrophy is predominantly transferred to larger wavenumbers. This undoubtedly implies that the enstrophy dynamics have relatively more degrees of freedom than the energy dynamics. Hence, it is somewhat counterintuitive that equations (2.21) and (2.27) do not differ by much. A possible explanation is that (2.21) may not be as optimal as (2.27). There are a number of interesting consequences of the linear scaling of N with the Reynolds number. First, this means that from equation (2.12) the enstrophy dissipation rate at the dissipation wavenumber $r_d = \nu k_d^2$ is bounded by a constant, independent of the Reynolds number, that is $r_d \sim Re^0$. This suggests that the direct enstrophy flux may not be particularly strong, which agrees with the arguments above about vanishing enstrophy dissipation in the inviscid limit. The scaling $k_d^2 \sim 1/\nu$ is also useful in numerical simulations for the following reason. It seems reasonable that the number of Fourier-space grid points should be proportional to the number of active Fourier modes, that is $R^2 \propto k_d^2 \sim 1/\nu$, or in other words $\nu = \Upsilon R^{-2}$. This means that when the resolution is doubled ($R \rightarrow 2R$) the viscosity can be reduced by a factor of 4 while still ensuring sufficient dissipation to stop contamination of the small-scale wavenumber boundary. The constant of proportionality Υ can be found through trial and error for small resolution simulations, after which the scaling law above can be utilised for higher resolutions.

2.3 Forced-dissipative Navier–Stokes

While the lack of a nontrivial attractor to the unforced 2DNS equations means that many classical analytic techniques, which measure the dimension of the attractor, are not applicable, the forced NS equations, given by

$$\frac{\partial \omega}{\partial t} + \mathbf{u} \cdot \nabla \omega = \nu \Delta \omega + \mathbf{f}, \quad (2.28)$$

$$\nabla \cdot \mathbf{u} = 0. \quad (2.29)$$

are known to possess a global attractor, of which a number of dimensional estimates of the Hausdorff dimension D_H have been made (Babin & Vishik, 1983; Constantin *et al.*, 1985*b*, 1988). In the present notation, the respective bounds for D_H in the energy and enstrophy spaces are given by

$$D_H \leq c' \frac{L \|\nabla^{-1} \mathbf{f}\|}{\nu^2} \leq c' \frac{L^2 \|\mathbf{f}\|}{\nu^2} = c' G \quad (2.30)$$

and

$$D_H \leq c'' \left(\frac{L^2 \|\mathbf{f}\|}{\nu^2} \right)^{2/3} \left(1 + \ln \frac{L^2 \|\mathbf{f}\|}{\nu^2} \right)^{1/3} = c'' G^{2/3} (1 + \ln G)^{1/3}, \quad (2.31)$$

respectively, where c' and c'' are constant and G is known as the generalised Grasshopper number. Although G has some certain physical significance, its highly superlinear dependence on ν^{-1} appears to make equations (2.30) and (2.31) in disagreement with the bounds for N_c and N derived earlier. We claim that this apparent disagreement is due entirely to the particular form of \mathbf{f} and could be fully reconciled. For the remainder of this section, we will elaborate on this claim.

Due to rigour requirements in the mathematical formulation in (Babin & Vishik, 1983; Constantin *et al.*, 1985*b*, 1988), a time-independent forcing \mathbf{f} was used as a model for energy and enstrophy injection. The forced NS equations

$$\frac{\partial \mathbf{u}}{\partial t} + (\mathbf{u} \cdot \nabla) \mathbf{u} + \nabla p = \nu \Delta \mathbf{u} + \mathbf{f}, \quad (2.32)$$

then admit the following evolution equations:

$$\begin{aligned}
\frac{1}{2} \frac{d}{dt} \|\mathbf{u}\|^2 &= -\nu \|\nabla \mathbf{u}\|^2 + \langle \mathbf{u} \cdot \mathbf{f} \rangle, \\
&\leq -\nu \|\nabla \mathbf{u}\|^2 + \|\nabla \mathbf{u}\| \|\nabla^{-1} \mathbf{f}\|, \\
&\leq -\frac{\nu}{2} \|\nabla \mathbf{u}\|^2 + \frac{\|\nabla^{-1} \mathbf{f}\|^2}{2\nu},
\end{aligned} \tag{2.33}$$

and

$$\begin{aligned}
\frac{1}{2} \frac{d}{dt} \|\nabla \mathbf{u}\|^2 &= -\nu \|\Delta \mathbf{u}\|^2 - \langle \Delta \mathbf{u} \cdot \mathbf{f} \rangle, \\
&\leq -\nu \|\Delta \mathbf{u}\|^2 + \|\Delta \mathbf{u}\| \|\mathbf{f}\|, \\
&\leq -\frac{\nu}{2} \|\Delta \mathbf{u}\|^2 + \frac{\|\mathbf{f}\|^2}{2\nu},
\end{aligned} \tag{2.34}$$

for the energy $\|\mathbf{u}\|^2/2$ and enstrophy $\|\nabla \mathbf{u}\|^2/2$, respectively. In equations (2.33) and (2.34), the terms $\|\nabla^{-1} \mathbf{f}\|^2/(2\nu)$ and $\|\mathbf{f}\|^2/(2\nu)$ represent upper bounds for the energy and enstrophy injection rates, respectively. Their dependence on ν is inescapable because the injection rates $\langle \mathbf{u} \cdot \mathbf{f} \rangle$ and $-\langle \Delta \mathbf{u} \cdot \mathbf{f} \rangle$ are themselves flow dependent.

We now demonstrate how the viscosity dependence of the injection rates (or more precisely of the upper bounds for the injection rates) contributes to the superlinear scaling of D_H with ν^{-1} . To this end, let us recall the intermediate steps (Constantin *et al.*, 1985*b*, 1988; Temam, 1997) towards equations (2.30) and (2.31) given below:

$$D_H \leq c' \frac{L \overline{\|\Delta \mathbf{u}\|^2}^{1/2}}{\nu} \tag{2.35}$$

and

$$D_H \leq c'' \left(\frac{L^2 \overline{\|\Delta \mathbf{u}\|^2}^{1/2}}{\nu} \right)^{2/3} \left(1 + \ln \frac{L^2 \overline{\|\Delta \mathbf{u}\|^2}^{1/2}}{\nu} \right)^{1/3}, \tag{2.36}$$

where the overline denotes the supremum of an asymptotic average. From equations

(2.33) and (2.34) we can deduce the forced dissipative balance equations

$$\overline{\|\nabla \mathbf{u}\|^2}^{1/2} \leq \frac{\|\nabla^{-1} \mathbf{f}\|}{\nu} \quad (2.37)$$

and

$$\overline{\|\Delta \mathbf{u}\|^2}^{1/2} \leq \frac{\|\mathbf{f}\|}{\nu}. \quad (2.38)$$

Upon substituting these into equations (2.35) and (2.36), we recover equations (2.30) and (2.31), respectively. However, if the driving force could somehow be modelled in such a way that the averaged energy and enstrophy injection rates would be bounded independently of viscosity, say by ϵ and η , respectively, then equations (2.37) and (2.38) would become

$$\overline{\|\nabla \mathbf{u}\|^2}^{1/2} \leq \frac{\epsilon^{1/2}}{\nu^{1/2}} \quad (2.39)$$

and

$$\overline{\|\Delta \mathbf{u}\|^2}^{1/2} \leq \frac{\eta^{1/2}}{\nu^{1/2}}. \quad (2.40)$$

Upon substituting these into equations (2.35) and (2.36), we obtain

$$D_H \leq c' \frac{L\epsilon^{1/2}}{\nu^{3/2}} \quad (2.41)$$

and

$$D_H \leq c'' \left(\frac{L^2 \eta^{1/2}}{\nu^{3/2}} \right)^{2/3} \left(1 + \ln \frac{L^2 \eta^{1/2}}{\nu^{3/2}} \right)^{1/3}. \quad (2.42)$$

One can see that equation (2.42) has the desired scaling, *i.e.* linear dependence on ν^{-1} with a logarithmic ‘correction’ as in equation (2.31). Hence, for the dimension estimate in the enstrophy space, the ‘extra’ dependence on ν^{-1} would be completely removed if the enstrophy injection could be bounded independently of viscosity. Note, however, that only part of the extra dependence on ν^{-1} would be removed from the dimension estimate in energy space when the energy injection is made independent of viscosity. This strengthens our earlier suggestion that the estimate for N (and D_H) in the energy space may not be as optimal as its counterpart in the enstrophy space.

It is worth mentioning that numerical simulations of two-dimensional turbulence have routinely used a variety of forcing that provides steady energy and enstrophy injection rates ϵ and η . This class of forcing includes white-noise and flow-dependent forcing. While such a class of forcing is numerically desirable and realistic in some sense, it may render equation (2.28) incompatible with the mathematical formulation leading to the desired estimate (2.42). Nevertheless, for the present approach, there are no technical difficulties in arriving at this estimate as an upper bound for the number of degrees of freedom in the present sense. An undesirable numerical artifact that does cause concern, however, is the build-up of energy at the largest scales, which is unavoidable as a fundamental result of the dual cascade. Simulations use various large-scale dissipation mechanisms to absorb this large scale energy, with negative powers of the Laplacian (also called hypoviscosity by a number of authors) and mechanical friction (also known as Ekman drag in the geophysical context) in common use. The former primarily operates at large scales, and its effects on small scales are not well understood. The latter is scale neutral, removing enstrophy (and energy) at all scales. This has serious ‘side effects’ on the small-scale dynamics. Most importantly, the vorticity remains bounded in the inviscid limit. Such behaviour is in sharp contrast to the Kraichnan picture, in which the enstrophy grows without bound as the enstrophy inertial range becomes increasingly wider for smaller viscosity. An undesirable consequence is that viscous dissipation of enstrophy vanishes in the inviscid limit (Constantin & Ramos, 2007). It follows that for steady or quasisteady dynamics at sufficiently small viscosity, frictional dissipation of enstrophy outweighs its viscous counterpart. The classical enstrophy inertial range then becomes a (frictional) dissipation range, possibly without dramatic changes in its appearance.

The above results have important theoretical and practical implications. On the one hand, mechanical friction should not be employed in numerical simulations aimed at addressing fundamental issues concerning the enstrophy flux and enstrophy inertial range of 2DNS turbulence as this scale-neutral dissipation mechanism apparently

renders dynamical behaviour inconsistent with the Kraichnan picture. On the other hand, relatively strong friction naturally occurs on the surfaces of thin films, at lateral boundaries of confined fluids, and at the interfaces of shallow layers in geophysical fluid models. Therefore, the frictional effects presently discussed are crucial in understanding the dynamics of these systems, particularly their departure from the classical picture. Note, however, that the present findings may not be relevant to 2DNS fluids having no-slip boundaries, although this type of boundary could impose some friction on the dynamics, particularly at large scales. The reason is that such boundaries can also act as vorticity sources (see Heijst *et al.* (2006) and references therein), apparently playing a role opposite to that of friction.

In the next section we analytically examine the effect of mechanical friction on forced 2DNS turbulence as discussed in the preceding paragraphs, showing a simple proof of vanishing viscous dissipation of enstrophy in the inviscid limit. In addition, for weak friction, the classical spectrum is used to deduce the critical viscosity separating the regimes of predominant frictional and viscous dissipation of enstrophy. In the final section of this chapter we report results from numerical simulations corroborating these theoretical findings.

2.3.1 A theoretical understanding of the effects of Ekman drag

As mentioned above, the addition of a viscous dissipation term into the NS equations totally changes the long-term statistical properties of turbulence, in particular the enstrophy is bounded independent of the viscosity, whereas in the Kraichnan picture it grows without bound. The 2D forced-dissipative NS equations with Ekman drag are given by

$$\frac{D\omega}{Dt} = \nu\Delta\omega - \alpha\omega + f, \quad (2.43)$$

where $D/Dt \equiv \partial/\partial t + \mathbf{u} \cdot \nabla$, α is the coefficient of friction, ν is the molecular viscosity and f is the forcing. Using the result $\Delta(\omega^2) \equiv 2|\nabla\omega|^2 + 2\omega\Delta\omega$, equation (2.43) can be

written as

$$\frac{D}{Dt} \frac{\omega^2}{2} = \nu \Delta \frac{\omega^2}{2} - \nu |\nabla \omega|^2 - \alpha \omega^2 + \omega f, \quad (2.44)$$

and further using the fact that

$$\frac{D|\omega|}{Dt} \equiv \frac{1}{2|\omega|} \frac{D}{Dt} \omega^2, \quad (2.45)$$

gives the equation for the evolution of the vorticity magnitude,

$$\frac{D|\omega|}{Dt} = \frac{\nu}{2|\omega|} \Delta \omega^2 - \frac{\nu}{|\omega|} |\nabla \omega|^2 - \alpha |\omega| + \frac{\omega f}{|\omega|}. \quad (2.46)$$

Let us now consider the fluid particle with the maximum vorticity magnitude, which means that by definition we have $\Delta \omega^2 \leq 0$. Equation (2.46) then gives us a bound for the growth rate of $|\omega|$ for this fluid particle, and thus the supremum of the vorticity over all space, given by

$$\frac{d}{dt} \|\omega\|_\infty \leq -\alpha \|\omega\|_\infty + F \quad (2.47)$$

where F is an upper bound for $|f|$. This can easily be solved using Grönwall's inequality, to give

$$\|\omega\|_\infty \leq \|\omega_0\|_\infty e^{-\alpha t} + \frac{F}{\alpha} (1 - e^{-\alpha t}), \quad (2.48)$$

where ω_0 is the vorticity field at $t = 0$. Thus the vorticity is bounded independent of the viscosity. Similarly, the other L_p -norms of ω can be bounded, using

$$\begin{aligned}
\frac{d}{dt}\|\omega\|_p &= \frac{d}{dt}\langle|\omega|^p\rangle^{1/p}, \\
&= \frac{1}{p}\langle|\omega|^p\rangle^{1/p-1}\left\langle\frac{\partial}{\partial t}|\omega|^p\right\rangle, \\
&= \frac{1}{p}\langle|\omega|^p\rangle^{1/p-1}\left\langle p|\omega|^{p-1}\frac{\partial}{\partial t}|\omega|\right\rangle, \\
&= \langle|\omega|^p\rangle^{1/p-1}\left\langle|\omega|^{p-1}\left(\frac{\nu}{2|\omega|}\Delta\omega^2 - \frac{\nu}{|\omega|}|\nabla\omega|^2\right.\right. \\
&\quad \left.\left.+ -\alpha|\omega| + \frac{\omega f}{|\omega|}\right)\right\rangle, \\
&= \langle|\omega|^p\rangle^{1/p-1}\left(\frac{\nu}{2}\langle|\omega|^{p-2}\Delta\omega^2\rangle - \nu\langle|\omega|^{p-2}|\nabla\omega|^2\rangle\right. \\
&\quad \left.- \alpha\langle|\omega|^p\rangle + \langle f\omega|\omega|^{p-2}\rangle\right), \\
&= \langle|\omega|^p\rangle^{1/p-1}\left(-\frac{\nu}{2}\langle\{\nabla|\omega|^{p-2}\}\{\nabla\omega^2\}\rangle - \nu\langle|\omega|^{p-2}|\nabla\omega|^2\rangle\right. \\
&\quad \left.- \alpha\langle|\omega|^p\rangle + \langle f\omega|\omega|^{p-2}\rangle\right), \\
&= -\nu(p-1)\langle|\omega|^p\rangle^{1/p-1}\langle|\omega|^{p-1}|\nabla\omega|^2\rangle - \alpha\langle|\omega|^p\rangle^{1/p}, \\
&\quad - \langle|\omega|^p\rangle^{1/p-1}\langle|\omega|^{p-2}\omega f\rangle, \\
&\leq -\alpha\|\omega\|_p + \langle|\omega|^p\rangle^{1/p-1}\langle|\omega|^{p-1}|f|\rangle, \\
&\leq -\alpha\|\omega\|_p + \|f\|_p,
\end{aligned} \tag{2.49}$$

where standard calculus has been used, along with Hölder's inequality with conjugate exponents p and $p/(p-1)$ in the final step. Finally, once again making use of Grönwall's inequality, we get

$$\|\omega\|_p \leq \|\omega_0\|_p e^{-\alpha t} + \frac{F_p}{\alpha}(1 - e^{-\alpha t}) \tag{2.50}$$

where F_p is an upper bound on $\|f\|_p$, or just $\|f\|_p$ itself if f is time independent.

Using the above result, it is possible to show that the viscous dissipation vanishes in the inviscid limit. Multiplying equation (2.43) by $-\Delta\omega$ and integrating over space

gives

$$\begin{aligned}
\frac{1}{2} \frac{d}{dt} \|\nabla\omega\|^2 &= \langle \Delta\omega(\mathbf{u} \cdot \nabla)\omega \rangle - \alpha \|\nabla\omega\|^2 - \nu \|\Delta\omega\|^2 + \sigma, \\
&= \langle \omega(\mathbf{u} \cdot \nabla)\Delta\omega \rangle - \alpha \|\nabla\omega\|^2 - \nu \|\Delta\omega\|^2 + \sigma, \\
&\leq \|\omega\|_\infty \langle |(\mathbf{u} \cdot \nabla)\Delta\omega| \rangle - \alpha \|\nabla\omega\|^2 - \nu \|\Delta\omega\|^2 + \sigma, \\
&\leq \|\omega\|_\infty \|\nabla\mathbf{u}\| \|\Delta\omega\| - \alpha \|\nabla\omega\|^2 - \nu \|\Delta\omega\|^2 + \sigma, \\
&= \frac{\|\Delta\omega\|^2}{\|\nabla\omega\|^2} \left[\|\omega\|_\infty \|\omega\| \frac{\|\nabla\omega\|^2}{\|\Delta\omega\|} + \frac{\|\nabla\omega\|^2}{\|\Delta\omega\|^2} \sigma - \alpha \frac{\|\nabla\omega\|^4}{\|\Delta\omega\|^2} - \nu \|\nabla\omega\|^2 \right].
\end{aligned} \tag{2.51}$$

where $\sigma = -\langle f\Delta\omega \rangle$ is bounded for a broad class of forces, particularly those acting at intermediate scales only. Because the enstrophy is uniformly bounded, it means that the enstrophy spectrum must either be steeper than k^{-1} or be k^{-1} with a limited extent, followed by a steeper tail. In either of these cases, the ratio $\|\nabla\omega\|^2/\|\Delta\omega\|$ vanishes as $\langle |\nabla\omega|^2 \rangle \rightarrow \infty$ (Tran & Dritschel, 2006). Each of the first three terms within the brackets in equation (2.51) thus vanishes in the limit, which means that the local maxima of $\nu\|\nabla\omega\|^2$ (which is achieved when $d\|\nabla\omega\|^2/dt = 0$) also vanish in this limit. It follows that $\nu\|\nabla\omega\|^2$ vanishes uniformly in time as $\nu \rightarrow 0$. Note that this result implies that the viscous term in equation (2.49) also vanishes since $\langle |\omega|^{p-2} |\nabla\omega|^2 \rangle \leq \|\omega\|_\infty^{p-2} \|\nabla\omega\|^2$. Hence, viscous dissipation of $\|\omega\|_p$ vanishes. The same is true for the unforced case.

An immediate implication of the above result is that for steady dynamics in the inviscid limit, the enstrophy injection η is totally dissipated by the scale-neutral mechanical friction. The enstrophy range is no longer inertial but rather becomes dissipative. This unusual and undesirable dissipation range presumably scales as k^{-3} because the scale-neutral friction is not known to have spectrally steepening effects (for small α). For such a range the dissipation of enstrophy occurs uniformly among its wavenumber octaves. Hence, one may expect a diminishing enstrophy flux through this range rather than the k -independent flux of Kraichnan.

Given a small value of α , two distinct dynamical regimes can be expected to exist. One corresponds to small viscosity and is characterised by the predominance of frictional

enstrophy dissipation. The other corresponds to moderate viscosity and is characterised by the predominance of viscous enstrophy dissipation. There then exists a critical viscosity, say ν_c , separating these two regimes, that is $\nu_c \|\nabla\omega\|^2 = \alpha \|\omega\|^2$. Thus, we have

$$\nu_c \|\nabla\omega\|^2 = \alpha \|\omega\|^2 = \eta' = \eta/2 \quad (2.52)$$

where η is the total enstrophy dissipation rate and η' is the dissipation rate of each dissipation channel. Past simulations of frictional 2D turbulence have belonged to the regime of predominantly viscous dissipation, for example Boffetta & Musacchio (2010) found $\nu \|\nabla\omega\|^2 \approx 0.9\eta$, which they considered strong evidence for the Kraichnan picture of a direct enstrophy cascade.

For power-law spectra, the critical viscosity ν_c can be readily determined from equation (2.52). Assuming that in the limit $\alpha \rightarrow 0$ ($\nu_c \rightarrow 0$), the turbulence approaches the Kraichnan–Batchelor power-law enstrophy spectrum

$$\mathcal{Z}(k) = C\eta^{2/3}k^{-1}, \quad (2.53)$$

the spectrum of $\|\nabla\omega\|^2$ is then given by $2C\eta^{2/3}k$. Integrating these spectra from the forcing wavenumber up to the dissipation wavenumber, after which there is presumably negligibly enstrophy, and using equation (2.52) gives

$$\begin{aligned} \eta' = \nu_c \|\nabla\omega\|^2 &= 2\nu_c \eta^{2/3} \int_{k_f}^{k_\nu} k \, dk, \\ \implies k_\nu^2 - k_f^2 &= \frac{\eta^{1/3}}{C\nu_c}, \end{aligned} \quad (2.54)$$

upon which noting that the forcing term is negligible for large k_ν gives us

$$k_\nu^2 \approx \frac{\eta^{1/3}}{C\nu_c}. \quad (2.55)$$

Similarly, for the enstrophy, we have

$$\begin{aligned}
 \eta' &= \alpha \|\omega\|^2 = 2\alpha C \eta^{2/3} \int_{k_f}^{f_\nu} k^{-1} dk, \\
 \implies \log(k_\nu/k_f) &= \frac{\eta^{1/3}}{2\alpha C}, \\
 \implies \frac{k_\nu^2}{k_f^2} &= \exp\left(\frac{\eta^{1/3}}{\alpha C}\right).
 \end{aligned} \tag{2.56}$$

Finally, putting in (2.55) we get the expression for the critical viscosity

$$\nu_c = \frac{\eta^{1/3}}{C k_f^2} \exp\left(\frac{-\eta^{1/3}}{C\alpha}\right). \tag{2.57}$$

The exponential decay of ν_c in equation (2.57) means that for small α , high resolutions are necessary to probe into the regime of predominant frictional dissipation of enstrophy. In the next section we numerically determine ν_c for a moderate range of α and the result is consistent with equation (2.57).

2.3.2 Simulation results

We now present the results of a set of numerical simulations that support the theoretical predictions discussed in the preceding section. Equation (2.43) was simulated using the method described in §1.4 up to 8192×8192 grid points. The frictional and viscous terms were both incorporated into the integrating factor, and the forcing used was such that there was constant enstrophy injection $\eta = 0.1$, being nonzero only for 16 selected wave vectors having magnitudes lying in the interval $K = (10, 11)$. Within K , a forcing of the form

$$\hat{f}(\mathbf{k}, t) = \frac{\eta}{16\hat{\omega}^*(\mathbf{k}, t)} \tag{2.58}$$

was used. The 16 forced modes were initialised to small nonzero values, while all other modes were initialised to zero. This allowed a direct transfer range of over two decades for the highest resolutions runs, with an inverse transfer range of a decade ensuring

negligible contamination by inverse energy transfer up to time $t = 35$. It should be noted, however, that the simulations could not have been continued for substantially longer without risking serious contamination of the inverse energy transfer range.

To show the dependence of viscous enstrophy dissipation on viscosity for frictionally damped turbulence, three simulations with $\alpha = 0.008$ and $\nu = 1.6 \times 10^{-5}$, 4×10^{-6} and 1×10^{-6} , corresponding to resolutions 2048×2048 , 4096×4096 and 8192×8192 , were run. The coefficient α was chosen such that frictional dissipation was weaker than viscous dissipation, and viscosity alone could adequately resolve the truncation scales. The correct value of the viscosity to ensure sufficient dissipation and prevent contamination of the highest wavenumbers was found through trial and error for the lowest resolution run, then when the resolution was doubled the viscosity was decreased by a factor of four according to the approximately linear scaling of the number of degrees of freedom with the Reynolds number, and the argument given at the end of §2.2.2. In order to compare with undamped turbulence, three simulations with the same viscosity, but setting $\alpha = 0$, were also run. Figure 2.1 shows the enstrophy dissipation rates versus time up to $t = 35$, after which the turbulence is apparently quasi-steady. The cases $\alpha = 0$ and $\alpha = 0.008$ are shown in figures 2.1a and 2.1b respectively. In the latter, the frictional, viscous and total dissipation rates *v.s.* time are depicted by dashed, solid and dashed-dotted lines respectively. The highest resolution runs are bold and in red, with the intermediate and lower resolution runs green and blue respectively. It is clear that as the viscosity is decreased, the viscous enstrophy dissipation rate decreases, while the frictional dissipation rate increases. It is interesting to note that the damped case seems to approach equilibrium faster than the undamped case. At equilibrium, in the undamped case the enstrophy dissipation rate is only around 20 percent of the enstrophy injection rate. This is presumably at least in part due to the upscale transfer of energy, meaning that some enstrophy is also transferred upscale, out of the reach of dissipation. In the damped case, however, there is significantly more total dissipation, and it seems reasonable that given sufficient time the total dissipation rate would match

the injection rate.

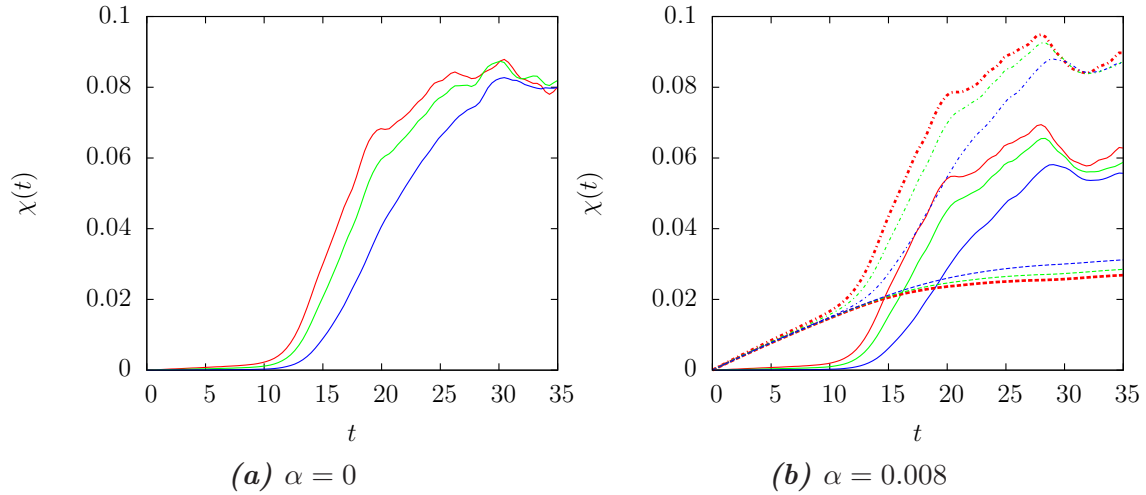


Figure 2.1: Viscous (solid), frictional (dashed) and total (dashed-dotted) enstrophy dissipation rates v.s. time for $\nu = 1.6 \times 10^{-5}$, 4×10^{-6} and 1×10^{-6} , respectively. In panel (a), smaller ν corresponds to less dissipation in the early stage. In panel (b), smaller ν corresponds to less viscous but more frictional dissipation throughout.

Figure 2.2 shows the enstrophy spectra $\mathcal{Z}(k) = k^2 \mathcal{E}(k)$ at $t = 30$ for the simulations shown in figure 2.1, with the undamped and damped cases in figures 2.2a and 2.2b respectively. In both cases, the spectra can be seen to be approaching the Kraichnan-Batchelor k^{-1} spectrum as the viscosity is decreased. This supports the suggestion that the scale-neutral Ekman drag does not affect the form of the spectrum of the enstrophy inertial range in a significant manner. This can be most clearly seen in figure 2.3 where the spectra for the highest resolution runs are plotted together, and they can be seen to be virtually indistinguishable.

Figure 2.4 shows the vorticity fields corresponding to the spectra in figure 2.3. It is remarkable that even when frictional dissipation of enstrophy becomes sufficiently strong (more than half as strong as viscous dissipation), there are hardly any noticeable differences between undamped and damped turbulence in both wavenumber and physical space.

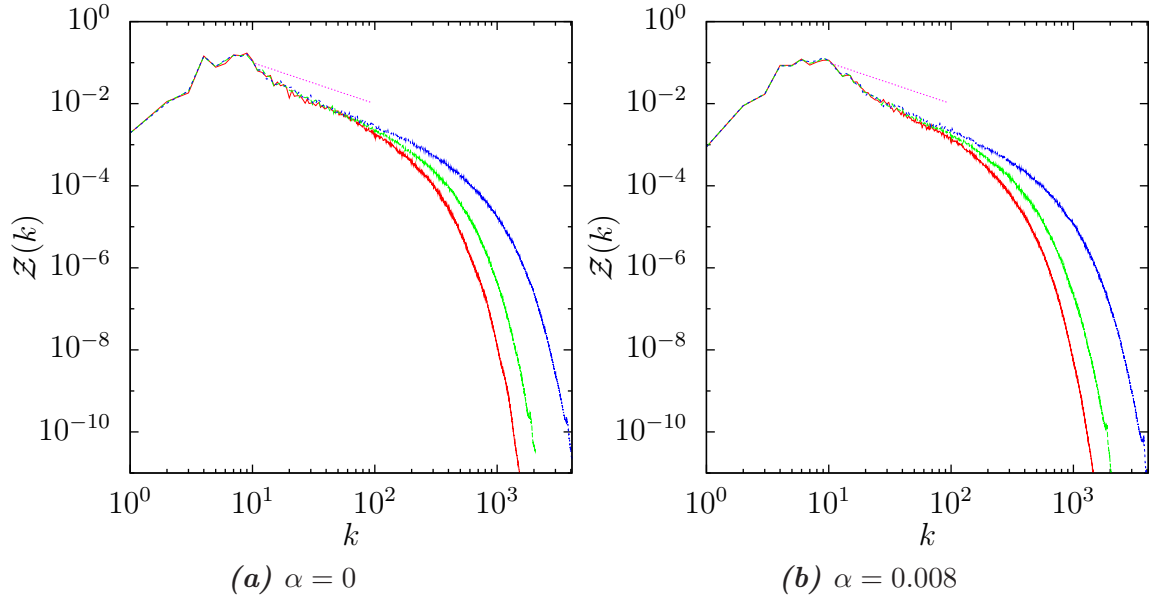


Figure 2.2: Enstrophy spectra at $t = 30$ for the same series of simulations as in figure 2.1. Shallower spectra correspond to smaller viscosity.

In order to test the result obtained in equation (2.57), a separate set of simulations up to resolutions 4096×4096 were carried out. For each of a dozen values of α in the range $[1/64, 1]$, ν_c was determined by varying ν until the equality $\alpha \|\omega\|^2 = \nu \|\nabla \omega\|^2$ approximately held during a short time period when the turbulence almost became quasisteady. Figure 2.5 shows a plot of $1/\alpha$ v.s. $\ln \nu_c$ which, according to (2.57) is expected to render a straight line, for small alpha, with slope $-C/\eta^{1/3}$ and intercept $(C/\eta^{1/3}) \ln[\eta^{1/3}/(Ck_f^2)]$. For the data points corresponding to the six smallest values of α , the line of best fit (the dashed line in figure 2.5), found using the method of least squares, is given by

$$\frac{1}{\alpha} = -10.2 \ln \nu_c - 58.6. \quad (2.59)$$

Using the slope and intercept of this line, the value of C was calculated to be $C = 3.8$ and $C = 3.2$, respectively. The slight discrepancy in these solutions is understandable and can be attributed to the fact that the range of α and ν_c under consideration is not small enough for the spectra to closely approximate the classical one.

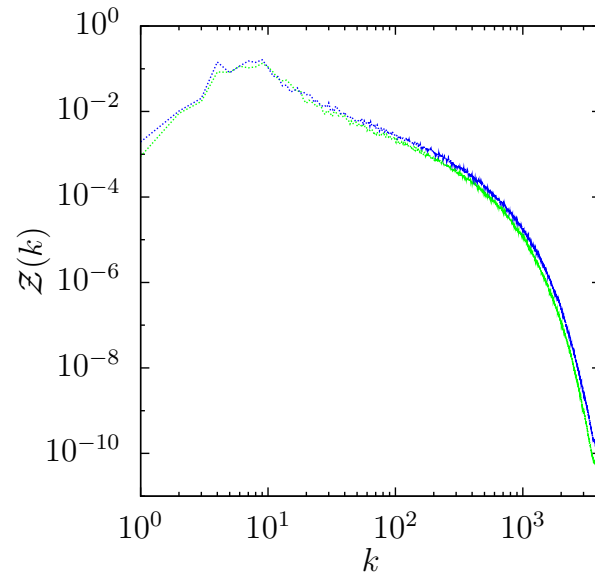
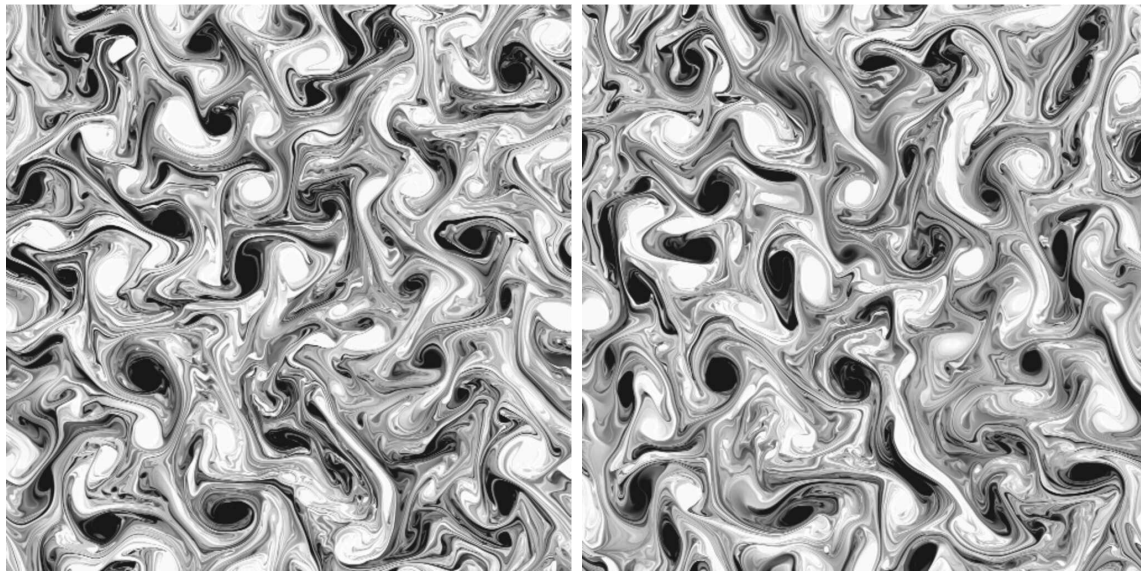


Figure 2.3: Enstrophy spectra for the highest resolution runs with $\alpha = 0$ (dotted blue line) and $\alpha = 0.008$ (solid green line).



(a) $\alpha = 0$

(b) $\alpha = 0.008$

Figure 2.4: Vorticity fields corresponding to the spectra of figure 2.3.

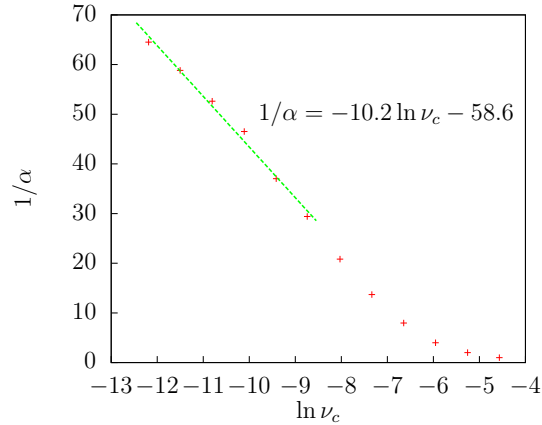


Figure 2.5: A plot of $1/\alpha$ v.s. $\ln \nu_c$ for simulations up to resolutions 4096×4096

2.4 Concluding remarks

In this chapter we have studied a number of aspects of 2DNS turbulence. We have derived upper bounds for the number of degrees of freedom N of the equations freely evolving from a smooth initial vorticity field in a double periodic domain and found that $N \leq C_1 Re$ in the energy space and $N \leq C_2 Re(1 + \ln Re)^{1/3}$ in the enstrophy space. Here C_1 and C_2 are constant and Re is the Reynolds number, which is defined in terms of the initial vorticity, the system size, and the viscosity. These results are consistent with the number of active modes deduced from a recent mathematical estimate of the viscous dissipation wavenumber $k_T = \|\nabla\omega\|/\|\omega\|$.

The present estimates for N have been compared with well-known bounds for the Hausdorff dimension D_H of the global attractor in the forced case, and the apparent difference between the linear (or nearly so) scaling of N with Re and the highly superlinear dependence of D_H on the inverse viscosity ν^{-1} has been discussed. We have argued that the superlinear dependence of D_H on ν^{-1} is not an intrinsic property of the turbulence dynamics and further suggested that this is a ‘removable artefact’, arising from the use of a time-independent forcing as a model for energy and enstrophy injection that drives the turbulence. This suggestion has been strengthened by the fact that the ‘extra’ dependence of D_H on ν^{-1} would be completely removed (at least for the

estimate of D_H in the enstrophy space) if one could model the driving force in such a way that the enstrophy injection rate does not depend on the viscosity. Such a forcing can be seen to be more realistic than ones with viscosity-dependent input.

In the present analysis, we have simply followed a trajectory starting from an arbitrary smooth initial vorticity field in the solution (function) space of the 2DNS equations and monitored the evolution (under the linearised dynamics) of the volumes of n -dimensional balls centred on the trajectory. We then estimated how large n should be to ensure that these volumes contract exponentially. This turns out to be equivalent to the method of estimating the Hausdorff dimension of the global attractor of the forced system. The present approach can be seen to be highly flexible in application. In general, it is applicable to either autonomous or nonautonomous, forced or unforced, and finite-dimensional or infinite-dimensional systems. There are virtually no special requirements, other than existence of solution, for the present definition (and method of analysis) of the number of degrees of freedom to make sense. In particular, the existence of the usual Lyapunov exponents is not an issue. Furthermore, there is no need for *a priori* knowledge of the existence of an attractor (or global attractor), whose generalised dimensions would normally be considered as the number of degrees of freedom of the dynamical system in question. Given all this, we may apply the present approach to less idealised and more realistic dynamical models without risking to compromise mathematical rigour.

We have also examined, both theoretically and numerically, the effects of mechanical friction on the enstrophy dynamics of forced 2DNS turbulence. On the theoretical side we have shown by an elementary method that friction gives rise to vanishing viscous enstrophy dissipation in the inviscid limit. Similar to freely decaying frictionless turbulence in the inviscid limit, where viscous dissipation of enstrophy vanishes uniformly in time (Tran & Dritschel, 2006; Dritschel *et al.*, 2007), the present result is valid uniformly in time. This uniformity in time is important and worth emphasising as it appears to have been misunderstood (in the freely decaying case) by some au-

thors (see the remark on page 352 of Fox & Davidson (2010)). The implication of the present findings is that given a fixed friction coefficient, frictional dissipation of enstrophy becomes predominant for sufficiently small viscosity. This inevitably results in the classical enstrophy inertial range becoming a dissipation range in which the dissipation of enstrophy by friction mainly occurs. This range can at best support a diminishing enstrophy flux rather than the k -independent flux of Kraichnan. For the classical spectrum, which is assumed to be valid in the limit of weak friction, we have derived an expression for the critical viscosity, which separates the regimes of predominant viscous and frictional dissipation of enstrophy. This critical viscosity decreases exponentially with the friction coefficient. On the numerical side, we have carried out a number of numerical integrations of the forced 2DNS equations with a friction term to confirm the theoretical results. Given all else fixed, including the friction coefficient, viscous dissipation of enstrophy has been observed to decrease as the viscosity is decreased. This decrease appears to be slow, probably logarithmically in viscosity as in the case of freely decaying turbulence (Tran & Dritschel, 2006; Dritschel *et al.*, 2007). The numerical results for the critical viscosity are in qualitative agreement with the theoretical finding. We have observed no significant differences between undamped and damped turbulence near the critical viscosity. In particular, the energy spectra of the enstrophy inertial range in the two cases are virtually indistinguishable, both being close to the classical k^{-3} spectrum.

Enstrophy divergence in the inviscid limit is an indispensable feature of the Kraichnan theory. One reason is that the predicted limiting inertial range simply has infinite enstrophy. Another reason, which is less obvious, is that the production of ever-smaller scales (effectively a linear process (Tran, 2009; Tran *et al.*, 2010)) would simply not be able to withstand viscous effects in the absence of a diverging vorticity. In other words, only in the presence of a diverging vorticity could the enstrophy be transferred to, and eventually dissipated at, ever-smaller scales, thereby maintaining the picture of quasisteady dynamics envisaged by Kraichnan. Therefore, in choosing large-scale

dissipation operators for numerical reasons or in designing thin film or shallow fluid layer experiments, one should be mindful of this constraint. Mechanical friction has been seen here to render ‘anti-Kraichnan’ behaviour in the inviscid limit. Another important effect of friction not discussed in this study is that it ‘stabilises’ the virtually inviscid forcing region, which, in Kraichnan’s picture, is kept bounded by the dual cascade alone. The implication is that the problem of universality or nonuniversality of the Kraichnan-Batchelor constant may not be reliably resolved by simulations with a friction term.

Chapter 3

The Surface Quasigeostrophic Equation

3.1 Introduction

One of the key forces driving the study of turbulence is the desire to understand the motion of our planet's atmospheres and oceans more thoroughly, for which purpose a vast number of models for stratified rapidly rotation fluids have been developed, among which are the geostrophic equations which describe the first-order departure from the balance between the Coriolis force and pressure gradient. The theory behind the geostrophic equations has been thoroughly studied and constitutes a huge literature (see *e.g.* Charney, 1948, 1971; Rhines, 1979; Pedlosky, 1987), while itself rendering a large variety of 2D models that are vastly simpler yet sophisticated enough to capture many of the underlying dynamics. Among these models is the surface quasigeostrophic equation (SQG), which is derived considering the geostrophic streamfunction ψ on a flat surface boundary $z = 0$, in which case the vertical gradient of ψ matches the temperature field $T(x, y)$, *i.e.* $\partial_z \psi|_{z=0} = T(\mathbf{x})|_{z=0}$. For flows with zero potential vorticity, this surface temperature is equivalent to $\Lambda \psi$ where Λ is known as the Zygmund operator, which is

a self-adjoint linear operator, sometimes symbolised by $|\nabla|$ or $(-\Delta)^{1/2}$, whose action on a function $\theta(\mathbf{x})$ is equivalent to a multiplicative operator in Fourier space which is given by

$$\widehat{\Lambda\theta}(\mathbf{k}) = |\mathbf{k}|\widehat{\theta}_{\mathbf{k}} \quad (3.1)$$

where $\widehat{}$ denotes the Fourier transform. The equations governing the advection of the potential temperature on the horizontal boundary is then given by

$$\frac{\partial\theta}{\partial t} + J(\psi, \theta) = \nu\Delta\theta \quad (3.2)$$

$$\theta = \Lambda\psi \quad (3.3)$$

where θ is the potential temperature, ψ is the streamfunction and ν is the viscosity. The dissipation mechanism used here is a single power of the Laplacian to put it on the same footing as the other equations in this thesis. The relationship between the potential temperature θ and the advecting velocity \mathbf{u} has a particularly simple description in Fourier space, however the physical-space relationship, given by the singular integral,

$$\mathbf{u}(\mathbf{x}) = -\frac{1}{2\pi} \int_{\Omega} \frac{\mathbf{y}^{\perp}\theta(\mathbf{x} - \mathbf{y})}{|\mathbf{y}|} d\mathbf{y} \quad (3.4)$$

can still tell us much, in particular in comparison to the equivalent Biot-Savart law in 2D hydrodynamic turbulence, which is given in equation (2.3). In particular, for SQG turbulence the streamfunction for a Dirac temperature distribution $\theta = \delta(\mathbf{x} - \mathbf{x}')$ is given by $\psi = -(2\pi|\mathbf{x} - \mathbf{x}'|)^{-1}$, while for hydrodynamic turbulence a point vortex $\omega = \delta(\mathbf{x} - \mathbf{x}')$ produces a flow $\psi = -(2\pi)^{-1} \ln(|\mathbf{x} - \mathbf{x}'|)$ (Held *et al.*, 1995). This means that circumferential velocities around the vortex are proportional to r^{-2} in SQG, rather than r^{-1} in 2DNS, with the result that point vortices rotate around each other more rapidly than in hydrodynamic turbulence, and thus needing a greater ambient strain to pull them apart, as rapid rotation averages out the rate of strain. On the other hand, more distant eddies are less tightly bound to each other, meaning that the tendency to form localised vortices is implied, and interactions tend to be spatially local. These

facts are commented upon further in §3.3.2 and in the next chapter.

Similarly to the usual 2D hydrodynamic equations, the nonlinear term in equation (3.2) gives rise to two inviscid invariants. By multiplying equation (3.2) by θ and averaging over the domain we obtain the equation governing the viscous decay, and inviscid conservation, of the mean square potential temperature, which is equal to twice the generalised enstrophy,

$$\frac{d}{dt} Z_g \equiv \frac{1}{2} \frac{d}{dt} \|\theta\|^2 = -\nu \|\nabla\theta\|^2 \equiv -\chi_g. \quad (3.5)$$

The relationship between the potential temperature and the streamfunction means that the spectrum of the generalised enstrophy $Z_g(k)$ and the spectrum $\mathcal{E}(k)$ of the usual energy $E = \frac{1}{2} \|\mathbf{u}\|^2 = \frac{1}{2} \|\nabla\psi\|^2$ are identical, meaning that we have the equality

$$Z_g(t) \equiv \frac{1}{2} \|\theta\|^2 = \frac{1}{2} \|\mathbf{u}\|^2 \equiv E(t). \quad (3.6)$$

The fact that θ is a same-scale copy of the velocity field \mathbf{u} will be seen to have a strong effect in the dynamics of the system. The second conservation law comes about by multiplying equation (3.2) by $\psi = \Lambda^{-1}\theta$ and averaging over the domain, giving rise to the equation for the evolution of the generalised energy

$$\frac{d}{dt} E_g \equiv \frac{1}{2} \frac{d}{dt} \|\Lambda^{-1/2}\theta\|^2 = -\nu \|\Lambda^{1/2}\theta\|^2 \equiv -\epsilon_g. \quad (3.7)$$

The generalised enstrophy and generalised energy have obvious similarities with the energy and enstrophy in hydrodynamic turbulence, and as such may be expected to obey many of the same dynamic principles and be amenable to similar analysis. On this basis, Pierrehumbert *et al.* (1994) carried out phenomenological analysis using Kolmogorov theory¹, suggesting the existence of two inertial ranges, a forward-cascading generalised enstrophy (usual energy) inertial range, with a generalised enstrophy spectrum of the

¹In fact Pierrehumbert did this analysis in the more general framework of alpha turbulence, which we discuss in the next chapter, of which SQG turbulence is a special case.

form

$$\mathcal{Z}_g(k) = C\chi_g^{2/3}k^{-5/3} \quad (3.8)$$

and an inverse-cascading generalised energy inertial range having the scaling

$$\mathcal{E}_g(k) = C'\epsilon_g^{2/3}k^{-2}. \quad (3.9)$$

where C and C' are constants. Thus far, however, there has been no other theoretical evidence for this spectrum, and numerical studies have been limited (Held *et al.*, 1995; Ohkitani & Yamada, 1997; Smith *et al.*, 2002; Scott, 2006; Capet *et al.*, 2008).

As well as possibly possessing a $k^{-5/3}$ forward-cascading spectrum, the SQG system has many similarities with the 3DNS equations that are not found in the usual 2D hydrodynamic case. This comes about because the generalised enstrophy spectrum is the same as the classical energy spectrum, meaning that θ is a same-scale copy of \mathbf{u} . The relevance of this can be most clearly seen by examining the equation for the perpendicular gradient of θ ,

$$\left(\frac{\partial}{\partial t} + \mathbf{u} \cdot \nabla\right) \nabla^\perp \theta = (\nabla \mathbf{u}) \nabla^\perp \theta + \nu \Delta \nabla^\perp \theta, \quad (3.10)$$

where $\nabla^\perp \theta$ has a role that is analogous to the usual 3D vorticity $\boldsymbol{\omega}$. Of particular importance is that the stretching term $(\nabla \mathbf{u}) \nabla^\perp \theta$ is the product of two functions of the same scale, $\nabla \mathbf{u}$ and $\nabla^\perp \theta$, in fact we have the equality $\langle |\nabla \mathbf{u}|^2 \rangle = \langle |\nabla^\perp \theta|^2 \rangle$. This means that the transfer of θ downscale, which necessarily results in a growth of $\nabla^\perp \theta$, also magnifies the velocity gradient $\nabla \mathbf{u}$, leading to a positive feedback which could result in explosive growth of $\nabla^\perp \theta$, possibly leading to finite-time singularities, unless the dissipative term is strong enough to sufficiently control the growth. It has been found that a dissipation mechanism of the form $(-\Delta)^\gamma$, where $\gamma \geq 1/2$, is strong enough to regularise the dynamics (see Kiselev *et al.*, 2007; Caffarelli & Vasseur, 2010), however the behaviour in the inviscid case is still an open problem. This means that for equation (3.2) with $\nu > 0$, given a smooth initial temperature field $\theta_0(x, y) = \theta(x, y, 0)$ and a

fixed $\nu > 0$, the energy dissipation rate $\epsilon(t)$ will be bounded, and eventually decay to zero. For high Reynolds number $\|\nabla\theta\|$ will grow initially, with the dissipation rate reaching a global maximum $\epsilon_T = \epsilon(T)$ at some time $t = T$. The question of whether ϵ_T and T depend on ν in the inviscid limit is still not answered. For the present case, Ohkitani & Yamada (1997) suggested that ϵ_T vanishes in the inviscid limit while T diverges, thus favouring the possibility of no finite-time singularities in the inviscid dynamics. In a study using the very initial conditions of Ohkitani & Yamada (1997), Constantin *et al.* (1998) suggested no finite-time blowup. If this is indeed the case, then $\epsilon(t) \rightarrow 0$ as $\nu \rightarrow 0$ for all $t < \infty$ because $\|\nabla\theta\| < \infty$. However, the possibility that $\|\nabla\theta\|$ diverges as $t \rightarrow \infty$ cannot be ruled out. This means that further investigation is needed to determine whether or not $\epsilon_T \rightarrow 0$. In any case, the detailed behaviour of ϵ_T is not a major concern in the present study (more detail in due course). In what follows, we make use of ϵ_T in key derivations, pending further knowledge of this important dynamical quantity.

The remainder of this chapter is laid out in the following manner. In §3.2.1, which is based on the paper (Tran *et al.*, 2011), we apply the concept of number of degrees of freedom, introduced earlier, to the SQG equation, deriving the result $N \leq Re^{3/2}$, while in §3.3.1, which is based on the same paper, we present the results from a number of simulations carried out at resolutions up for 4096×4096 which seem to show the possibility of finite-time singularity in the inviscid limit. There are, however, potential problems with the form of the initial conditions used in these simulations, so in §3.3.2 we use the results from a new set of simulations up to 16384×16384 resolution, with slightly different initial conditions, in an attempt to address these concerns.

3.2 Analysis

We now use the methods described in §1.3.1 and in the previous chapter to derive a bound for the number of degrees of freedom of SQG turbulence, which naturally leads

to confirmation of a number of classically-derived results which have until now been derived phenomenologically.

3.2.1 Lyapunov stability analysis and degrees of freedom

Let $\theta(x, y, t)$ be a solution for equation (3.2) (with the corresponding streamfunction ψ), starting from some smooth initial temperature field $\theta_0(x, y) = \theta(x, y, 0)$. Now consider a disturbance ϑ to θ (corresponding to a disturbance φ of ψ). The evolution of ϑ is then governed by

$$\frac{\partial \vartheta}{\partial t} + J(\psi, \vartheta) = -J(\varphi, \theta) - J(\varphi, \vartheta) + \nu \Delta \vartheta \quad (3.11)$$

where $\vartheta = \Lambda \varphi$. Linearising this equation by ignoring the $J(\varphi, \vartheta)$ term, multiplying by ϑ and averaging over space gives

$$\|\vartheta\| \frac{d\|\vartheta\|}{dt} = -\langle \vartheta J(\varphi, \theta) \rangle - \nu \|\nabla \vartheta\|^2, \quad (3.12)$$

where one of the triple-product terms, namely $\langle \vartheta J(\psi, \vartheta) \rangle$, vanishes due to equation (1.50). It follows that the exponential decay rate λ of $\|\vartheta\|$ is given by

$$\lambda = \frac{1}{\|\vartheta\|} \frac{d\|\vartheta\|}{dt} = -\frac{1}{\|\vartheta\|^2} (\langle \vartheta J(\varphi, \theta) \rangle + \nu \|\nabla \vartheta\|^2). \quad (3.13)$$

We now construct an orthonormal set of n least stable disturbances $\{\vartheta_1, \vartheta_2, \dots, \vartheta_n\}$ (with the associated set of streamfunctions $\{\varphi_1, \varphi_2, \dots, \varphi_n\}$, where $\vartheta_i = \Lambda \varphi_i$) and the corresponding greatest growth rates $\{\lambda_1, \lambda_2, \dots, \lambda_n\}$ (local Lyapunov exponents) by following the method of §1.3.1 with the φ_i orthonormal with respect to the energy inner product, or equivalently the ϑ_i are orthonormal with respect to the usual L^2 -space inner product, that is $\langle \varphi_i, \varphi_j \rangle_E = \langle \vartheta_i \vartheta_j \rangle = \delta_{i,j}$, where $\delta_{i,j}$ is the Kronecker delta. Since

each normalised solution (λ_i, ϑ_i) satisfies equation (3.11), we have

$$\begin{aligned}
\sum_{i=1}^n \lambda_i &= - \sum_{i=1}^n (\langle \vartheta_i J(\varphi_i, \theta) \rangle + \nu \|\nabla \vartheta_i\|^2), \\
&\leq \sum_{i=1}^n (\langle |\vartheta_i| |\nabla \varphi_i| |\nabla \theta| \rangle - \nu \|\nabla \vartheta_i\|^2), \\
&\leq \|\nabla \theta\| \left\| \sum_{i=1}^n \vartheta_i^2 \right\|^{1/2} \left\| \sum_{i=1}^n |\nabla \varphi_i|^2 \right\|^{1/2} - \nu \sum_{i=1}^n \|\nabla \vartheta_i\|^2, \\
&\leq c_2 L \|\nabla \theta\| \left(\sum_{i=1}^n \|\nabla \vartheta_i\|^2 \right)^{1/2} - \nu \sum_{i=1}^n \|\nabla \vartheta_i\|^2, \\
&\leq \left(\sum_{i=1}^n \|\nabla \vartheta_i\|^2 \right)^{1/2} \left(c_2 L \frac{\epsilon_T^{1/2}}{\nu^{1/2}} - c_1^{1/2} \nu \frac{n}{L} \right).
\end{aligned} \tag{3.14}$$

In equation (3.14), we have used the Cauchy–Schwartz inequality in the third step, the Lieb–Thirring inequality (1.58) for ϑ_i together with equation (1.59) for $\nabla \varphi_i$ in the penultimate step, and equation (1.54) in the final step. The condition that $\sum_{i=1}^n \lambda_i \leq 0$ is satisfied when

$$n \geq \frac{c_2 L^2 \epsilon_T^{1/2}}{c_1^{1/2} \nu^{3/2}}. \tag{3.15}$$

It then follows that

$$\begin{aligned}
N &\leq \frac{c_2}{c_1^{1/2}} \frac{L^2 \epsilon_T^{1/2}}{\nu^{3/2}}, \\
&= \frac{c_2}{c_1^{1/2}} \left(\frac{L^{4/3} \epsilon_T^{1/3}}{\nu} \right)^{3/2}, \\
&= Re^{3/2},
\end{aligned} \tag{3.16}$$

where Re is the Reynolds number, defined in the same way as in 3DNS turbulence (Tran, 2009).

The estimate (3.16) can be optimal up to a factor not tending to zero as rapidly as $Re^{-\gamma}$, for $\gamma > 0$. In other words, the exponent $3/2$ of $Re^{3/2}$ can be exact. The reason

is that all the inequalities used in (3.14) are relatively sharp. For example, by virtue of equations (1.54) and (1.58), the norm $\|\sum_{i=1}^n \vartheta_i^2\|$ amounts to approximately n . This is an optimal estimate as there are no reasons to expect this norm to be of order n^γ for $\gamma < 1$. The sharpness of this highly sophisticated estimate in (3.14) provides us with confidence in the optimality of (3.16). In 3D turbulence, however, the situation is not so optimistic. For this case, a similar line of estimates for the number of degrees of freedom yields the bound $N \leq Re^{18/5}$ (see the discussion in Tran (2009) and references therein). When compared to the improved estimate $N \approx Re^{9/4}$, which is the Landau prediction on the basis of Kolmogorov’s theory, this bound is an overestimate by a factor of $Re^{27/20}$. Tran (2009) attributes this to the excessive nature of the Lieb–Thirring inequality in three dimensions (when applied to turbulence). In order to appreciate this claim, we note that the norm $\|\sum_{i=1}^n \mathbf{v}_i^2\|$, where \mathbf{v}_i is the 3D counterpart of ϑ_i , when estimated by (7) and (25) of Tran (2009) – the 3D counterparts of equations (1.54) and (1.58), which are given by equation (1.57) and (1.61) – amounts to $n^{5/4}$. There is an apparent difference by a factor of $n^{1/4}$ for the values of $\|\sum_{i=1}^n \vartheta_i^2\|$ and $\|\sum_{i=1}^n \mathbf{v}_i^2\|$. This implies that the Lieb–Thirring inequality can be potentially excessive by a factor of $n^{1/4}$ in the context of 3DNS turbulence. Interestingly, if this factor were to be removed, one would then recover the Landau prediction. In §3.3 the result $N \leq Re^{3/2}$ is fully justified by numerical simulations of equation (3.2), where adequate dissipation is observed when we set the ratio $N/Re^{3/2}$ (more precisely the product $\nu^{3/2} k_{max}^2$, where $k_{max} \approx N^{1/2}/L$ is the truncation wavenumber) at order unity. This can be considered numerical evidence for the result (3.16) and is discussed in more detail in the next section.

3.2.2 Inertial-range scaling

This subsection makes use of the analytic estimate (3.16) to deduce the spectral scaling $k^{-5/3}$ for the energy inertial range. This approach can be seen as an analytic alternative to the familiar phenomenological dimensional analysis method. We briefly discuss the implication of the present results in conjunction with related results in the

literature.

At the instant of maximum energy dissipation, consider the power-law spectrum $Ck^{-\alpha}$ of the inertial range, extending to some dissipation wavenumber k_d , where C is a constant of suitable dimension. For such a spectrum, it is straightforward to deduce α from equation (3.16) under the assumption that the number of Fourier modes within the inertial range, say N' , is comparable to N . To this end, we note that $\epsilon_T \approx \nu C k_d^{3-\alpha} / (3-\alpha)$, assuming $\alpha < 3$. It follows that N' is given by

$$N' \approx L^2 k_\nu^2 \approx L^2 \left(\frac{3-\alpha}{C\nu} \epsilon_T \right)^{2/(3-\alpha)}. \quad (3.17)$$

From our assumption $N \approx N'$ and the two estimates (3.16) and (3.17) we deduce that

$$\left(\frac{\epsilon_T}{C\nu} \right)^{2/(3-\alpha)} \leq \frac{\epsilon_T^{1/2}}{\nu^{3/2}}, \quad (3.18)$$

where the respective constant factors $(3-\alpha)^{2/(3-\alpha)}$ and $c_2/c_1^{1/2}$ on the left-hand and right-hand sides have been omitted. It follows that

$$\epsilon_T^{1+\alpha} \leq C^4 \nu^{3\alpha-5}. \quad (3.19)$$

Given $\epsilon_T > 0$ in the inviscid limit, equation (3.19) implies $\alpha \leq 5/3$. Thus we have recovered a bound for the classical spectrum by the present method. Furthermore, for the critical value $\alpha = 5/3$, the constant C can be seen to be proportional to $\epsilon_T^{2/3}$, consistent with the Kolmogorov spectrum $C_K \epsilon_T^{2/3} k^{-5/3}$, where C_K is the Kolmogorov constant. In passing, it is worth noting that the *a priori* condition $\epsilon_T > 0$ is not crucial and can be relaxed to a certain extent. In particular, the result remains valid when ϵ_T tends to zero logarithmically (see the concluding remarks for more detail).

It is remarkable that no values of α other than $5/3$ are admissible, provided that the estimate (3.16) is optimal in the sense discussed above. This result can be ‘half’ anticipated for the following reason. Onsager (1949) conjectured that solutions of the

3D Euler equations satisfying $|\mathbf{u}(\mathbf{x} + \mathbf{r}) - \mathbf{u}(\mathbf{x})| \propto |\mathbf{r}|^\gamma$, where $\gamma > 1/3$, conserve energy. Such solutions correspond to energy spectra steeper than $k^{-5/3}$ and indeed Constantin *et al.* (1994c) showed that solutions of the Euler equations conserve energy if the velocity field is contained in the Besov spaces $B_3^{\alpha, \infty}$ for $\alpha > 1/3$. Equation (3.19) is consistent with this result since $\alpha > 5/3$ readily implies that ϵ_T vanishes in the inviscid limit. On the other hand, the regime $\alpha < 5/3$ would require ϵ_T to grow without bound in the same limit, again provided that (3.16) is optimal. Such a behaviour would be an insult to the Kolmogorov spirit and is highly improbable for smooth solutions satisfying the decay (3.7).

We earlier equated the number of active Fourier modes N' within the energy inertial range with the derived number of degrees of freedom N . This amounts to $k_d^2 \approx N/L^2 \approx \epsilon_T^{1/2}/\nu^{3/2}$. It follows that the exponential dissipation rate $r_d = \nu k_d^2$ at the dissipation wavenumber k_d is given by

$$r_d \approx \frac{\epsilon_T^{1/2}}{\nu^{1/2}}. \quad (3.20)$$

Hence r_d grows as $Re^{1/2}$ when Re is increased. By setting $k_{max} = k_d$ in numerical simulations, we have the practical version of (3.20)

$$\nu \approx \frac{\epsilon_T^{1/3}}{k_{max}^{4/3}}, \quad (3.21)$$

which is used in §3.3.2 for setting ν in numerical simulations at various resolutions. Note that equation (3.20) is a straightforward consequence of the classical spectrum $C_K \epsilon_T^{2/3} k^{-5/3}$. Here it has been derived independently of this scaling, just assuming $N' \approx N$. For a comparison, this same rate scales as Re^1 (Tran & Dritschel, 2010), $Re^{1/2}$ (Tran, 2009) and Re^0 (see the end of §2.2.2) for one-dimensional (1D) Burgers flows, 3D and 2D turbulence, respectively. The difference in r_d for these systems can be attributed to fundamental differences in their dynamics and is worthy of a closer look. The scaling $r_d \propto Re^0$ in 2D turbulence has long been expected and is well known to numerical analysts. This is due to the effectively linear behaviour of the vorticity

gradient dynamics (Tran *et al.*, 2010), rendering a relatively weak excitation of the small scales. This excitation is balanced by viscous effects at the scale where $r_d \propto Re^0$. The dependence $r_d \propto Re$ in Burgers flows reflects the fully quadratic nonlinearities of the velocity gradient dynamics, resulting in a relatively intense excitation of the small scales. This excitation is the strongest of all these cases, reaching the scale with $r_d \propto Re$, whereby viscous forces become sufficiently strong to balance nonlinear effects. Now, the ‘intermediate’ scaling $r_d \propto Re^{1/2}$ in both SQG and 3D turbulence means that relatively mild dissipation at k_d is needed for the same purpose. This implies some partial depletion of nonlinear effects (from fully quadratic nonlinearities), which has been widely discussed and studied from different perspectives (see *e.g.* Hou & Li, 2006, 2008). This depletion could be the result of a phase shift brought about by the action of singular integral operators, displacing the positions of peak vorticity and strain rate (Ohkitani, 2011). This topic is beyond the scope of the present study and is briefly mentioned here in passing. A manifestation of this depletion is the relatively shallow $k^{-5/3}$ spectrum compared with its k^{-2} shock-dominated counterpart. This is consistent with the intuitive expectation that weaker nonlinearities allow for shallower spectra to develop – a justifiable fact on the basis of the present analysis. Indeed, weaker nonlinearities correspond to better Lyapunov stability, thereby implying smaller N and r_d . This in turn implies smaller α , i.e. shallower spectra.

Numerical evidence for the spectrum $k^{-5/3}$ in the literature is rather limited and inconclusive. For example, by directly simulating equation (3.2) without any modifications, Ohkitani & Yamada (1997) found an energy spectrum close to k^{-2} . A similar attempt by Capet *et al.* (2008), but with the usual molecular viscosity term replaced by a hyperviscosity term, found a slightly shallower spectrum: between k^{-2} and $k^{-5/3}$. Intuitively, these steep spectra may be attributable to low numerical resolutions, i.e. low Reynolds numbers. Another reason for the observed steep spectrum in Ohkitani & Yamada (1997) is due to the choice of the initial condition $\theta_0 = \sin x \sin y + \cos y$, which consists of the lowest ($k = 1$) and second lowest ($k = \sqrt{2}$) wavenumbers only.

For this initial condition, $\|\theta_0\|^2 = 3/4$ and $\|\Lambda^{-1/2}\theta_0\|^2 = 1/2 + 1/(4\sqrt{2})$. So by the dual conservation of $\|\theta\|^2$ and $\|\Lambda^{-1/2}\theta\|^2$, even in the idealised situation whereby all of $\|\Lambda^{-1/2}\theta\|^2$ got transferred to $k = 1$, no more than 9.8% $[(1 - 1/\sqrt{2})/3]$ of the energy would become available for transfer to the higher wavenumbers ($k \geq 2$). In practise, much less energy is available for transfer since the wavenumber $k = \sqrt{2}$ may not become completely depleted of energy. This inevitably results in weak small-scale dynamics and a steep spectrum. On the other hand, using both hyperviscosity and large-scale dissipation terms (plus a forcing term), Scott (2006) obtained energy spectra close to $k^{-5/3}$. With modern computers, it is quite possible to confirm the present prediction by a series of simulations with fixed θ_0 and increasingly higher resolutions (with corresponding increasingly higher Reynolds numbers). Note that in accord with equation (3.21), doubling the resolution (i.e. doubling k_{max} or quadrupling N) allows for the viscosity to be reduced by a factor of $2^{-4/3}$. The same reduction factor applies to numerical simulations of 3D turbulence (see the discussion of Tran & Dritschel (2010)) and 2D magnetohydrodynamic (MHD) turbulence (see §5.3).

3.3 Simulations

The next couple of sections describe simulations that were carried out to examine aspects of the SQG equations, in particular to check the expected scaling of the number of degrees of freedom with the dissipation rate, the form of the generalised enstrophy spectrum and the behaviour of the generalised enstrophy dissipation rate in the inviscid limit. The simulations in §3.3.1 (Tran *et al.*, 2011) use a set of initial conditions that suggest the possibility of the development of a finite-time singularity in the inviscid limit, yet in spite of the tantalising suggestion a number of factors render the result unsatisfactory. In §3.3.2 we attempt to address some of these problems, yet once again we are left just short of any real numerical breakthroughs. Both sets of runs are however consistent with the analysis in the previous section and in particular they demonstrate

the correctness of the derived result for the number of degrees of freedom.

3.3.1 Simulations with bimodal initial conditions

A set of simulations were run to examine the form of the energy spectrum, and the energy dissipation rate, in the inviscid limit. The initial temperature field θ_0 consisted of the Fourier modes $(7, 7)$ and $(7, 6)$, each with half-unit energy, while the modes $(-7, -7)$ and $(-7, -6)$ were initialised in such a way such that $\hat{u}(-\mathbf{k}) = \hat{u}^*(\mathbf{k})$, giving a total initial energy of two. The simulations were run with one 2048×2048 and two 4096×4096 resolutions, with viscosities $\nu = 8 \times 10^{-5}$ for the lower resolution and 4×10^{-5} and 2×10^{-5} for the higher resolutions. Using the Reynolds number as defined in equation (3.16), these correspond to $Re = 76,700$ for the highest viscosity, $Re = 158,800$ for the intermediate viscosity and $Re = 333,000$ for the lowest viscosity.

Figure 3.1 shows the evolution of $\epsilon(t)$ from $t = 0$ to $t = 9$ for the simulations described above. It can be seen that $\epsilon(t)$ peaks are roughly the same time, around $t = 6.5$, for all three Reynolds numbers under consideration, and increases with Re , presumably growing towards a finite limit, however the limited range of Reynolds numbers under consideration means it is not possible to make any general statements of the behaviour of ϵ_T in the inviscid limit. While there does seem to be some numerical instability around and just after the time of maximum dissipation, it is too small in magnitude to significantly alter the above conclusion.

Figure 3.2 shows the initial generalised enstrophy field. The central line in the initial conditions provides a number of hyperbolic saddle points, which Constantin *et al.* (1994b) showed was necessary for the development of singularities. While this initial field is morphologically similar to the one used by (Ohkitani & Yamada, 1997; Constantin *et al.*, 1998), it is only possible for the modes $(7n, m)$, for integers n and m , to be excited in the subsequent dynamics. This can be seen in figure 3.3 which shows the temperature field $\theta(t)$ at times $t = 2, 4, 6, 8$, and where it can be seen that

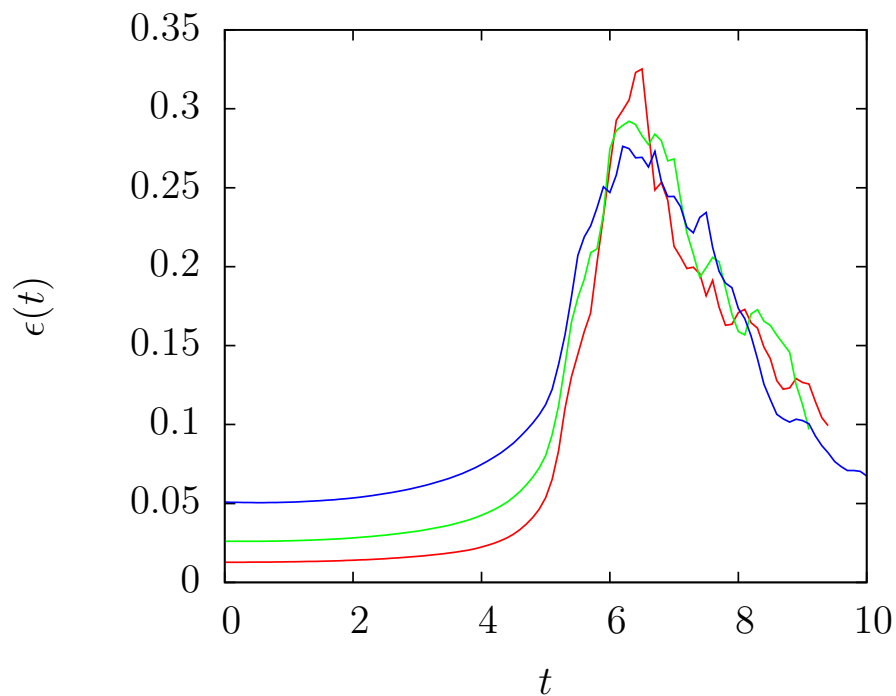


Figure 3.1: Energy dissipation rate $\epsilon(t)$ versus t for numerical integrations with resolutions 2048×2048 and 4095×4096 . The diffusion coefficients are $\nu \approx 8 \times 10^{-5}$ (blue) for the lower resolution and $\nu \approx 4 \times 10^{-5}$ (green) and 2×10^{-5} (red) for the higher resolution. Smaller ν corresponds to smaller ϵ_0 and larger ϵ_T .

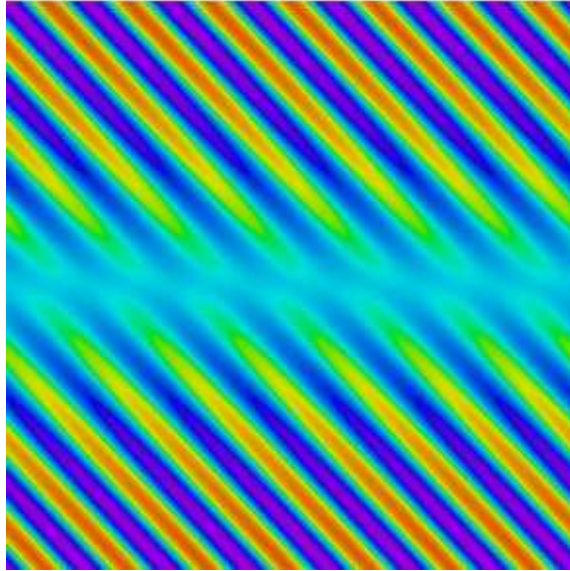


Figure 3.2: Initial temperature field θ_0 for the simulations described above.

the domain is essentially divided horizontally into seven identical pieces. Although it is obvious that the limited number of excited modes means that there was a large waste of computing resources, it does not seem to have had any effect on the forward cascade, with figure 3.3 demonstrating that the production of small scales does not seem to be constrained. The form of the initial conditions used also allows a much larger inverse-cascading range than in previous studies, which has an important consequence on the dynamics, which we discuss later.

Figure 3.4 shows the energy spectrum *v.s.* k taken at the time of maximum dissipation $T = 6$. As would be expected the energy spectra get shallower as the Reynolds number and resolution are increased. While the large-scale spectrum seems to have been affected by the limited number of excited modes, leading to a very ‘spiky’ spectrum around $k = 10$, the small-scale spectrum is not noticeably changed, and it seems to be tending towards the expected $k^{-5/3}$ spectrum as the viscosity is decreased.

It must be conceded that the range of Reynolds numbers considered here is insuf-

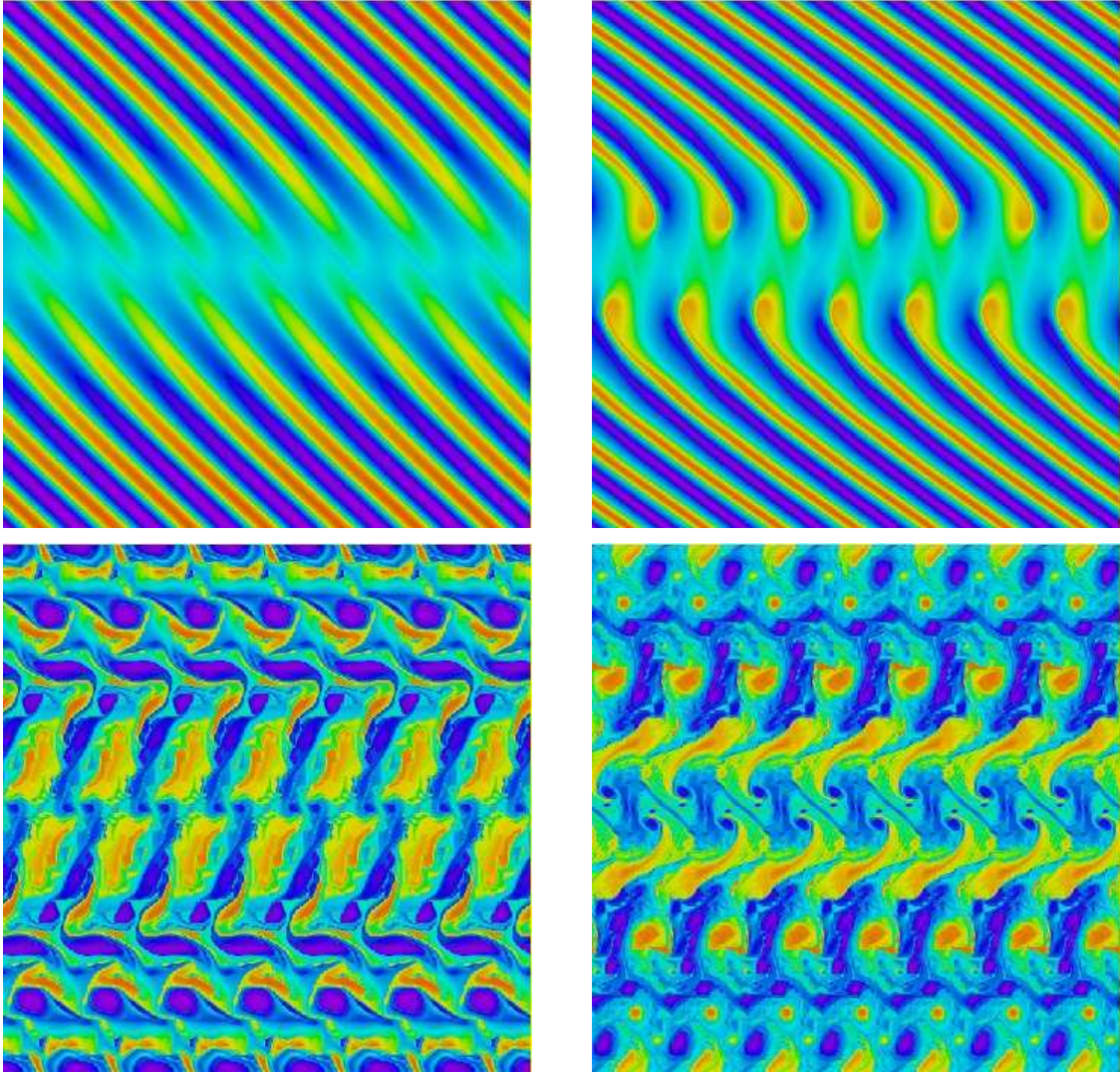


Figure 3.3: Temperature field $\theta(t)$ at $t = 2$ (top left), $t = 4$ (top right), $t = 6$ (bottom left) and $t = 8$ (bottom right)

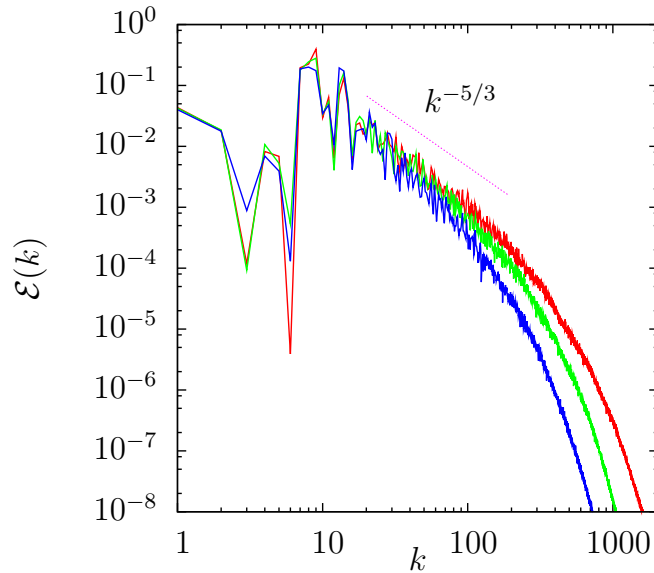


Figure 3.4: Energy spectra for the simulations described above, taken at the time of maximum dissipation, with $\nu = 8 \times 10^{-5}$ (blue) 4×10^{-5} (green) and 2×10^{-5} (red).

ficient to determine with any confidence whether the time of maximum dissipation T and maximum dissipation rate ϵ_T tend to some finite values, or perhaps exhibit some weak logarithmic dependence on the viscosity ν . Further investigation with significantly higher resolution is necessary to address this issue convincingly. In any case, the theoretical analysis presented in the previous sections is independent of whether or not $T < \infty$ in the inviscid limit, and indeed remains valid even if ϵ_T tends to zero logarithmically with increasing Re .

3.3.2 Simulations with trimodal initial conditions

While the simulations in the previous subsection show some suggestion of the possibility of finite-time blowup in the inviscid limit, both the limited Reynolds numbers covered and the choice of initial conditions leave the results unsure. In order to address these concerns, another set of simulations were run, up to resolutions of 16384×16384 . Noting that the initial conditions from earlier give tantalising hints of tending towards singular behaviour in the inviscid limit, similar initial conditions were used in these runs,

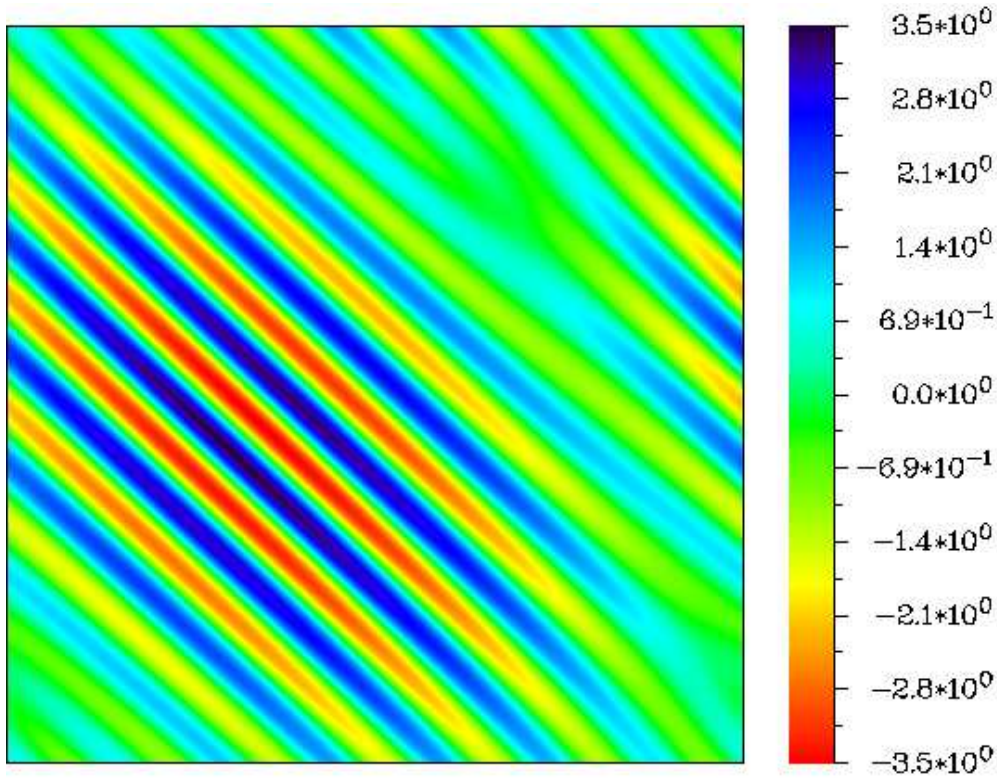


Figure 3.5: Initial θ -field

with initial modes $(6, 6)$, $(6, 7)$ and $(7, 7)$ initialised to uniformly distributed initial enstrophy, with $\hat{\theta}(-\mathbf{k})$ initialised to $-\hat{\theta}(\mathbf{k})$ to ensure the reality of the initial temperature field, which is shown in figure 3.5. These form of the initial conditions ensured that the whole wavenumber spectrum eventually became excited, while coming as close as possible to the initial field described in the previous section. Four different simulations were run, at resolutions 2048×2048 , 4096×4096 , 8192×8192 and 16384×16384 , with viscosity $\nu = 2 \times 10^{-4}$, 7.94×10^{-5} , 3.15×10^{-5} and 1.25×10^{-5} respectively. These correspond to Reynolds number of around 26,000, 65,400, 165,000 and 400,000 respectively. For this set of simulations when the resolution was doubled the viscosity was decreased by a factor of $2^{4/3}$ in line with the estimate for the number of degrees of freedom derived in the previous section.

Figure 3.6a shows the energy dissipation rate $\epsilon(t)$ *v.s.* time from $t = 0$ to $t = 10$

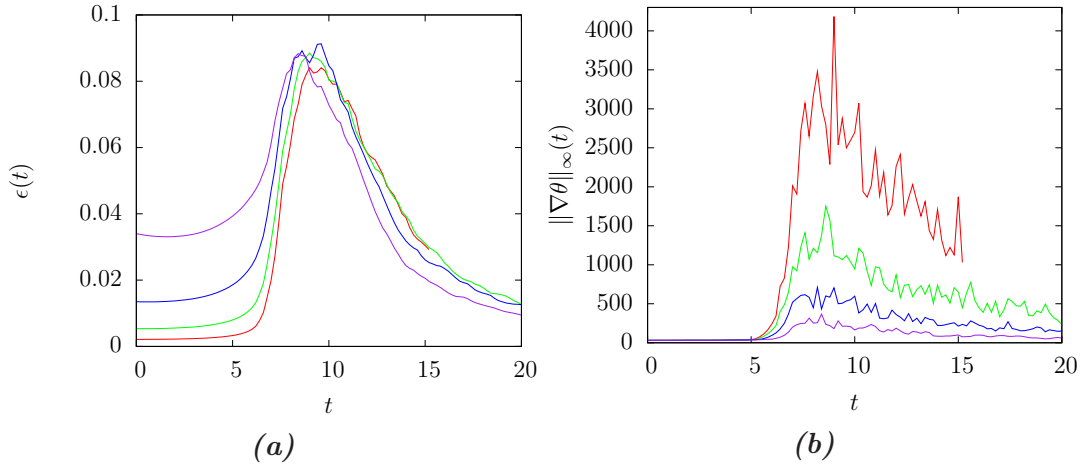


Figure 3.6: Energy dissipation rate $\epsilon(t)$ (left) and maximum temperature gradient $\|\nabla\theta\|_\infty$ (right) v.s. time for resolutions 2048×2048 (purple), 4096×4096 (blue), 8192×8192 (green) and 16384×16384 (red), corresponding to viscosities 2×10^{-4} , 7.94×10^{-5} , 3.15×10^{-5} and 1.25×10^{-5} respectively.

for the simulations described above. For the three lowest resolutions the maximum energy dissipation rate can be seen to be approximately constant, while the time of maximum dissipation appears to be increasing slowly, probably logarithmically. For the highest resolution simulation, however, the maximum dissipation rate seems to have decreased slightly from this high point. It is impossible to say whether this is the result of a real decrease in ϵ_T or merely a result of numerical instability, which seems plausible given the jagged top present for the 4096×4096 simulation. Figure 3.6b, which shows the maximum temperature gradient $\|\nabla\theta\|_\infty$ plotted over time, seems to suggest explosive growth of the maximum value, approximately doubling when the resolution is doubled. The behaviour of $\|\nabla\theta\|_\infty$ is important because, similarly to the BKM criterion in NS turbulence, it controls the blowup of solutions to the inviscid SQG equations (Constantin *et al.*, 1994a).

Figure 3.7 shows the energy spectra $\mathcal{E}(k)$, modified by multiplying by $k^{5/3}$ v.s. k for the simulations, taken at the time of maximum dissipation. As would be expected the spectra are increasingly shallow for lower viscosities, and seem to tend towards a $k^{-5/3}$

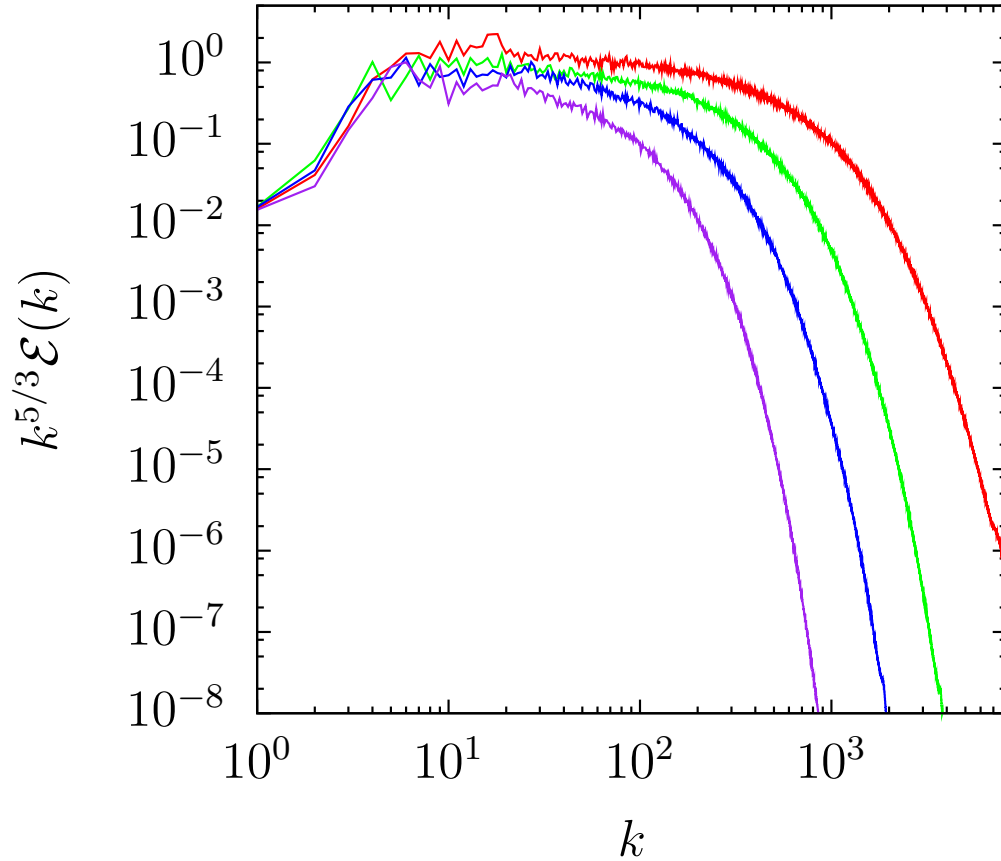


Figure 3.7: Energy spectra for the same simulations as shown in figure 3.6.

limit. The lack of numerical instability at the smallest scales for all of the simulations suggests that the method of multiplying the viscosity by $2^{-4/3}$ when the resolution is doubled is spot on, which gives us confidence in the accuracy of the derived formula for the number of degrees of freedom presented earlier.

Figure 3.8 shows the temperature field θ at times $t = 5$, $t = 10$, $t = 15$ and $t = 20$. While the turbulence does eventually homogenise, it is interesting to note that the approximately unimodal area just below to the left of centre takes until just past $t = 10$, the time of maximum dissipation, to lose information about the form of the initial conditions. This is because in this part of the domain the Jacobian is essentially zero, because for a unimodal area with wavenumber \mathbf{k} we have $\theta \sim |\mathbf{k}|\psi$. This means that any motion must be brought about from the action in other parts

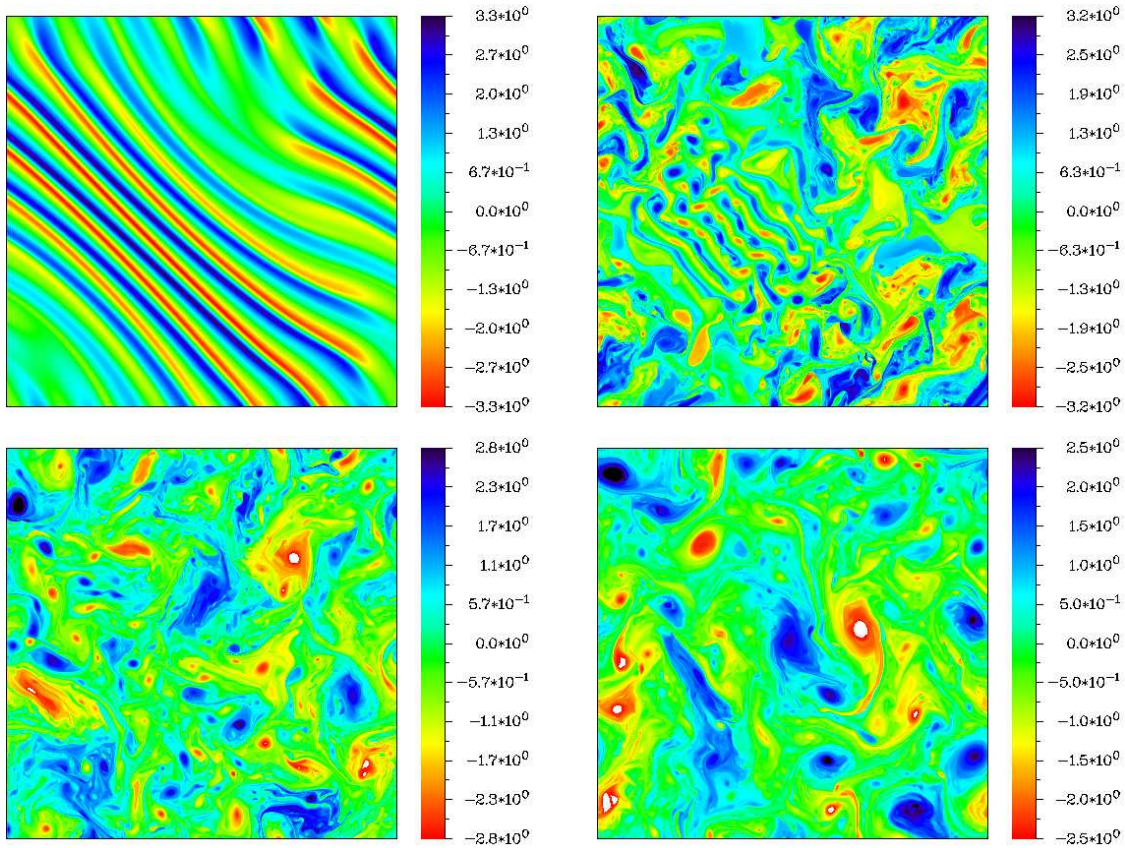


Figure 3.8: Temperature field θ at $t = 5$ (top left), $t = 10$ (top right), $t = 15$ (bottom left) and $t = 20$ (bottom right) for the 8192×8192 resolution simulations.

of the domain, however as mentioned in the introduction to this chapter, interactions in SQG turbulence are physically local, a topic which we shall discuss more in the next chapter. A consequence of this is that it takes a long time for the centre of the unimodal area to be disturbed. It is unclear whether this effect has any consequences on the behaviour of the energy dissipation rate, although it is possible that dissipation would have been higher at $t = 10$ if the field had been ‘fully mixed’ at that time.

3.4 Conclusion

In this chapter we have investigated a number of aspects of the SQG equation, including showing evidence for the $k^{-5/3}$ energy spectrum in the inertial range, which has previously been predicted on the basis of Kolmogorov phenomenology. This has been achieved by both analytical and numerical methods. In the former approach, we have derived the estimate $N \leq Re^{3/2}$ for the system's number of degrees of freedom N , where Re is the Reynolds number defined in terms of the energy dissipation rate, the viscosity and the system's size. Upon identifying N with the number of dynamically active Fourier modes, *i.e.* the modes within the energy inertial range, we deduce the result $\alpha = 5/3$ for the exponent α of the power-law spectrum $Ck^{-\alpha}$. This approximation also renders the scaling $Re^{1/2}$ for the exponential dissipation rate $r_d = \nu k_d^2$ at the dissipation wavenumber k_d . Given that r_d is linear in Re for Burgers flows, whose nonlinearity is fully quadratic, the sublinear scaling of r_d with Re in the present case (and in 3D turbulence) is a manifestation of partial depletion of nonlinearity. In the latter approach, we have simulated the unforced SQG equation (3.2) in two sets of simulations, one up to the moderate resolution of 4096×4096 and one up to the high resolution 16384×16384 with slightly different initial conditions. The results obtained include a series of spectra that become shallower for larger Reynolds numbers, appearing to tend to the predicted $k^{-5/3}$ spectrum for both sets of runs. Furthermore, for the first set of simulations, within the narrow range of accessible Reynolds number and for our choice of initial temperature field with relatively well-defined lines of large gradient, the energy dissipation rate appears to peak sharply in time and to be approximately independent of Reynolds number. This behaviour is consistent with a positive limiting dissipation rate in the inviscid limit. In the second set of simulations, up to much larger resolutions the slightly different initial conditions, the energy dissipation rate shows similar behaviour although it is not so obvious that the maximum dissipation rate does not decrease for the highest resolution. In order to get a definitive answer higher resolution simulations are needed than are accessible with the currently available

hardware.

Although the dynamical parameter ϵ_T plays an important role in the present study, its detailed behaviour does not effect our results or conclusion in a significant way. In the event that ϵ_T vanishes logarithmically, the Reynolds number Re would have a logarithmic correction to its conventional form, which is proportional to $1/\nu$, and the key result $N \leq Re^{3/2}$ remains intact. In addition, the arguments leading to the conclusion $\alpha = 5/3$ remain valid, although it would not be possible to express the energy spectrum in the classical form $C_K \epsilon_T^{2/3} k^{-5/3}$ without modifications. This situation is analogous to 2D turbulence, for which the -1 slope of the predicted enstrophy spectrum $\mathcal{Z}(k) \propto \eta^{2/3} k^{-1}$ is not invalidated by the fact that the enstrophy dissipation rate η slowly vanishes in the inviscid limit for such a slope (Tran & Dritschel, 2006). However, the vanishing factor $\eta^{2/3}$ may not give the correct collapsing rate of $\mathcal{Z}(k)$ when a finite vorticity reservoir forever spreads out over an increasingly wider inertial range. Indeed, for such a vorticity distribution, Dritschel *et al.* (2007) show that $\mathcal{Z}(k)$ scales as $(\ln Re)^{-1} k^{-1}$, thereby requiring η in the above expression of $\mathcal{Z}(k)$ to behave as $(\ln Re)^{-3/2}$. This vanishing rate for η is relatively more rapid than the recent mathematical estimate $(\ln Re)^{-1/2}$ of Tran & Dritschel (2006) and the numerical estimate $(\ln Re)^{-1}$ of Dritschel *et al.* (2007).

Chapter 4

A Family of Generalised Models of 2D Turbulence

4.1 Introduction

Before the mathematics of two-dimensional turbulence was thoroughly understood, it was noted by Kraichnan (1971) that the k^{-3} form of the enstrophy inertial range resulted in non-local interactions, which is what lead him to propose his log-corrected version. In an effort to address this problem, Pierrehumbert *et al.* (1994) proposed a family of two-dimensional models of turbulence, indexed by a value α that controls the locality of transfer, called the α -turbulence models, which are governed by the equations

$$\frac{\partial \theta}{\partial t} + J(\psi, \theta) = \nu \Delta \theta, \quad (4.1)$$

$$\theta = \Lambda^\alpha \psi, \quad (4.2)$$

where Λ is the Zygmund operator and is defined in the previous chapter¹. This equation encompasses a number of physically realisable systems. When $\alpha = 1$, the system is the

¹In the original paper ω was actually defined as $-\Lambda^\alpha \psi$, however the extra minus sign can be incorporated into the definition of ω and does not have an effect on the subsequent arguments.

SQG equation, which we have encountered in chapter 3. The case $\alpha = 2$ gives the usual 2DNS equation, discussed in chapter 2, while $\alpha = 3$ gives the equation for rotating shallow flow (Weinstein *et al.*, 1989). While this equation also includes the cases of negative α , while for example $\alpha = -2$ is associated with shallow water SQG dynamics in the limit of strong rotation Smith *et al.* (2002), although we shall not be considering the case $\alpha < 0$ here.

Like the 2DNS and SQG equations, the nonlinear term in (4.1) gives rise to two integrated inviscid conserved quantities. The first, known as the *generalised energy*, decays under viscous stresses under the relationship

$$\frac{d}{dt}E_g(t) \equiv \frac{1}{2} \frac{d}{dt} \|\Lambda^{-\alpha/2}\theta\|^2 = -\nu \|\Lambda^{(2-\alpha)/2}\theta\| \equiv -\epsilon_g, \quad (4.3)$$

and is equivalent to the usual energy when $\alpha = 2$. The second quantity, the *generalised enstrophy*, decays according to the equation

$$\frac{d}{dt}Z_g(t) \equiv \frac{1}{2} \frac{d}{dt} \|\theta\|^2 = -\nu \|\nabla\theta\|^2 \equiv -\chi_g. \quad (4.4)$$

Both of these quantities have power spectra associated with them, with generalised energy spectrum $\mathcal{E}_g(k)$ and generalised enstrophy spectrum $\mathcal{Z}_g(k)$ satisfying the condition

$$E_g = \sum_k \mathcal{E}_g(k) = \sum_k k^\alpha \Psi(k), \quad (4.5)$$

$$Z_g = \sum_k \mathcal{Z}_g(k) = \sum_k k^{2\alpha} \Psi(k), \quad (4.6)$$

where $\Psi(k)$ is the wavenumber power spectrum.

In his original paper, Pierrehumbert *et al.* (1994) used classical methods to show that the energy is expected to be transferred upscale, to lower wavenumbers, while the enstrophy is transferred downscale. The strength of the downscale transfer of enstrophy has a vital role in the dynamics of the system, in particular the possibility

of dissipative anomaly and finite-time singularities. Using dimensional analysis, the generalised energy spectrum in the inverse-transfer inertial range was calculated to be

$$\mathcal{E}_g(k) \sim C(\alpha)\epsilon_g^{2/3}k^{-7/3+\alpha/3} \quad (4.7)$$

where ϵ_g is the inverse generalised energy flux, while in the forward-cascading generalised enstrophy range we have

$$\mathcal{Z}_g(k) \sim C'(\alpha)\chi_g^{2/3}k^{-7/3+2\alpha/3} \quad (4.8)$$

where χ_g is the generalised enstrophy flux, presumably equal to the generalised enstrophy dissipation in a forced quasi-steady flow. As could be expected, these results give the same scaling for the NS and SQG equations as the phenomenological results from the previous chapters.

The change in locality which Pierrehumbert was studying comes about by considering Kraichnan's formula that the strain rate due to eddies with scales between $1/k$ and $2/k$ is given by

$$k^{2-\alpha}\sqrt{k\mathcal{Z}_g(k)}, \quad (4.9)$$

which on using equation (4.8) we get that the rate of strain is proportional to $k^{4/3-2\alpha/3}$, showing that for $\alpha < 2$ the enstrophy cascade is dominated by the local strain rate, while for $\alpha > 2$ it is dominated by nonlocal strain. In fact for an enstrophy spectrum $\mathcal{Z}(k) \sim k^{-\beta}$, you need $\beta > 5 - 2\alpha$ to have local transfer in the generalised enstrophy inertial range. This led (Held *et al.*, 1995, page 15) to suggest that the Kolmogorov-Kraichnan scaling breaks down for $\alpha > 2$ since in this case the dynamics consists of non-local interactions, meaning that the system behaves more like the advection of a passive scalar, which is equivalent to saying that there is essentially no feedback from θ onto the advecting velocity \mathbf{u} . This locality of transfer in spectral space can be studied through an analysis of the triad interactions that make up the nonlinear term in equation (4.1). As well as spectral space transfer, α also controls the locality of

transfer in physical space, a topic that was touched upon in the previous chapter for the SQG ($\alpha = 1$) case. We discuss both of these α dependencies in the next section.

One method of understanding the effect of the change in α on the dynamics of the system is through the notion of ‘number of degrees of freedom’ introduced by Tran *et al.* (2010). Taking the gradient of equation (4.1) gives the equation governing the evolution of the scalar gradient,

$$\frac{\partial \nabla \theta}{\partial t} + (\mathbf{u} \cdot \nabla) \nabla \theta = (\nabla \times \mathbf{u}) \times \nabla \theta - (\nabla \theta \cdot \nabla) \mathbf{u} + \nu \Delta \nabla \theta. \quad (4.10)$$

The only term on the right-hand side of equation (4.10) that affects the magnitude of the scalar gradient (apart from the dissipation term) is $(\nabla \theta \cdot \nabla) \mathbf{u}$. The system dynamics will then depend heavily on the effect that the transfer of θ to small scales has on this term. In SQG dynamics, when $\alpha = 1$, the scalar θ is a same-scale copy of the velocity field, with both having the same power spectrum, and thus we have the result that $\|\mathbf{u}\| = \|\theta\|$. Phenomenologically, $\nabla \theta$ and $\nabla \mathbf{u}$ would be expected to behave similarly, with a possible phase change due to the effects of the singular operator linking θ and ψ (see Ohkitani, 2011). This could mean that the $(\nabla \theta \cdot \nabla) \mathbf{u} \sim |\nabla \theta|^2$, which would presumably lead to explosive growth in the scalar gradient and possibly finite-time singularities. For the $\alpha = 2$ case, on the other hand, due to the conservation of energy $\frac{1}{2} \|\mathbf{u}\|^2$, $\nabla \mathbf{u}$ is expected to be well behaved, which means that $(\nabla \theta \cdot \nabla) \mathbf{u}$ could behave almost linearly with respect to $\nabla \theta$, and the growth of scalar gradients may merely be exponential in time. This agrees with the proven result that there are no finite-time singularities in the 2DNS system. For even larger values of α , the transfer of θ to smaller scales is expected to have an increasingly negligible effect on $\nabla \mathbf{u}$, meaning that for large α the system is expected to have a very small degree of nonlinearity. This can be seen for $\alpha \in [2, 4]$ using the following heuristic argument. The evolution of the

scalar gradient is bounded in terms of the velocity gradient by

$$\begin{aligned} \frac{\partial}{\partial t} |\nabla \theta| + (\mathbf{u} \cdot \nabla) |\nabla \theta| &= - \frac{\nabla \theta}{|\nabla \theta|} \cdot (\nabla \theta \cdot \nabla) \mathbf{u}, \\ &\leq |\nabla \mathbf{u}| |\nabla \theta|, \end{aligned} \quad (4.11)$$

which, using Grönwall's inequality, gives a bound for the gradient of a fluid particle starting at point \mathbf{x}_0 at $t = 0$ with initial value $\theta_0 = \theta(x_0, 0)$ as

$$|\nabla \theta| \leq |\nabla \theta_0| \exp \left\{ \int_0^t |\nabla \mathbf{u}| d\tau \right\}. \quad (4.12)$$

This may be expected to remain finite in finite time assuming that $|\nabla \mathbf{u}|$ is well behaved, which could be expected for $\alpha > 2$ due to the interpolation-type inequality

$$\|\nabla \mathbf{u}\| \leq E_g^{1-2/\alpha} Z_g^{2/\alpha-1/2} \quad (4.13)$$

from Tran *et al.* (2010) which holds when $\alpha \in [2, 4]$. Since both E_g and Z_g are bounded by their initial value, this means that $\|\nabla \mathbf{u}\|$ is uniformly bounded in time. In this case $\nabla \mathbf{u}$ is virtually unaffected by the direct transfer of $\langle \theta^2 \rangle$. In the limit $\alpha \rightarrow 0$, on the other hand, the system could behave highly nonlinearly, although Ohkitani (2011) argues that change in the temporal scales as $\alpha \rightarrow 0$ could counteract this effect, meaning any singularities take increasingly long to occur, with singularities only appearing in infinite time as $\alpha \rightarrow 0$.

4.2 Smoothness and locality of transfer in physical and Fourier space

Given an initial generalised vorticity field θ , there are two different ‘actions’ on it that determine its evolution. The first is the determination of the advecting velocity

field, which is given by the inversion operator

$$\mathbf{u} = \nabla^\perp \Lambda^{-\alpha} \theta. \quad (4.14)$$

As we have seen this has a particularly simple description in Fourier space which operates pointwise on the wavenumbers, however in physical space, where we are working in a periodic box of side-length 2π , it takes the form of a singular integral

$$\begin{aligned} \mathbf{u}(\mathbf{x}) &= i \sum_{\mathbf{k}} \hat{\mathbf{u}}_{\mathbf{k}} e^{i\mathbf{k}\cdot\mathbf{x}}, \\ &= i \sum_{\mathbf{k}} \frac{\mathbf{k}^\perp}{k^\alpha} \hat{\theta}_{\mathbf{k}} e^{i\mathbf{k}\cdot\mathbf{x}}, \\ &= i \sum_{\mathbf{k}} \frac{\mathbf{k}^\perp}{k^\alpha} \left(\int_{\Omega} \theta(\mathbf{y}) e^{-i\mathbf{k}\cdot\mathbf{y}} d\mathbf{y} \right) e^{i\mathbf{k}\cdot\mathbf{x}}, \\ &= \int_{\Omega} \theta(\mathbf{y}) \left(i \sum_{\mathbf{k}} \frac{\mathbf{k}^\perp}{k^\alpha} e^{i\mathbf{k}(\mathbf{x}-\mathbf{y})} \right) d\mathbf{y}, \\ &= \theta(\mathbf{x}) \star K(\mathbf{x}), \end{aligned} \quad (4.15)$$

where \star denotes convolution and

$$\begin{aligned} K(\mathbf{x}) &= \mathcal{F}^{-1} \left(\hat{K}(\mathbf{k}) \right), \\ &= \mathcal{F}^{-1} \left(i \frac{\mathbf{k}^\perp}{k^\alpha} \right), \end{aligned} \quad (4.16)$$

with \mathcal{F}^{-1} the usual inverse Fourier transform for two-dimensional fields with periodic boundary conditions. In the case $\alpha = 2$ and the limit of infinitely large domain, this corresponds to the usual Biot-Savart kernel. For large values of α , $\hat{K}(\mathbf{k})$ is a quickly decaying function of \mathbf{k} , which means that by Heisenberg's uncertainty principle $K(\mathbf{x})$ is spatially spread out. This means that when inverting the Zygmund operator to retrieve the velocity field information from the whole domain is used, suggesting that there is a large degree of nonlocality in the evolution. For small α , on the other hand, $K(\mathbf{x})$ becomes more concentrated about the origin. Thus, for small α the transfer could be

highly local, which agrees with the results about SQG turbulence that we have seen previously.

The nonlinear term of the evolution equation is in many ways the polar opposite of the inversion term. While the operator acts pointwise in physical space, in Fourier space it connects the wavenumbers together, distributing generalised enstrophy between them. This transfer is governed by the equation

$$\frac{\partial}{\partial t} \hat{\theta}_{\mathbf{k}}(t) = \sum_{\boldsymbol{\ell} + \mathbf{m} = \mathbf{k}} \frac{(l^\alpha - m^\alpha) \boldsymbol{\ell} \times \mathbf{m}}{l^\alpha m^\alpha} \hat{\theta}_{\boldsymbol{\ell}}(t) \hat{\theta}_{\mathbf{m}}(t). \quad (4.17)$$

For the rest of this section we follow the work presented in Tran *et al.* (2010) in order to fully understand the importance that α plays in the spectral-space modal transfer process. Equation (4.17) is easily manipulated to give the equations governing the change in generalised enstrophy density in the three modes of a triad $\boldsymbol{\ell}$, \mathbf{m} and \mathbf{k} ,

$$\begin{aligned} \frac{d}{dt} |\hat{\theta}_{\mathbf{k}}|^2 &= \frac{(m^\alpha - l^\alpha) \boldsymbol{\ell} \times \mathbf{m}}{l^\alpha m^\alpha} \times \left[\hat{\theta}_{\boldsymbol{\ell}} \hat{\theta}_{\mathbf{m}} \hat{\theta}_{\mathbf{k}}^* + \hat{\theta}_{\boldsymbol{\ell}}^* \hat{\theta}_{\mathbf{m}}^* \hat{\theta}_{\mathbf{k}} \right] \\ &= C_{\mathbf{k}} \times \left[\hat{\theta}_{\boldsymbol{\ell}} \hat{\theta}_{\mathbf{m}} \hat{\theta}_{\mathbf{k}}^* + \hat{\theta}_{\boldsymbol{\ell}}^* \hat{\theta}_{\mathbf{m}}^* \hat{\theta}_{\mathbf{k}} \right] \end{aligned} \quad (4.18)$$

$$\begin{aligned} \frac{d}{dt} |\hat{\theta}_{\boldsymbol{\ell}}|^2 &= \frac{(k^\alpha - m^\alpha) \boldsymbol{\ell} \times \mathbf{m}}{l^\alpha m^\alpha} \times \left[\hat{\theta}_{\boldsymbol{\ell}} \hat{\theta}_{\mathbf{m}} \hat{\theta}_{\mathbf{k}}^* + \hat{\theta}_{\boldsymbol{\ell}}^* \hat{\theta}_{\mathbf{m}}^* \hat{\theta}_{\mathbf{k}} \right] \\ &= C_{\boldsymbol{\ell}} \times \left[\hat{\theta}_{\boldsymbol{\ell}} \hat{\theta}_{\mathbf{m}} \hat{\theta}_{\mathbf{k}}^* + \hat{\theta}_{\boldsymbol{\ell}}^* \hat{\theta}_{\mathbf{m}}^* \hat{\theta}_{\mathbf{k}} \right] \end{aligned} \quad (4.19)$$

$$\begin{aligned} \frac{d}{dt} |\hat{\theta}_{\mathbf{m}}|^2 &= \frac{(l^\alpha - k^\alpha) \boldsymbol{\ell} \times \mathbf{m}}{l^\alpha m^\alpha} \times \left[\hat{\theta}_{\boldsymbol{\ell}} \hat{\theta}_{\mathbf{m}} \hat{\theta}_{\mathbf{k}}^* + \hat{\theta}_{\boldsymbol{\ell}}^* \hat{\theta}_{\mathbf{m}}^* \hat{\theta}_{\mathbf{k}} \right] \\ &= C_{\mathbf{m}} \times \left[\hat{\theta}_{\boldsymbol{\ell}} \hat{\theta}_{\mathbf{m}} \hat{\theta}_{\mathbf{k}}^* + \hat{\theta}_{\boldsymbol{\ell}}^* \hat{\theta}_{\mathbf{m}}^* \hat{\theta}_{\mathbf{k}} \right]. \end{aligned} \quad (4.20)$$

where we have used the fact that when $\boldsymbol{\ell} + \mathbf{m} = \mathbf{k}$ we have the identities $\boldsymbol{\ell} \times \mathbf{m} = \boldsymbol{\ell} \times \mathbf{k} = \mathbf{k} \times \mathbf{m}$. The conservation of E_g and Z_g for individual triad interactions is then verified by the fact that $C_{\mathbf{k}}$, $C_{\boldsymbol{\ell}}$ and $C_{\mathbf{m}}$ satisfy

$$C_{\mathbf{k}} + C_{\boldsymbol{\ell}} + C_{\mathbf{m}} = 0 = \frac{C_{\mathbf{k}}}{k^\alpha} + \frac{C_{\boldsymbol{\ell}}}{l^\alpha} + \frac{C_{\mathbf{m}}}{m^\alpha}. \quad (4.21)$$

Details of the transfer of E_g and Z_g can also be derived from (4.18) by noting the

signs of the coupling coefficients, which show that the transfer is from the intermediate wavenumber to the higher and lower wavenumber, or vice versa (although the transfer from lower/higher to intermediate seems to be unphysical and has never been observed in numerical simulations). This is different to the transfer in the quadratically nonlinear Burgers equation, where energy can be transferred from the two lower wavenumbers to the higher wavenumber (Tran & Dritschel, 2010). This in itself suggests that the downscale flux of generalised enstrophy could be partially reduced when compared with the cascade of energy in the Burgers equation.

We now consider two different types of triad interactions between wavenumbers $\mathbf{k}, \boldsymbol{\ell}, \mathbf{m}$ where $\mathbf{k} = \boldsymbol{\ell} + \mathbf{m}$, one equilateral in shape, with $k \lesssim l \lesssim m$ and one isosceles, which are of the form $k \ll l \lesssim m$. These two types of triads make up the majority of triad interactions in Fourier space.

We first consider the equilateral case, where generalised enstrophy is passed between wavenumbers of approximately equal magnitude, and we can easily obtain the bounds for the coefficients $C_{\mathbf{k}}, C_{\boldsymbol{\ell}}$ and $C_{\mathbf{m}}$ given by

$$|C_{\mathbf{k}}| = \frac{|(m^\alpha - l^\alpha)\boldsymbol{\ell} \times \mathbf{m}|}{m^\alpha l^\alpha} < kl^{1-\alpha} \sim k^{2-\alpha}, \quad (4.22)$$

$$|C_{\boldsymbol{\ell}}| = \frac{|(k^\alpha - m^\alpha)\boldsymbol{\ell} \times \mathbf{m}|}{k^\alpha m^\alpha} < lk^{1-\alpha} \sim k^{2-\alpha}, \quad (4.23)$$

$$|C_{\mathbf{m}}| = \frac{|(l^\alpha - k^\alpha)\boldsymbol{\ell} \times \mathbf{m}|}{l^\alpha k^\alpha} < lk^{1-\alpha} \sim k^{2-\alpha}, \quad (4.24)$$

where we have used the fact that $|\boldsymbol{\ell} \times \mathbf{m}| = |\boldsymbol{\ell} \times \mathbf{k}| \leq lk$. From this result we can see that for $\alpha > 2$ as $k \rightarrow \infty$ the transfer coefficients tend to zero, meaning that triads of the equilateral type effectively ‘switch off’, with the decay happening more rapidly for larger α . In the critical case $\alpha = 2$ it may be that $C_{\mathbf{k}}, C_{\boldsymbol{\ell}}$ and $C_{\mathbf{m}}$ could remain at order unity if $|m^\alpha - l^\alpha| \sim |k^\alpha - m^\alpha| \sim |l^\alpha - k^\alpha| \sim k^\alpha$ as well as $|\boldsymbol{\ell} \times \mathbf{m}| \sim k^2$, which could occur if the triads are neither highly equilateral or highly isosceles. This means that the local triads at small scales could be moderately active in the 2DNS case. Finally, when $\alpha < 2$ the interaction coefficients could diverge as $k \rightarrow \infty$, possibly as

rapidly as $k^{2-\alpha}$, which suggests that in this case the direct transfer is overwhelmingly dominated by these equilateral triads. This divergence of the coefficients for small values of α is potentially problematic for numerical simulation, with the (possibly superlinear) divergence of the coefficients meaning that numerical stability can only occur if there is negligible generalised enstrophy at the smallest scales, resulting in the need for relatively high diffusion to keep the dynamics under control. This problem rears its head in the numerical simulations that are run in §4.3.

On the other extreme we have the highly isosceles triads, those that satisfy the relation (up to renaming) $k \ll l \lesssim m$. Using the fact that, for small k , we have approximately $||\mathbf{k} - \boldsymbol{\ell}|^\alpha - l^\alpha|/k \sim \alpha l^{\alpha-1}$, we can then estimate the coefficients as

$$|C_{\mathbf{k}}| = \frac{|(m^\alpha - l^\alpha)\boldsymbol{\ell} \times \mathbf{m}|}{m^\alpha l^\alpha} \approx \frac{\alpha k^2}{l^\alpha}, \quad (4.25)$$

$$|C_{\boldsymbol{\ell}}| = \frac{|(k^\alpha - m^\alpha)\boldsymbol{\ell} \times \mathbf{m}|}{k^\alpha m^\alpha} \approx l k^{1-\alpha}, \quad (4.26)$$

$$|C_{\mathbf{m}}| = \frac{|(l^\alpha - k^\alpha)\boldsymbol{\ell} \times \mathbf{m}|}{l^\alpha k^\alpha} \approx l k^{1-\alpha}. \quad (4.27)$$

In this case, in the limit $l \rightarrow \infty$, (while $k < \infty$), $C_{\mathbf{k}}$ vanishes, while both $C_{\boldsymbol{\ell}}$ and $C_{\mathbf{m}}$ diverge as rapidly as l , while becoming essentially independent of α . This means that there is a vigorous exchange of generalised enstrophy between the neighbouring wavenumbers $\boldsymbol{\ell}$ and \mathbf{m} , which is mediated by the virtually inert wavenumber \mathbf{k} , with this ‘ultra-local’ transfer holding for all values of α .

4.3 Numerical results

This section describes a set of simulations that were run to investigate the behaviour of the dissipation rates, time of maximum dissipation and spectra as α is varied in the range $[0.5, 4]$. For the values $\alpha = 0.5, 1, 1.5, 2, 2.5, 3, 3.5$ and 4 equation (4.1) was numerically integrated, using the same pseudo-spectra code as described earlier, until around three times the time of maximum dissipation. For each value of α a set of

low-resolution simulations were run (not included here) to determine the approximate viscosity needed to ensure there was no build-up at the high-wavenumber boundary, and to deduce the factor to decrease ν by as the resolution was doubled. Using these scalings, simulations at resolutions 2048×2048 , 4096×4096 and 8192×8192 were run. The initial conditions consisted of a set of Fourier modes with wavenumbers in the range $[9, 12]$ where the generalised vorticity modes were initialised with equal magnitudes and random phases such that there was unity initial generalised enstrophy. The same field was used for all of the simulations in this section. One outcome of this initialisation method is that the advecting velocity field \mathbf{u} is weaker for larger values of α , having an initial magnitude approximately

$$\begin{aligned} \|\mathbf{u}_0\| &= \|\nabla^\perp \Lambda^{-\alpha} \theta_0\| \\ &\approx k_c^{1-\alpha} \|\theta_0\| \\ &\approx \sqrt{2} k_c^{1-\alpha}, \end{aligned} \tag{4.28}$$

where $k_c \approx 11$ is the initial centroid wavenumber. This means that $\|\mathbf{u}_0\|$ varied from around 4.5 for $\alpha = 0.5$ to only 0.0011 for $\alpha = 4$. Since the advecting velocity is weaker for larger α the evolution of the flow will be much slower, for reasons that do not have any fundamental connection with the control of α over the nonlinearity of the flow. In order to partially counteract this, when comparing different values of α we scale the time by the initial eddy turnover time τ , which is derived from the initial length scale $l = 2\pi/k_c$ and the initial velocity $\|\mathbf{u}_0\|$ by

$$\begin{aligned} \tau &= \frac{l}{\|\mathbf{u}_0\|}, \\ &= \frac{2\pi}{\sqrt{2} k_c \times k_c^{1-\alpha}}, \\ &= \sqrt{2}\pi \times k_c^{\alpha-2}, \\ &\approx \sqrt{2}\pi \times 11^{\alpha-2}. \end{aligned} \tag{4.29}$$

One further problem that presented itself was the behaviour of the velocity field for small α , in which case there is initially very strong advection. Because of the CFL condition used in the timestepping (see §1.4.2), which keeps the timestep inversely proportional of $\|\mathbf{u}\|_\infty$, this meant that for high Reynolds numbers the time increment decreased dramatically as the time of maximum dissipation rate was approached. This behaviour was so dramatic for $\alpha = 0.5$ that it was not possible to run the 8192×8192 resolution simulation with a reasonable timestep without incurring numerical instability and NaN errors. For this reason for the simulations where $\alpha = 0.5$ the highest resolution that could be run was only 4096×4096 .

Figure 4.1 shows the generalised enstrophy $\frac{1}{2}\|\theta\|^2$ plotted *v.s.* time for the runs at 2048×2048 , 4096×4096 and 8192×8192 resolution. It is immediately obvious that for higher α the total dissipation of the generalised enstrophy is larger than that for smaller α . This result may seem contradictory to the idea that smaller α gives a more nonlinear system, presumably resulting in higher dissipation rates, until it is noticed that, as explained above, as α is increased the timescale also increases, meaning that a lower dissipation rate, acting for a longer time, could be enough to explain the greater loss of generalised enstrophy for larger α . This is backed up in figure 4.2 which shows the generalised enstrophy dissipation rate *v.s.* time. From these figures you can see that the maximum dissipation rate is indeed larger for smaller values of α , although in all cases the maximum dissipation rate $\chi_g^T = \chi_g(T)$ is decreasing with increasing Reynolds number, while the time of maximum dissipation T likewise increases. This occurs for all the values of α , including $\alpha = 1$, which suggests that the initial conditions used here are not ‘optimal’ for the development of finite-time singularities, if they do in fact exist.

The development of singularities is presumably dependent on the concentration of θ into dense sets, which would necessarily lead to growth in θ -gradients. We investigate this possibility in figure 4.3 where we plot $\|\nabla\theta\|_\infty/\|\nabla\theta\|$ *v.s.* time. It is interesting to note that the maximum value of $\|\nabla\theta\|_\infty/\|\nabla\theta\|$ occurs when $\alpha = 2.5$ and decays when α moves away from this value. For larger α this seems to be a clear indication of

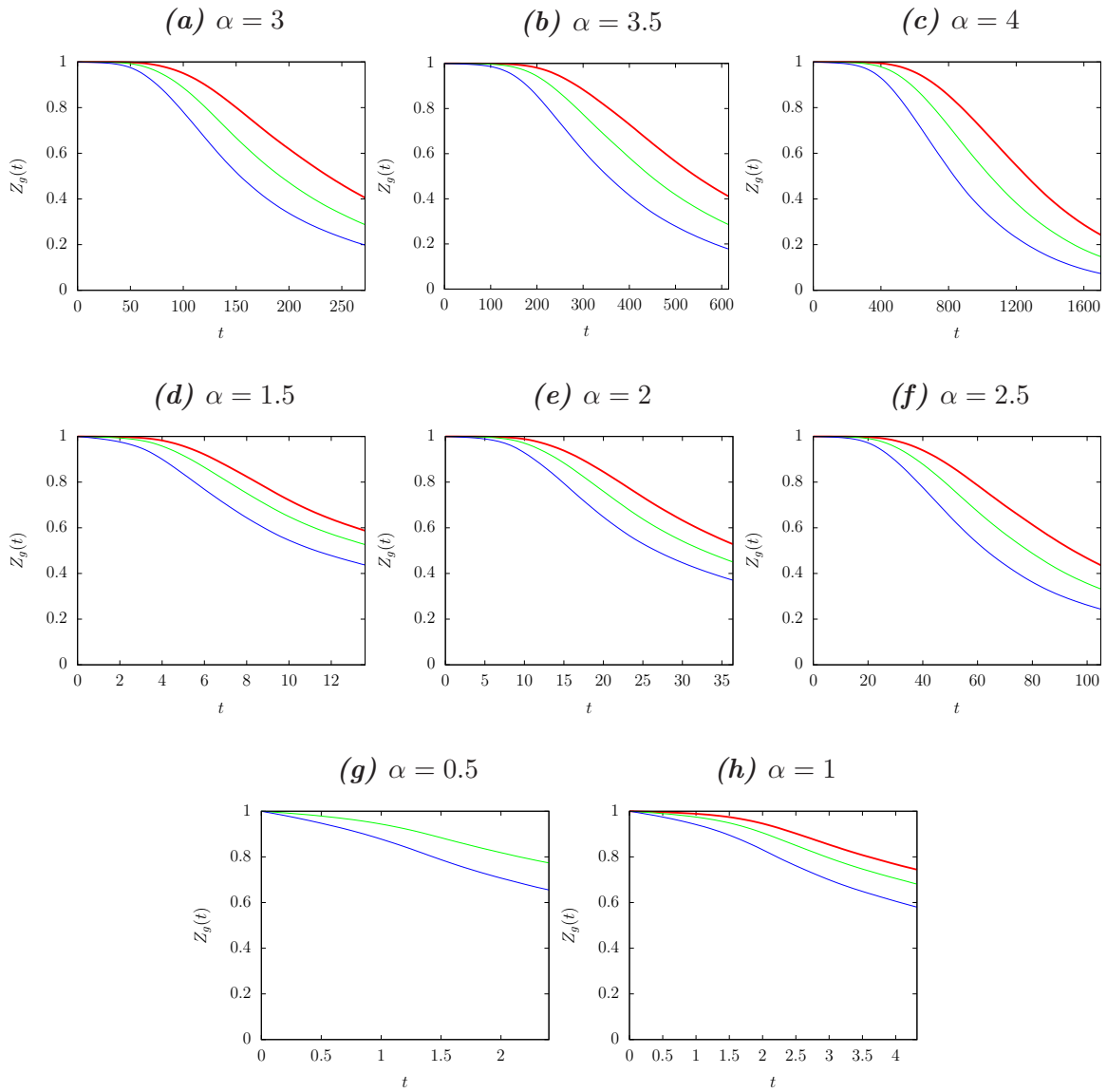


Figure 4.1: Generalised enstrophy v.s. time for numerical simulations with resolutions 2048×2048 (blue), 4096×4096 (green) and 8192×8192 (red), in decreasing order of α from top left to bottom right, going across.

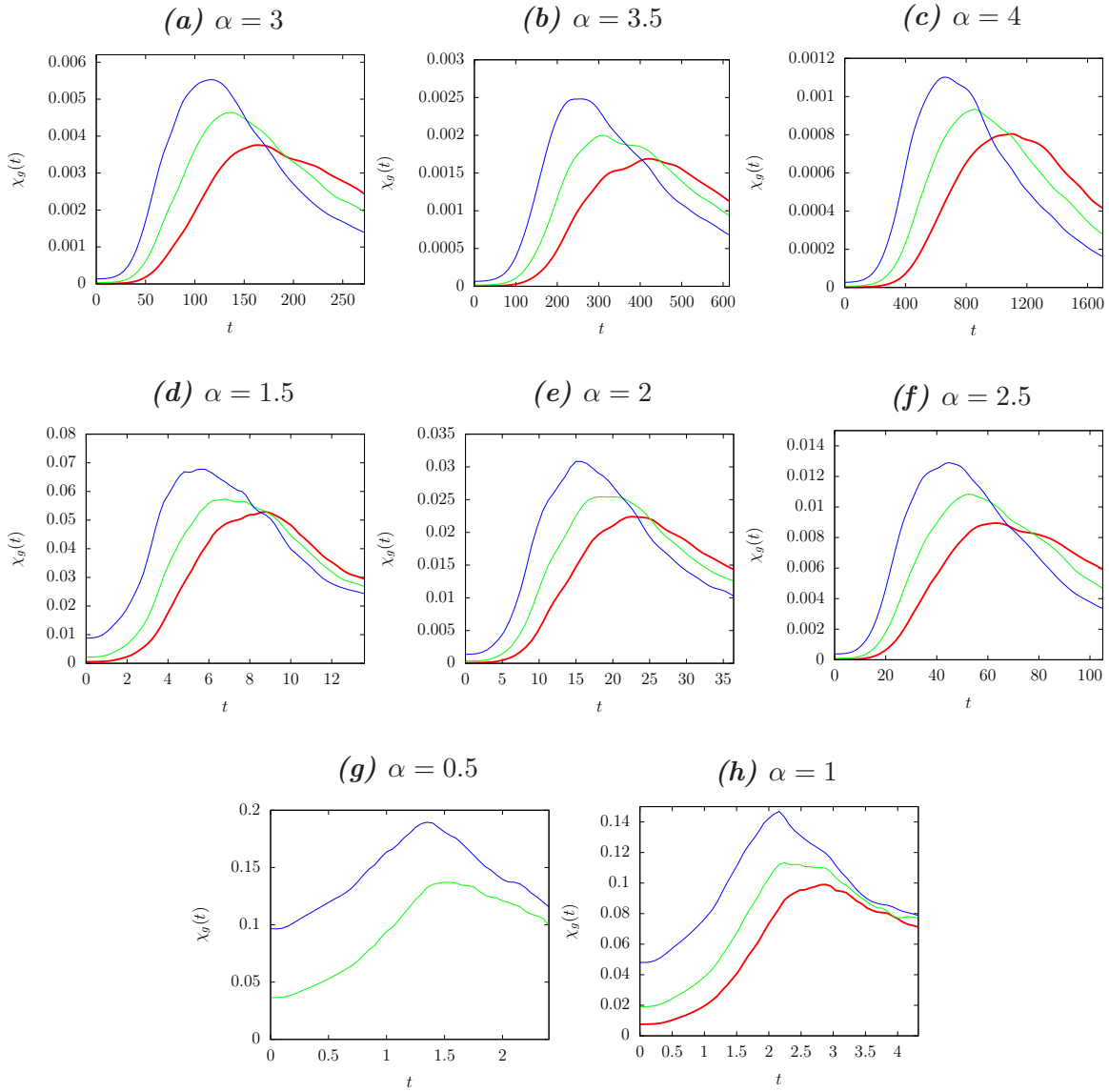


Figure 4.2: Generalised enstrophy dissipation rates v.s. time for numerical simulations with resolutions 2048×2048 (blue), 4096×4096 (green) and 8192×8192 (red), in increasing order of α from bottom left to top right.

depletion of nonlinearity, since for larger α the simulations were run at smaller viscosity. For smaller α , it is possible that the lesser values of $\|\nabla\theta\|_\infty/\|\nabla\theta\|$ are a product of the higher values of ν used in the simulations to keep the smallest scales under control. This effect of the generalised enstrophy flux on the small scales can be seen for small α by the large fluctuations in $\|\nabla\theta\|_\infty/\|\nabla\theta\|$, while it is relatively smooth for larger values of α .

From studying the graphs described above it seems that there are relatively simple relationships between α and a number of other quantities such as the maximum generalised enstrophy dissipation rate χ_g^T and the time of maximum dissipation T , with the obvious note that these laws may well hold to a greater or lesser extent for this particular set of simulations and initial conditions only. However, while the constants will almost certainly be simulation specific, it is possible that the form of each law, exponential, power-law *etc.*, is universal. With this in mind, in figure 4.4 we have plotted the maximum dissipation rate χ_g^T on a logarithmic scale *v.s.* α for the highest resolution runs. The line of best fit, found using the least-squares method on the logarithm of χ_g^T , is given by

$$\chi_g^T = 0.43 \times e^{-1.5\alpha}. \quad (4.30)$$

Similarly figure 4.5 shows the time of maximum dissipation, on a logarithmic scale, *v.s.* α , with the least-squares method giving a line of best fit

$$T = 0.52 \times e^{1.9\alpha}. \quad (4.31)$$

Equation (4.31) suffers from the problem mentioned above that the scaling of T with α depends on the strength of the initial advecting velocity field and does not necessarily give a good representation of the actual degree of nonlinearity of the system. If we then consider the time of maximum dissipation scaled with the initial eddy turnover time, we get the new relationship

$$T/\tau \sim 14.6 \times e^{-0.5\alpha}, \quad (4.32)$$

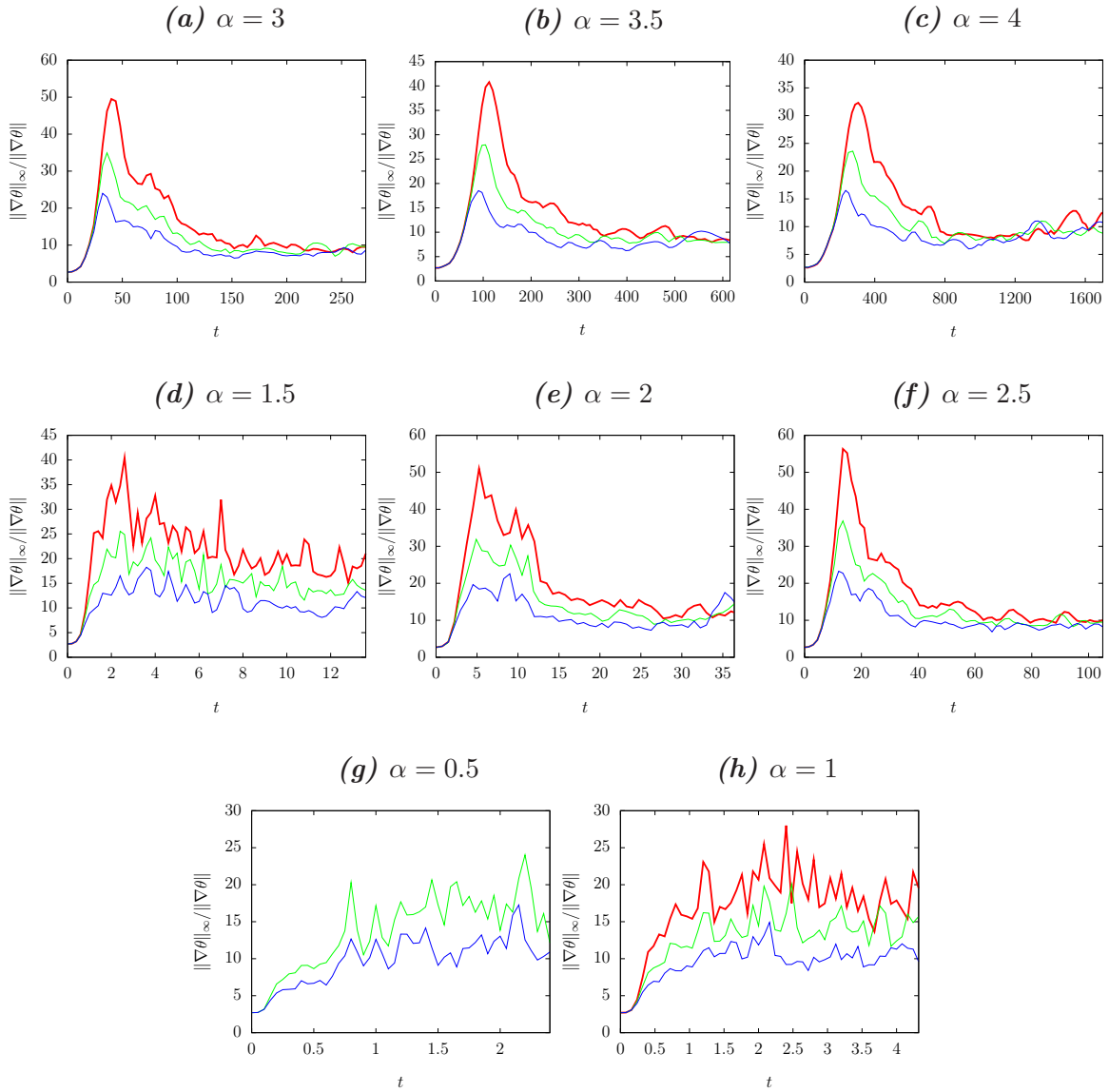


Figure 4.3: Ratio $\|\nabla\theta\|_\infty/\|\nabla\theta\|$ v.s. time for numerical simulations with resolutions 2048×2048 (blue), 4096×4096 (green) and 8192×8192 (red), in increasing order of α from bottom left to top right.

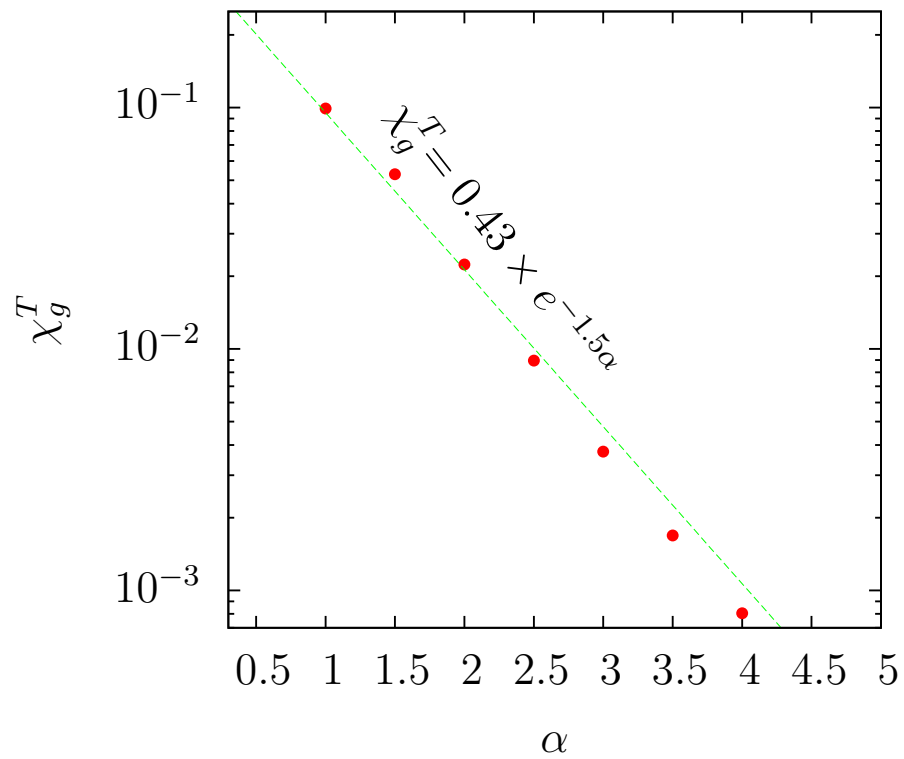


Figure 4.4: Maximum dissipation rate χ_g^T v.s. α on a log-lin scale. The green line is the line of best fit, determined using the method of least squares on the linear graph $\ln \chi_g^T$ v.s. α .

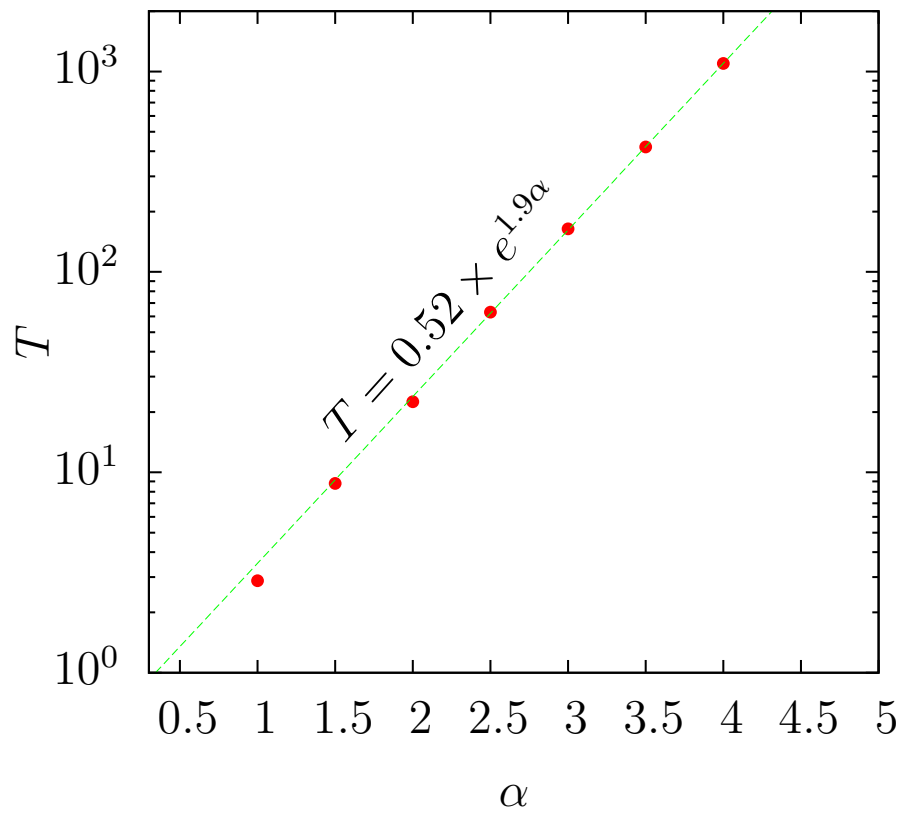


Figure 4.5: Time of maximum dissipation T v.s. α for the highest-resolution runs in figure 4.2, given by the red circles. The green line is the line of best fit, with equation $T = 0.52 \times e^{1.9\alpha}$.

so when scaled with the eddy turnover time we get the opposite behaviour, with T/τ decreasing as α is increased. Figure 4.6 shows the generalised enstrophy dissipation rates for the highest-resolution runs with the time scaled by the initial eddy turnover time. (Note that the case $\alpha = 0.5$ is not included here as the 8192×8192 run did not make it past the first few timesteps). Here we can clearly see that as α is decreased the maximum dissipation rate increases dramatically, in line with the idea that smaller α corresponds to larger nonlinearity in the system. At the same time, however, the scaled time of maximum dissipation T/τ increases slowly as α decreases. It is not obvious whether this is an outcome of the scaling or a real reflection on the strength of the downscale flux, however it could suggest that as $\alpha \rightarrow 0$ the time of maximum dissipation diverges. This agrees with the analysis in Ohkitani (2012) which suggests that for small α a stretched time variable means that while the equation is more singular the singularity does not appear in finite time. This suggests that if you can discount the effect of a stronger velocity field, in the two limits $\alpha \rightarrow 0$ and $\alpha \rightarrow \infty$ singularities are absent for different reasons, in the former case the time of maximum dissipation diverges, meaning that any singularities can only occur in infinite time, while in the latter case the maximum dissipation rate converges to zero.

When doing the initial low-resolution sets of runs, for each resolution the viscosity was varied until there was just enough dissipation to prevent any anomalous build-up around the maximum wavenumber. When the resolution was doubled the viscosity was decreased by a factor of 4 for $\alpha \geq 1.5$, by a factor of $2^{4/3}$ for $\alpha = 1$ and a factor of 2.65 for $\alpha = 0.5$. These scalings were found to be sufficient over resolutions from 512×512 up to 8192×8192 , with no reason to suppose the scaling should break down at higher resolutions. For large values of α , the viscosity needed for the highest-resolution runs were found to scale with the simple relationship

$$\nu = 2.95 \times 10^{-5} \alpha^{-6.0}, \quad (4.33)$$

which seems to hold for $\alpha \geq 1$ (see figure 4.7). For $\alpha = 0.5$ the 8192×8192 simulation

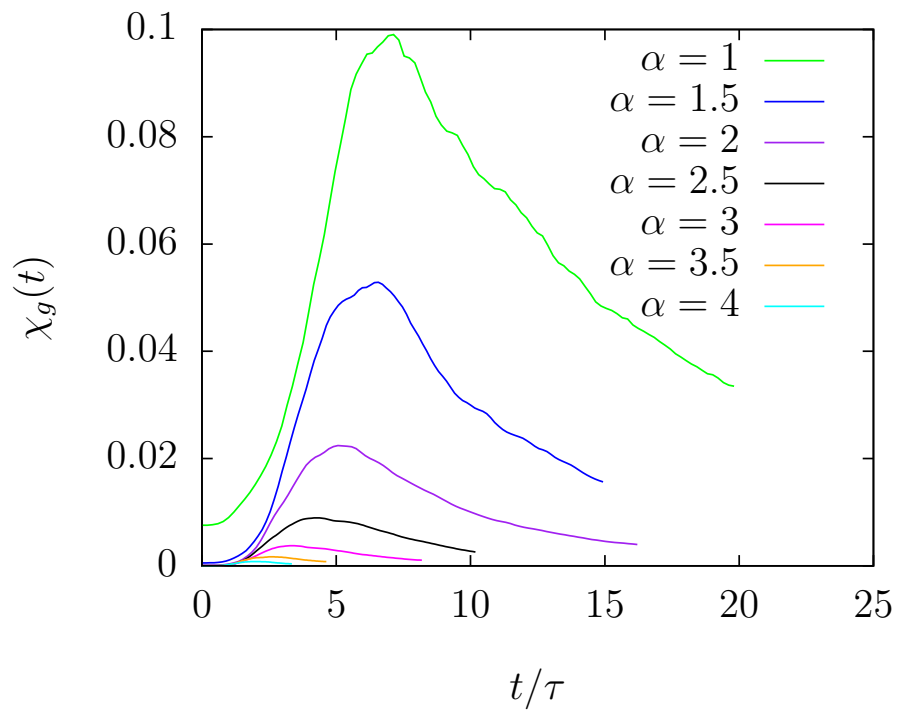


Figure 4.6: Dissipation rate for the highest-resolution runs scaled by the initial eddy turnover time.

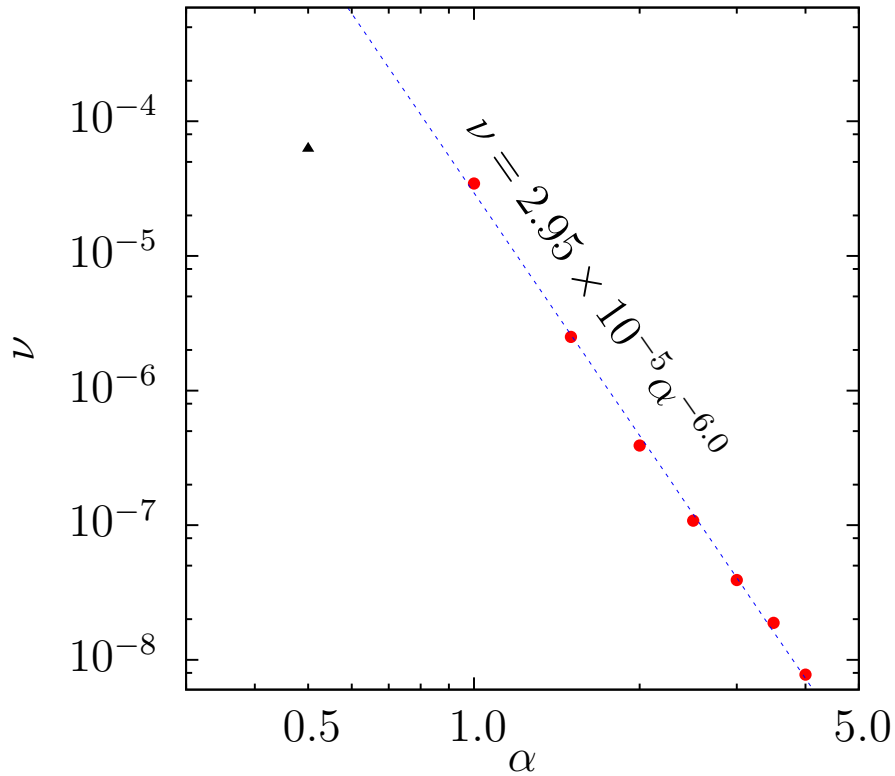


Figure 4.7: Plot of the viscosity ν used in the highest-resolution simulations for $\alpha = 1.0, 1.5, 2.0, 2.5, 3.0, 3.5, 4.0$ (red dots) along with the line of best fit. For $\alpha = 0.5$ the value of ν (black triangle) was extrapolated using the values used for lower resolution simulations.

did not complete as described above, however extrapolating from the lower resolution runs the value of ν that should be sufficient to control the small scales in a 8192×8192 simulation is significantly lower than the scaling given by equation (4.33), which holds for larger α , would suggest. It is impossible to say for now whether this is an indication of a depletion of nonlinearity for small values of α or due to some other factor, in particular whether the naïve extrapolation is actually valid.

Figure 4.10 shows the generalised enstrophy spectra for the simulations as described above, taken at the time of maximum dissipation. As expected, in all cases, as the viscosity is decreased the spectra become shallower, with the limiting spectra depending strongly on α . While there is qualitative agreement between the scaling of the spectra in the inertial range and the phenomenological results of Pierrehumbert described in

the introduction, in that larger values of α correspond to shallower spectra, there is a significant quantitative disagreement in that for higher values of α the spectra in the numerical simulations are significantly steeper than the phenomenological arguments may predict, indeed there is no sign of a positive slope for $\alpha \geq 3.5$ that equation (4.8) predicts. The spectra are, however, shallower for large α than the k^{-1} spectrum that is often suggested due to supposed similarities between the high-alpha case and the advection of a passive scalar by a large-scale flow, where nonlocal interactions supposedly cause a breakdown of Kolmogorov theory. This may partially be explained by (4.9), because the steeper spectra mean that the strain rate is ‘nearly’ local, more so than for the spectra predicted by Pierrehumbert, so the passive scalar assumption may not hold. For $\alpha \leq 1$ the spectrum looks as if the system has been overdamped, with the SQG spectrum ($\alpha = 1$) significantly steeper than the expected $k^{-5/3}$ spectrum, however this could be due to the fact that for small α the transfer coefficient for equilateral triads diverges, meaning that there needs to be negligible generalised enstrophy at the smallest scales to avoid spurious dynamics.

Figure 4.9 plots the power of the spectrum in the inertial range *v.s.* the value of α . For a generalised enstrophy spectrum $\mathcal{Z}_g(k) = Ck^{-\gamma}$ in the inertial range, it is seen that there is approximately an inverse exponential relationship $\gamma = 2.35 \times e^{-0.40\alpha}$. As with all of the laws above derived from numerical results, this relationship is tenuous, however it seems to hold reasonably well for a range of α . For comparison the phenomenologically derived result $\gamma = 7/3 - 2\alpha/3$ is included in the graph, although it seems to be a very bad approximation to the actual exponent, especially for large values of α , where it completely diverges from the numerically derived values.

Figure 4.8 shows the spectra and flux for the highest-resolution simulations, using the same colour scheme as figure 4.6. Smaller values of α are seen to correspond to steeper spectra and stronger flux. This agrees with the heuristic argument that smaller α gives a higher degree of nonlinearity, leading to a stronger transfer of generalised enstrophy downscale. Because the transfer progresses very quickly there is no time for

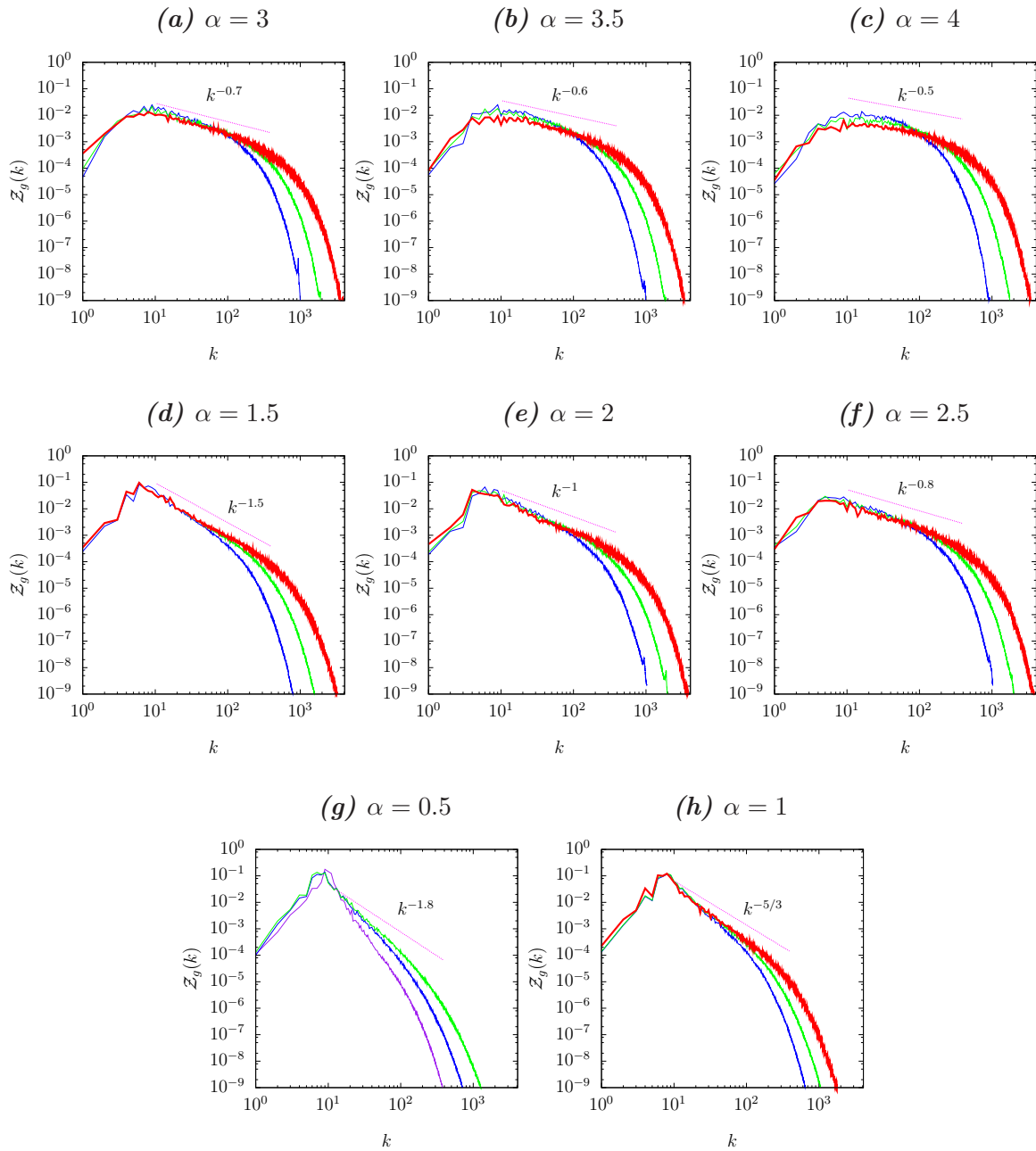


Figure 4.8: Generalised enstrophy spectra $Z_g(k)$ v.s. k for the same set of simulations as figure 4.2, for resolutions 1024×1024 (purple $\alpha = 0.5$ only), 2048×2048 (blue), 4096×4096 (green) and 8192×8192 (red apart from $\alpha = 0.5$).

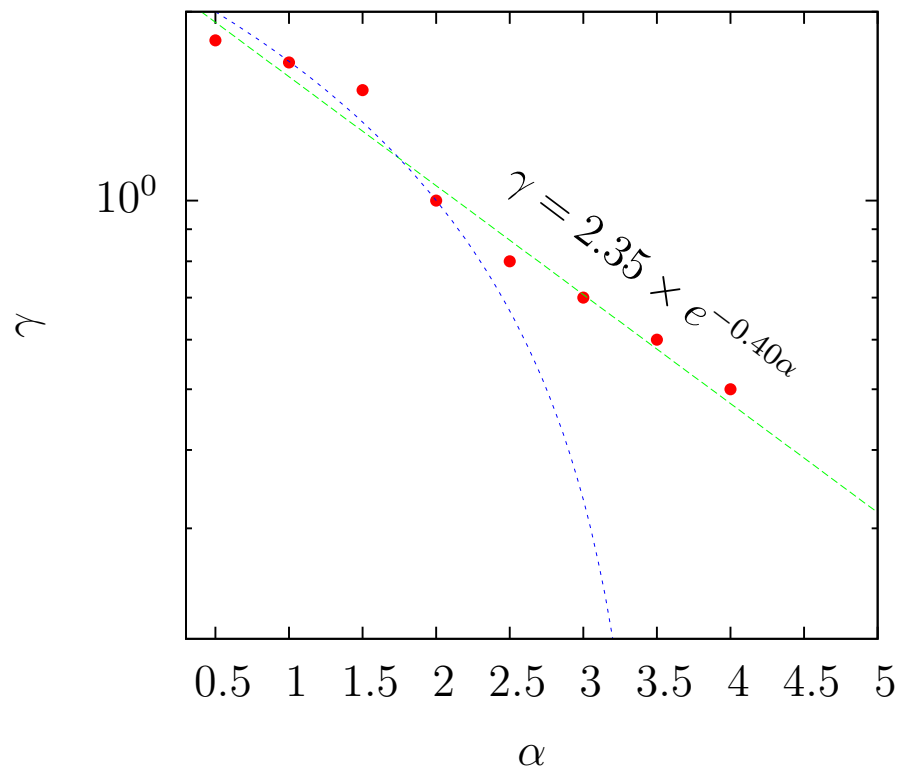


Figure 4.9: Index of the power spectrum in the inertial range v.s. α on a log-lin scale. The green line is the line of best fit, with equation $\gamma = 2.35 \times e^{-0.40\alpha}$, while the blue line is the phenomenologically derived result from §4.1.

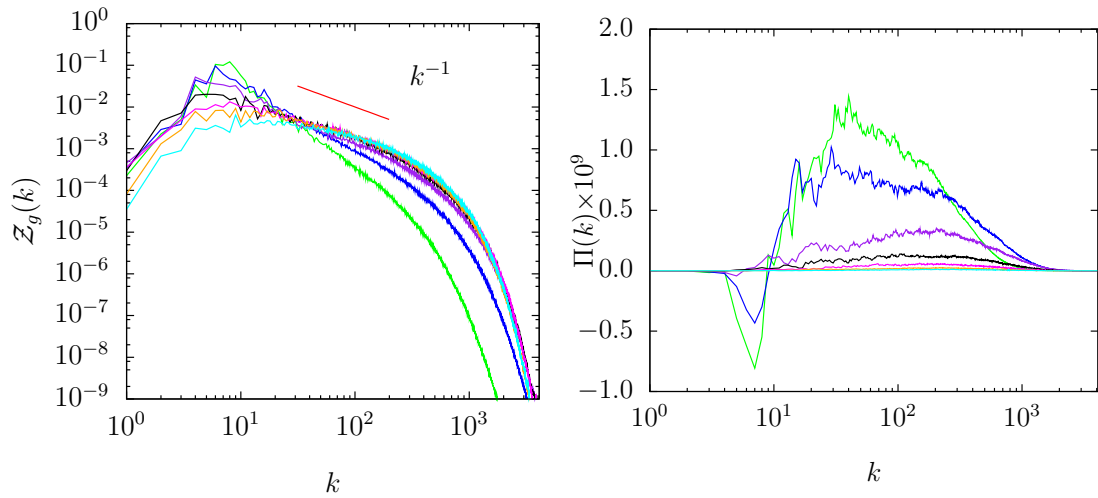


Figure 4.10: Generalised enstrophy spectra and fluxes taken at the time of maximum dissipation rate for the highest resolution simulations. The colour scheme used is identical to that from figure 4.6.

the generalised enstrophy to build up in the inertial range, leading to steep spectra. On the other hand for large α the transfer is sluggish, allowing a buildup of generalised enstrophy in the inertial range, although once again it is possible that the weak transfer is due, at least partly, to the weak advecting velocity field rather than any intrinsic property of the system.

Figure 4.11 shows the initial generalised vorticity field used for all of the above simulations, while figure 4.12 shows the generalised vorticity fields taken at the time of maximum dissipation for the highest-resolution runs (8192×8192 for $\alpha \geq 1$ and 4096×4096 for $\alpha = 0.5$) described above, using the same scale as figure 4.11. It is immediately obvious that the structure of the fields is drastically different for different value of α . For small α the field is largely composed of coherent structures, which are of a similar size as those initially present, although noticeably distorted. As α is increased these structure become significantly stretched, until for $\alpha = 4$ the field consists almost solely of vortex filaments. This is consistent with the description of the generalised enstrophy spectrum seen in figure 4.8, where for small values of α the spectrum is very steep, with all of the generalised enstrophy concentrated around the initial reservoir.

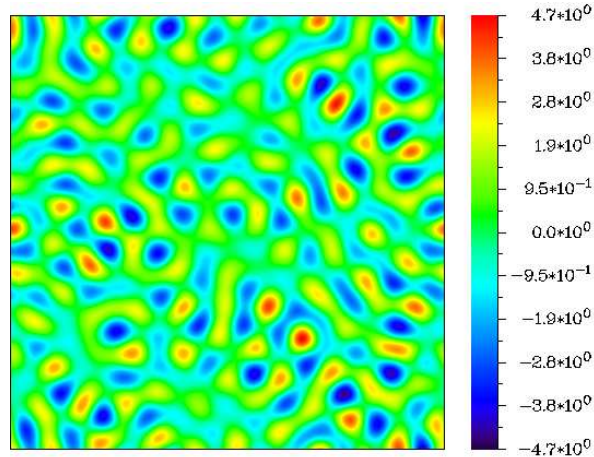


Figure 4.11: Initial generalised vorticity field used for the simulations described above. The Fourier-space modes were initialised to constant values within the wavenumber shell $[9, 12]$ which were then given random phases, with all other modes initialised to zero.

As α increases the generalised enstrophy spectrum shallows significantly, becoming even shallower than k^{-1} , which corresponds to having a large amount of generalised enstrophy at the smallest scales, corresponding to large gradients and the appearance of the filamentary structures.

4.4 Conclusion

In this chapter we have studied mathematically and numerically various aspects of alpha turbulence, which is a family of model systems that generalises the 2DNS and SQG equations. The variable α controls the relationship between the advected generalised vorticity and the advecting velocity field, which changes the locality of transfer in both physical and spectral space space, as well as the degree of nonlinearity of the system. We have seen evidence for a number of theories put forward in the previous two chapters, in particular the relationships between some of the fundamental properties of turbulence. From the equations themselves we have seen how larger values of α correspond to a lesser degree of nonlinearity, where the transfer of the generalised

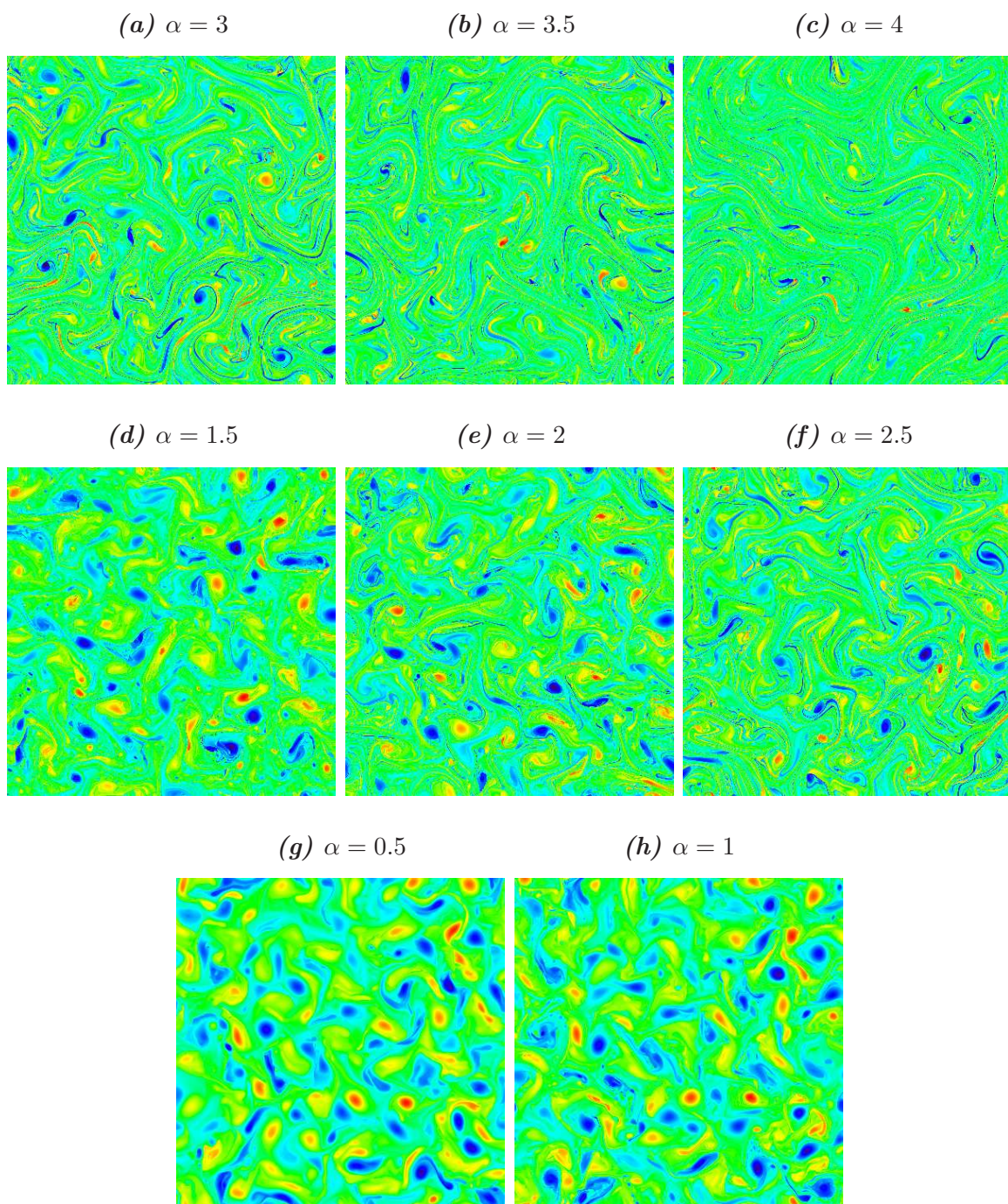


Figure 4.12: Generalised vorticity fields shown at the time of maximum dissipation for the simulations described above.

enstrophy downscale has less of an effect on the advecting velocity field. This comes about through the inversion of the generalised vorticity used to recover the velocity field, which has a greater smoothing effect for larger α . It has been shown how this inversion also has an effect on the locality of the nonlinear interactions in physical space, with larger α corresponding to more nonlocal interaction, resulting in an absence of coherent vortical structures. For small α , on the other hand, interactions are highly physically constrained, suggesting that coherent structures could dominate. The spectral-space interactions have also been examined, with an emphasis on the strength of the transfer coefficients for two different shapes of triads, ‘equilateral’ triads and ‘isosceles’ triads, in the limit of small scales. For $\alpha > 2$, equilateral triads, those $\ell, \mathbf{m}, \mathbf{k}$ where $\ell + \mathbf{m} = \mathbf{k}$ and $k \lesssim l \lesssim m$, the transfer coefficients decay to zero as $k \rightarrow 0$, while for equilateral triads where $k \ll l \lesssim m$, as $l, m \rightarrow \infty$ (with $k < \infty$), the transfer coefficients between wavenumbers ℓ and \mathbf{m} diverge while that of \mathbf{k} decays. This means that for large α ‘ultra-local’ interactions dominate spectral space. For $\alpha = 2$, which coincides with hydrodynamic turbulence, equilateral triads are relatively active at small scales, with the transfer coefficients remaining of order unity, while isosceles triads diverge. For $\alpha < 2$ the coefficients of both types of triads diverge, with the isosceles triads being more active for $1 < \alpha < 2$, both types being equivalently strong for $\alpha = 1$, and the equilateral triads dominating when $\alpha < 1$.

We then discussed the results from a comprehensive set of simulations covering eight values of α from 0.5 to 4 with resolutions up to 8192×8192 . These results largely agreed with those of our analysis, and partially agreed with a number of previously derived phenomenological results. The generalised enstrophy dissipation rate behaves as would be expected from the analysis above, with greater dissipation for smaller α . Some care has to be taken over the interpretation of this result, however, given the fact that the strength of the initial advecting velocity field depends on α , in particular for small α a large initial field could drive a strong initial downscale transfer of generalised enstrophy, independent of any explicit difference in the nonlinearity of the system. The

increasing of the time of maximum dissipation T as α is decreased must similarly be treated carefully, since larger initial velocities could be expected to drive the dynamics more quickly. This problem has been partially remedied by scaling with the initial eddy turnover time, however it is not clear that the behaviour of T is a fundamental property of the system rather than a product of the initial conditions.

Using the results from the numerical simulations a number of relationships between dynamical quantities and the variable α were deduced. It should be made clear that these hold only for this set of simulations with these specific initial conditions and parameters, however they presumably hint at some deeper laws that for now we cannot discover. We found that the maximum dissipation rate was approximately given by $\chi_g^T = 0.43 \times e^{-1.2\alpha}$, the time of maximum dissipation obeyed the law $T = 0.52 \times e^{1.9\alpha}$, although this changed to $T/\tau \sim 14.6 \times e^{-0.5\alpha}$ when scaled with the initial eddy turnover time, the viscosity necessary to keep the system numerically stable at 8192×8192 resolution was $\nu = 2.95 \times 10^{-5} \alpha^{-5.6}$ and the generalised enstrophy spectrum in the inertial range is given by $\mathcal{Z}(k) = k^{2.35 \times e^{-0.40}}$. This exponential shallowing of the spectrum with increasing α agrees with the concept of depletion of nonlinearity causing shallower spectra, as a weak flux allows the buildup of generalised enstrophy in the inertial range, in qualitative agreement with the result by Held *et al.* (1995), although the agreement is not quantitative as the dimensional analysis predicts a linear decay of the exponent. The reasons for this discrepancy are not clear, it is possible that the limited range of Reynolds numbers covered or the form of the initial conditions could have had an effect on the numerical result, although it does not seem likely that they are as different from the ‘true’ spectrum as the phenomenological argument suggests. The agreement with the well-known $k^{-5/3}$ and k^{-1} spectra for $\alpha = 1$ and $\alpha = 2$ gives us confidence that the numerics are at least reasonably reliable.

While the results here are interesting, there are some obvious problems with the simulations as presented. The first is the changing of the strength of the velocity field as α is altered, which by affecting the strength of the initial velocity field meant that for

$\alpha = 0.5$ the CLF condition did not allow for the completion of a simulation of the highest resolution. In order to address this problem, we plan to run another set of simulations, similar to those described in this chapter but keeping the initial energy $\frac{1}{2}\|\mathbf{u}\|^2$ at unity. A problem that is rather harder to solve is the ‘correct’ value of viscosity to use in order to be able to properly compare different values of α . It is not possible to use the same viscosity for all cases, as that would either result in either highly overdamped $\alpha = 4$ or underdamped $\alpha = 0.5$ cases. The solution that we came up with, using ‘just enough’ dissipation for each resolution in order to prevent significant build-up of generalised enstrophy at the smallest scales, seems to have worked reasonably well, however it is not an ideal solution. This problem will hopefully be addressed more thoroughly in future work.

Chapter 5

Magnetohydrodynamics

5.1 Introduction

The study of turbulence in fluids has been extended in many directions from the ‘simple’ hydrodynamic case, to encompass a diverse range of different fluid-type interactions. One of these addresses the evolution of the velocity and magnetic field in a conducting fluid, described by the MHD equations. In three dimensions, the MHD equations are given by

$$\frac{\partial \mathbf{u}}{\partial t} + (\mathbf{u} \cdot \nabla) \mathbf{u} = -\nabla p + (\mathbf{b} \cdot \nabla) \mathbf{b} + \nu \Delta \mathbf{u}, \quad (5.1)$$

$$\frac{\partial \mathbf{b}}{\partial t} + (\mathbf{u} \cdot \nabla) \mathbf{b} = (\mathbf{b} \cdot \nabla) \mathbf{u} + \mu \Delta \mathbf{b}, \quad (5.2)$$

$$\nabla \cdot \mathbf{u} = \nabla \cdot \mathbf{b} = 0 \quad (5.3)$$

where $\mathbf{u}(\mathbf{x}, t)$ is the fluid velocity, $\mathbf{b}(\mathbf{x}, t)$ is the magnetic field, $p(\mathbf{x}, t)$ is the sum of the usual and magnetic pressure, ν is the kinematic viscosity and μ is the magnetic diffusivity. The advection term $\mathbf{u} \cdot \nabla \mathbf{u}$ in equation (5.1) gives rise to the usual vortex-stretching term in the vorticity equation, the term $(\mathbf{b} \cdot \nabla) \mathbf{b}$ represents the Lorentz force, while the magnetic stretching term $(\mathbf{b} \cdot \nabla) \mathbf{u}$ in equation (5.2) may be expected

to similarly amplify magnetic field gradients. The Lorentz force is a manifestation of Lenz's law which states that an induced electromotive force always gives rise to a current whose magnetic field opposes the original change in magnetic flux. These produce a mechanism for the downscale cascade of kinetic and magnetic energy, with the dissipation of total energy expected to approach a finite non-zero constant in the inviscid limit. This forms the basis of Kolmogorov-style phenomenology for 3D MHD turbulence. In the absence of viscosity and magnetic diffusivity, equations (5.1) and (5.2) possess a number of conservation laws, most importantly the conservation of total energy, $E = E_{\mathbf{u}} + E_{\mathbf{b}} = \|\mathbf{u}\|^2/2 + \|\mathbf{b}\|^2/2$. This is readily seen from the kinetic and magnetic energy evolution equations

$$\frac{1}{2} \frac{d}{dt} \|\mathbf{u}\|^2 = \langle \mathbf{u} \cdot (\mathbf{b} \cdot \nabla) \mathbf{b} \rangle - \nu \|\nabla \mathbf{u}\|^2 = \langle \mathbf{u} \cdot (\mathbf{b} \cdot \nabla) \mathbf{b} \rangle - \epsilon_{\mathbf{u}}, \quad (5.4)$$

$$\frac{1}{2} \frac{d}{dt} \|\mathbf{b}\|^2 = \langle \mathbf{b} \cdot (\mathbf{b} \cdot \nabla) \mathbf{b} \rangle - \mu \|\nabla \mathbf{b}\|^2 = \langle \mathbf{b} \cdot (\mathbf{b} \cdot \nabla) \mathbf{u} \rangle - \epsilon_{\mathbf{b}}, \quad (5.5)$$

where the triple-product terms on the right-hand sides exactly cancel each other out. These terms represent the conversion between kinetic and magnetic energy and play important roles in the turbulent dynamics. It is interesting to note that the conservation of total energy (which is true in two dimensions as well as three) is not as restrictive as the conservation of kinetic energy in hydrodynamic turbulence. This will have a strong effect on the dynamics of the system, as described later. Another well-known invariant is the cross-helicity $\langle \mathbf{u} \cdot \mathbf{b} \rangle$. This, together with the conservation of total energy, further implies the conservation of $\|\mathbf{Z}^{\pm}\|^2$ where $\mathbf{Z}^{\pm} = \mathbf{u} \pm \mathbf{b}$ are known as the Elsässer variables. When expressed in terms of these variables, the MHD equations take a symmetric form, which is convenient for the study of Alfvén waves, although they are not explicitly covered in this thesis.

The study of the 3D MHD equations suffers the same difficulties as the 3DNS equations with regard to solving the problems of solution regularity. In fact solving the 3D MHD equations for arbitrary initial conditions automatically solves the 3DNS equa-

tions by setting $\mathbf{b}(0) = 0$. Many of the same phenomenological arguments apply, and simple dimensional analysis gives a $k^{-5/3}$ energy spectrum in the energy inertial range. There has been some debate over this scaling, however, with Iroshnikov and Kraichnan (IK) (Iroshnikov, 1964; Kraichnan, 1965) arguing that when the magnetic energy in sub-inertial wavenumber exceeds the total energy in the inertial range, Alfvén wave effects reduce the energy transfer to small scales, allowing a shallower $k^{-3/2}$ spectrum to build up, an argument in line with our findings that depletion of nonlinearity produces shallower spectra. Kraichnan (1965) further predicts energy equipartition in the inertial range, *i.e.* identical magnetic and kinetic energy spectra within this range. This prediction has found little support as there is ample evidence for a clear mismatch between these spectra (Grappin *et al.*, 1983; Müller & Grappin, 2005; Podesta *et al.*, 2007; Tessein *et al.*, 2009). Since the inertial range generally has little energy, one would expect the Kraichnan condition to hold for a majority of numerical simulations and physical systems. Yet evidence has been presented for both Kolmogorov’s and IK’s spectra under conditions presumably in favour of the latter (Bresnyak, 2011; Galtier *et al.*, 2005; Ng *et al.*, 2012; Verma *et al.*, 1996). Furthermore, on the basis of numerical results for 3D MHD turbulence at unity magnetic Prandtl number ($Pm = \nu/\mu = 1$), Lee *et al.* (2012) even suggested the realisability of the shock-dominated Burgers spectrum k^{-2} , together with the Kolmogorov and IK spectra, depending on the form of the initial conditions.

One of the main tools in proving regularity of the MHD equations, with or without dissipation, is the Caffisch-Klapper-Steel (CKS) criterion (Caffisch *et al.*, 1997) which states that a solution evolving from smooth initial conditions $\{\mathbf{u}, \mathbf{b}\} = \{\mathbf{u}_0, \mathbf{b}_0\}$ remains smooth at least shortly beyond $t = T$ if

$$\int_0^T (\|\boldsymbol{\omega}\|_\infty + \|\mathbf{j}\|_\infty) dt < \infty, \quad (5.6)$$

where $\boldsymbol{\omega} = \nabla \times \mathbf{u}$ and $\mathbf{j} = \nabla \times \mathbf{b}$ are the vorticity and current, respectively. This criterion is a straightforward extension of the celebrated BKM criterion (Beale *et al.*,

1984) of usual (non-magnetic) fields governed by the Euler or NS equations. As in the BKM criterion, where the BMO norm of the vorticity $\|\boldsymbol{\omega}\|_{BMO}$ can replace $\|\boldsymbol{\omega}\|_\infty$ (Kozono & Tanuichi, 2000), we have the following slightly weaker version of (5.6):

$$\int_0^T (\|\boldsymbol{\omega}\|_{BMO} + \|\mathbf{j}\|_{BMO}) dt < \infty. \quad (5.7)$$

Indeed, (5.7) is weaker since (5.6) because for any function f , we have $\|f\|_{BMO} \leq 2\|f\|_\infty$. While we do not go into aspects of the BMO norm in this thesis, for more information see the Appendix of Tran *et al.* (2013a).

In two dimensions, the usual simplifications can be made, with the divergence-free condition on the velocity and magnetic fields meaning that the velocity field \mathbf{u} written as $\mathbf{u} = \nabla^\perp \psi$ where ψ is the streamfunction and $\nabla^\perp = (\partial_y, -\partial_x)$, while the magnetic field \mathbf{b} is written in terms of a scalar magnetic potential a as $\mathbf{b} = -\nabla^\perp a$. In this case, equations (5.1) and (5.2) become

$$\frac{\partial \omega}{\partial t} + J(\psi, \omega) = -J(a, j) + \nu \Delta \omega, \quad (5.8)$$

$$\frac{\partial a}{\partial t} + J(\psi, a) = \mu \Delta a. \quad (5.9)$$

where $\omega = \Delta \psi$ is the vorticity and $j = -\Delta a$ is the current. This reduction in the dimension of the system produces another invariant, the variance of the magnetic potential $\|a\|^2/2$, which has a profound effect on the dynamics, similar to the way that the extra conservation of enstrophy in 2D hydrodynamic turbulence totally alters the behaviour of the system. It is generally assumed, given the similarities with the 2DNS system, that the total energy (the smaller-scale quantity) is transferred downscale while the variance of the magnetic potential (larger-scale) is transferred upscale (see *e.g.* Pouquet, 1978). However the constraint in 2D MHD are not as strong as in hydrodynamic turbulence, since it is only the total energy $\|\nabla \psi\|^2/2 + \|\nabla a\|^2/2$ which is conserved, rather than just the magnetic energy, so the magnetic potential could presumably still be transferred significantly downscale, producing an increase in magnetic energy with

a corresponding decrease in kinetic energy so as to conserve the total energy. This is effectively a conversion of kinetic into magnetic energy, which in three dimensions is known as dynamo. In the absence of an external field, the magnetic potential a (and thus the magnetic field \mathbf{b}) eventually decay to zero, even in the presence of a persistent injection of kinetic energy (Pouquet, 1978), meaning that there can be no self-sustained dynamo in two dimensions. However we shall still refer to the conversion of kinetic into magnetic energy as dynamo action, with the conversion of magnetic into kinetic energy called anti-dynamo, in deference to the ‘proper’ three-dimensional process.

The downscale cascade of total energy is also not so certain in two dimensions, because there is no vortex stretching term, indeed in the absence of the Lorentz force the kinetic energy would be transferred upscale. While this transfer mechanism operates on a relatively slow time scale and limited spectral extent (Dritschel *et al.*, 2008), it is still active in the present case. One would therefore expect some inverse flow of kinetic energy, although this flow could be partially or completely cancelled out by the ‘more vigorous’ direct transfer of the total energy. This means that the only mechanism for the downscale transfer of kinetic energy is through dynamo and antidynamo. Thus we can see that the transfer between kinetic and magnetic energy has a fundamental role to play, which we shall discuss in more depth below.

The 2D MHD system possesses globally smooth solutions when both ν and μ are positive. It turns out that dissipation mechanisms much weaker than the usual molecular diffusion of both the velocity and magnetic fields are capable of regularising the dynamics. Furthermore, global regularity can be secured with partial hyperdissipation. More precisely, consider the MHD equations

$$\frac{\partial \mathbf{u}}{\partial t} + (\mathbf{u} \cdot \nabla) \mathbf{u} + \nabla p = (\mathbf{b} \cdot \nabla) \mathbf{b} - \nu \Lambda^{2\alpha} \mathbf{u}, \quad (5.10)$$

$$\frac{\partial \mathbf{b}}{\partial t} + (\mathbf{u} \cdot \nabla) \mathbf{b} = (\mathbf{b} \cdot \nabla) \mathbf{u} - \mu \Lambda^{2\beta} \mathbf{b}, \quad (5.11)$$

$$\nabla \cdot \mathbf{u} = 0 = \nabla \cdot \mathbf{b}, \quad (5.12)$$

where the viscous and magnetic diffusion terms are replaced by $-\nu\Lambda^{2\alpha}\mathbf{u}$ and $-\mu\Lambda^{2\beta}\mathbf{b}$, respectively, where Λ is the Zygmund operator defined in §3.1. Given $\{\mathbf{u}_0, \mathbf{b}_0\}$ as smooth as necessary (essentially twice differentiable), the system is globally regular for any one of the following conditions

- i) $\alpha \geq 1/2$ and $\beta \geq 1$,
- ii) $0 < \alpha < 1/2$ and $2\alpha + \beta > 2$,
- iii) $\nu = 0$ and $\beta > 2$,
- iv) $\alpha \geq 2$ and $\mu = 0$.

In the next couple of sections, we shall see that theoretical and numerical evidence suggests that the bounds for α and β in *iii*) and *iv*) can be reduced to unity.

5.2 Triad analysis

In this section, which is based on part of the paper Blackburn & Tran (2012), we examine the Fourier-space representation of the processes that are responsible for dynamo and anti-dynamo. Assuming a periodic domain of side 2π , let $\hat{\psi}_{\mathbf{k}}(t)$ and $\hat{a}_{\mathbf{k}}(t)$ denote, respectively, the Fourier transforms of $\psi(\mathbf{x}, t)$ and $a(\mathbf{x}, t)$, where $\mathbf{x} = (x, y)$ and $\mathbf{k} = (k_x, k_y)$. The reality of both $\psi(\mathbf{x}, t)$ and $a(\mathbf{x}, t)$ requires $\hat{\psi}_{\mathbf{k}}(t) = \hat{\psi}_{-\mathbf{k}}^*(t)$ and $\hat{a}_{\mathbf{k}}(t) = \hat{a}_{-\mathbf{k}}^*(t)$, where the asterisk denotes the complex conjugate. Transforming equations (5.9) and (5.8) into Fourier space then gives the equations governing the evolution of $\hat{\psi}_{\mathbf{k}}$ and $\hat{a}_{\mathbf{k}}$,

$$\frac{d}{dt}\hat{\omega}_{\mathbf{k}} = \sum_{\ell+\mathbf{m}=\mathbf{k}} (\ell \times \mathbf{m})\hat{\psi}_{\ell}\hat{\omega}_{\mathbf{m}}, - \sum_{\ell+\mathbf{m}=\mathbf{k}} (\ell \times \mathbf{m})m^2\hat{a}_{\ell}\hat{a}_{\mathbf{m}} - \nu k^2\hat{\omega}_{\mathbf{k}}, \quad (5.13)$$

$$\frac{d}{dt}\hat{a}_{\mathbf{k}} = \sum_{\ell+\mathbf{m}=\mathbf{k}} (\ell \times \mathbf{m})\hat{\psi}_{\ell}\hat{a}_{\mathbf{m}} - \mu k^2\hat{a}_{\mathbf{k}}, \quad (5.14)$$

where $k = |\mathbf{k}|$, $l = |\boldsymbol{\ell}|$, $m = |\mathbf{m}|$ and $\boldsymbol{\ell} \times \mathbf{m} = l_x m_y - l_y m_x$. Since $\hat{\omega}_{\mathbf{k}} = -k^2 \hat{\psi}_{\mathbf{k}}$, these can then be written as

$$\frac{d}{dt} k^2 \hat{\psi}_{\mathbf{k}} = - \sum_{\boldsymbol{\ell} + \mathbf{m} = \mathbf{k}} (\boldsymbol{\ell} \times \mathbf{m}) \hat{\psi}_{\boldsymbol{\ell}} \hat{\omega}_{\mathbf{m}} + \sum_{\boldsymbol{\ell} + \mathbf{m} = \mathbf{k}} (\boldsymbol{\ell} \times \mathbf{m}) m^2 \hat{a}_{\boldsymbol{\ell}} \hat{a}_{\mathbf{m}} + \nu k^2 \hat{\omega}_{\mathbf{k}}, \quad (5.15)$$

$$\frac{d}{dt} k^2 \hat{a}_{\mathbf{k}} = \sum_{\boldsymbol{\ell} + \mathbf{m} = \mathbf{k}} k^2 (\boldsymbol{\ell} \times \mathbf{m}) \hat{\psi}_{\boldsymbol{\ell}} \hat{a}_{\mathbf{m}} - \mu k^4 \hat{a}_{\mathbf{k}}. \quad (5.16)$$

The first term on the right-hand side of (5.15) is the standard advection term, which by itself is known to transfer kinetic energy to smaller k and enstrophy to larger k . In order to investigate the interactions that cause dynamo action, that is the conversion between kinetic and magnetic energy, we shall ignore this term for now, concentrating only on the nonlinear terms that connect the magnetic and mechanical modes, which give the equations

$$\frac{d}{dt} k^2 \hat{\psi}_{\mathbf{k}} = \sum_{\boldsymbol{\ell} + \mathbf{m} = \mathbf{k}} (\boldsymbol{\ell} \times \mathbf{m}) m^2 \hat{a}_{\boldsymbol{\ell}} \hat{a}_{\mathbf{m}}, \quad (5.17)$$

$$\frac{d}{dt} k^2 \hat{a}_{\mathbf{k}} = \sum_{\boldsymbol{\ell} + \mathbf{m} = \mathbf{k}} k^2 (\boldsymbol{\ell} \times \mathbf{m}) \hat{\psi}_{\boldsymbol{\ell}} \hat{a}_{\mathbf{m}}. \quad (5.18)$$

The equations governing the modal energy components $k^2 |\hat{\psi}_{\mathbf{k}}|^2 / 2$, $l^2 |\hat{a}_{\boldsymbol{\ell}}|^2 / 2$ and $m^2 |\hat{a}_{\mathbf{m}}|^2 / 2$ of a single wavenumber triad $\hat{\psi}_{\mathbf{k}}$, $\hat{a}_{\boldsymbol{\ell}}$ and $\hat{a}_{\mathbf{m}}$, where $\boldsymbol{\ell} + \mathbf{m} = \mathbf{k}$, is then given by

$$\frac{d}{dt} k^2 |\hat{\psi}_{\mathbf{k}}|^2 = (l^2 - m^2) (\boldsymbol{\ell} \times \mathbf{m}) \left(\hat{\psi}_{\mathbf{k}}^* \hat{a}_{\boldsymbol{\ell}} \hat{a}_{\mathbf{m}} + \hat{\psi}_{\mathbf{k}} \hat{a}_{\boldsymbol{\ell}}^* \hat{a}_{\mathbf{m}}^* \right) \quad (5.19)$$

$$\frac{d}{dt} l^2 |\hat{a}_{\boldsymbol{\ell}}|^2 = -l^2 (\boldsymbol{\ell} \times \mathbf{m}) \left(\hat{\psi}_{\mathbf{k}}^* \hat{a}_{\boldsymbol{\ell}} \hat{a}_{\mathbf{m}} + \hat{\psi}_{\mathbf{k}} \hat{a}_{\boldsymbol{\ell}}^* \hat{a}_{\mathbf{m}}^* \right) \quad (5.20)$$

$$\frac{d}{dt} m^2 |\hat{a}_{\mathbf{m}}|^2 = m^2 (\boldsymbol{\ell} \times \mathbf{m}) \left(\hat{\psi}_{\mathbf{k}}^* \hat{a}_{\boldsymbol{\ell}} \hat{a}_{\mathbf{m}} + \hat{\psi}_{\mathbf{k}} \hat{a}_{\boldsymbol{\ell}}^* \hat{a}_{\mathbf{m}}^* \right) \quad (5.21)$$

The right-hand sides of equations (5.19), (5.20) and (5.21) sum up to zero, so the interaction within individual triads conserves total energy as expected. Without loss of generality, we let $l < m$ in what follows.

Equations (5.19), (5.20) and (5.21) fully describe the triad energetics and reveal a

great deal about the nature of the energy transfer and dynamo action. In general, one magnetic mode gains energy at the expense of the other since the right-hand sides of (5.20) and (5.21) have opposite signs. Now suppose that the smaller-scale mode, i.e. mode \mathbf{m} , is the ‘winner’. In this case, the right-hand side of (5.19) is negative, implying a conversion from kinetic to magnetic energy (dynamo action). This is true whether $k > m$ or $k \leq m$ (including $k \leq \ell$) and establishes that the dynamo is accompanied by a direct magnetic energy flux. As far as the direct transfer of the total energy is concerned, the case $k > m$ corresponds to a relatively inefficient transfer, in the sense that the intermediate scale receives energy from both larger and smaller scales. Note that in 2D non-conducting fluids, transfer from the intermediate scale to both smaller and larger scales (and vice versa) is universal among interacting triads, nonetheless still giving rise to a net direct transfer. The case $k \leq m$ corresponds to a transfer of energy from the two larger scales to the third and smaller scale. This apparently more efficient transfer behaviour is characteristic of Burgers flows (Tran & Dritschel, 2010), for which velocity discontinuities develop in finite times, and has not been seen in other fluid systems. Thus, an efficient mechanism for direct energy transfer similar to that in Burgers flow is present in the 2D MHD equations. However, unlike the Burgers case, where each small scale can receive energy from larger ones to sustain a persistent direct energy flux, the energy of the mechanical mode $\hat{\psi}_{\mathbf{k}}(t) \exp\{i\mathbf{k} \cdot \mathbf{x}\}$ in the dynamo triads cannot be replenished in the same fashion. Instead, a mechanical small scale can be ‘recharged’ only through triad interactions that involve a return of energy from smaller scales to larger ones. This has a profound implication and is discussed presently. Figure 5.1 gives a qualitative description of these triad interactions.

Suppose that in the above triad interaction, the larger-scale magnetic mode, i.e. mode ℓ , gains energy. This gain is at the expense of its smaller-scale counterpart \mathbf{m} , which also loses some energy to the mechanical mode \mathbf{k} (the right-hand side of (5.19) is positive). Hence, any anti-dynamo is associated with an inverse magnetic energy flux. Similar to the above dynamo triad, this anti-dynamo triad can have either $k > m$ or

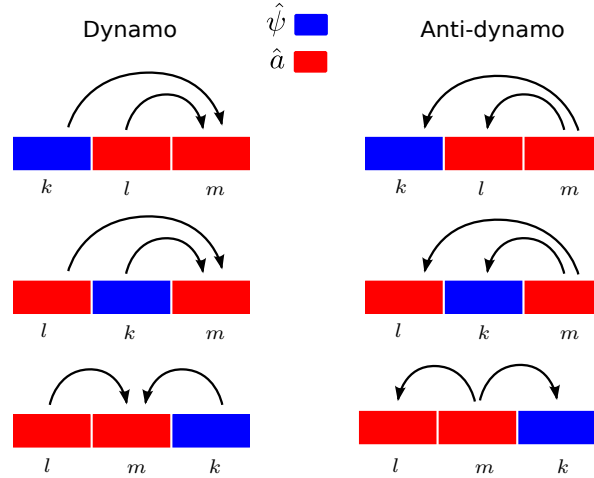


Figure 5.1: A schematic description of dynamo and anti-dynamo wave triads for a single triad $\mathbf{k} = \boldsymbol{\ell} + \mathbf{m}$ ($|\boldsymbol{\ell}| = \ell < m = |\mathbf{m}|$) responsible for energy conversion and transfer. The arrows indicate the direction of energy transfer.

$k \leq m$ (including $k \leq \ell$). The latter case corresponds to an inverse energy transfer from the smaller scale to both the intermediate and larger scales. In both of these cases, the mechanical mode is energetically replenished, thereby making it possible for a persistent operation of the dynamo triads discussed in the preceding paragraph. Note that dynamo triads by themselves are able to excite the small scales magnetically but not mechanically. On the other hand, anti-dynamo triads by themselves cannot rid the large scales of any kinetic energy.

The analysis in the preceding paragraphs indicates that two distinct types of triads operate concurrently in the direct energy transfer. One of these is a dynamo while the other one is an anti-dynamo. The operation of dynamo triads relies on the recharging of their mechanical modes by anti-dynamo triads. While this does not guarantee dynamo saturation (or more accurately quasi-saturation) any better than the constraint due to energy conservation discussed above, it does provide another look at this widely observed phenomenon. Here ‘quasi-saturation’ means that the magnetic-to-kinetic energy ratio $r(t) = E_{\mathbf{b}}(t)/E_{\mathbf{u}}(t)$ becomes quasi-steady and does not necessarily imply that the dynamo and anti-dynamo triads cease to be active. For high-resolution numerical anal-

ysis of anti-dynamo behaviour of both forced and unforced turbulence, see the recent studies of Loureiro *et al.* (2009) and Servidio *et al.* (2010).

5.3 Degrees of freedom

In this section we present a result derived by Tran & Yu (2012), in order to compare it with the previously derived results for the number of degrees of freedom for other systems. We shall work in the space spanning both the velocity and magnetic fields, with components $\mathbf{U}_i = (\mathbf{u}_i, \mathbf{b}_i)$ and the inner product $\langle \mathbf{U}_i, \mathbf{U}_j \rangle_* = \langle \mathbf{u}_i \cdot \mathbf{u}_j \rangle + \langle \mathbf{b}_i \cdot \mathbf{b}_j \rangle$, which then defines the natural norm $\|\mathbf{U}\|_*^2 = \|\mathbf{u}\|^2 + \|\mathbf{b}\|^2$. We now consider a solution $\mathbf{U} = (\mathbf{u}, \mathbf{b})$ to the 2D MHD equations (5.1) and (5.2), starting from some smooth initial condition $\mathbf{U}_0 = (\mathbf{u}_0, \mathbf{b}_0)$, with a corresponding pressure p . We now introduce a perturbation $\mathbf{U}' = (\mathbf{u}', \mathbf{b}')$ with perturbed pressure p' at some arbitrary time. Linearising equations (5.1) and (5.2) with respect to the perturbations gives the equations for the evolution of this perturbation

$$\frac{\partial \mathbf{u}'}{\partial t} + (\mathbf{u} \cdot \nabla) \mathbf{u}' + (\mathbf{u}' \cdot \nabla) \mathbf{u} + \nabla p' = (\mathbf{b} \cdot \nabla) \mathbf{b}' + \nu \Delta \mathbf{u}', \quad (5.22)$$

$$\frac{\partial \mathbf{b}'}{\partial t} + (\mathbf{u} \cdot \nabla) \mathbf{b}' + (\mathbf{u}' \cdot \nabla) \mathbf{b} = (\mathbf{b} \cdot \nabla) \mathbf{u}' + (\mathbf{b}' \cdot \nabla) \mathbf{u} + \mu \Delta \mathbf{b}'. \quad (5.23)$$

Multiplying equations (5.22) and (5.23) by \mathbf{u}' and \mathbf{b}' respectively, averaging over the domain and adding them gives the equation governing the norm described above,

$$\begin{aligned} \|\mathbf{U}'\|_* \frac{d}{dt} \|\mathbf{U}'\|_* &= \langle \mathbf{b}' \cdot (\mathbf{b}' \cdot \nabla) \mathbf{u} \rangle - \langle \mathbf{b}' \cdot (\mathbf{u}' \cdot \nabla) \mathbf{b} \rangle + \langle \mathbf{u}' \cdot (\mathbf{b}' \cdot \nabla) \mathbf{b} \rangle \\ &\quad - \langle \mathbf{u}' \cdot (\mathbf{u}' \cdot \nabla) \mathbf{u} \rangle - \nu \|\nabla \mathbf{u}'\|^2 - \mu \|\nabla \mathbf{b}'\|^2, \end{aligned}$$

where we have used the fact that two of the triple-product terms cancel exactly. The exponential growth or decay rate of $\|\mathbf{U}\|_*$ is then given by

$$\begin{aligned} \lambda &= \frac{1}{\|\mathbf{U}\|_*} \frac{d}{dt} \|\mathbf{U}\|_*, \\ &= \frac{1}{\|\mathbf{U}\|_*^2} (\langle \mathbf{b}' \cdot (\mathbf{b}' \cdot \nabla) \mathbf{u} \rangle - \langle \mathbf{b}' (\mathbf{u}' \cdot \nabla) \mathbf{b} \rangle + \langle \mathbf{u}' \cdot (\mathbf{b}' \cdot \nabla) \mathbf{b} \rangle \\ &\quad - \langle \mathbf{u}' \cdot (\mathbf{u}' \cdot \nabla) \mathbf{u} \rangle - \nu \|\nabla \mathbf{u}'\| - \mu \|\nabla \mathbf{b}'\|). \end{aligned} \quad (5.24)$$

An orthonormal set of n least stable disturbances $\{\mathbf{U}_1, \mathbf{U}_2, \dots, \mathbf{U}_n\}$ and the corresponding greatest growth rates $\{\lambda_1, \lambda_2, \dots, \lambda_n\}$ can then be derived by successively maximising λ with respect to all admissible disturbances \mathbf{U}' subject to the following orthonormality constraint. At each step i in the process, \mathbf{U}' is required to satisfy both $\|\mathbf{U}'\| = 1$ and $\langle \mathbf{U}', \mathbf{U}_j \rangle_* = 0$, for $j = 1, 2, \dots, i-1$, where \mathbf{U}_j is the maximiser obtained at the j -th step. This process eventually exhausts all unstable mutually orthogonal disturbances and reaches a regime where $\lambda_i < 0$. It follows that there exists an integer N satisfying

$$\sum_{i=0}^N \lambda_i \leq 0 < \sum_{i=0}^{N-1} \lambda_i. \quad (5.25)$$

The orthonormal set $\{\mathbf{U}_1, \mathbf{U}_2, \dots, \mathbf{U}_n\}$ then consists of all unstable modes and a number of stable modes, which can adequately describe the solution \mathbf{U} at least locally in time. As in the previous chapters, N is known as the number of degrees of freedom of the

system. Since each solution satisfies equation (5.24), we have that

$$\begin{aligned}
\lambda_n &= \sum_{i=1}^n (\langle \mathbf{b}_i \cdot (\mathbf{b}_i \cdot \nabla) \mathbf{u} \rangle - \langle \mathbf{b}_i \cdot (\mathbf{u}_i \cdot \nabla) \mathbf{b} \rangle + \langle \mathbf{u}_i \cdot (\mathbf{b}_i \cdot \nabla) \mathbf{b} \rangle \\
&\quad - \langle \mathbf{u}_i \cdot (\mathbf{u}_i \cdot \nabla) \mathbf{u} \rangle - \nu \|\nabla \mathbf{u}_i\|^2 - \mu \|\nabla \mathbf{b}_i\|^2), \\
&\leq \sum_{i=1}^n (\langle (|\mathbf{u}_i|^2 + |\mathbf{b}_i|^2) |\nabla \mathbf{u}| \rangle + 2 \langle |\mathbf{u}_i| |\mathbf{b}_i| |\nabla \mathbf{b}| \rangle - \nu \|\nabla \mathbf{u}_i\|^2 - \mu \|\nabla \mathbf{b}_i\|^2), \\
&\leq \sum_{i=1}^n (\langle |\mathbf{U}_i|^2 (|\nabla \mathbf{u}| + |\nabla \mathbf{b}|) \rangle - \nu \|\nabla \mathbf{u}_i\|^2 - \mu \|\nabla \mathbf{b}_i\|^2), \\
&\leq \left\| \sum_{i=1}^n |\mathbf{U}_i|^2 \right\| (\|\nabla \mathbf{u}\| + \|\nabla \mathbf{b}\|) - \min(\nu, \mu) \sum_{i=1}^n \|\nabla \mathbf{U}_i\|^2, \\
&\leq \left(\sum_{i=1}^n \|\nabla \mathbf{U}_i\|^2 \right)^{1/2} \left(c_3 L (\|\nabla \mathbf{u}\| + \|\nabla \mathbf{b}\|) - \min(\nu, \mu) \left(\sum_{i=1}^n \|\nabla \mathbf{U}_i\|^2 \right)^{1/2} \right), \\
&\leq \left(\sum_{i=1}^n \|\nabla \mathbf{U}_i\|^2 \right)^{1/2} \left(c_3 L (\|\nabla \mathbf{u}\|^2 + \|\nabla \mathbf{b}\|^2)^{1/2} - \min(\nu, \mu) c_1^{1/2} \frac{n}{L} \right),
\end{aligned} \tag{5.26}$$

where we have used the Cauchy-Schwarz, Lieb-Thirring (1.58) and Rayleigh-Ritz (1.54) inequalities. The condition $\sum_{i=1}^n \lambda_i < 0$ is then satisfied if

$$n \geq \frac{L^2}{\min(\nu, \mu)} (\|\nabla \mathbf{u}\| + \|\nabla \mathbf{b}\|), \tag{5.27}$$

from which it follows that

$$N \leq \frac{cL^2 (\|\nabla \mathbf{u}\|^2 + \|\nabla \mathbf{b}\|^2)^{1/2}}{\min(\nu, \mu)}. \tag{5.28}$$

If we define the kinetic and magnetic Reynolds numbers

$$Re = \frac{L^{4/3} \epsilon_{\mathbf{u}}^{1/3}}{\nu}, \tag{5.29}$$

$$Rm = \frac{L^{4/3} \epsilon_{\mathbf{b}}^{1/3}}{\mu}, \tag{5.30}$$

which is the same form as previously defined for the 3DNS (Tran, 2009) and SQG equation (see §3.2.1), we get from equation (5.28)

$$N \leq PmRe^{3/2} + Rm^{3/2} \quad \text{for } Pm > 1, \quad (5.31)$$

$$N \leq Re^{3/2} + Pm^{-1}Rm^{3/2} \quad \text{for } Pm < 1. \quad (5.32)$$

Looking at the case $Pm = 1$, it is now possible to deduce that the dissipation wavenumber k_d is equivalent to

$$k_d \approx \frac{N^{1/2}}{L} \leq \frac{c^{1/2}\epsilon^{1/4}}{\nu^{3/4}}. \quad (5.33)$$

The same arguments as used in §3.2.1 now hold for the energy spectrum. For a total energy spectrum of the form $\mathcal{E}(k) = Ck^{-\alpha}$, using equation (5.33), the dissipation rate is given by

$$\begin{aligned} \epsilon_* &= C\nu \int_{k_0}^{k_\nu} k^{2-\alpha} dk, \\ &= \frac{C\nu}{3-\alpha} (k_\nu^{3-\alpha} - k_0^{3-\alpha}), \\ &\leq \frac{c^{(3-\alpha)/2}C\nu}{3-\alpha} \frac{\epsilon_*^{(3-\alpha)/4}}{\nu^{3(3-\alpha)/4}}, \end{aligned} \quad (5.34)$$

which on rearranging gives

$$\epsilon_*^{1+\alpha} \leq c' C^4 \nu^{3\alpha-5}, \quad (5.35)$$

where $c' = c^{2(3-\alpha)}/(3-\alpha)^4$. An interesting implication of (5.35) is that spectra steeper than $k^{-5/3}$ are incompatible with a nonzero limiting energy dissipation rate. Now if $\epsilon_*(t)$ remains nonzero in the inviscid limit, (5.35) requires $\alpha = 5/3$, provided that the estimate (5.28) is optimal. For this value of α , $C \propto \epsilon_\nu^{2/3}$ and the energy spectrum takes the classical form $\mathcal{E}(k) \propto \epsilon_\nu^{2/3} k^{-5/3}$. In passing, it is worth mentioning that for turbulence with predominant magnetic energy, the presence of strong Alfvén waves could suppress nonlinear effects (Kraichnan, 1965), probably making the estimate (5.28), and hence (5.35), excessive. This allows for the possibility $\alpha < 5/3$. In fact, Iroshnikov (1964) and

Kraichnan (1965) predicted $\alpha = 3/2$ for this case. This problem is investigated further in the upcoming sections.

5.4 Limit of zero and infinite Prandtl Number

One extra complication in MHD is the fact that there are two dissipation mechanisms, the kinetic energy viscous dissipation $\epsilon_{\mathbf{u}} = \nu \|\nabla \mathbf{u}\|^2$ and the magnetic energy diffusion $\epsilon_{\mathbf{b}} = \mu \|\nabla \mathbf{b}\|^2$. This means that the ‘inviscid limit’ depends not only on $\nu \rightarrow 0$ and $\mu \rightarrow 0$ but also the relative speeds on which each of these terms is reduced to zero. The measure of this is given by the magnetic Prandtl number $Pm = \nu/\mu$. In the next section, which is based on the paper (Tran *et al.*, 2013a), we show how the Prandtl number can have a significant effect on the dynamics of the 2D MHD system, including the possibility of the appearance of finite-time singularities.

5.4.1 Theoretical understanding

Recent mathematical studies of the 2D MHD equations have derived several regularity criteria concerning the strength of the generalised diffusion operators $(-\Delta)^\alpha$, for $\alpha \geq 0$, which replace the usual molecular diffusion operator Δ (Wu, 2011; Tran *et al.*, 2013c). Since the induction equation is linear in the magnetic field, global regularity is possible in the absence of magnetic diffusion, provided that a strong enough dissipation mechanism is applied to the velocity field, so as to keep the velocity gradients bounded (this is true for any number of dimensions, see Tran *et al.* (2013b) and references therein). On the other hand, since vortex stretching is absent in two dimensions, global regularity is possible in the absence of momentum diffusion, provided that a sufficiently strong dissipation mechanism is applied to the magnetic field, so as to suppress magnetic stretching and keep the current gradients (which appear in the vorticity equation) bounded. Indeed, Tran *et al.* (2013c) have proven global regularity

for either hyperviscosity (represented by $(-\Delta)^\alpha$) alone with $\alpha \geq 2$ or magnetic hyperdiffusion alone with $\alpha > 2$. As far as the classical energy method is concerned, these bounds for α appear optimal. However, physical arguments and numerical analysis indicate otherwise. In §5.5.1 we suggest that for fully developed turbulence evolving from a large-scale energy reservoir, the conversion between kinetic and magnetic energy becomes quasi-steady (dynamo saturation in the three-dimensional context). This may correspond to a state of complete or nearly complete depletion of nonlinearities. Hence, excessively strong dissipation mechanisms would be unnecessary to prevent finite-time singularities. This can be clearly seen in the following analysis, which shows that both $\|\omega\|$ and $\|j\|$ are uniformly bounded for $Pm = 0$, i.e. $\nu = 0$, $\mu > 0$. Scalar multiplying (5.1) by \mathbf{u} and (5.2) by \mathbf{b} and adding gives

$$\frac{1}{2} \frac{d}{dt} (\|\mathbf{u}\|^2 + \|\mathbf{b}\|^2) = -\nu \|\omega\|^2 - \mu \|j\|^2 \leq -\mu \|j\|^2. \quad (5.36)$$

It then follows that

$$\int_0^t \|j\|^2 d\tau \leq \frac{1}{2\mu} (\|\mathbf{u}_0\|^2 + \|\mathbf{b}_0\|^2), \quad (5.37)$$

for all t , including $t = \infty$, for which the inequality becomes an equality if $\nu = 0$. By taking the Laplacian of (5.9) the evolution equation for the current j is found to be

$$\frac{\partial j}{\partial t} + \mathbf{u} \cdot \nabla j = \mathbf{b} \cdot \nabla \omega + B(\nabla \mathbf{u}, \nabla \mathbf{b}) + \mu \Delta \quad (5.38)$$

where $B(\nabla \mathbf{u}, \nabla \mathbf{b})$ is bilinear in \mathbf{u} and \mathbf{b} and given by

$$B(\nabla \mathbf{u}, \nabla \mathbf{b}) = 2 \frac{\partial b_1}{\partial x} \left(\frac{\partial u_2}{\partial x} + \frac{\partial u_1}{\partial y} \right) + 2 \frac{\partial u_2}{\partial y} \left(\frac{\partial b_2}{\partial x} + \frac{\partial b_1}{\partial y} \right), \quad (5.39)$$

where $\mathbf{u} = (u_1, u_2)$ and $\mathbf{b} = (b_1, b_2)$. By multiplying (5.8) and (5.38) by ω and j , respectively, summing up and integrating the resulting equations, we obtain

$$\frac{1}{2} \frac{d}{dt} (\|\omega\|^2 + \|j\|^2) = \int j B(\nabla \mathbf{u}, \nabla \mathbf{b}) d\mathbf{x} - \nu \|\nabla \omega\|^2 - \mu \|\nabla j\|^2, \quad (5.40)$$

where only the triple-product term involving B survives (the two triple-product terms involving \mathbf{u} vanish while the two triple-product terms involving \mathbf{b} cancel each other, thanks to the divergence-free properties $\nabla \cdot \mathbf{u} = \nabla \cdot \mathbf{b} = 0$). This term can be estimated as follows:

$$\begin{aligned}
\int jB(\nabla \mathbf{u}, \nabla \mathbf{b}) &\leq \|\nabla \mathbf{u}\| \|j\|_{L^4} \|\nabla \mathbf{b}\|_{L^4} \\
&\leq c \|\omega\| \|j\|_{L^4}^2 \\
&\leq c \|\omega\| \|j\| \|\nabla j\| \\
&\leq \frac{c}{2\mu} \|\omega\|^2 \|j\|^2 + \frac{\mu}{2} \|\nabla j\|^2.
\end{aligned} \tag{5.41}$$

Here the first inequality is due to Hölder's inequality and the second inequality follows from the relation $\|\nabla \mathbf{b}\|_{L^4} \leq c \|j\|_{L^4}$, which is a consequence of the boundedness of Riesz operators on L^p spaces ($1 < p < \infty$) (see *e.g.* Stein, 1970). The Gagliardo–Nirenberg inequality $\|j\|_{L^4}^2 \leq c \|j\| \|\nabla j\|$ (see *e.g.* Nirenberg, 1959, for a complete discussion of such a class of inequalities) and the geometric-arithmetic mean inequality have been used in the subsequent steps. Substituting (5.41) into (5.40) yields

$$\begin{aligned}
\frac{d}{dt} (\|\omega\|^2 + \|j\|^2) + \mu \|\nabla j\|^2 &\leq \frac{c}{\mu} \|\omega\|^2 \|j\|^2, \\
&\leq \frac{c}{\mu} (\|\omega\|^2 + \|j\|^2) \|j\|^2.
\end{aligned} \tag{5.42}$$

By applying Grönwall's lemma to (5.42) (or directly integrating (5.42) with the integrating factor $\exp\{-c \int_0^t \|j\|^2 d\tau/\mu\}$) we obtain

$$\begin{aligned}
\|\omega\|^2 + \|j\|^2 + \mu \int_0^t \|\nabla j\|^2 d\tau &\leq (\|\omega_0\|^2 + \|j_0\|^2) \exp \left\{ \frac{c}{\mu} \int_0^t \|j\|^2 d\tau \right\}, \\
&\leq (\|\omega_0\|^2 + \|j_0\|^2) \exp \left\{ \frac{c}{2\mu^2} (\|\mathbf{u}_0\|^2 + \|\mathbf{b}_0\|^2) \right\},
\end{aligned} \tag{5.43}$$

where $\omega_0 = \omega(x, y, 0)$ and $j_0 = j(x, y, 0)$.

Given $\mu > 0$, two important results can be readily deduced from (5.43). First, both

$\|\omega\|$ and $\|j\|$ are bounded independently of viscosity for $t > 0$. This result was known to Lei & Zhou (2009) and Cao & Wu (2011). The implication is that in the presence of vanishingly small viscosity, the kinetic energy dissipation rate $\nu\|\omega\|^2$ tends to zero. Furthermore, for sufficiently small Pm , the approach $\nu\|\omega\|^2 \rightarrow 0$ becomes linear in ν , approximately given by $\nu\Omega^2$, where Ω is an upper bound for $\|\omega\|$. The regime of this linear behaviour turns out to be fully accessible to numerical simulations. Indeed, the results reported in §5.4 show a nearly linear decrease of $\nu\|\omega\|^2$ with ν even for moderately small Pm . Second, we have

$$\int_0^t \|\nabla j\|^2 < \infty. \quad (5.44)$$

Since in two dimensions, $\|j\|_{BMO}$ can be bounded from above in terms of $\|\nabla j\|$, namely $\|j\|_{BMO} \leq c\|\nabla j\|$, one has

$$\int_0^t \|j\|_{BMO} d\tau < \infty, \quad (5.45)$$

which is half of the improved CKS regularity criterion. The other half of the CKS criterion, concerning $\|\omega\|_{BMO}$, is however not available, even though $\|\omega\|$ is uniformly bounded. This half would follow if $\|\omega\|_{BMO}/\|\omega\| < \infty$, and global regularity would be secured. In fact, for solutions $\|\omega\|_{BMO}/\|\omega\| \leq F(t)$, regularity beyond $t = T$ is guaranteed once $\int_0^T F(t) dt$ is bounded, since it is sufficient to require that

$$\begin{aligned} \int_0^T \|\omega\|_{BMO} dt &\leq \int_0^T \|\omega\| F(t) dt \\ &\leq \Omega \int_0^T F(t) dt < \infty \end{aligned} \quad (5.46)$$

where Ω is an upper bound for $\|\omega\|$. In particular, for regularity beyond $t = T$, it is sufficiently to require that

$$\frac{\|\omega\|_{BMO}}{\|\omega\|} \leq C(T-t)^{-\alpha} \quad (5.47)$$

for $\alpha < 1$. In the next section we show results from numerical simulations which indicate mild growth of the ratio $\|\omega\|_\infty/\|\omega\|$ for a range of small Pm , thereby suggesting global

regularity.

Further results from Tran *et al.* (2013a) regarding the limit $Pm \rightarrow \infty$, which we do not prove here, state that regularity is guaranteed if either $\|j\|_\infty/\|j\|$ or $\|\nabla u\|_\infty/\|\omega\|$ do not grow too rapidly in time, in particular it is sufficient to require either

$$\frac{\|j\|_\infty}{\|j\|} \leq C(T-t)^{-\alpha} \quad (5.48)$$

or

$$\frac{\|\nabla u\|_\infty}{\|\omega\|} \leq C(T-t)^{-\alpha}, \quad (5.49)$$

for $\alpha < 1/2$. Through monitoring these ratios the numerical simulations in the next section give some support to the idea of regularity for the 2D MHD equations in the limits $Pm \rightarrow 0$ and $Pm \rightarrow \infty$.

5.4.2 Numerical results

In this section we present the results from a series of numerical simulations, which support the above theories and confirm the mathematical result of the linear scaling of $\nu\|\omega\|^2$ with ν in the limit $Pm \rightarrow 0$. Interestingly, a slightly less rapid decrease of $\mu\|j\|^2$ with μ is observed in the large Pm regime.

Equations (5.8) and (5.9) were integrated using the pseudo-spectral method described in §1.4, with the dissipative terms incorporated exactly using an integrating factor. The initial magnetic modes lay within the wavenumber range $[5, 8]$, having random phases and an energy of 0.5. The initial mechanical modes were also confined to the range $[5, 8]$, having random phases and an energy of 0.5. This amounts to a total energy of 1.0. The initial vorticity and current fields are given in figure 5.2. Seven different values of Pm were chosen: $Pm = 1/64, 1/16, 1/4, 1, 4, 16$ and 64 . The case $Pm = 1$ corresponds to $\nu = \mu = 8 \times 10^{-4}$. For $Pm \neq 1$ one of the diffusion coefficients was fixed at 8×10^{-4} and the other was decreased accordingly. The cases $Pm = 1/64$

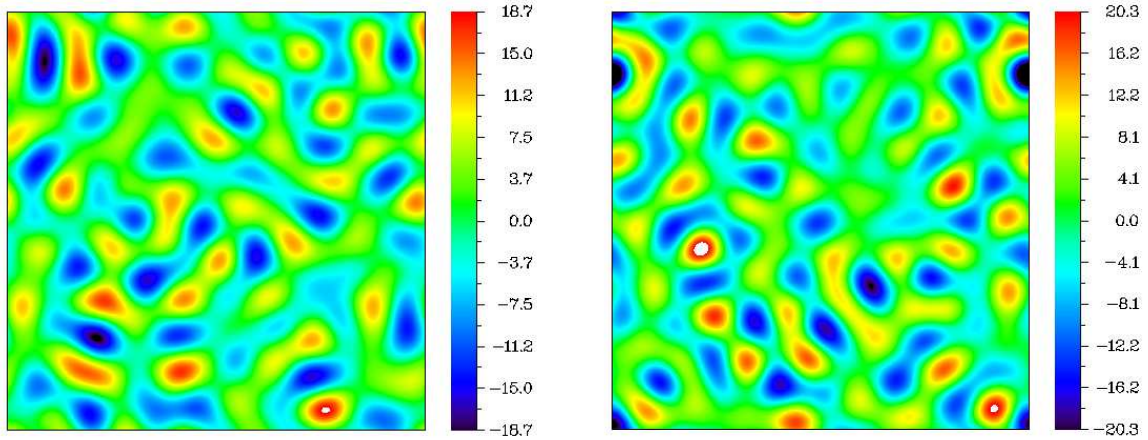


Figure 5.2: Vorticity (left) and current (right) initial condition fields.

and $Pm = 64$ were simulated at the highest resolution of 8192×8192 . For $Pm = 1/64$, the magnetic and kinetic Reynolds numbers Re and Rm , defined in (5.29) and (5.30), are $Rm = 10,500$ and $Re = 173,700$. On the other hand, for $Pm = 64$, these numbers are $Rm = 325,000$ and $Re = 9,700$. For each Pm , the energy conversion (primarily from kinetic to magnetic) is observed to become saturated when $t \gtrsim 1$, shortly after which the energy dissipation achieves its peak. In agreement with the findings discussed in §5.5.1, the saturated ratio of magnetic to kinetic energy (not shown) has been found to be within the range $[2, 3]$.

Figure 5.3 shows the kinetic, magnetic and total energy dissipation rates *v.s.* time for $Pm = 1, 1/4, 1/16, 1/64$. It can be seen that energy loss is primarily due to Ohmic dissipation, in agreement with previous studies for the regime of moderate and small Pm (cf. Brandenburg (2011b)). The decrease of $\nu\|\omega\|^2$ is not quite linear with Pm , but nonetheless appears to accelerate as Pm is decreased. This implies that the simulations have approached the regime of maximal enstrophy (more details later). The time taken for each kinetic, magnetic and total energy dissipation rate to achieve its maximum increases, a result consistent with the results discussed in §5.5 for the case $Pm = 1$ when $\nu = \mu$ is decreased. Another feature in agreement with these results is the decrease of the peak of the total energy dissipation rate as Pm is decreased. Note,

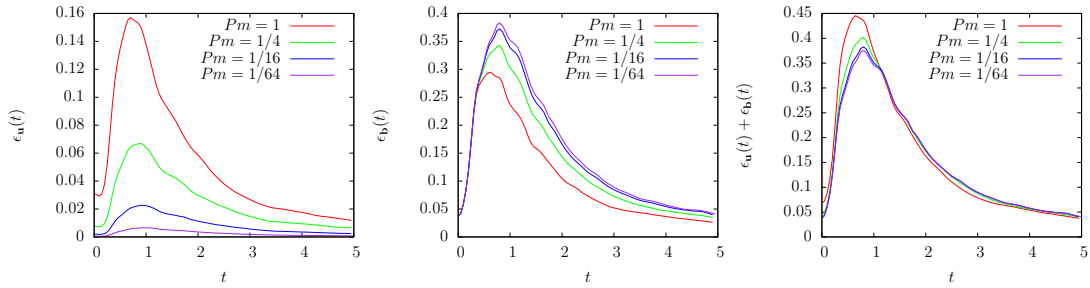


Figure 5.3: Kinetic (left), magnetic (centre) and total (right) energy dissipation rates v.s. time for the simulations with $Pm = 1, 1/4, 1/16, 1/64$. These correspond to $\nu = 8 \times 10^{-4}, 2 \times 10^{-4}, 5 \times 10^{-5}$ and 1.25×10^{-5} respectively while μ is held at 8×10^{-4} .

however, that for the present case, this peak decreases toward a positive limit (which is the maximum of $\mu\|j\|^2$) because μ is fixed. The vanishing of kinetic energy dissipation in the limit $Pm \rightarrow 0$ partly justifies the numerical approach of Dritschel & Tobias (2012), who simulated 2D MHD turbulence at low Pm using a conservative numerical scheme for the vorticity. Given strong support for solution regularity discussed below, this justification could be considered complete.

The evolution of the kinetic, magnetic and total energy dissipation rates for $Pm = 1, 4, 16, 64$ is shown in figure 5.4. It can be seen that Ohmic dissipation is greater than its viscous counterpart for the case $Pm = 1$ only. The latter overtakes the former for $Pm = 4$ and becomes dominant for $Pm > 4$. Like the cases $Pm \leq 1$, the time of each maximum dissipation rate increases slowly as Pm is increased. Furthermore, the peak of the total energy dissipation rate decreases (presumably towards a positive limit, which is the maximum of $\nu\|\omega\|^2$) as Pm is increased. An interesting behaviour of $\mu\|j\|^2$ is that it decreases quite rapidly as Pm is increased from unity. The decrease is less rapid (approximately like $Pm^{-0.6}$, more detail below) than that of $\nu\|\omega\|^2$ in the previous case ($Pm \leq 1$) when Pm is decreased from unity. This means that a much wider range of Pm is required to access the regime of maximal $\|j\|^2$ if $\|j\|^2$ is to remain bounded in the limit $Pm \rightarrow \infty$ (a behaviour suggested by further numerical results on the issue of regularity, see below).

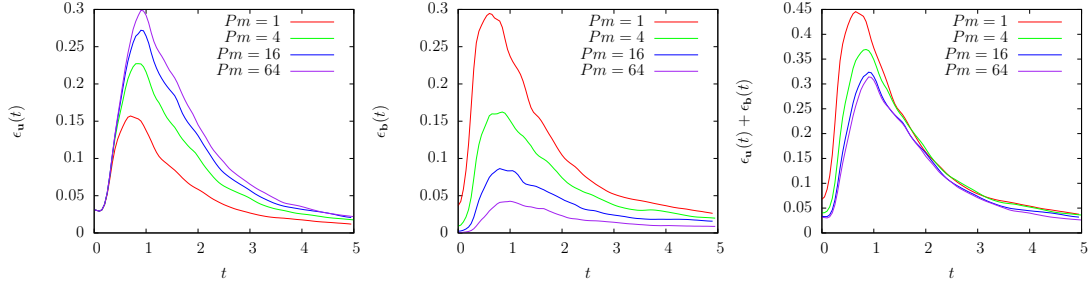


Figure 5.4: Kinetic (left), magnetic (center) and total (right) energy dissipation rates *v.s.* time for the simulations with $Pm = 1, 4, 16, 64$. These correspond to $\mu = 8 \times 10^{-4}$, 2×10^{-4} , 5×10^{-5} and 1.25×10^{-5} respectively while ν is held at 8×10^{-4} .

In passing, it is worth noting that for the range of Pm under consideration, the ratio of kinetic-to-magnetic energy dissipation rates has an apparent power-law behaviour. Figure 5.5 shows the ratio of the maximum of $\nu\|\omega\|^2$ to that of $\mu\|j\|^2$ *v.s.* Pm . For small Pm , this ratio, say R_d , is given by $R_d \approx 0.57Pm^{0.83}$, which is slightly sublinear in Pm . This behaviour of R_d implies a similar behaviour of $\nu\|\omega\|^2$ because $\mu\|j\|^2$ becomes independent of Pm in the small Pm limit. The exponent 0.83 provides a quantitative measure of how close our simulations were to the maximal enstrophy regime. On the other hand, for large Pm , R_d scales approximately as $0.56Pm^{0.62}$. The exponent 0.62 is significantly less than unity, implying that our simulations were still quite far from the expected regime of maximal $\|j\|$, if such a regime exists. For a mechanically forced 3D model, Brandenburg (2011a) found $R_d \approx 0.8Pm^{0.6}$ over six decades of Pm , where his R_d is the ratio of averaged energy dissipation rates. While the analysis in §5.4.1 has provided mathematical proof that the exponent 0.83 in $R_d \approx 0.57Pm^{0.83}$ increases toward unity for lower ranges of Pm , the exponent 0.6 in Brandenburg’s result appears to be robust.

As far as we know, no algorithms for computing the BMO norm have been put forth in the literature. Given the unavailability of such algorithms, we monitored the (slightly stronger) ratio $\|\omega\|_\infty/\|\omega\|$ instead of $\|\omega\|_{BMO}/\|\omega\|$, although the boundedness of the latter is sufficient for regularity when $Pm = 0$. Figure 5.6a shows the evolution of $\|\omega\|_\infty/\|\omega\|$ for $Pm = 1, 1/4, 1/16, 1/64$. As Pm is decreased by a factor of 64,

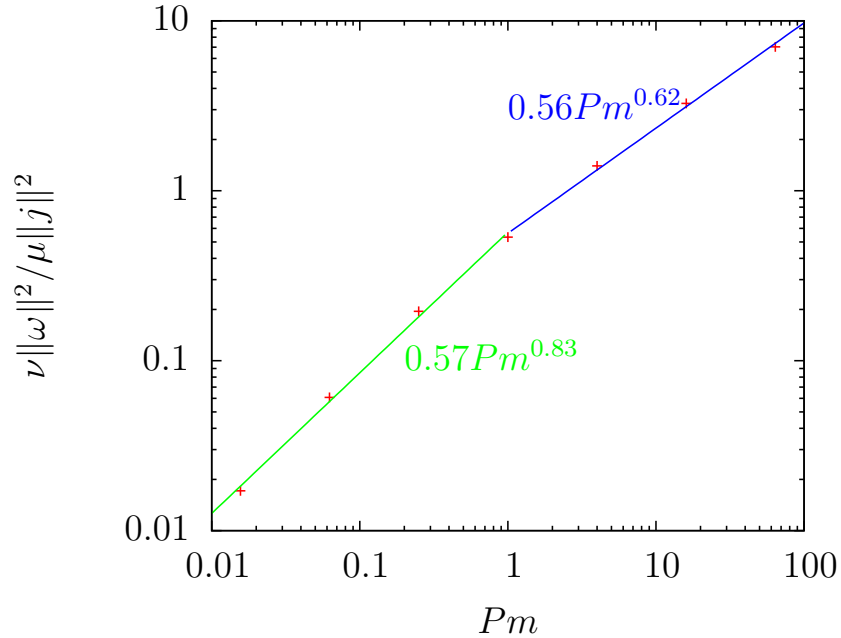


Figure 5.5: Ratio of peak kinetic to peak magnetic energy dissipation rates v.s. magnetic Prandtl number. The straight lines are best fit lines.

$\|\omega\|_\infty/\|\omega\|$ approximately increases by a factor of 2. This can be considered support for the possibility $\|\omega\|_\infty/\|\omega\| < \infty$ in the limit $Pm \rightarrow 0$. A quantitative dependence of $\|\omega\|_\infty/\|\omega\|$ is required to address this possibility, and hence the issue of regularity for $Pm = 0$, but is not possible by the present set of simulations without undermining the Reynolds number. For comparison, we have included figure 5.6b, which describes the evolution of $\|\omega\|_\infty/\|\omega\|$ for the cases $Pm = 1, 4, 16, 64$. It will be seen shortly that $\|\omega\|_\infty/\|\omega\|$ and $\|\nabla\mathbf{u}\|_\infty/\|\omega\|$ are virtually the same for these cases.

With regard to the issue of regularity for the case $Pm = \infty$, we have obtained evidence as strong as figure 5.6a for the case $Pm = 0$. Figure 5.7b described the evolution of the ratio $\|\nabla\mathbf{u}\|/\|\omega\|$ for $Pm = 1, 4, 16, 64$. As Pm is increased from unity to 64, this ratio approximately increases twofold, thereby suggesting the possibility $\|\nabla\mathbf{u}\|_\infty/\|\omega\| < \infty$ in the limit $Pm \rightarrow \infty$. Note that no appreciable discrepancies between $\|\nabla\mathbf{u}\|/\|\omega\|$ and $\|\omega\|_\infty/\|\omega\|$ can be observed (cf. figure 5.6). This makes sense since $\|\nabla\mathbf{u}\|_\infty$ and $\|\omega\|$ are not expected to differ by much, although the fields $|\omega|$ and

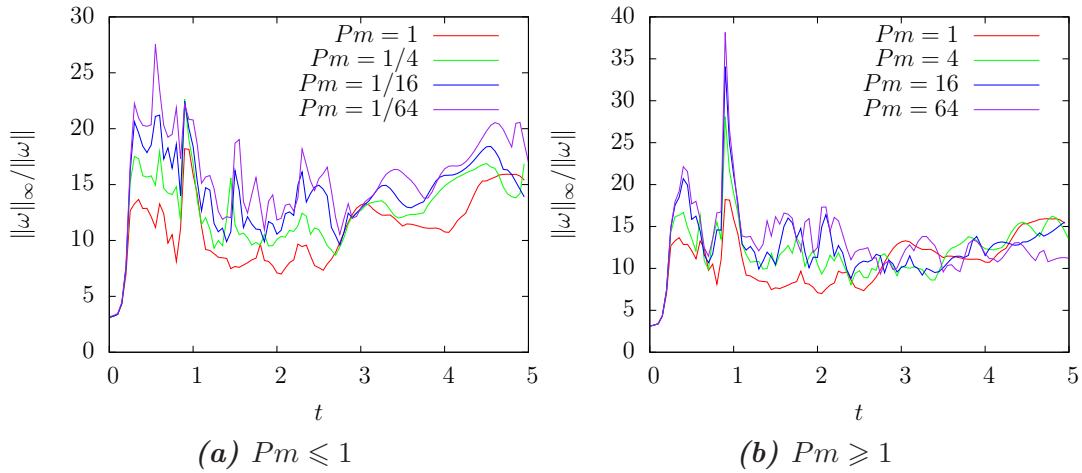


Figure 5.6: $\|\omega\|_\infty$ v.s. time for $Pm = 1, 1/4, 1/16, 1/64$ (a) and for $Pm = 1, 4, 16, 64$ (b)

$|\nabla\mathbf{u}|$ may disagree substantially locally. Interestingly, vortex and velocity gradient ‘filaments’ look alike (see below), suggesting that $|\nabla\mathbf{u}| \approx |\omega|$ at large values.

Figure 5.8b shows the plots of $\|j\|_\infty/\|j\|$ v.s. time for $Pm = 1, 4, 16, 64$. It can be seen over the range $Pm \in [1, 64]$, $\|j\|_\infty/\|j\|$ increases approximately threefold. This provides slightly weaker support for regularity than the milder behaviour of $\|\nabla\mathbf{u}\|_\infty/\|\omega\|$ (with twofold increase) discussed above. For comparison, figure 5.8a shows a relatively much weaker response of $\|j\|_\infty/\|j\|$ to the decrease of Pm from unity to $1/64$.

The distributions of large value of the fields $|\omega|$, $|j|$ and $|\nabla\mathbf{u}|$ are of interest as these distributions provide a sense of the magnitude of the ratios discussed above. Figures 5.9, 5.10 and 5.11 show the images of $|\omega|$ for $|\omega| \geq 2\|\omega\|$, $|j|$ for $|j| \geq 2\|j\|$ and $|\nabla\mathbf{u}|$ for $|\nabla\mathbf{u}| \geq 2\|\omega\|$, for the cases $Pm = 1/64$ and $Pm = 64$ at $t = 1.0$. This time is shortly after the energy dissipation in each case becomes greatest. For $Pm = 1/64$, the vortex and current filamentary structures are comparable in magnitude and density. On the other hand, for $Pm = 64$, these ‘filaments’ are significantly less dense and are an order of magnitude greater than their $Pm = 1/64$ -counterparts. In any case, at both magnetic Prandtl numbers vortex filaments are qualitatively the same (this is true for velocity gradient filaments, whose image for the case $Pm = 1/64$ is omitted).

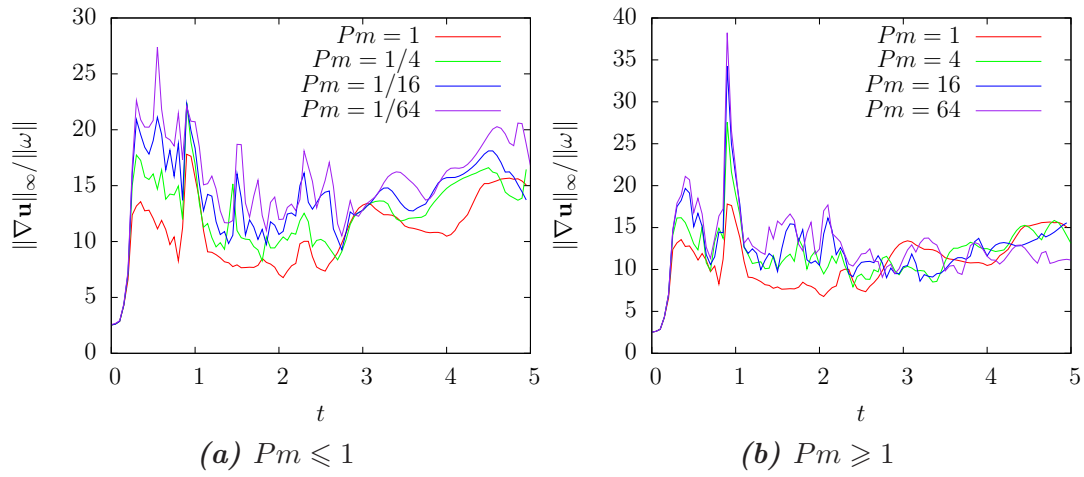


Figure 5.7: $\|\nabla\mathbf{u}\|_\infty/\|\omega\|$ v.s. time for $Pm = 1, 1/4, 1/16, 1/64$ (a) and for $Pm = 1, 4, 16, 64$ (b)

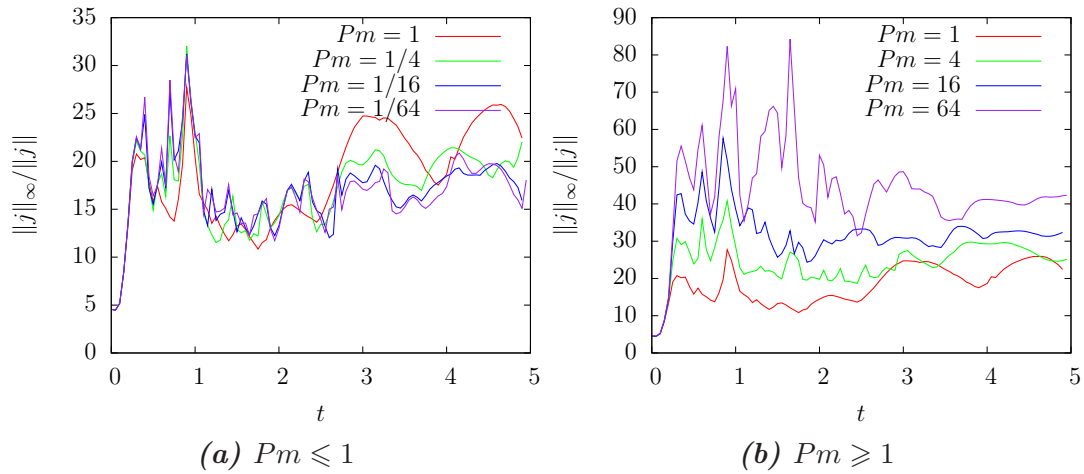


Figure 5.8: $\|j\|_\infty/\|j\|$ v.s. time for $Pm = 1, 1/4, 1/16, 1/64$ (a) and for $Pm = 1, 4, 16, 64$ (b)

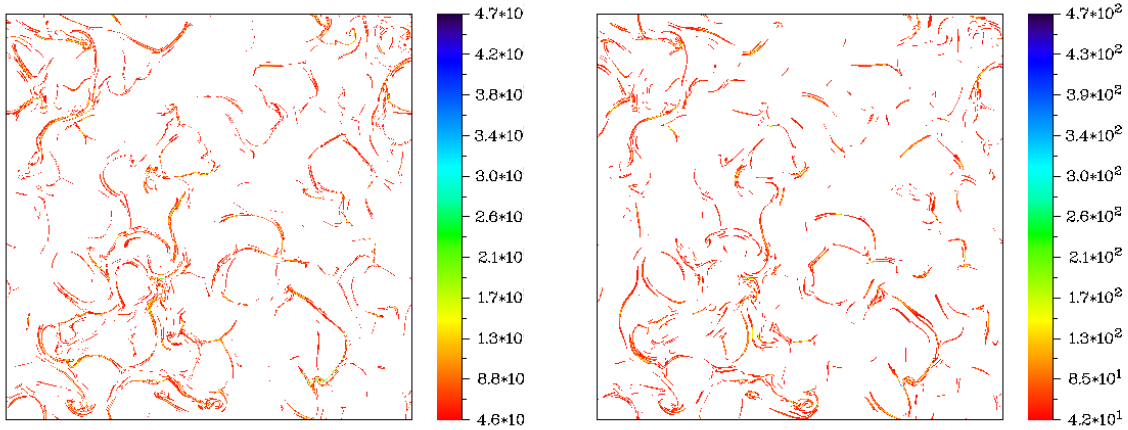


Figure 5.9: Vorticity (a) and current (b) fields at $t = 1$ for $Pm = 1/64$. The images are for $|\omega| \geq 2\|\omega\| \approx 4.6 \times 10^1$ and $|j| \geq 2\|j\| \approx 4.2 \times 10^1$.

So the change in $|\omega|$ (and $|\nabla\mathbf{u}|$) is relatively mild over a significantly wide range of Pm . The heavy population of vortex and velocity gradient filaments is indicative of moderate values of $\|\omega\|_\infty/\|\omega\|$ and $\|\nabla\mathbf{u}\|/\|\omega\|$. On the other hand, over the same range of Pm , $|j|$ can be seen to change significantly. Nonetheless, this poses no risk to the possibility of regularity, given the mild behaviour of $\|j\|_\infty/\|j\|$ (and of $\|\nabla\mathbf{u}\|_\infty/\|\omega\|$). An interesting feature to note is that the images of $|\omega|$ and $|\nabla\mathbf{u}|$ for $Pm = 64$ differ only in minute details.

At $t = 3$ the turbulence can be considered fully developed. Figures 5.12, 5.13 and 5.14 are similar to figures 5.9, 5.10 and 5.11, albeit at $t = 3$, and are presented here for comparison. Somewhat surprisingly, over the time interval $[1, 3]$, $\|\omega\|_\infty$, $\|\nabla\mathbf{u}\|_\infty$ and $\|j\|_\infty$ decrease much more rapidly than their L^2 -norm counterparts as the scales of the figures indicate (see also figures 5.6, 5.7 and 5.8). This is in sharp contrast to 2DNS turbulence, for which $\|\omega\|$ decays much more rapidly than $\|\omega\|_\infty$ throughout the course of its evolution (Dritschel *et al.*, 2007). While it is fairly easy to understand why $\|\omega\|_\infty$ is better conserved than $\|\omega\|$ in 2DNS turbulence, we have no obvious explanation for the above observation in the present case.

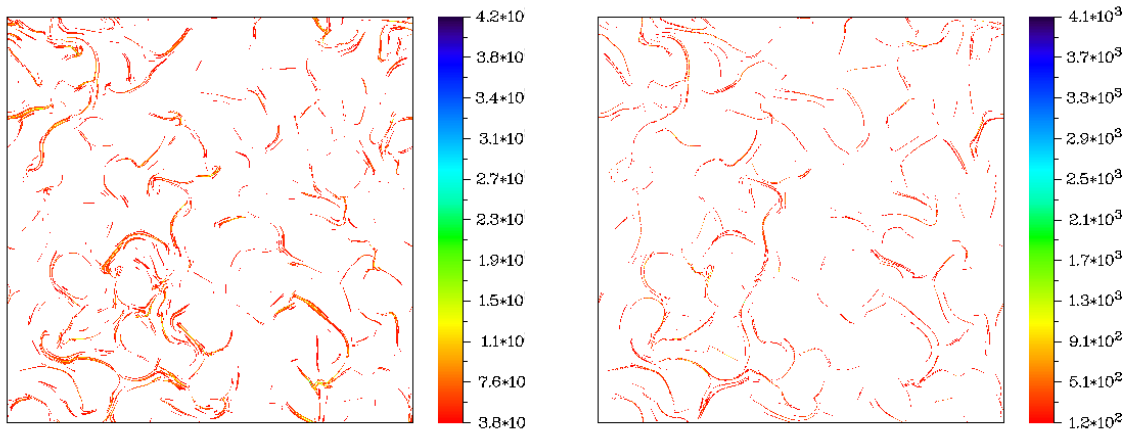


Figure 5.10: Vorticity (a) and current (b) fields at $t = 1$ for $Pm = 64$. The images are for $|\omega| \geq 2\|\omega\| \approx 3.8 \times 10^1$ and $|j| \geq 2\|j\| \approx 1.2 \times 10^2$.

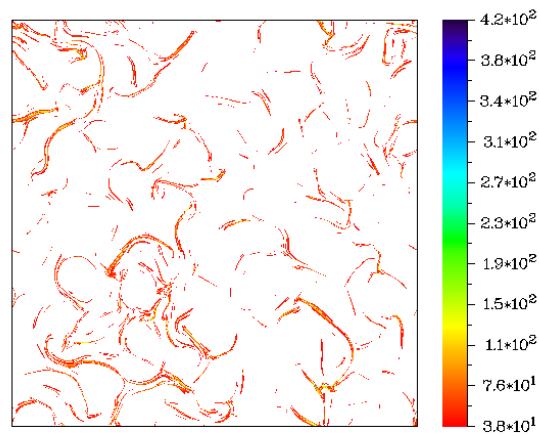


Figure 5.11: Velocity gradient field at $t = 1$ for $Pm = 64$. The image is for $|\nabla \mathbf{u}| \geq 2\|\omega\| \approx 3.8 \times 10^1$

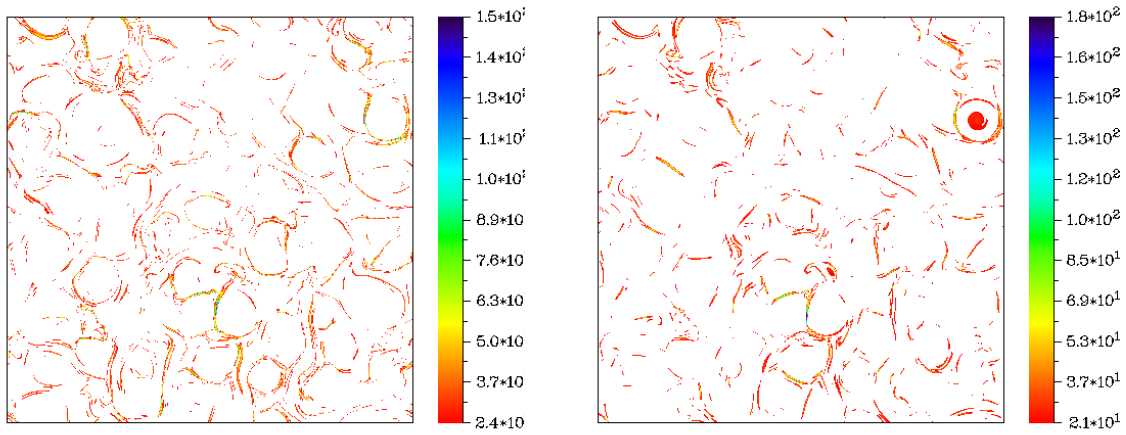


Figure 5.12: Vorticity (a) and current (b) fields at $t = 3$ for $Pm = 1/64$. The images are for $|\omega| \geq 2\|\omega\| \approx 2.4 \times 10^1$ and $|j| \geq 2\|j\| \approx 2.1 \times 10^1$.

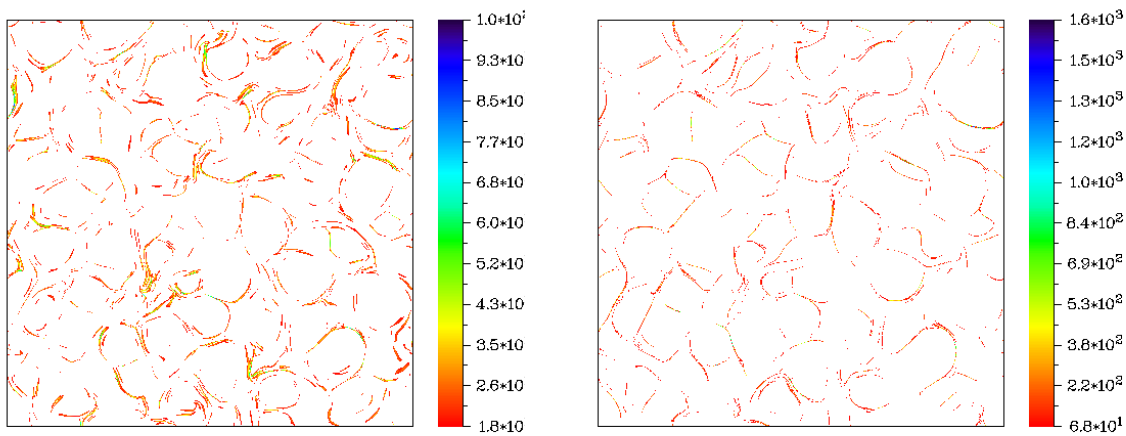


Figure 5.13: Vorticity (a) and current (b) fields at $t = 3$ for $Pm = 64$. The images are for $|\omega| \geq 2\|\omega\| \approx 1.8 \times 10^1$ and $|j| \geq 2\|j\| \approx 6.8 \times 10^1$.

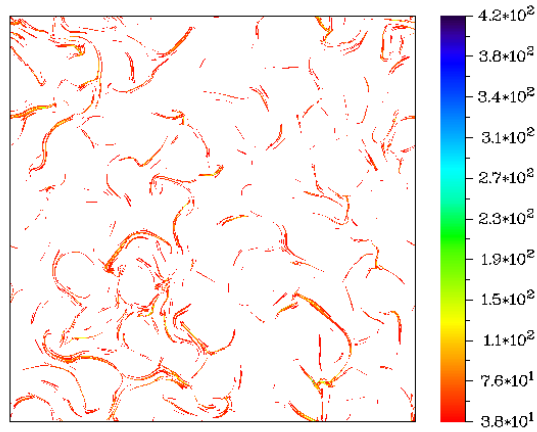


Figure 5.14: Velocity gradient field at $t = 3$ for $Pm = 64$. The image is for $|\nabla \mathbf{u}| \geq 2\|\omega\| \approx 1.8 \times 10^1$

5.5 Dynamical behaviour in the moderate and strong advection regimes

In three dimensions, the usual vortex-stretching mechanism provides a route for the downscale transfer of kinetic energy. However in two dimensions this mechanism is no longer present, so dynamo action is the only way for kinetic energy to be transferred downscale. However, as described in §5.2, dynamo can only deplete the mechanical modes, so for modes in the inertial range, the only way they can be replenished is through anti-dynamo, which subsequently transfers magnetic energy back upscale. This could be expected to lead to a cycle of dynamo and anti-dynamo, supposedly resulting in saturation and a reduction of the downscale transfer of energy. In line with the arguments from previous chapters, this could be expected to lead to shallower spectra. It is interesting to note that Kraichnan and Iroshnikov suggested something similar (Kraichnan, 1965; Iroshnikov, 1964) on the basis that Alfvén waves reduce the downscale transfer of energy and result in a shallower $k^{-3/2}$ energy spectrum.

One outcome of all of this is that the dynamics of the system could be very sensitive to the initial conditions, in particular the initial ratio of magnetic-to-kinetic energy, here

denoted by $r_0 = r(t = 0)$. When r_0 is large, with little initial kinetic energy, advection can be expected to be very weak, and any downscale transfer very slow. This is caused by the lack of energy in the magnetic modes, meaning that strong anti-dynamo action is necessary to replenish them, thus greatly retarding the downscale transfer of energy. In this case, the system may be expected to behave almost linearly, possibly with zero energy dissipation in the inviscid limit.

When r_0 is small, on the other hand, there is initially very strong advection caused by the relatively large amount of kinetic energy. This could be expected to drive a very strong downscale flux of both kinetic and magnetic energy. In particular, strong dynamo could dump a large amount of magnetic energy in the inertial range, while the strength of the kinetic energy means that anti-dynamo could be very weak. This could presumably lead to the build-up of small scales, with the possibility of finite-time singularity and non-zero energy dissipation in the inviscid limit.

The next section §5.5.1 is based on the paper (Blackbourn & Tran, 2012), while §5.5.2 is based on (Blackbourn & Tran, 2013).

5.5.1 Moderate advection regime

In order to test the dependence of the behaviour of the 2D MHD system on r_0 , a number of simulations were run. The vorticity field was first initialised in the wavenumber shell $[5, 7]$ while the current was initialised in the shell $[4, 6]$, with each mode given a random phase with equal energy. These initial fields were then scaled for each value of r_0 so that the total energy was unity. Figure 5.15 shows the initial vorticity and magnetic potential fields. For each value of r_0 taking values in $1/16$, $1/4$, 1 , 4 and 16 , three simulations with resolutions 1024×1024 , 2048×2048 and 4096×4096 were run at unity magnetic Prandtl number, with $\nu = \mu = 7.94 \times 10^{-4}$, 3.15×10^{-4} and 1.24×10^{-4} respectively. The viscosity ν and magnetic diffusivity μ were decreased by a factor of $2^{4/3}$ when the resolution was doubled, in line with the arguments presented

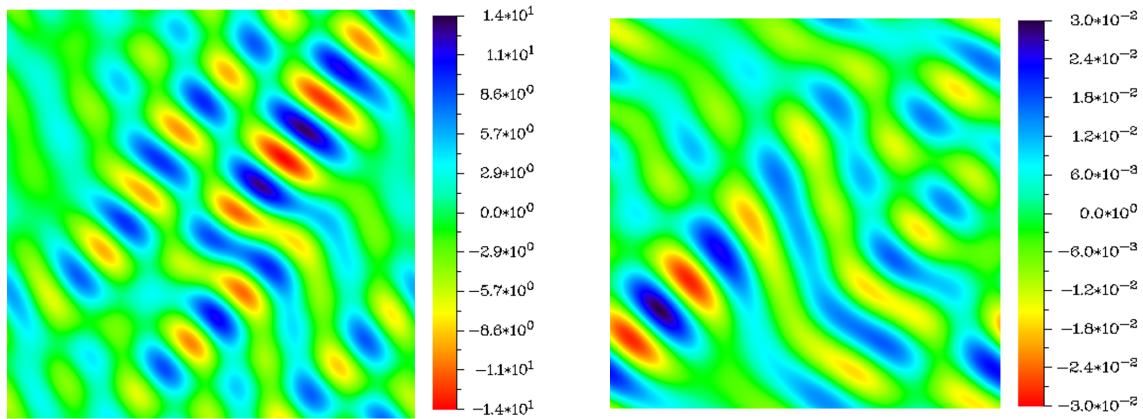


Figure 5.15: Vorticity (left) and magnetic potential (right) initial condition fields.

at the end of §3.2.2 and the estimate for the number of degrees of freedom derived in §5.3. For the five simulations at the highest resolution, the kinetic and magnetic Reynolds numbers, Re and Rm respectively, defined in equations (5.29) and (5.30), are approximately 68,000 at the time of maximum dissipation.

The evolution of the energy is shown in figure 5.16 which shows $E_{\mathbf{u}}(t)$, $E_{\mathbf{b}}(t)$ and $E_{\mathbf{u}}(t) + E_{\mathbf{b}}(t)$ versus t for the five sets of simulations described in the preceding paragraph and presented in decreasing order of r_0 . The blue, green and red lines represent the low-, middle- and high-resolution simulations respectively.

Figure 5.17 shows the ratio of magnetic-to-kinetic energy, $n(t)$, for the highest resolution runs. It can be seen that in the early stage, dynamo action takes place briefly for all r_0 , including $r_0 = 16$ where there is predominant magnetic energy), followed by anti-dynamo action. The cycle of dynamo and anti-dynamo then seems to repeat itself, more prominently for greater r_0 , as can be recognised from the wavy appearance of the curves of $E_{\mathbf{b}}(t)$ and $E_{\mathbf{u}}(t)$. This is probably a signature of Alfvén waves, a detailed knowledge of which seems crucial for understanding MHD turbulence but is nonetheless not within the scope of this study. In all cases, dynamo saturation occurs with $r \geq 2$ after a few cycles. This is consistent with a finding by Biskamp & Welter (1989) for $r_0 = 1$, where dynamo saturates at $r \approx 2$.

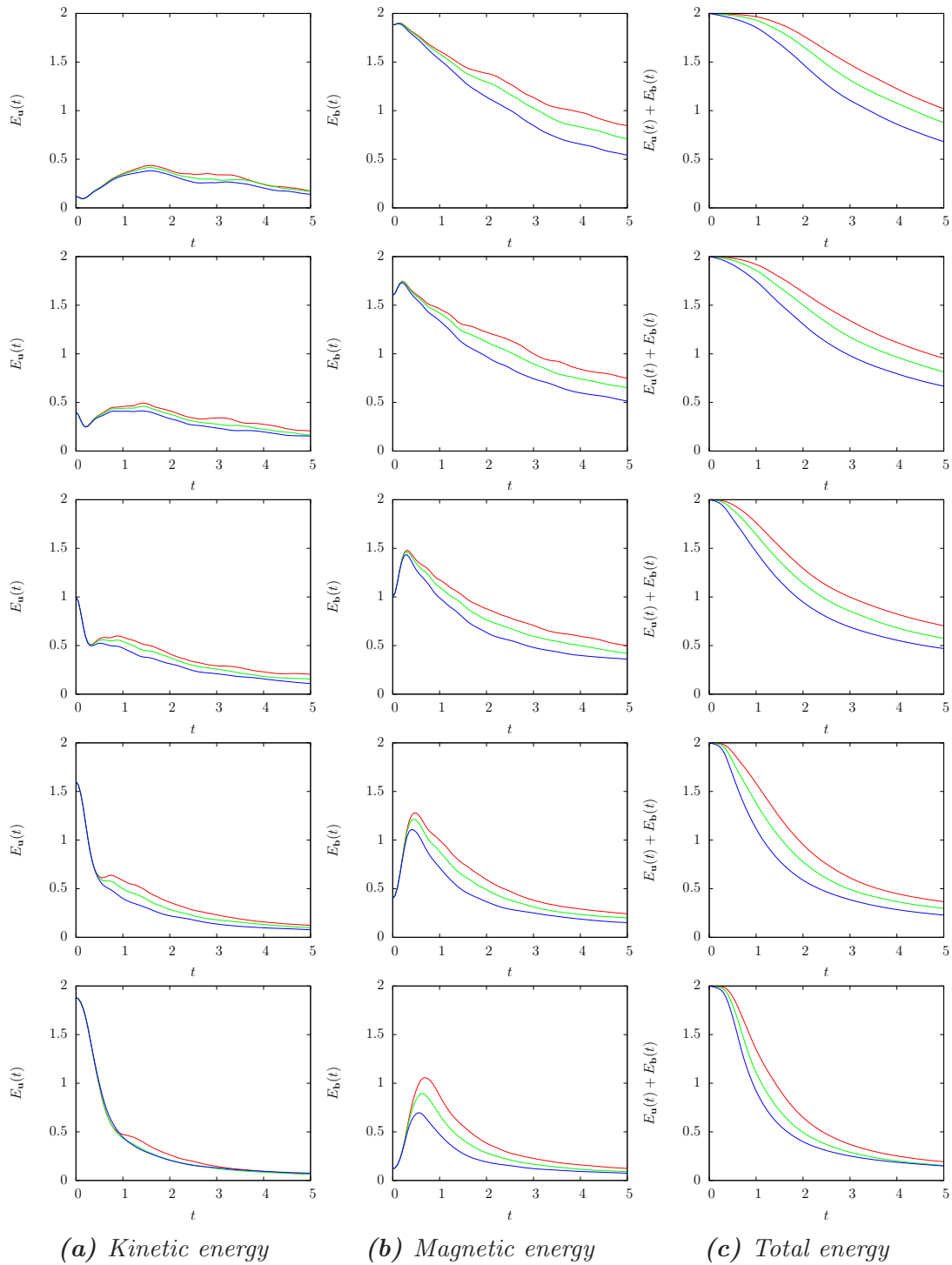


Figure 5.16: Kinetic (a), magnetic (b) and total (c) energy v.s. time for numerical simulations with resolutions 1024×1024 (blue), 2048×2048 (green) and 4096×4095 (red). The rows are arranged in decreasing order of the initial magnetic-to-kinetic energy ratios ($r_0 = 16, 4, 1, 1/4, 1/16$).

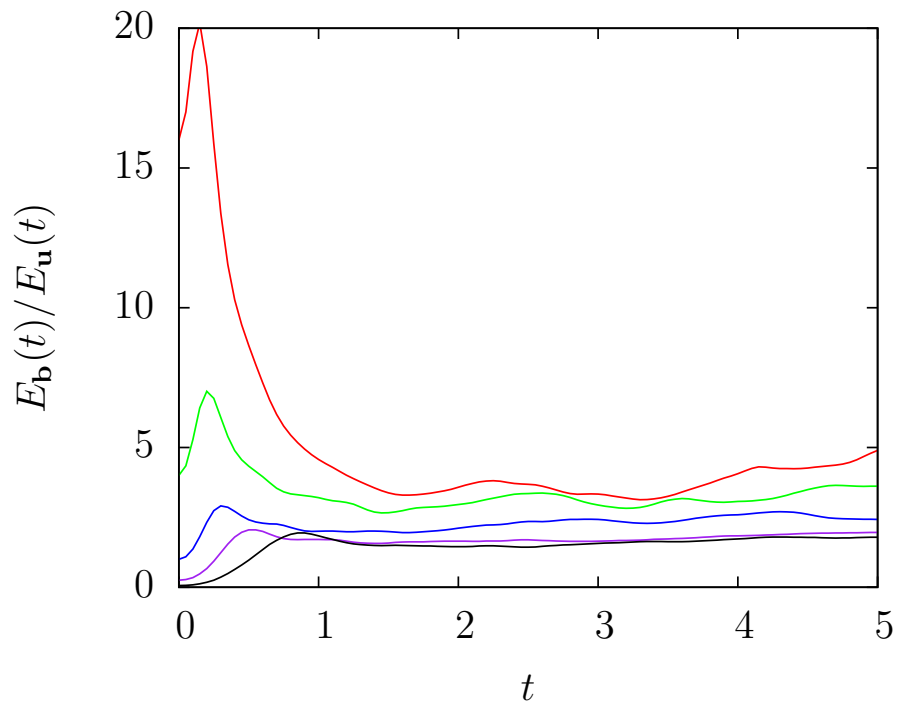


Figure 5.17: Magnetic-to-kinetic energy ratio $r(t)$ v.s. t corresponding to the highest resolution simulations of figure 5.16. After the time of maximum dissipation, r ranges approximately from 2, for $r_0 = 1/16$, to 5 for $r_0 = 16$. Here $r_0 = 16, 4, 1, 1/4, 1/16$ corresponds to the red, green, blue, purple and black lines respectively.

Figure 5.18 shows $\epsilon_{\mathbf{u}}(t)$ (a), $\epsilon_{\mathbf{b}}(t)$ (b) and $\epsilon(t)$ (c) versus t for the above five sets of simulations, laid out in the same decreasing order of r_0 as figure 5.16. It can be seen across the board that energy loss through Ohmic dissipation is more than that through viscous dissipation, in agreement with previous studies for $Pm = 1$ by Haugen *et al.* (2003), for $Pm \leq 0.1$ by Brandenburg (2011*b*) and for $Pm = 1$ in §5.4.2. However, this is due mainly to the fact that the turbulence has more magnetic than kinetic energy ($r \geq 2$) and does not necessarily imply a significant difference in the level of excitation of the mechanical and magnetic small scales.

In fact, for all r_0 and $t \geq T$, it can be readily deduced from figure 5.19 that

$$\frac{\epsilon_{\mathbf{u}}}{E_{\mathbf{u}}} \geq \frac{\epsilon_{\mathbf{b}}}{E_{\mathbf{b}}}. \quad (5.50)$$

This implies that the exponential dissipation rate of magnetic energy is not greater than that of kinetic energy. Note that this behaviour may not hold for all Pm , especially in the regime $Pm \ll 1$. The correlation between dynamo and direct magnetic energy flux manifests itself through the fact that a stronger dynamo (during the early stages) is accompanied by greater $\epsilon_{\mathbf{b}}$, which peaks shortly after $E_{\mathbf{b}}$ achieves its global maximum (see the cases $r_0 \leq 1$ of figures 5.16 and 5.17). An interesting feature is the more rapid decrease of ϵ_T for smaller r_0 when the resolution is increased. On this basis, one can anticipate that although ϵ_T is greater for smaller r_0 at the present resolution of 4096×4096 , it may not necessarily be so at moderately higher resolutions. The interpretation is that dynamo is very much an inertial-range phenomenon and that the turbulence is not necessarily more dissipative in the presence of a stronger dynamo.

The decrease of ϵ_T , as well as of the global maxima of $\epsilon_{\mathbf{u}}(t)$ and $\epsilon_{\mathbf{b}}(t)$, as ν is decreased, is accompanied by an increase in T . This allows the possibility of the divergence of T and convergence of ϵ_T in the limit $\nu \rightarrow 0$. However, it is not known whether ϵ_T asymptotically vanishes or tends to a positive constant. This uncertainty can be appreciated by the fact that the ‘tail’ of $\epsilon(t)$ is higher for smaller ν . In any case, the

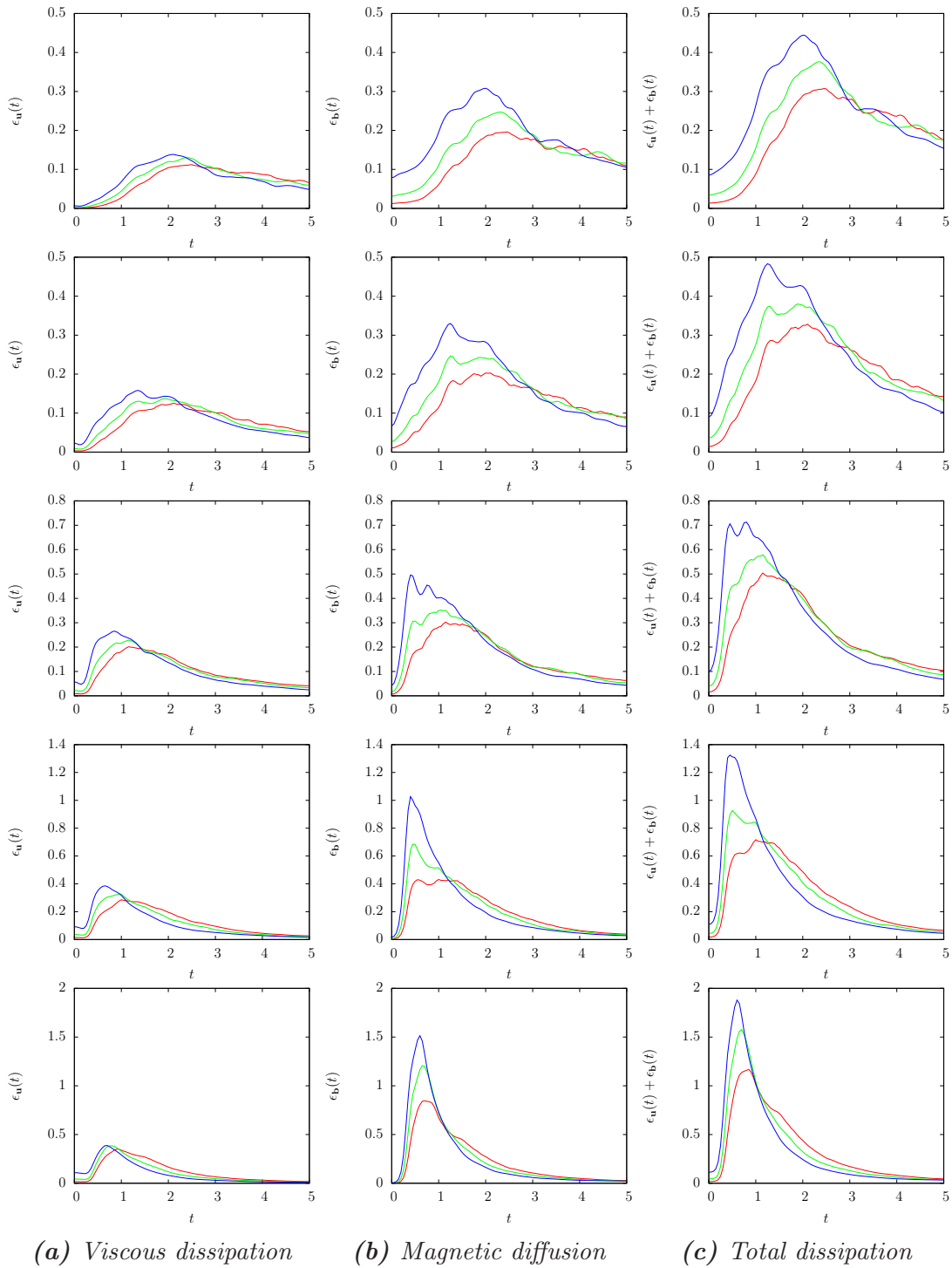


Figure 5.18: Kinetic (a), magnetic (b) and total (c) energy dissipation rates v.s. t for the five sets of simulations described in figure 5.16. Again, the blue, green and red curves correspond to the lower, intermediate and higher resolutions, respectively.

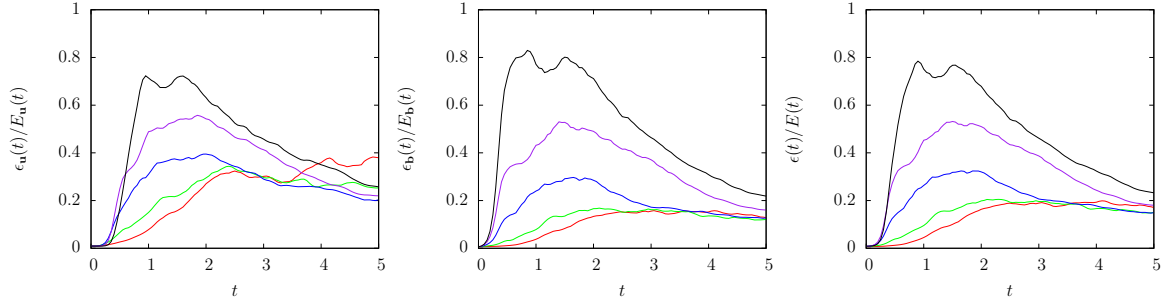


Figure 5.19: Exponential energy dissipation rates $\epsilon_{\mathbf{u}}/E_{\mathbf{u}}$, $\epsilon_{\mathbf{b}}/E_{\mathbf{b}}$ and ϵ/E v.s. t for the five highest-resolution runs.

possible dependence of T and ϵ_T on ν in the limit of small ν can be seen to be weak, probably in some logarithmic manner in ν .

Figure 5.20 shows the kinetic energy spectrum $\mathcal{E}_{\mathbf{u}}(k)$ (a), magnetic energy spectrum $\mathcal{E}_{\mathbf{b}}$ (b) and total energy spectrum $\mathcal{E}(k)$ (c) at $t = 3$ for the above series of simulations. The blue, green and red lines correspond to the lowest-, middle- and highest-resolution runs, respectively. Quite expectedly, within the inertial range (which approximately extends over one decade of wavenumbers for the highest-resolution case), these spectra become shallower for higher resolutions. However, their asymptotic behaviour, especially that of $\mathcal{E}(k)$, as can be inferred from their shallowing tendency, may not be understood in terms of existing theories. At the highest resolution and for all r_0 , $\mathcal{E}_{\mathbf{u}}(k)$ is significantly shallower than $k^{-3/2}$ and clearly shallower than $\mathcal{E}_{\mathbf{b}}(k)$, which is slightly shallower than $k^{-3/2}$ for $r_0 = 1/4, 1/16$ and can be expected to become shallower than $k^{-3/2}$ for $r_0 = 1, 4, 16$ at moderately higher resolutions. Hence, it is plausible that $\mathcal{E}(k)$ is asymptotically shallower than the IK spectrum. The main questions raised are how much shallower $\mathcal{E}(k)$ can become and whether or not its asymptotic slope is universal. In §5.5.2 we will examine this question for the case $r_0 \rightarrow 0$.

In passing, it is noted that the lowest wavenumber $k = 1$ is more strongly excited mechanically than magnetically, even for the case $r_0 = 16$ having predominant magnetic energy throughout: $r(t) \geq 4$. Given that the magnetic energy reservoir is closer to $k = 1$ than the kinetic energy reservoir, one can infer that the inverse transfer of $\langle a^2 \rangle$

is relatively weak, much weaker than the net inverse flow of $E_{\mathbf{u}}$ (net effect of inverse kinetic energy transfer by the vorticity advection term and direct total energy transfer). Hence, the concern over finite-size effects in numerical simulations of the present case is relatively minor compared with that of 2DNS turbulence.

Results from the numerical simulations suggest a weak dependence of the energy dissipation rate $\epsilon(t)$ on the viscosity ν . In particular, as ν is decreased, the time $t = T$ of the peak energy dissipation rate $\epsilon_T = \epsilon(T)$ increases while ϵ_T decreases. Both the increase of T and decrease of ϵ_T appear to be slow, probably logarithmic in ν in its small limit. This suggests the possibility of slow divergence of T and (equally slow) convergence of ϵ_T . However, it is not known whether ϵ_T would tend to a non-zero constant. Much higher resolutions than currently available to the present study are required to convincingly address this issue (partially resolved in next section).

5.5.2 Strong advection Regime

As seen in the previous section, the parameter $r_0 = E_{\mathbf{b}}(0)/E_{\mathbf{u}}(0)$ plays a very important role in the dynamics of MHD turbulence. While the previous study covered a moderate range of r_0 around unity, a couple of further studies were carried out to examine the behaviour in the limit $r_0 \rightarrow 0$, (the strong advection limit). This allows us to examine in detail the dependence of the inertial-range dynamics and scaling laws on r_0 in the strong advection regime, i.e. $r_0 \ll 1$.

Unity initial total energy

An initial set of simulations were carried out with $r_0 = 1/4, 1/16, 1/64, 1/256$ and $1/1024$ with unity total energy. For each value of r_0 , four simulations at resolutions $1024 \times 1024, 2048 \times 2048, 4096 \times 4096$ and 8192×8192 were run, with $\nu = \mu$ taking values $9.60 \times 10^{-4}, 3.81 \times 10^{-4}, 1.51 \times 10^{-4}$ and 6.00×10^{-5} respectively, which again represents a decrease of $2^{-4/3}$ when the resolution is doubled, for the reasons given in

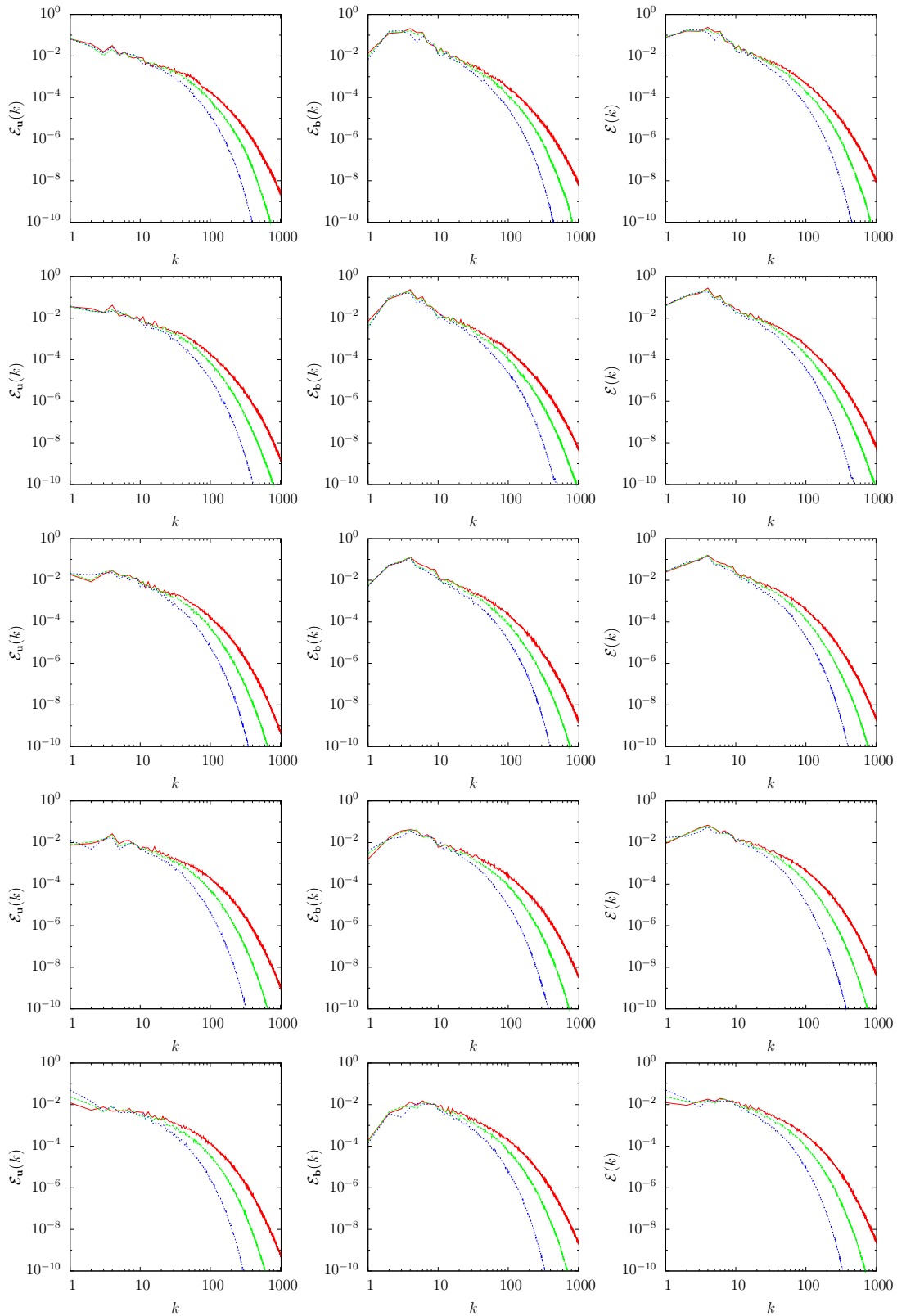


Figure 5.20: Kinetic (a), magnetic (b) and total (c) energy spectra v.s. k for the five sets of simulations described in figure 5.16. Again, the blue, green and red curves correspond to the lower, intermediate and higher resolutions, respectively.

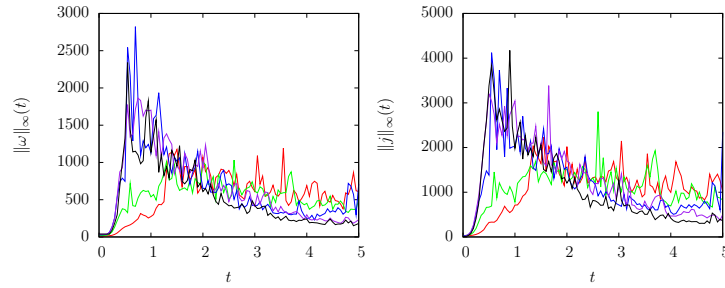


Figure 5.21: Maximum vorticity $\|\omega\|_\infty$ and current $\|j\|_\infty$ v.s. t for the five highest-resolution runs. $r_0 = 16, 4, 1, 1/4$ and $1/16$ represented by red, green, blue, purple and black lines respectively.

the previous sections. The choice of $Pm = 1$ was mainly for computational expediency rather than physical relevance.

Figure 5.22 shows the evolution of the energy components $E_{\mathbf{u}}(t)$ and $E_{\mathbf{b}}(t)$ and their ratio $r(t) = E_{\mathbf{b}}/E_{\mathbf{u}}$. For all simulations, strong dynamo action is a prominent dynamical feature during the early stage. For $r_0 = 1/4, 1/16$, $r(t)$ becomes quasi-steady upon attaining values about 2.0, in agreement with our previous results. From the highest resolution runs (least diffusive effects), it can be seen that (maximal) dynamo amplification of magnetic energy is approximately by threefold for $r_0 = 1/4$, eightfold for $r_0 = 1/16$, twentyfold for $r_0 = 1/64$, fortyfold for $r_0 = 1/256$ and fiftyfold for $r_0 = 1/1024$. The case $r_0 = 1/64$ appears critical, in the sense that dynamo action is barely able to give rise to a parity of $E_{\mathbf{u}}(t)$ and $E_{\mathbf{b}}(t)$ (at $t \approx 1.7$). Note that the conservation of $\langle a^2 \rangle$ imposes a stiff constraint on magnetic energy amplification in the vicinity of the magnetic reservoir, but in principle allowing for this amplification to proceed toward smaller scales until saturation. It is not known whether there exists a bound for the ratio r_m/r_0 , where r_m denotes the peak value of $r(t)$, as $r_0 \rightarrow 0$. The numerical results in §5.5.2 suggest a negative answer to this question. In any case, $r(t)$ diminishes in the NS regime. Indeed, figure 5.22 indicates that for $r_0 = 1/64, 1/256$ and $1/1024$ the relation between r_m and r_0 is virtually linear.

The ratio r_m/r_0 is a measure of the strength of dynamo action. As can be seen from

the discussion above, this ratio increases as r_0 is decreased. The asymptotic behaviour of r_m/r_0 in the NS regime (and limit of ideal dynamics) is interesting. This problem is explored in some detail on the basis of the results in §5.5.2.

It is remarkable that the total energy E decays most rapidly for the case $r_0 = 1/64$, where an approximate parity of $E_{\mathbf{u}}(t)$ and $E_{\mathbf{b}}(t)$ is attained for fully developed turbulence. Qualitatively speaking, this parity ensures both effective magnetic stretching and relatively strong anti-dynamo excitation of the mechanical modes in the inertial range, required for optimal dissipation. Towards the NS regime, E becomes better conserved as expected. Also for $r_0 = 1/64$ (and $r_0 = 1/256$), $E_{\mathbf{u}}(t)$ becomes smaller (for $t > 1$) as ν is decreased. This somewhat counter-intuitive behaviour can be understood by noting the relatively strong surge in $E_{\mathbf{b}}(t)$ in response to weaker diffusion.

Figure 5.23 shows the evolution of the energy dissipation rates $\epsilon_{\mathbf{u}}(t)$, $\epsilon_{\mathbf{b}}(t)$ and $\epsilon(t)$. As observed in §5.5.1, for similar but twice as energetic initial fields and for $r_0 = 1/4, 1/16$, each of these rates achieve a smaller maximum at increasingly greater time as ν is decreased. This is no longer the case for lower r_0 . More precisely, when $r_0 = 1/256, 1/1024$ (and sufficiently small ν), each of these rates achieve a greater maximum at increasingly greater time as ν is decreased. This behaviour is consistent with the possibility of positive limiting dissipation rate achievable in infinite time.

The exponential energy dissipation rate (energy dissipation rates per unit energy) $\epsilon_{\mathbf{u}}/E_{\mathbf{u}}$, $\epsilon_{\mathbf{b}}/E_{\mathbf{b}}$ and ϵ/E versus time for the highest resolution runs are plotted in figure 5.24. The case $r_0 = 1/64$ corresponds to optimal dissipation (highest peak of ϵ/E as observed earlier). The rapid decrease of $\epsilon_{\mathbf{u}}/E_{\mathbf{u}}$ toward the strong advection regime is fully expected as kinetic energy is an inviscid invariant of NS turbulence. Given $r \ll 1$, this decrease entails a corresponding decrease in ϵ/E . What is interesting is the increase of $\epsilon_{\mathbf{b}}/E_{\mathbf{b}}$ and its relatively large magnitude, implying an increasingly shallow magnetic energy spectrum in the inertial range.

Figure 5.25 shows the respective kinetic, magnetic and total energy spectra $\mathcal{E}_{\mathbf{u}}(k)$, $\mathcal{E}_{\mathbf{b}}(k)$ and $\mathcal{E}(k)$ at time $t = 2.5$, which is well after the time of peak energy dissipation,

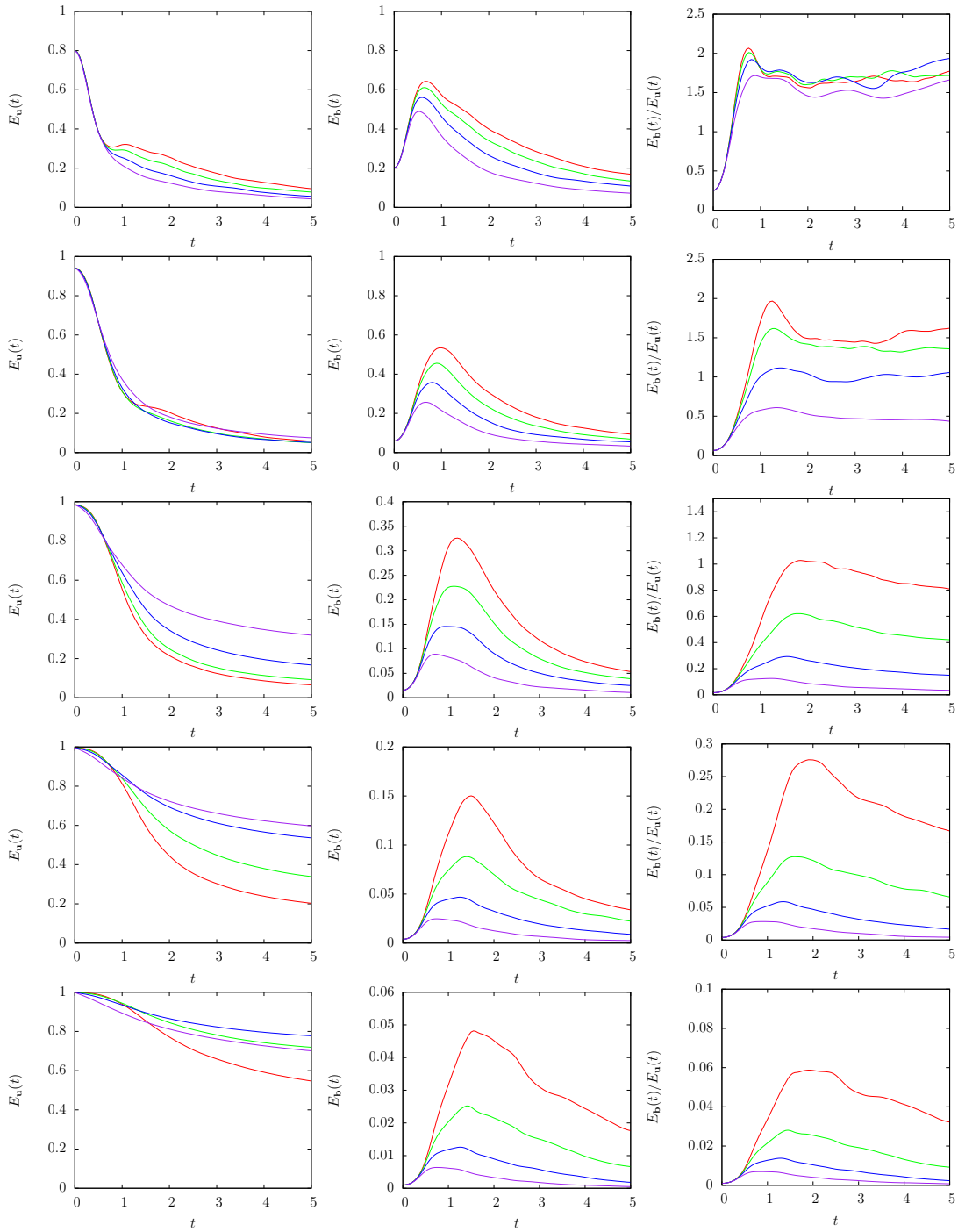


Figure 5.22: Kinetic energy $E_u(t)$, magnetic energy $E_b(t)$ and their ratio $r(t) = E_b/E_u$ v.s. t for numerical simulations with resolutions 1024×1024 (purple), 2048×2048 (blue), 4096×4096 (green) and 8192×8192 (red) and $r_0 = 1/4, 1/16, 1/64, 1/256, 1/1024$. The rows are in decreasing order of r_0 .

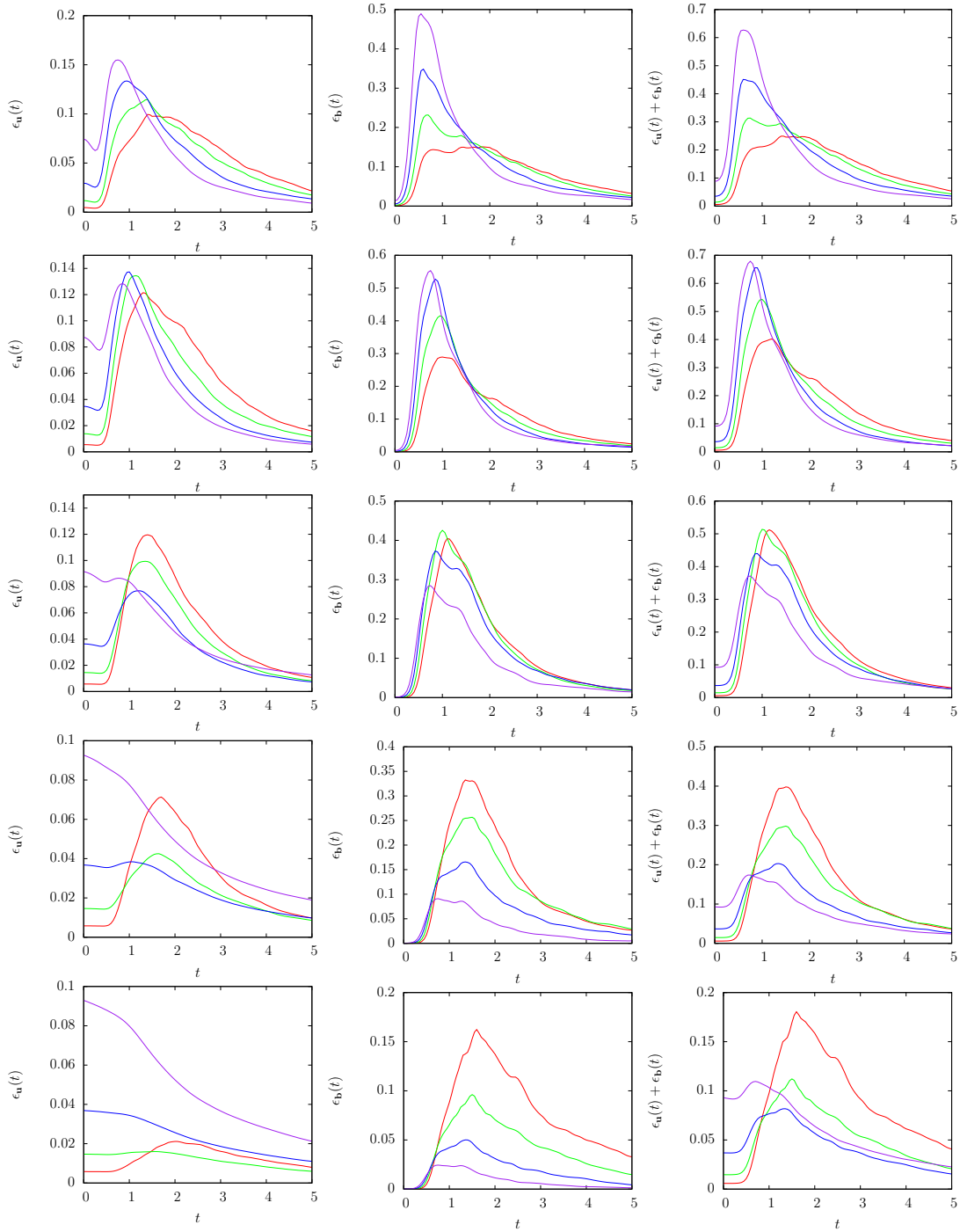


Figure 5.23: Kinetic energy dissipation $\epsilon_u(t)$, magnetic energy dissipation $\epsilon_b(t)$ and total energy dissipation $\epsilon(t)$ for the same set of simulations as described in figure 5.22.

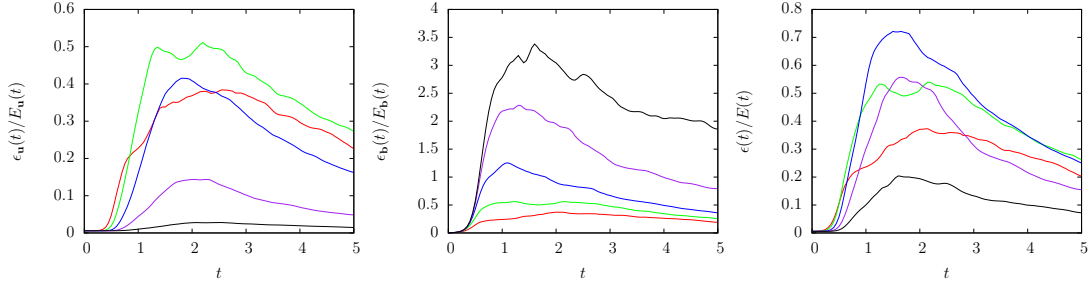


Figure 5.24: Evolution of the exponential energy dissipation rates $\epsilon_{\mathbf{u}}/E_{\mathbf{u}}$, $\epsilon_{\mathbf{b}}/E_{\mathbf{b}}$ and ϵ/E for the highest resolution runs, with $r_0 = 1/4, 1/16, 1/64, 1/256$ and $1/1024$ given by the red, green, blue, purple and black lines respectively.

when the turbulence can be considered fully developed. Across the board, the inertial range becomes shallower for higher resolutions as expected. The kinetic energy reservoir becomes less depleted for lower r_0 as a smaller amount of kinetic energy per unit kinetic energy may be converted. In the energy inertial range of the lower- r_0 cases, $\mathcal{E}_{\mathbf{u}}(k)$ is significantly steeper than k^{-1} , though with a relatively shallower tail due to anti-dynamo excitation. Meanwhile $\mathcal{E}_{\mathbf{b}}(k)$ is surprisingly shallow (with limited extent), approximately k^1 . Thanks to the latter, $\mathcal{E}(k)$ is slightly shallower than k^{-1} . Note that a k^1 scaling corresponds to equipartition of magnetic energy (among the Fourier modes of the inertial range). An interesting question is whether this behaviour is universal for the strong advection limit. Evidence for a positive answer to this question is presented shortly.

It is evident from the observed energy spectra, particularly from those for a relatively stronger advection cases, that energy tends to linger in the inertial range rather than to cascade to the dissipation range. This is an indication of weak energy transfer discussed in the preceding sections.

The magnetic modes in the higher-wavenumber end of the inertial range and in the dissipation range are more strongly excited than their neighbouring mechanical modes (see figure 5.26). This discrepancy in the level of excitation becomes more conspicuous toward the NS regime (i.e. for lower r_0). As discussed in the preceding section, the said

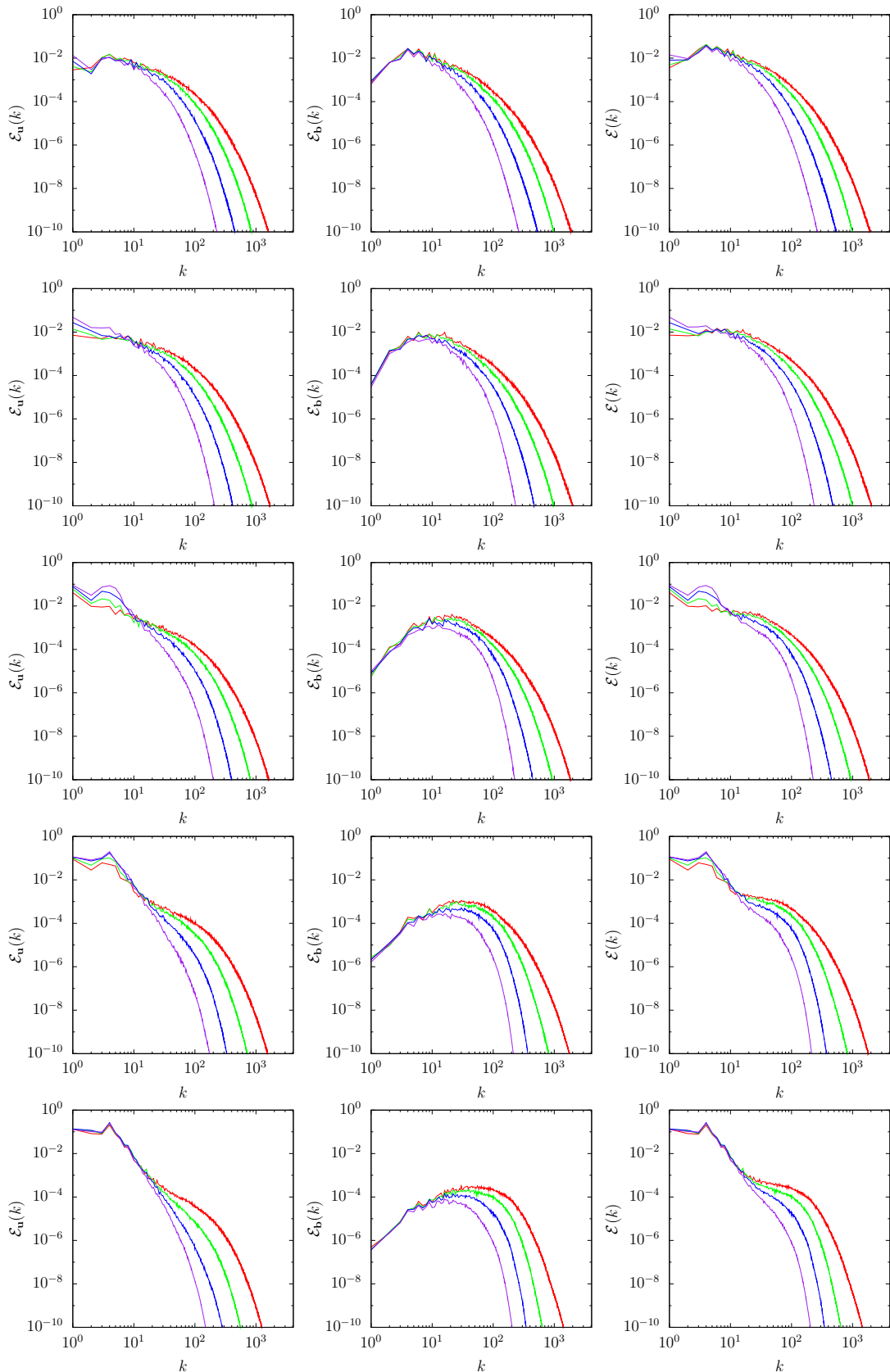


Figure 5.25: Kinetic, magnetic and total energy spectra $\mathcal{E}_u(k)$, $\mathcal{E}_b(k)$ and $\mathcal{E}(k)$, respectively, for fully developed turbulence (at $t = 2.5$). for numerical simulations with resolutions 1024×1024 (purple), 2048×2048 (blue), 4096×4096 (green) and 8192×8192 (red) and $r_0 = 1/4, 1/16, 1/64, 1/256, 1/1024$. The rows are in decreasing order of r_0 .

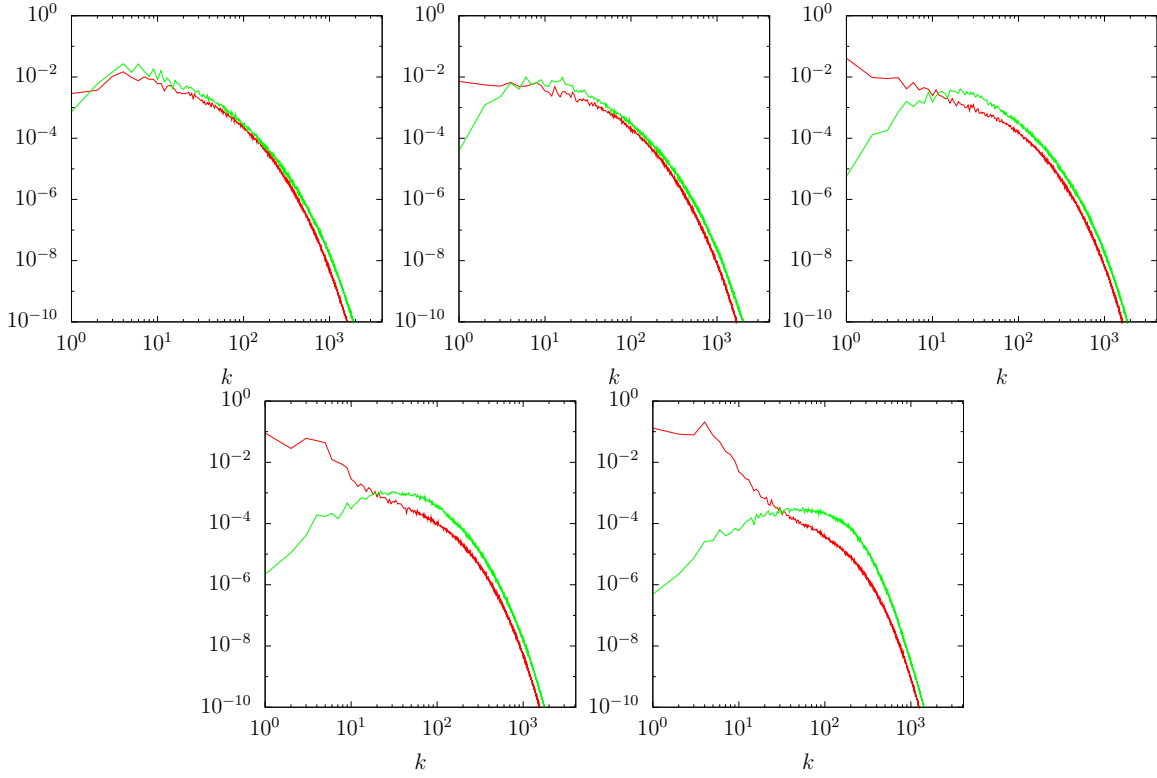


Figure 5.26: Kinetic (red), magnetic (green) energy spectra for the highest resolution from figure 5.25 in decreasing order of r_0 from top left to bottom right.

mechanical modes are excited and replenished by their magnetic counterparts through anti-dynamo interactions. On physical grounds, it is plausible to expect the ‘excitees’ to remain weaker than their ‘excitors’. Our results are consistent with this expectation. The implication is that energy equipartition (i.e. $\mathcal{E}_u(k) = \mathcal{E}_b(k)$) in the inertial range, which was predicted by Kraichnan (1965) in the 3D context and subsequently questioned by a number of authors (Grappin *et al.*, 1983; Müller & Grappin, 2005; Podesta *et al.*, 2007; Boldyrev & Perez, 2009; Tessein *et al.*, 2009), is unrealisable.

Constant initial magnetic energy

No appreciable inverse transfer of $\|a\|^2$ has been observed across the series of simulations presented above. On the contrary, for the higher- r_0 cases, the redistribution of

$\|a\|^2$ from the reservoir (initially confined to $k \in [4, 6]$) is in favour of the higher rather than the lower wavenumbers. This dynamo-induced direct transfer can be recognised from the spectrum of $\|a\|^2$, which is given by $k^{-2}\mathcal{E}_{\mathbf{b}}(k)$ and can be inferred from $\mathcal{E}_{\mathbf{b}}(k)$ in figures 5.25 and 5.26. This spectrum is sufficiently steep and shallow for $k \lesssim 5$ and $k \gtrsim 5$, respectively, clearly indicating a biased distribution of $\|a\|^2$ towards $k \gtrsim 5$. This is due to exceedingly strong dynamo action in these cases. A more quantitative knowledge of the direct transfer of $\|a\|^2$ in the small- r_0 limit can be gained from the results of the second set of simulations described below.

The second set of simulations correspond to $r_0 = 1/256$, $1/1024$ and $1/4096$, with $E_{\mathbf{b}}(0) = 0.001$ fixed. This amounts to a total energy of 4.097 for the case $r_0 = 1/4096$. For each r_0 , one simulation at 8192×8192 gridpoints was run, with $\nu = \mu = 7.9 \times 10^{-5}$. Note that an increase in ν and μ in these simulations compared with the previous ones at the same resolution is necessary due to the more energetic initial conditions for $r_0 = 1/4096$.

Figure 5.27 shows the vorticity and magnetic potential fields for the case $r_0 = 1/256$ at $t = 3$, approximately the time of peak magnetic energy dissipation. Because of limited scale resolution, the values of $|\omega|$ exceeding $3\|\omega\| = 30$ have been filtered out. As large vorticity is highly concentrated in space, this practice does not change the image in a recognisable manner. Clearly, the magnetic potential has evolved toward the small scales (see the initial potential field in figure 5.15 for a comparison). From the image of these fields for $r_0 = 1/256$, $1/1024$ and $1/4096$ shown in figure 5.28, the tendency of a to evolve toward the small scale becomes increasingly more pronounced for smaller r_0 . A quantitative description of this behaviour is given by figure 5.29, where the direct flux of $\|a\|^2$, say $\Pi(k)$, is stronger for smaller r_0 . Note that for the case $r_0 = 1/4096$, $\Pi(k)$ is non-negative throughout, including the wavenumber region lower than that of the initial reservoir. The reason is that in the early stage, a weak and brief inverse transfer has occurred and excited this region. The negative flux associated with this transfer is short-lived and, by the time $t = 1$, is replaced by a non-negative flux.

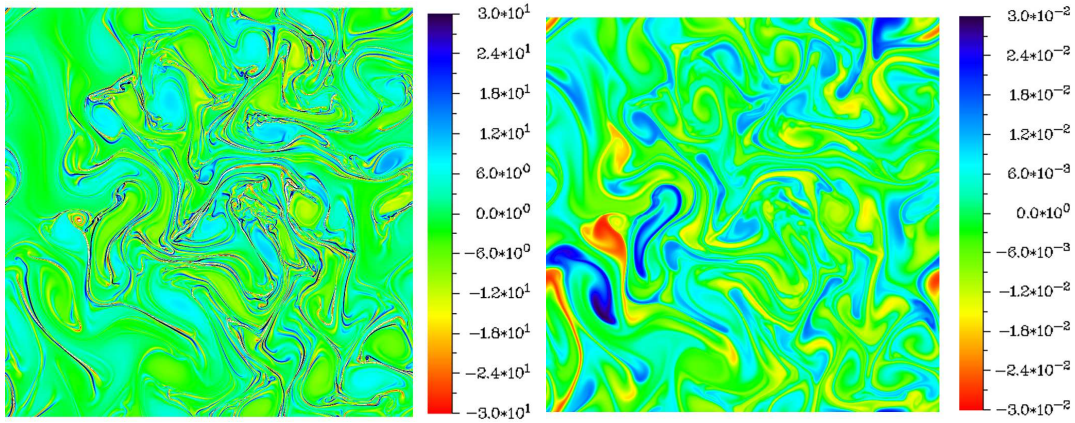


Figure 5.27: Vorticity (a) and magnetic potential (b) fields at peak magnetic energy dissipation, $t = 3$, for $r_0 = 1/256$. The former is plotted with values between $-3\|\omega\|$ and $3\|\omega\| = 30$, which the maximum value is ≈ 140 .

This is clearly seen in figure 5.30 where the magnetic energy at wavenumber $k = 1$ increases up to $t = 1.0$, which corresponding to a negative flux, then decreases giving the positive flux shown in figure 5.29.

Figure 5.31 shows $E_b(t)$ versus t and $\mathcal{E}_b(k)$ versus k (at peak magnetic energy dissipation). As r_0 decreases, $E_b(t)$ grows more rapidly, achieving a higher peak in a shorter time. Intuitively, this time has some bearing on the turnover time of the turbulence. Unfortunately, a quantitative knowledge of this issue is not possible due to insufficient data. For all cases, the spectrum $\mathcal{E}_b(k)$ has a positive slope and becomes wider for smaller r_0 . Remarkably, this positive slope appears to tend to unity in the small- r_0 limit. Such limiting scaling corresponds to equipartition of magnetic energy and magnetic potential variance among the Fourier modes and wavenumber octaves of the inertial range, respectively.

Some remarks about the asymptotic behaviour of $\mathcal{E}_b(k)$ are in order. Compelling evidence from figure 5.31 suggests the spectrum $\mathcal{E}_b(k) = Ck^1$, which extends to an ever-higher wavenumber, say k_m , as $r_0 \rightarrow 0$ (and in the limit of ideal dynamics). For

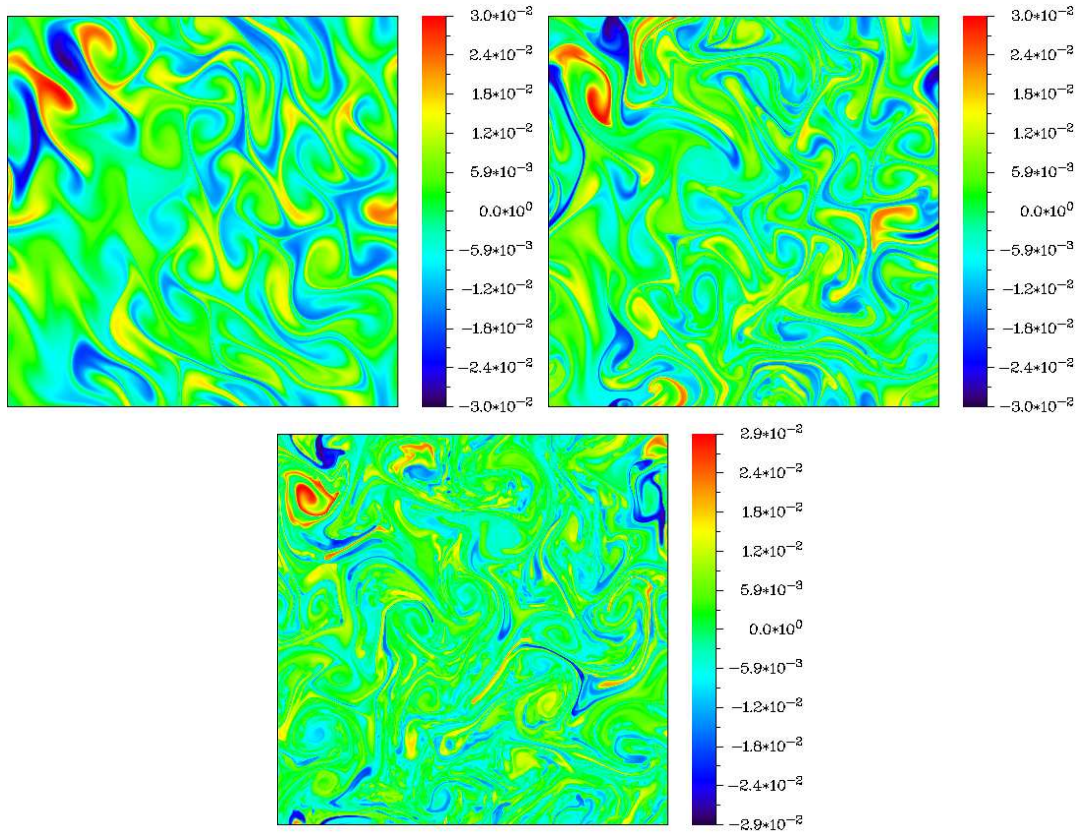


Figure 5.28: Magnetic potential fields at time $t = 1.5$ for $r_0 = 1/256$ (top left), $1/1024$ (top right) and $1/4096$ (bottom).

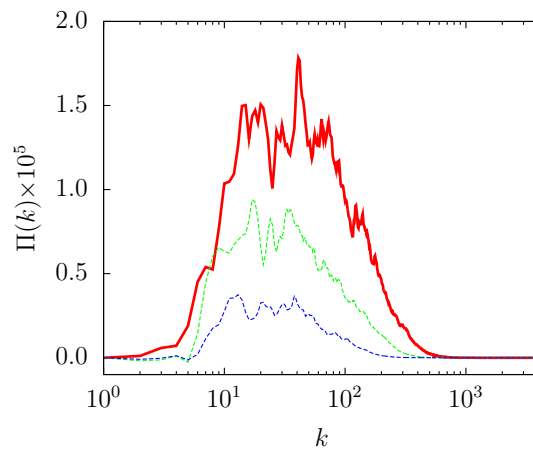


Figure 5.29: Flux of magnetic potential variance at peak magnetic energy dissipation for $r_0 = 1/256$ (blue $t = 3$), $r_0 = 1/1024$ (green $t = 1.6$) and $r_0 = 1/4096$ (red $t = 1$).

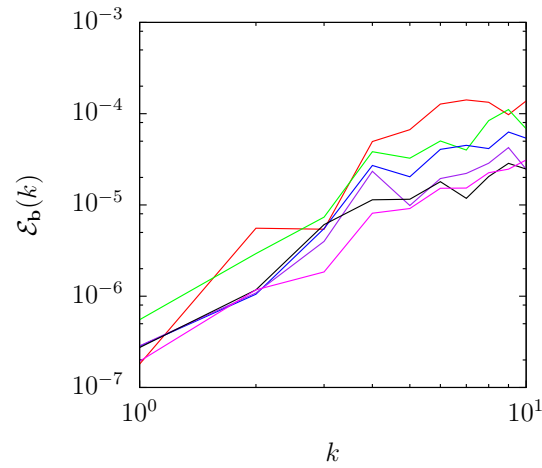


Figure 5.30: Large-scale magnetic energy spectra at time $t = 0.5$ (red), 1.0 (green), 1.5 (blue), 2.0 (purple), 2.5 (black) and 3.0 (magenta) for $r_0 = 1/1024$. Note the increase in the magnetic energy density at $k = 1$ until $t = 1.0$, after which it decays, causing a positive downscale flux.

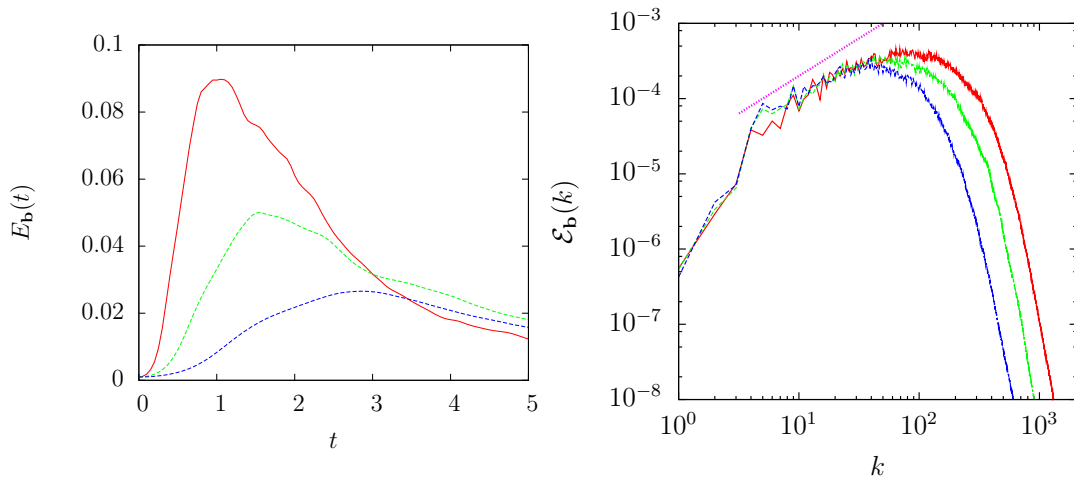


Figure 5.31: Magnetic energy evolution (a) and magnetic energy spectra (b) at peak magnetic energy dissipation for $r_0 = 1/256$ (blue), $r_0 = 1/1024$ (green) and $r_0 = 1/4096$ (red). The reference line has a slope of +1.

such a spectrum, the conservation of $\|a\|^2$ requires

$$\|a_0\|^2 = C \int_{k_0}^{k_m} k^{-1} dk = C \ln \left(\frac{k_m}{k_0} \right), \quad (5.51)$$

where k_0 can be taken as the system's smallest wavenumber. The divergence of k_m implies a logarithmic decrease of C , i.e. a logarithmic collapse of $\mathcal{E}_b(k)$. Meanwhile the magnetic energy is given by

$$E_b = C \int_{k_0}^{k_m} k^1 dk \approx C k_m^2 = \frac{\|a_0\|^2}{\ln(k_m/k_0)} k_m^2. \quad (5.52)$$

Apparently, this corresponds to there being no upper bound for E_b in the limit $r_0 \rightarrow 0$, or equivalently, the kinetic energy available for conversion is unlimited. Note that this theoretical picture would become complete if a dependence of k_m on r_0 could be established.

Similar to the previous set of simulations, the residual energy $\mathcal{E}_b(k) - \mathcal{E}_u(k)$ in the inertial and dissipation ranges is positive (see figure 5.32). The wavenumber at which this energy becomes positive increases as r_0 is decreased. In the picture described by the preceding paragraph, this wavenumber grows (presumably logarithmically) without bound in the limit $r_0 \rightarrow 0$.

5.6 Conclusion

In this chapter we have studied the problem of regularity, energy transfer and inertial-range spectra in MHD turbulence. By examining the triad interactions that govern the nonlinear terms in the equations we were able to discern a strong connection between dynamo (in this context the conversion of kinetic energy into magnetic energy) and downscale energy transfer, which plays a vital role in both the possibility of singularity formation and the shape of the inertial-range spectrum.

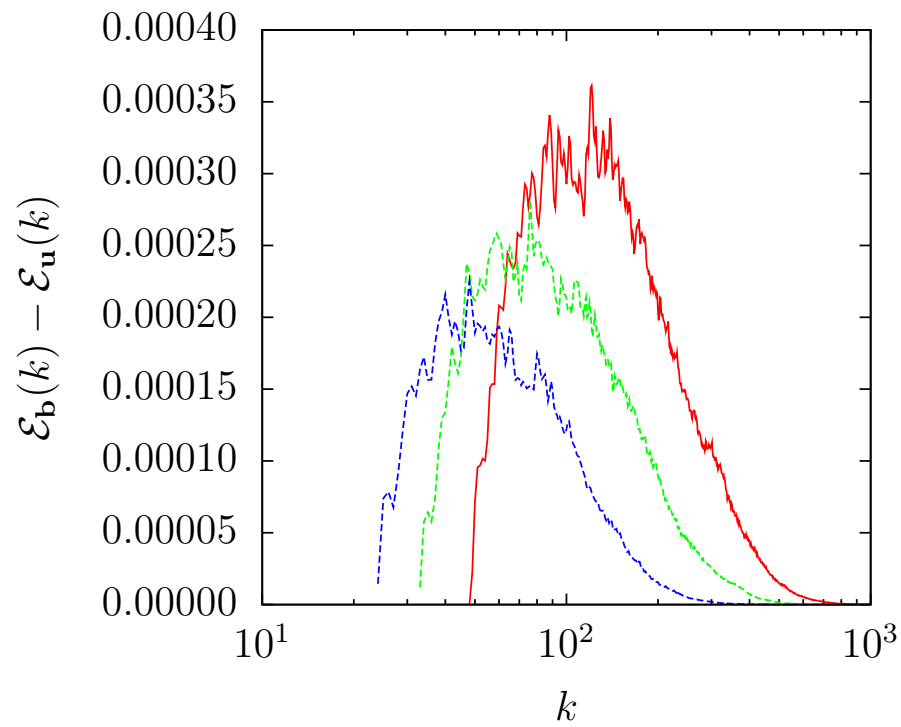


Figure 5.32: Residual energy $\mathcal{E}_b(k) - \mathcal{E}_u(k)$ versus k at peak magnetic energy dissipation for $r_0 = 1/256$ (blue), $r_0 = 1/1024$ (green) and $r_0 = 1/4096$ (red).

We studied both theoretically and numerically 2D MHD turbulence in the limits of infinite and vanishing magnetic Prandtl number $Pm = \nu/\mu$, as well as the partial dissipation cases, *i.e.* $Pm = 0$ and $Pm = \infty$. For positive magnetic diffusivity $\mu > 0$, $\|\nabla j\|^2$ is integrable over $[0, \infty)$. Furthermore, both $\|\omega\|^2$ and $\|j\|^2$ are uniformly bounded independently of the viscosity ν . This means that given $\nu \rightarrow 0$ at fixed $\mu > 0$, the kinetic energy dissipation rate $\nu\|\omega\|^2$ tends to zero. For sufficiently small Pm , the approach $\nu\|\omega\|^2$ is linear in ν . A regularity criterion has been derived for the partial dissipation case $Pm = 0$, where smooth solutions remain smooth up to $t = T$ provided that $\|\omega\|_{BMO}/\|\omega\| \leq C(T - t)^{-\alpha}$, for $\alpha < 1$. We also noted the result that when $Pm = \infty$, either $\|j\|_\infty/\|j\| \leq C(T - t)^{-\alpha}$ or $\|\nabla \mathbf{u}\|_\infty/\|\omega\| \leq C(T - t)^{-\alpha}$, for $\alpha < 1/2$, is sufficient. The results from high-resolution numerical simulations over the range $Pm \in [1/64, 64]$ support these criteria and demonstrate the nearly linear behaviour of the kinetic energy dissipation rate with ν for fixed $\mu > 0$. As Pm is decreased from unity, the ratio $\|\omega\|_\infty/\|\omega\|$ has been observed to increase relatively slowly. On the other hand, an equally slow increase of $\|\nabla \mathbf{u}\|_\infty/\|\omega\|$ has been observed when Pm is increased from unity. These results lend strong support for solution regularity for the partial dissipation cases. Further evidence for the mild behaviour of the said ratios has been observed from the filamentary structures of large values of the vorticity and velocity gradients fields. These filaments are heavily populated, an indication of moderate values of $\|\omega\|_\infty/\|\omega\|$ and $\|\nabla \mathbf{u}\|_\infty/\|\omega\|$.

We then revisited the problem of energy transfer and inertial range scaling in 2D MHD turbulence. The applicability of the IK theory, which was formulated for 3D MHD turbulence, to the present case has been examined both theoretically and numerically. While our results are consistent with the qualitative aspects of this theory on energy transfer reduction by Alfvén wave effects, its quantitative predictions of energy equipartition and $k^{-3/2}$ spectrum in the inertial range have been found to be unrealisable for fully developed turbulence satisfying the Kraichnan condition of magnetic energy at large scales exceeding total energy in the inertial range. More precisely, for turbulence

at unity magnetic Prandtl number developed from a spectrally localised energy reservoir, the kinetic energy spectrum has been found to be significantly shallower than its magnetic counterpart, thereby suggesting no energy equipartition. Furthermore, the total energy spectrum has been observed to be shallower than $k^{-3/2}$, particularly for turbulence having moderate magnetic-to-kinetic energy ratios (approximately 2). Further results from our numerical simulations suggest a weak dependence of the energy dissipation rate $\epsilon(t)$ on the viscosity ν . In particular, as ν is decreased, the time $t = T$ of the peak energy dissipation rate $\epsilon_T = \epsilon(T)$ increases while ϵ_T decreases. Both the increase in T and decrease of ϵ_T appear to be slow, probably logarithmic in ν in its small limit. This suggests the possibility of slow divergence of T and (equally slow) convergence of ϵ_T . However, it is not known whether ϵ_T would tend to a nonzero constant. Much higher resolutions than currently available to the present study are required to convincingly address this issue.

The IK theory was originally formulated for 3D MHD turbulence, where the notion of energy transfer reduction (or turbulence suppression) was apparently in reference to (and to be understood in terms of) the transfer of kinetic and magnetic energy in 3D without Alfvén wave effects. In the present context, this notion becomes largely irrelevant. The reason is that if the coupling between \mathbf{u} and \mathbf{b} via the Lorentz force were to be switched off, then the 2D kinetic energy would undergo an inverse transfer, while its magnetic counterpart would be transferred to small scales through linear advection by a velocity field whose energy migrates the wrong way, to increasingly larger instead of smaller scales. The coupling between the velocity and magnetic fields acts through energy conversion to redirect the flow of kinetic energy. In other words, dynamo and anti-dynamo are responsible for a direct kinetic energy flux. The important point to note here is that 2D MHD turbulence does not have the underpinning direct transfer of energy of the 3D case to fully make sense of Kraichnan’s concept of transfer reduction. Hence, it is hardly surprising that the present results are not in line with the IK theory.

This study was then extended by investigating the dynamical aspects and inertial-

range scaling in the strong advection regime. This was achieved by doubling the numerical resolution and broadening the initial magnetic-to-kinetic energy ratio r_0 by almost two more decades towards the small r_0 limit, *i.e.* towards the strong advection (NS) regime. The dynamics of this regime is characterised by strong magnetic stretching, with intense conversion of kinetic to magnetic energy. The present focus is on quantitative effects of r_0 on the inertial-range dynamics and scaling laws. Two series of direct numerical simulations up to 8192×8192 grid points at unity magnetic Prandtl number and over $r_0 = 1/4, 1/16, 1/64, 1/256, 1/1024$ and $1/4096$ were carried out. In one of these series, the initial total energy was fixed at unity, while in the other the initial magnetic energy was fixed at 0.001. The latter setup allows for probing into detailed behaviour of dynamo action on a fixed magnetic seed field under increasingly stronger advection.

The total energy spectrum $\mathcal{E}(k)$ has been observed to be much shallower than previously thought. This spectrum depends on r_0 since its constituents, *i.e.* the magnetic and kinetic energy spectra $\mathcal{E}_b(k)$ and $\mathcal{E}_u(k)$, strongly depend on r_0 . In particular, $\mathcal{E}_b(k)$ becomes shallower as r_0 is decreased. The extent of this shallow spectrum is limited and becomes broader for smaller r_0 , probably without bound in the limit $r_0 \rightarrow 0$ (with fixed initial magnetic energy). Furthermore, in this limit, the slope of $\mathcal{E}_b(k)$ appears to tend to +1. This corresponds to equipartition of magnetic energy among the Fourier modes, or equivalently, equipartition of magnetic potential variance among the wavenumber octaves of the inertial range. The latter spectral distribution is reminiscent of that of the variance of a passive scalar advected by large-scale flows. Note, however, that the observed dynamical resemblance between a passive scalar and the magnetic potential is rather superficial. In the former, advection can amplify the mean-square scalar gradient without bound in the large-time limit, whereas in the latter, $E_b(t)$ is uniformly bounded in time. The implication is that the direct transfer of magnetic potential, which can be said to be induced by strong dynamo, is relatively less spontaneous than that of its passive counterpart.

Dynamo action (a manifestation of magnetic stretching) may be considered the primary interaction, while the reverse process is of a secondary nature. Hence, it is not surprising that the inertial and dissipation ranges have been found to be more strongly excited magnetically than mechanically.

Some arguments in the present study may apply to 3D MHD turbulence. Intuitively, dynamo action can be expected to bring about similar effects in both 2D and 3D cases. These include the deposition of the converted magnetic energy in the inertial range and the weakening of the velocity field by dynamo action. Note, however, that in 3D, dynamo action is not known to be constrained by the conservation of a positive-definite quadratic quantity other than the total energy. An implication is that if the magnetic energy grows without bound in the limit $r_0 \rightarrow 0$ (with fixed initial magnetic energy), its spectrum need not collapse as in the present case.

New theories and further numerical analysis are required to address the issue of inertial range scaling of 2D MHD turbulence. This study has laid some of the groundwork for both. Improving the current numerical results could be as simple as extending the series of simulations in §5.5.2 to higher resolutions, with or without further broadening the range of r_0 and varying Pm . In this regard, particular attention should be given to how the spectra shallow towards the ‘ultimate’ scaling k^{-1} , representing uniform distribution of energy among the wavenumber octaves. This distribution is realisable for some linear or nearly linear systems, such as passive scalar transport by large-scale flows (Batchelor, 1959) and 2DNS turbulence (Tran *et al.*, 2010), and, for the present case, is plausible if $T \rightarrow \infty$. The reason is that the divergence of T means no excitation of ever-smaller dissipation scales in finite time – a manifestation of effectively linear behaviour of the small scales. The main question that a new theory may need to sort out is whether dynamo saturation represents a state of complete or nearly complete depletion of nonlinearity. Nearly linear small-scale dynamics would require good behaviour of the source terms in the following equations governing the vorticity ω and

current j :

$$\frac{\partial \omega}{\partial t} + J(\psi, \omega) = J(j, a) + \nu \Delta \omega, \quad (5.53)$$

$$\frac{\partial j}{\partial t} + J(\psi, j) = J(\omega, a) + 2J(\psi_x, a_x) + 2J(\psi_y, a_y) + \mu \Delta j. \quad (5.54)$$

Now, for ideal dynamics ($\nu = \mu = 0$), the smoothness of either magnetic or velocity field implies that of the other and therefore of the system as a whole (Tran & Yu, 2012; Ohkitani, 2006). Hence, in order for T to diverge, it is sufficient to require good behaviour of the vorticity source term $J(j, a)$ alone. Here ‘good’ behaviour means $J(j, a)$ does not diverge significantly more rapidly than ω . A weaker and more tractable condition is $\langle \omega J(j, a) \rangle \lesssim \langle \omega^2 \rangle \ln \langle \omega^2 \rangle$, which allows for up to double exponential growth of $\langle \omega^2 \rangle$. Note that our numerical results for $\epsilon_{\mathbf{u}}(t)$ in §5.5.1 indicate much milder behaviour of $\langle \omega^2 \rangle$ during the stage of most rapid growth. In handling this condition, one should watch out for possible high correlation between ω and j , in the sense that $\langle |J(\omega, j)| \rangle$ does not diverge so strongly. In particular, if $\langle |J(\omega, j)| \rangle$ does not diverge more strongly than $\langle \omega^2 \rangle \ln \langle \omega^2 \rangle$, then the required condition is satisfied since $\langle \omega J(j, a) \rangle = \langle a J(\omega, j) \rangle \leq \|a\|_{\infty} \langle |J(\omega, j)| \rangle$.

Chapter 6

Summary and outlook

In this thesis the dynamics of a number of two-dimensional advection-diffusion equations have been investigated, namely the Navier–Stokes, surface quasigeostrophic, alpha turbulence and magnetohydrodynamic equations, concentrating on the degrees of freedom, energetics, inertial-range scaling laws and inviscid-limit dissipation rate. A variety of techniques have been utilised to do so, ranging from phenomenology to mathematical analysis to numerical simulations. Each method has its strengths and weaknesses, so by taking this approach it is hoped to gain as broad an understanding of each system as possible.

In chapter 2 an upper bound for the number of degrees of freedom of two-dimensional Navier–Stokes turbulence freely evolving from a smooth initial vorticity field has been derived. This number is defined as the minimum dimension such that arbitrary phase-space volume elements of no lower dimension along the solution curve in phase-space contract exponentially under the linearised dynamics. This means that the (locally in time) turbulent dynamics could be sufficiently ‘contained’ within a linear subspace whose dimension does not exceed N . In essence, N represents a reduced dimension that a modelled system should achieve in order to describe the turbulence adequately. It was found that $N \leq C_1 Re$ in the energy space and $N \leq C_2 Re(1 + \ln Re)^{1/3}$ in the enstrophy

space. Here C_1 and C_2 are constant and Re is the Reynolds number, which is defined in terms of the initial vorticity, the system size, and the viscosity. The present estimates for N have been compared with well-known bounds for the Hausdorff dimension D_H of the global attractor in the forced case, and the apparent difference between the linear (or nearly so) scaling of N with Re and the highly superlinear dependence of D_H on the inverse viscosity ν^{-1} has been discussed. It has been argued that the superlinear dependence of D_H on ν^{-1} is not an intrinsic property of the turbulent dynamics, rather it is a ‘removable artefact’ arising from the use of a time-independent forcing as a model for the energy and enstrophy injection that drives the turbulence. This suggestion has been strengthened by the fact that the ‘extra’ dependence of D_H on ν^{-1} would be completely removed (at least for the estimate of D_H in the enstrophy space) if one could model the driving force in such a way that the enstrophy injection rate does not depend on the viscosity. Such a forcing can be seen to be more realistic than ones with viscosity-dependent input.

The effects of mechanical friction on the enstrophy dynamics of forced 2D Navier–Stokes turbulence have also been examined both theoretically and numerically. On the theoretical side it has been shown by elementary methods that the presence of friction alters the system by ensuring a vanishing enstrophy dissipation rate in the inviscid limit. This result is valid uniformly in time, similarly to the case of freely decaying frictionless turbulence in the inviscid limit. These findings imply that for a fixed friction coefficient the frictional dissipation of enstrophy becomes predominant given sufficiently small viscosity. This has the inevitable result that the classically inviscid enstrophy inertial range becomes a dissipation range in which the dissipation of enstrophy by friction mainly occurs. This range can then at best support a diminishing flux of enstrophy rather than the k -independent flux envisaged by Kraichnan. Assuming that a classical spectrum is valid in the limit of weak friction an expression for the critical viscosity, which divides the regimes of predominant viscous and frictional dissipation of enstrophy, has been derived. It has been found that this critical viscosity decreases

exponentially with the friction coefficient. These theoretical results have been backed up by a number of simulations of the forced 2D Navier–Stokes equations that were carried out under similar conditions both with and without a friction term. Given all else fixed, including a nonzero friction coefficient, it has been seen that the viscous enstrophy dissipation rate decreased as the viscosity decreased. This decrease appears to be slow, probably logarithmic in viscosity as in the case of freely decaying turbulence. The numerical results aimed at calculating the critical viscosity have been found to be in qualitative agreement with the theoretical finding. No significant differences have been found between the undamped and damped turbulence near this critical viscosity. In particular, the energy spectra of the enstrophy inertial range in the two cases are virtually indistinguishable, both being close to the classical k^{-3} spectrum.

In chapter 3 the estimate $N \leq Re^{3/2}$ for the number of degrees of freedom of the SQG system has been derived. Upon identifying N with the number of dynamically active Fourier modes, *i.e.* the modes within the energy inertial range, the result $\alpha \leq 5/3$ has been deduced for the exponent α of the power-law spectrum $k^{-\alpha}$, with equality in the case where the bounds for the number of degrees of freedom are sharp. This approximation renders the scaling $Re^{1/2}$ for the exponential dissipation rate $r = \nu k_d^2$ at the dissipation wavenumber k_d . Given that r is linear in Re for Burgers flows, whose nonlinearity is fully quadratic, the sublinear scaling of r with Re in the present case (and in three-dimensional turbulence) is a manifestation of depletion of nonlinearity. The method presented here represents the first derivation of the classical $k^{-5/3}$ spectrum using analytical methods. Results from a set of numerical simulations of the unforced SQG equation up to the high resolution of 16384×16384 grid points have then been discussed. These results include a series of spectra that become shallower for increasingly higher Reynolds numbers, appearing to tend to the predicted $k^{-5/3}$ spectrum. Furthermore, within the narrow range of accessible Reynolds numbers and for the choice of initial temperature field with relatively well-defined lines of large gradient, the energy dissipation rate appears to peak sharply in time and to be approximately

independent of the Reynolds number. This behaviour is consistent with a positive limiting dissipation rate in the inviscid limit.

The behaviour of the maximum energy dissipation rate ϵ_T and the corresponding time T is an interesting problem for fluid equations whose solutions are known to be regular in the presence of viscosity but not known to be so otherwise. By monitoring ϵ_T and T against ν , one can obtain invaluable insights into the question of inviscid singularities. Strong evidence for a positive answer to this question would be that both ϵ_T and T become independent of ν for small ν . In this case, the smooth viscous solution presumably approaches the (possibly weak) inviscid solution. In the event that T grows without bound as ν is decreased (irrespective of the behaviour of ϵ_T), finite-time inviscid singularities seem highly unlikely. Since viscous dynamics are much easier to simulate than their inviscid counterparts, the above approach can be particularly useful in addressing the issue of inviscid singularities.

In chapter 4 the results from a number of numerical simulations of generalised SQG equation have been discussed, in particular the effect of varying the parameter α , which controls the relationship between the advected scalar and advecting velocity field. These results have been seen to qualitatively agree with the phenomenologically derived result that larger values of α leads to a decrease in nonlinearity of the system and shallower generalised enstrophy spectra, although with quantitative disagreement on the inertial-range exponent. For large α the spectra have been seen to be shallower than the k^{-1} spectrum of a passively advected scalar, suggesting that passive advection is a poor approximation to the system in the high- α case. For small α the maximum generalised enstrophy dissipation rate and the downscale flux of generalised enstrophy have been seen to increase as α is decreased, in agreement with the argument that smaller values of α correspond to more highly nonlinear systems. The increase in the time of maximum dissipation rate (when scaled by the initial eddy turnover time) in this same limit may be evidence for the stretched timescale as envisaged by Ohkitani (2012) in which depletion of nonlinearity by the symmetry in the Jacobian causes the

time of maximum dissipation T to increase without bound in the limit $\alpha \rightarrow 0$.

In chapter 5 a number of aspects of MHD turbulence have been investigated. The applicability of IK theory, which was formulated for 3D MHD turbulence, to the present case of 2D turbulence has been examined both theoretically and numerically. While the results are consistent with the qualitative aspects of this theory of energy transfer reduction by Alfvén wave effects, its quantitative predictions of energy equipartition and $k^{-3/2}$ spectrum in the inertial range have been found to be unrealisable for fully developed turbulence satisfying the Kraichnan condition of magnetic energy at large scales exceeding total energy in the inertial range. More precisely, for turbulence at unity magnetic Prandtl number developed from a spectrally localised energy reservoir, the kinetic energy spectrum has been found to be significantly shallower than its magnetic counterpart, thereby suggesting a lack of energy equipartition. In fact the total energy spectrum strongly depends on r_0 since both the magnetic and kinetic energy spectra $\mathcal{E}_b(k)$ and $\mathcal{E}_u(k)$, each themselves strongly depend on r_0 . In particular, \mathcal{E}_b becomes shallower as r_0 is decreased, while \mathcal{E}_u exhibits a steep inertial range followed by a relatively shallower tail caused by anti-dynamo excitation, thus poorly represented overall by a single scaling exponent. The extent of the shallow magnetic energy spectrum is limited and becomes broader for smaller r_0 , probably without bound in the limit $r_0 \rightarrow 0$ (with fixed initial magnetic energy). Furthermore, in this limit, the slope of $\mathcal{E}_b(k)$ appears to tend to $+1$. While this form of the energy spectrum is reminiscent of that of the variance of a passive scalar advected by large-scale flows, the observed dynamical resemblance between a passive scalar and the magnetic potential is rather superficial as there are fundamental differences. One difference is that advection can amplify the mean-square scalar gradient without bound in the large-time limit, whereas $E_b(t)$ is uniformly bounded in time. This means that the direct transfer of magnetic potential, which can be said to be induced by strong magnetic stretching, is relatively less spontaneous than that of its passive scalar counterpart.

There are still many topics worth exploring in each of the areas covered by this

thesis, any of which could be a basis for future work. The 2DNS system is certainly the best understood of the systems, yet even here there are still a number of open problems. One of these is the question as to whether the Kolmogorov constant C of the enstrophy spectrum $\mathcal{Z}(k) = C\chi^{2/3}k^{-1}$ in the enstrophy inertial range is universal, as suggested in Batchelor (1969), or dependent on the form of the energy (enstrophy) injection as surmised by Kraichnan (1967). While an analytic solution is not currently forthcoming it should not be difficult to test numerically the effect of different types of forcing on the Kolmogorov constant in two dimensions. In SQG turbulence, the question of inviscid singularities is still open, and while the numerical results presented have given tantalising hints that the energy dissipation rate tends to a nonzero constant in the inviscid limit, much higher resolutions are needed to come anywhere near giving a definitive answer. Such simulations should be possible by making use of massively parallel supercomputer systems such as the cluster run by the Solar Theory group in St Andrews. For alpha turbulence a whole new set of simulations could be run to address the problems raised in §4.4, namely that the initial conditions used resulted in the initial kinetic energy differing by several orders of magnitude as α was varied. As well as the effect this had on changing the eddy turnover time, which presumably changes the speed of the evolution of the system, it is not known what other effects this could have on the degree of nonlinearity of the system. Finally, there is still much that can be done with the 2D MHD system. As yet there is no theory that comprehensively describes the effect that different initial kinetic-to-magnetic energy ratios have on the system, and it is not clear if there is a limit on the amount of kinetic energy that can be converted into magnetic energy through dynamo action. Numerically there is also the whole region where $r_0 \gg 1$ to be explored, which has not been touched upon in this thesis and has been largely ignored in the literature. By taking a holistic approach to these and other mathematical problems and attacking them using a mixture of analytical, phenomenological and numerical methods one can significantly increasing the likelihood of making real progress in understanding these highly complex of systems.

Bibliography

- APPEL, K. & HAKEN, W. 1976 Every planar map is four colorable. *Bull. Amer. Math. Soc* **82**, 711–712.
- ASCHER, U. M. & PETZOLD, L. R. 1998 *Computer methods for ordinary differential equations and differential–algebraic equations*. SIAM.
- BABIN, A. V. & VISHIK, M. I. 1983 Attractors of partial differential evolution equations and estimates of their dimension. *Russ. Math. Surveys* **38:4**, 151–213.
- BATCHELOR, G. K. 1959 Small-scale variation of convected quantities like temperature in turbulent fluid Part 1: General discussion and the case of small conductivity. *J. Fluid Mech.* **5**, 113–133.
- BATCHELOR, G. K. 1969 Computation of the energy spectrum in homogeneous two-dimensional turbulence. *Phys. Fluids Supp. II* **12**, 233–239.
- BATCHELOR, G. K. & TOWNSEND, A. A. 1949 The nature of turbulence at large wave-numbers. *Proc. R. Soc. A* **199**, 238–255.
- BEALE, J. T., KATO, T. & MAJDA, A. 1984 Remarks on the breakdown of smooth solutions for the 3-D Euler equations. *Commun. Math. Phys.* **94**, 61–66.
- BERNOULLI, D. 1738 *Hydrodynamica, sive de veribus et motibus fluidorum commentarii, opus academicum*. Strasbourg: Johannis Reinholdi Dulseckeri.

- BISKAMP, D. & WELTER, H. 1989 Dynamics of decaying two-dimensional magneto-hydrodynamic turbulence. *Phys. Fluids B* **1**, 1964–1979.
- BLACKBOURN, L. A. K. & TRAN, C. V. 2011 Effects of friction on two-dimensional Navier–Stokes turbulence. *Phys. Rev. E* **84**, 046322.
- BLACKBOURN, L. A. K. & TRAN, C. V. 2012 On energetics and inertial range scaling laws of two-dimensional magnetohydrodynamic turbulence. *J. Fluid Mech.* **703**, 238–254.
- BLACKBOURN, L. A. K. & TRAN, C. V. 2013 Inertial-range dynamics and scaling laws of two-dimensional magnetohydrodynamic turbulence in the strong advection regime. Preprint.
- BOFFETTA, G. & MUSACCHIO, S. 2010 Evidence for the double cascade scenario in two-dimensional turbulence. *Phys. Rev. E* **82**, 016307.
- BOLDYREV, S. & PEREZ, J. C. 2009 Spectrum of weak magnetohydrodynamic turbulence. *Phys. Rev. Lett.* **103**, 225010.
- BRANDENBURG, A. 2011*a* Dissipation in dynamos at low and high magnetic Prandtl numbers. *Astron. Nachr.* **332**, 51–56.
- BRANDENBURG, A. 2011*b* Nonlinear small-scale dynamos at low magnetic Prandtl numbers. *Astrophys. J.* **741**, 92.
- BRESNYAK, A. 2011 Spectral slope and Kolmogorov constant of MHD turbulence. *Phys. Rev. Lett.* **106**, 075001.
- BURGERS, J. M. 1940 Application of a model system to illustrate some points of the statistical theory of free turbulence. *Proc. Acad. Sci. Amst.* **43**, 2–12.
- CAFFARELLI, L. A. & VASSEUR, A. 2010 Drift diffusion equations with fractional diffusion and the quasi-geostrophic equation. *Ann. Math.* **171**, 1903–1930.

- CAFLISCH, R. E., KLAPPER, I. & STEEL, G. 1997 Remarks on singularities, dimension, and energy dissipation for ideal hydrodynamics and MHD. *Commun. Math. Phys.* **184**, 443–455.
- CAO, C. & WU, J. 2011 Global regularity for the 2D MHD equations with mixed partial dissipation and magnetic diffusion. *Adv. Math.* **226**, 1803–1822.
- CAPET, X., KLEIN, P., HUA, B. L., LAPEYRE, G. & MCWILLIAMS, J. C. 2008 Surface kinetic energy transfer in surface quasi-geostrophic flows. *J. Fluid Mech.* **604**, 165–174.
- CHARNEY, J. G. 1948 On the scale of atmospheric motions. *Geophys. Publ.* **17**, 3–17.
- CHARNEY, J. G. 1971 Geostrophic turbulence. *J. Atmos. Sci.* **28**, 1087–1095.
- CONSTANTIN, P. 1987 Collective L^∞ estimates for families of functions with orthonormal derivatives. *Indiana Univ. Math. J.* **36**, 603–616.
- CONSTANTIN, P., FOIAS, C., MANLEY, O. P. & TEMAM, R. 1985a Determining modes and fractal dimension of turbulent flows. *J. Fluid Mech.* **150**, 427–440.
- CONSTANTIN, P., FOIAS, C. & TEMAM, R. 1985b *Attractors representing turbulent flows*, *Mem. Am. Math. Soc.*, vol. 53. American Mathematical Society.
- CONSTANTIN, P., FOIAS, C. & TEMAM, R. 1988 On the dimension of the attractors in two-dimensional turbulence. *Physica D* **30**, 284–296.
- CONSTANTIN, P., LAX, P. D. & MAJDA, A. 1985c A simple one-dimensional model for the three-dimensional vorticity equation. *Commun. Pure Appl. Math.* **38**, 715–724.
- CONSTANTIN, P., MAJDA, A. & TABAK, E. 1994a Formation of strong fronts in the 2D quasi-geostrophic thermal active scalar. *Nonlinearity* **7**, 1495–1533.

- CONSTANTIN, P., MAJDA, A. & TABAK, E. 1994*b* Singular front formation in a model for quasigeostrophic flow. *Phys. Fluids* **6**, 9–11.
- CONSTANTIN, P., NIE, Q. & SCHÖRGHOFER, N. 1998 Nonsingular surface quasigeostrophic flow. *Phys. Lett. A* **241**, 168–172.
- CONSTANTIN, P. & RAMOS, F. 2007 Inviscid limit for damped and driven incompressible Navier-Stokes equations in \mathbb{R}^2 . *Commun. Math. Phys.* **275**, 529–551.
- CONSTANTIN, P., WEINAN, E. & E, S. TITI 1994*c* Onsager’s conjecture on the energy conservation for solutions to Euler’s equation. *Commun. Math. Phys.* **165**, 207–209.
- COURANT, R., FRIEDRICHS, K. & LEWY, H. 1928 Über die partiellen differenzgleichungen der mathematischen physik. *Math. Annal.* **100**, 32–74.
- COWLING, T. G. 1934 The magnetic field of sunspots. *Mon. Not. R. Astron. Soc.* pp. 39–48.
- DAVIDSON, P. A. 2004 *Turbulence: an introduction for scientists and engineers*. Oxford University Press.
- DMITRUK, P. & MONTGOMERY, D. C. 2005 Numerical study of the decay of enstrophy in a two-dimensional Navier–Stokes fluid in the limit of very small viscosities. *Phys. Fluids* **17**, 035114.
- DOERING, C. & GIBBON, J. D. 1991 Note on the Constantin–Foias–Temam attractor dimension estimate for two-dimensional turbulence. *Physica D* **48**, 471–480.
- DRITSCHEL, D. G., SCOTT, R. K., MACASKILL, C., GOTTWALD, G. A. & TRAN, C. V. 2008 Unifying scaling theory for vortex dynamics in two-dimensional turbulence. *Phys. Rev. Lett.* **101**, 094501.
- DRITSCHEL, D. G. & TOBIAS, S. M. 2012 Two-dimensional magnetohydrodynamic turbulence in the small magnetic Prandtl limit. *J. Fluid Mech.* **703**, 85–98.

- DRITSCHEL, D. G., TRAN, C. V. & SCOTT, R. K. 2007 Revisiting Batchelor's theory of two-dimensional turbulence. *J. Fluid Mech.* **591**, 379–391.
- EULER, M. 1757 Principes generaux du mouvement des fluides. *Mémoires de l'académie des sciences de Berlin* **11**, 274–315.
- FARMER, J. D. 1981 Chaotic attractors of an infinite-dimensional dynamical system. *Physica D* **4**, 366–393.
- FEFFERMAN, C. L. 2000 Existence and smoothness of the Navier–Stokes equation. http://www.claymath.org/millennium/Navier-Stokes_Equations/.
- FJØRTOFT, R. 1953 On the changes in the spectral distribution of kinetic energy for twodimensional, nondivergent flow. *Tellus* **5**, 225–230.
- FOIAS, C., MANLEY, O., TEMAN, R. & ROSA, R. 2001 *Navier–Stokes Equations and Turbulence*. Cambridge: Cambridge University Press.
- FOX, S. & DAVIDSON, P. A. 2010 Freely decaying two-dimensional turbulence. *J. Fluid Mech.* **659**, 351–364.
- FRIGO, M. & JOHNSON, S. G. 2005 The design and implementation of FFTW3. *Proceedings of the IEEE* **93**, 216–231, special issue on “Program Generation, Optimization, and Platform Adaptation”.
- FRISCH, U. 1995 *Turbulence: The legacy of A. N. Kolmogorov*. Cambridge University Press.
- GALTIER, S., POUQUET, A. & MANGENEY, A. 2005 Spectral scaling laws for incompressible anisotropic magnetohydrodynamic turbulence. *Phys. Plasmas* **12**, 092310.
- GIBBON, J. D. & TITI, E. S. 1997 Attractor dimension and small length scale estimates for the three-dimensional Navier–Stokes equations. *Nonlinearity* **10**, 109.

- GRAPPIN, R., POUQUET, A. & LÉORAT, J. 1983 Dependence of MHD turbulence spectra on the velocity field–magnetic field correlation. *Astron. Astrophys.* **126**, 51–58.
- HAUGEN, N. E. L., BRANDENBURG, A. & DOBLER, W. 2003 Is nonhelical hydro-magnetic turbulence peaked at small scales? *Astrophys. J.* **597**, L141–L144.
- HEIJST, G. J. F. VAN, CLERX, H. J. H. & MOLENAAR, D. 2006 The effects of solid boundaries on confined two-dimensional turbulence. *J. Fluid Mech.* **554**, 411–431.
- HELD, I. M., PIERREHUMBERT, R. T., GARNER, S. T. & SWANSON, K. L. 1995 Surface quasi-geostrophic dynamics. *J. Fluid Mech.* **282**, 1–20.
- HOU, T. Y. & LI, R. 2006 Dynamic depletion of vortex stretching and non-blowup of the 3D incompressible Euler equations. *J. Nonlinear Sci.* **16**, 639–664.
- HOU, T. Y. & LI, R. 2007 Computing nearly singular solutions using pseudo-spectral methods. *J. Comput. Phys.* **226**, 379–397.
- HOU, T. Y. & LI, R. 2008 Blowup or no blowup? The interplay between theory and numerics. *Physica D* **237**, 1937–1944.
- HUNT, B. R. 1996 Maximum local Lyapunov dimension bounds the box dimension of chaotic attractors. *Nonlinearity* **9**, 845–852.
- IROSHNIKOV, P. S. 1964 Turbulence of a conducting fluid in a strong magnetic field. *Sov. Astron.* **7**, 566–571.
- KAPLAN, J. & YORKE, J. 1979 *Functional differential equations and approximation of fixed points*. New York: Springer.
- KASSAM, A. & TREFETHEN, L. 2005 Fourth-order time-stepping for stiff PDEs. *SIAM J. Sci. Comput.* **26**, 1214–1233.

- KISELEV, A., NAZAROV, F. & VOLBERG, A. 2007 Global well-posedness for the critical 2D dissipative quasi-geostrophic equation. *Invent. Math.* **167**, 445–453.
- KOLMOGOROV, A. N. 1941*a* Dissipation of energy in locally isotropic turbulence. *Dokl. Akad. Nauk. SSSR* **32**, 19–21, reprinted in Proc R. Soc. A Vol 434 Pages 15-17 1991.
- KOLMOGOROV, A. N. 1941*b* Local structure of turbulence in incompressible fluid at very high Reynolds numbers. *Dokl. Akad. Nauk. SSSR* **30**, 299–303, reprinted in Proc. R. Soc. Lon. A Vol. 434 Pages 9-12 1991.
- KOLMOGOROV, A. N. 1941*c* On the degeneration of isotropic turbulence in an incompressible viscous liquid. *Dokl. Akad. Nauk. SSSR* **31**, 538–541.
- KOZONO, H. & TANUICHI, Y. 2000 Limiting case of the Sobolev inequality in BMO, with application to the Euler equations. *Commun. Math. Phys.* **214**, 191–200.
- KRAICHNAN, R. H. 1965 Inertial-range spectrum of hydromagnetic turbulence. *Phys. Fluids* **8**, 1385–1387.
- KRAICHNAN, R. H. 1967 Inertial ranges in two-dimensional turbulence. *Phys. Fluids* **10**, 1417–1423.
- KRAICHNAN, R. H. 1971 Inertial-range transfer in two- and three-dimensional turbulence. *J. Fluid Mech.* **47**, 525–535.
- LADYZHENSKAYA, O. A. 1969 *The Mathematical Theory of Viscous Incompressible Flow*. New York: Gordon and Breach.
- LEE, E., BRACHET, M. E., POUQUET, A., MININNI, P. D. & ROSENBERG, D. 2012 Lack of universality in decaying magnetohydrodynamic turbulence. *Phys. Rev. E* **81**, 016318.
- LEE, T. D. 1951 Difference between turbulence in a two-dimensional and three-dimensional fluid. *J. Appl. Phys.* **22**, 524.

- LEI, Z. & ZHOU, Y. 2009 BKM's criterion and global weak solutions for magnetohydrodynamics with zero viscosity. *Discrete Contin. Dyn. Syst.* **25**, 575–583.
- LOUREIRO, N. F., UZDENSKY, D. A. & SCHEKOCHIHIN, A. A. 2009 Turbulent magnetic reconnection in two dimensions. *Mon. Not. R. Astron. Soc.* **399**, L146–L150.
- MÜLLER, W. & GRAPPIN, R. 2005 Spectral energy dynamics in magnetohydrodynamic turbulence. *Phys. Rev. Lett.* **95**, 114502.
- NAVIER, C. L. M. H. 1822 Mémoire sur les lois du mouvement des fluides. *Mém. Acad. Sci. Inst. France* **6**, 389–440.
- NG, C. S., BHATTACHARJEE, A., MUNSI, D. & ISENBERG, P. A. 2012 Kolmogorov versus Iroshnikov–Kraichnon spectra: consequence for ion heating in the solar wind. *J. Geophys. Res.* **115**, A02101.
- NIRENBERG, L. 1959 On elliptic partial differential equations. *Ann. Scuola Norm. Sup. Pisa* **13**, 115–162.
- OBUKHOV, A. M. 1941*a* On the distribution of energy in the spectrum of turbulent flow. *Dokl. Akad. Nauk. SSSR* **32**, 22–24.
- OBUKHOV, A. M. 1941*b* Spectral energy distribution in a turbulent flow. *Izv. Akad. SSSR Ser. Geogr. Geofiz.* **5**, 453–466.
- OHKITANI, K. 2006 A note on regularity conditions on ideal magnetohydrodynamic equations. *Phys. Plasmas* **13**, 044504.
- OHKITANI, K. 2011 Growth rates analysis of scalar gradient in generalized surface quasi-geostrophic equations of ideal fluids. *Phys. Rev. E* **83**, 036317.
- OHKITANI, K. 2012 Asymptotics and numerics of a family of two-dimensional generalized surface quasi-geostrophic equations. *Phys. Fluids* **24**, 095101.

- OHKITANI, K. & YAMADA, M. 1997 Inviscid and inviscid-limit behavior of a surface quasi-geostrophic flow. *Phys. Fluids* **9**, 876–882.
- ONSAGER, L. 1949 Statistical hydrodynamics. *Nuovo Cimento (Suppl.)* **6**, 279–287.
- ORSZAG, S. A. 1971 On the elimination of aliasing in finite-difference schemes by filtering high-wavenumber components. *J. Atmos. Sci* **28**, 1074.
- PEDLOSKY, J. 1987 *Geophysical fluid dynamics*, 2nd edn. Springer.
- PIERREHUMBERT, R. T., HELD, I. M. & SWANSON, K. L. 1994 Spectra of local and nonlocal twodimensional turbulence. *Chaos, Solitons and Fractals* **4**, 1111–1116.
- PODESTA, J. J., ROBERTS, D. A. & GOLDSTEIN, M. L. 2007 Spectral exponents of kinetic and magnetic energy spectra in solar wind turbulence. *Astrophys. J.* **664**, 543–548.
- POUQUET, A. 1978 On two-dimensional magnetohydrodynamic turbulence. *J. Fluid Mech.* **88**, 1–16.
- REYNOLDS, O. 1883 An experimental investigation of the circumstances which determine whether the motion of water shall be direct or sinuous, and of the law of resistance in parallel channels. *Philos. Trans.* **174**, 935–982.
- RHINES, P. B. 1979 Geostrophic turbulence. *Ann. Rev. Fluid Mech.* **11**, 401–441.
- RICHARDSON, L. F. 1911 The approximate arithmetical solution of finite differences of physical problems involving differential equations, with an application to the stresses in a masonry dam. *Trans. Cambridge Phil. Soc., Series A* **210**, 307–357.
- RICHARDSON, L. F. 1922 *Weather prediction by numerical process*. Cambridge University Press.
- RUELLE, D. 1982 Large volume limit of the distribution of characteristic exponents in turbulence. *Commun. Math. Phys.* **87**, 287–302.

- SCOTT, R. K. 2006 Local and nonlocal advection of a passive scalar. *Phys. Fluids* **18**, 116601.
- SERVIDIO, S., MATTHAEUS, W. H., SHAY, M. A. & DMITRUK, P. 2010 Statistics of magnetic reconnection in two-dimensional magnetohydrodynamic turbulence. *Phys. Plasmas* **17**, 032315.
- SMITH, K. S., BOCCALETTI, G., HENNING, C. C., MARINOV, I., TAM, C. Y., HELD, I. M. & VALLIS, G. K. 2002 Turbulent diffusion in the geostrophic inverse cascade. *J. Fluid Mech.* **469**, 13–48.
- STEIN, E. M. 1970 *Singular integrals and differentiability properties of functions*. Princeton University Press.
- STOKES, G. G. 1845 On the theories of the internal friction of fluids in motion, and of the equilibrium and motion of elastic solids. *Trans. Cambridge Phil. Soc.* **8**, 287–305.
- TAYLOR, G. I. 1917 Observations and speculations on the nature of turbulent motion. *Reports and Memoranda of the Advisory Committee on Aeronautics* Reprinted in Scientific Papers of Sir Geoffrey Ingram Taylor, Vol. 2, Cambridge University Press, Cambridge, 1960, pp. 69–78, edited by G. K. Batchelor.
- TEMAM, R. 1997 *Infinite-dimensional dynamical systems in mechanics and physics*, 2nd edn. Springer.
- TESSEIN, J. A., SMITH, C. W., MACBRIDE, B. T., MATTHAEUS, W. H., FORMAN, M. A. & BOROVSKY, J. E. 2009 Spectral indices for multi-dimensional interplanetary turbulence at 1 AU. *Astrophys. J.* **692**, 684–693.
- TRAN, C. V., & BLACKBOURN, L. 2009 Number of degrees of freedom of two-dimensional turbulence. *Phys. Rev. E* **79**, 056308.
- TRAN, C. V. 2005 Enstrophy dissipation in freely evolving two-dimensional turbulence. *Phys. Fluids* **17**, 081704.

- TRAN, C. V. 2009 The number of degrees of freedom of three-dimensional Navier–Stokes turbulence. *Phys. Fluids* **21**, 125103.
- TRAN, C. V. & BLACKBOURN, L. A. K. 2012 A dynamical systems approach to fluid turbulence. *Fluid Dyn. Res.* **44**, 031417.
- TRAN, C. V., BLACKBOURN, L. A. K. & SCOTT, R. K. 2011 Number of degrees of freedom and energy spectrum of surface quasi-geostrophic turbulence. *J. Fluid Mech.* **684**, 427–440.
- TRAN, C. V. & DRITSCHER, D. G. 2006 Vanishing enstrophy dissipation in two-dimensional Navier–Stokes turbulence in the inviscid limit. *J. Fluid Mech.* **559**, 107–116.
- TRAN, C. V. & DRITSCHER, D. G. 2010 Energy dissipation and resolution of steep gradients in one-dimensional Burgers flow. *Phys. Fluids* **22**, 037102.
- TRAN, C. V., DRITSCHER, D. G. & SCOTT, R. K. 2010 Effective degrees of nonlinearity in a family of generalized models of two-dimensional turbulence. *Phys. Rev. E* **81**, 016301.
- TRAN, C. V. & YU, X. 2012 Bounds for the number of degrees of freedom of incompressible magnetohydrodynamic turbulence in two and three dimensions. *Phys. Rev. E* **85**, 066323.
- TRAN, C. V., YU, X. & BLACKBOURN, L. A. K. 2013a Two-dimensional magnetohydrodynamic turbulence in the limits of infinite and vanishing magnetic Prandtl number. *J. Fluid Mech.* **725**, 195–215.
- TRAN, C. V., YU, X. & ZHAI, Z. 2013b Note on solution regularity of the generalized magnetohydrodynamic equations with partial dissipation. *Nonlinear Analysis* **85**, 43–51.

- TRAN, C. V., YU, X. & ZHAI, Z. 2013*c* On global regularity of the 2D generalized magnetohydrodynamic equations. *J. Differ. Equations* **254**, 4194–4216.
- UNIVERSITY OF YORK 2013 CPU History. <http://www-users.cs.york.ac.uk/pcc/pc-history/index.html>.
- VERMA, M. K., ROBERTS, D. A., GOLDSTEIN, M. L., GOSH, S. & STRIBLING, W. T. 1996 A numerical study of the nonlinear cascade of energy in magnetohydrodynamic turbulence. *J. Geophys. Res.* **101**, 21619–21625.
- WEINBERGER, H. F. 1987 *Variational Methods for Eigenvalue Approximation*, 2nd edn., *CBMS–NSF Regional Conference Series in Applied Mathematics*, vol. 15. Society of Industrial and Applied Mathematics.
- WEINSTEIN, S., OLSON, P. & YUEN, D. 1989 Time-dependent large aspect-ratio thermal-convection in the earth's mantle. *Geophys. Astrophys. Fluid Dyn* **47**, 157–197.
- WU, J. 2011 Global regularity for a class of generalized magnetohydrodynamic equations. *J. Math. Fluid Mech.* **13**, 295–305.